

CRANFIELD UNIVERSITY

Alice Miranda

Numerical Simulations of the Wing Wake and Tip Vortex
for Air-to-Air Refuelling

School of Engineering
MSc by Research

MSc by Research Thesis
Academic Year: 2011-2012

Supervisor: Dr. David MacManus
October 2012

C Cranfield University

Alice Miranda

Numerical Simulations of the Wing Wake and Tip Vortex
for Air-to-Air Refuelling

School of Engineering
MSc by Research

MSc by Research Thesis
Academic Year: 2011-2012

Supervisor: Dr. David MacManus
October 2012

This thesis is submitted in fulfilment of the requirements
for the degree of Master of Science by Research

© Cranfield University 2012. All rights reserved. No part of this publication may
be reproduced without the written permission of the copyright owner

Abstract

The present research was carried out in the framework of the ASTRAEA II project, in collaboration with Cobham Mission Equipment. One part of the overall ASTRAEA II project is to design an autonomous air-refuelling system based on a wake model computed in real-time, which allows the flow field to be visualised in a Synthetic Environment. In a previous part of the ASTRAEA project a MATLAB® code was developed based on the extended lifting line method (referred to as the ELL code) which provides a refuelling tanker wake model. The aim of this project is to understand the tanker wake, to provide more detailed flow field predictions and to compare the results with the results from the ELL code to validate this reduced fidelity method.

The understanding of the tanker wake and tip vortices was carried out through the use of computational fluid dynamics (CFD) methods. CFD simulations of three geometries were carried out and post-processed: the DLR-F6 aircraft geometry, the CRM aircraft geometry (both similar to the A330) and the NACA0015 swept wing model of Gerontakos and Lee. The latter was used as a validation test case for the CFD modelling of the wake and the tip vortex. The CFD simulations were performed using a geometry definition compatible with the idealised model scale aircraft definitions used in the wind tunnel experiments. Finally comparisons between the available CFD results and the ELL code were carried out.

The ELL code computes a qualitatively similar wake and tip vortex flow field, but only when the code is run with a different set-up which requires more computing resources. The addition of the simple fuselage model to the ELL code has provided an improvement in the results compared with the CFD solutions. The ELL code does not model the vortex roll up and there are notable differences in the near-field region in particular. Although the flow field structure is similar between the ELL and the CFD results, there are notable differences in the local disturbance flow field. In particular, for some configurations, the tip vortex strength is underpredicted by up to a factor of three relative to the CFD results.

Acknowledgements

I would like to express my deepest gratitude to my supervisor, Dr David MacManus, for all the lessons, help and guidance he provided during this research project year. Moreover, I would like to thank him for giving me the opportunity to work on this project and have this unforgettable experience at Cranfield University.

I would also like to acknowledge Cobham Mission Equipment and Dr. James Whidborne for their extremely useful collaboration.

I must thank Robert, Grant, Kishor and Tom, the PhD students that provided very useful advice for my research. A big thanks to Antonio, a colleague who worked on a different aspect of the same project.

I am deeply thankful to my life partner Adi for supporting me throughout this intense year. Without him I would not be where I am.

Moreover, I would like to thank my friend Sophie, with whom I shared a lot of lunches at Cranfield, for having encouraged me in the hard times and a big thanks also to all the office colleagues, in particular Mohammed and Suleiman. Thanks to them the long working days have been funnier.

Last but not least, I must thank my friends back in Italy, in particular Lorenzo, Simone and Nicoletta, who despite the distance, stayed next to me and never stopped giving me their help and support.

Table of Contents

Abstract	v
Acknowledgements	vii
Table of Contents	ix
List of Figures	xii
List of Tables	xx
Nomenclature	xxi
1 Introduction	1
1.1 Introduction to work	1
1.2 Project rationale	1
1.3 Scope of the project	2
1.4 Aim and objectives	2
1.5 Project roadmap	3
1.6 Thesis outline	4
2 Literature review	7
2.1 Air-refuelling	7
2.2 Wake flow field and tip vortices	9
2.3 Experimental studies	12
2.3.1 “Gerontakos swept wing”	13
2.4 Numerical studies	15
2.5 Low fidelity model (ELL code)	18
2.5.1 Prandtl’s classical lifting line theory	18
2.5.2 Weissinger’s extended lifting line theory	20
2.5.3 ELL code summary	21
3 Project overview and methodology	23
3.1 Introduction	23
3.2 Numerical codes	23
3.2.1 ANSYS Fluent code	23
3.2.2 ANSYS CFX code	26
3.3 Identification of the test cases	28
3.4 DLR-F6 geometry	32
3.4.1 Introduction	32

3.4.2	Experimental data available.....	33
3.4.3	CFD simulations domain and boundary conditions.....	34
3.4.4	Grids	35
3.5	Common Research Model (CRM).....	36
3.5.1	Introduction	36
3.5.2	Experimental data available for the CRM.....	37
3.5.3	CFD simulations domain and boundary conditions.....	39
3.5.4	Grids	42
3.6	CFD models of the Gerontakos swept wing test case.....	44
3.6.1	Introduction.....	44
3.6.2	Experimental data available.....	45
3.6.3	CFD simulations domain and boundary conditions.....	45
3.6.4	Grids	47
3.7	Convergence criteria	50
3.7.1	ANSYS Fluent criteria	50
3.7.2	ANSYS CFX criteria	52
3.8	Post-processing.....	54
3.8.1	Tecplot	54
3.8.2	Vortex core and circulation.....	55
4	DLR-F6 results and analysis	59
4.1	Introduction	59
4.2	DLR-F6 Results.....	59
5	CRM at wind tunnel scale.....	69
5.1	Introduction	69
5.2	Wing-body CRM geometry at wind tunnel scale results.....	69
6	Validation test case results	79
6.1	Introduction	79
6.2	“Gerontakos swept wing” simulations.....	79
6.3	Comparison with the experimental data	83
7	Results from the ELL method	93
7.1	Introduction.....	93
7.2	ELL code study.....	94
7.3	ELL code with fuselage of the CRM at wind tunnel scale	96
7.4	ELL code of the CRM full-scale geometry under air-refuelling conditions	111

7.4.1 Flight condition 1 results	112
7.4.2 Flight condition 2 results	116
7.4.3 Flight condition 3 results	122
7.4.4 Flight condition 4 results	124
7.5 Summary of findings.....	127
8 Conclusions	129
8.1 Introduction.....	129
8.2 Main findings.....	129
References	131
Appendix A.....	136
ELL code of the “Gerontakos swept wing”	136

List of Figures

Fig. 1.1 Project roadmap.....	4
Fig. 2.1 Air-refuelling “flying boom” [14] and “hose-and-drogue” [15] methods. 8	
Fig. 2.2 Aircraft trailing vortices [26]	9
Fig. 2.3 Tip vortex formation at the trailing edge [26]	10
Fig. 2.4 Schematic representation of a simplified model configuration [27]	12
Fig. 2.5 Geometric characteristics of the Gerontakos and Lee model [31]	14
Fig. 2.6 Superposition of horseshoe vortices along the lifting line in Prandtl’s classical lifting line theory [12]	19
Fig. 2.7 Superposition of horseshoe vortices along the lifting line in Weissinger’s extended lifting line theory [12]	21
Fig. 3.1 Airbus A330 main dimensions [33]	28
Fig. 3.2 DLR-F6 main dimensions at model scale [36]	29
Fig. 3.3 Main dimensions of the full-scale CRM geometry [37]	29
Fig. 3.4 Aircraft geometric characteristics	30
Fig. 3.5 DLR-F6 wind tunnel model [17]	33
Fig. 3.6 Cartesian far-field domain of the DLR-F6 geometry	34
Fig. 3.7 Surface mesh of the medium grid (5 million cells)	36
Fig. 3.8 Density of the volume mesh in the wing wake of the 9 million cells grid	36
Fig. 3.9 NASA CRM wind tunnel model [18]	38
Fig. 3.10 NASA Common Research Model	38
Fig. 3.11 Cartesian far-field domain of the CRM geometry	41
Fig. 3.12 Surface mesh on the CRM geometry of the no-tail scaled at wind tunnel conditions 7 million cells grid	43
Fig. 3.13 Far-field of the no-tail scaled at wind tunnel conditions 7 million cells grid	44
Fig. 3.14 Density of the volume mesh in the wing wake of the 7 million cells grid	44

Fig. 3.15 “Gerontakos swept wing” downstream velocity measurements configuration [31]	46
Fig. 3.16 Domain (left image) and boundaries main dimensions (right image) of the “Gerontakos swept wing” model	47
Fig. 3.17 Far-field (left image) and prism layers (right image) of the “Gerontakos swept wing” 7 million cells grid	48
Fig. 3.18 Densities of the volume mesh in the wing wake of the “Gerontakos swept wing” 7 million cells grid	48
Fig. 3.19 Densities of the volume mesh in the wing wake of the “Gerontakos swept wing” 12 million cells grid	49
Fig. 3.20 Detail of the densities of the volume mesh in the wing wake of the “Gerontakos swept wing” 12 million cells grid in a XY plane	49
Fig. 3.21 Detail of the densities of the volume mesh in the wing wake of the “Gerontakos swept wing” 12 million cells grid in a YZ plane.....	50
Fig. 3.22 Typical residual plot of a CRM geometry simulation	51
Fig. 3.23 Lift and drag coefficients monitor plot of a CRM geometry simulation	51
Fig. 3.24 Typical residual plot of a Gerontakos swept wing case simulation.....	52
Fig. 3.25 Typical residual plot of a CRM geometry simulation	53
Fig. 3.26 Lift and drag coefficients monitor plot of a CRM geometry simulation	54
Fig. 3.27 Example of circular zone for one of the slices with the centre located in the centre of the vortex	56
Fig. 3.28 Example of circular zone for one of the slices with the centre located in the centre of the vortex	57
Fig. 3.29 Circular zone disc mesh	57
Fig. 4.1 Comparison of the lift coefficient values with different solvers and grids	60
Fig. 4.2 Drag coefficient values with different solvers and grids	61
Fig. 4.3 Comparison of the lift coefficient values of the 5 million cells grid with different solvers and turbulence models	62
Fig. 4.4 Drag coefficient values of the 5 million cells grid with different solvers and turbulence models	62

Fig. 4.5 Location of different η on the DLR-F6 geometry63

Fig. 4.6 Pressure coefficient distributions at $\eta=0.15$ of the 5 million cells grid with different solvers and turbulence models – $Re=3 \times 10^6$, CFD $\alpha=0.2007^\circ$, EXP $\alpha=0.490^\circ$ $C_L=0.4984$ 64

Fig. 4.7 Pressure coefficient distributions at $\eta=0.331$ of the 5 million cells grid with different solvers and turbulence models – $Re=3 \times 10^6$, CFD $\alpha=0.2007^\circ$, EXP $\alpha=0.490^\circ$ $C_L=0.4984$ 64

Fig. 4.8 Pressure coefficient distributions at $\eta=0.636$ of the 5 million cells grid with different solvers and turbulence models – $Re=3 \times 10^6$, CFD $\alpha=0.2007^\circ$, EXP $\alpha=0.490^\circ$ $C_L=0.4984$ 65

Fig. 4.9 Pressure coefficient distributions at $\eta=0.15$ with different solvers and grids – $Re=3 \times 10^6$, CFD $\alpha=0.2007^\circ$, EXP $\alpha=0.490^\circ$ $C_L=0.4984$ 65

Fig. 4.10 Pressure coefficient distributions at $\eta=0.331$ with different solvers and grids – $Re=3 \times 10^6$, CFD $\alpha=0.2007^\circ$, EXP $\alpha=0.490^\circ$ $C_L=0.4984$ 66

Fig. 4.11 Pressure coefficient distributions at $\eta=0.636$ with different solvers and grids – $Re=3 \times 10^6$, CFD $\alpha=0.2007^\circ$, EXP $\alpha=0.490^\circ$ $C_L=0.4984$ 66

Fig. 5.1 Lift coefficient distributions of the CRM geometry at wind tunnel scale 71

Fig. 5.2 C_L - C_d distributions of the CRM geometry at wind tunnel scale 71

Fig. 5.3 Location of different η on the CRM geometry at wind tunnel scale 72

Fig. 5.4 Pressure coefficient distribution at $\eta=0.131$ of the 5 million cells and 9 million cells grids with SST turbulence model – $Re=5 \times 10^6$, 7 million cells $\alpha=2.6^\circ$, 15 million cells $\alpha=2.26^\circ$, NASA FUN3D $C_L=0.5$ 73

Fig. 5.5 Pressure coefficient distribution at $\eta=0.283$ of the 5 million cells and 9 million cells grids with SST turbulence model – $Re=5 \times 10^6$, 7 million cells $\alpha=2.6^\circ$, 15 million cells $\alpha=2.26^\circ$, NASA FUN3D $C_L=0.5$ 74

Fig. 5.6 Pressure coefficient distribution at $\eta=0.397$ of the 5 million and 9 million cells grids with SST turbulence model – $Re=5 \times 10^6$, 7 million cells $\alpha=2.6^\circ$, 15 million cells $\alpha=2.26^\circ$, NASA FUN3D $C_L=0.5$ 74

Fig. 5.7 Pressure coefficient distribution at $\eta=0.502$ of the 5 million and 9 million cells grids with SST turbulence model – $Re=5 \times 10^6$, 7 million cells $\alpha=2.6^\circ$, 15 million cells $\alpha=2.26^\circ$, NASA FUN3D $C_L=0.5$ 75

Fig. 5.8 Pressure coefficient distribution at $\eta=0.727$ of the 5 million cells and 9 million cells grids with SST turbulence model – $Re=5 \times 10^6$, <u>7 million cells</u> $\alpha=2.6^\circ$, <u>15 million cells</u> $\alpha=2.26^\circ$, <u>NASA FUN3D</u> $C_L=0.5$	75
Fig. 5.9 Pressure coefficient distribution at $\eta=0.846$ of the 5 million cells and 9 million cells grids with SST turbulence model – $Re=5 \times 10^6$, <u>7 million cells</u> $\alpha=2.6^\circ$, <u>15 million cells</u> $\alpha=2.26^\circ$, <u>NASA FUN3D</u> $C_L=0.5$	76
Fig. 5.10 Pressure coefficient distribution at $\eta=0.950$ of the 5 million cells and 9 million cells grids with SST turbulence model – $Re=5 \times 10^6$, <u>7 million cells</u> $\alpha=2.6^\circ$, <u>15 million cells</u> $\alpha=2.26^\circ$, <u>NASA FUN3D</u> $C_L=0.5$	76
Fig. 6.1 “Gerontakos swept wing” downstream velocity measurements configuration [31]	80
Fig. 6.2 “Gerontakos swept wing” force and moment measurements configuration [31]	81
Fig. 6.3 “Gerontakos swept wing” model lift coefficient distributions.....	82
Fig. 6.4 Downstream locations of the considered planes	83
Fig. 6.5 V_θ distributions at $X/Cr=1$; $Z/Cr=0$ corresponds to the centre of the vortex.....	84
Fig. 6.6 Axial vorticity distributions at $X/Cr=1$; $Z/Cr=0$ corresponds to the centre of the vortex	85
Fig. 6.7 Axial velocity distributions at $X/Cr=1$; $Z/Cr=0$ corresponds to the centre of the vortex	85
Fig. 6.8 V_θ distributions at $X/Cr=2$; $Z/Cr=0$ corresponds to the centre of the vortex.....	86
Fig. 6.9 Axial vorticity distributions at $X/Cr=2$; $Z/Cr=0$ corresponds to the centre of the vortex	86
Fig. 6.10 Axial velocity distributions at $X/Cr=2$; $Z/Cr=0$ corresponds to the centre of the vortex	87
Fig. 6.11 Radial circulation distributions at $X/Cr=1$	87
Fig. 6.12 Radial circulation distributions at $X/Cr=2$	88
Fig. 6.13 Vortex core radius at different X/Cr planes.....	89
Fig. 6.14 $V_{\theta peak}$ values at different X/Cr planes.....	90
Fig. 6.15 Core circulation at different X/Cr planes.....	90
Fig. 6.16 Total vortex circulation at different X/Cr planes.....	91

Fig. 7.1 Vortex panels sample of the ELL code wing.....	95
Fig. 7.2 Wing model in the ELL code	95
Fig. 7.3 ELL vectors with 12 (Case C) and 40 (Case D) number of panels	97
Fig. 7.4 Wing-fuselage model dimensions of the ELL code	98
Fig. 7.5 Wing-fuselage model of the ELL code	99
Fig. 7.6 Near-field of the CRM geometry at wind tunnel scale	100
Fig. 7.7 Location of the CRM geometry wake considered planes	100
Fig. 7.8 V_y induced velocity of the ELL code with and without fuselage at $X/C_{ref}=5$ compared with the CFD results at the same wind tunnel flight conditions and downstream plane	101
Fig. 7.9 Vectors of the CRM geometry scaled at wind tunnel sizes. Comparison of the CFD and ELL code with fuselage results at CRM flight conditions (the vector magnitude is on the same scale) at $X/C_{ref}=0.5$	102
Fig. 7.10 Vectors of the CRM geometry scaled at wind tunnel sizes. Comparison of the CFD and ELL code with fuselage results at CRM flight conditions (the vector magnitude is on the same scale) at $X/C_{ref}=2.5$	103
Fig. 7.11 Vectors of the CRM geometry scaled at wind tunnel sizes. Comparison of the CFD and ELL code with fuselage results at CRM flight conditions (the vector magnitude is on the same scale) at $X/C_{ref}=5$	103
Fig. 7.12 Induced spanwise velocity field (V_y) for the CRM geometry scaled at wind tunnel sizes. Comparison of the CFD and ELL code with fuselage results at CRM flight conditions at $X/C_{ref}=0.5$	104
Fig. 7.13 Induced spanwise velocity field (V_y) for the CRM geometry scaled at wind tunnel sizes. Comparison of the CFD and ELL code with fuselage results at CRM flight conditions at $X/C_{ref}=5$	104
Fig. 7.14 Induced spanwise velocity field (V_z) for the CRM geometry scaled at wind tunnel sizes. Comparison of the CFD and ELL code with fuselage results at CRM flight conditions at $X/C_{ref}=0.5$	105
Fig. 7.15 Induced spanwise velocity field (V_z) for the CRM geometry scaled at wind tunnel sizes. Comparison of the CFD and ELL code with fuselage results at CRM flight conditions at $X/C_{ref}=5$	105

Fig. 7.16 Horizontal traverse V_z values of the CRM geometry scaled at wind tunnel sizes. Comparison of the CFD and ELL code with fuselage results at CRM flight conditions at $X/C_{ref}=0.5$ and $X/C_{ref}=5$	106
Fig. 7.17 Vertical traverse V_z values of the CRM geometry scaled at wind tunnel sizes. Comparison of the CFD and ELL code with fuselage results at CRM flight conditions at $X/C_{ref}=0.5$ and $X/C_{ref}=5$	107
Fig. 7.18 Induced spanwise velocity field (V_x) for the CRM geometry scaled at wind tunnel sizes. Comparison of the CFD and ELL code with fuselage results at CRM flight conditions at $X/C_{ref}=2.5$	107
Fig. 7.19 Dynamic pressure of the CRM geometry scaled at wind tunnel sizes. Comparison of the CFD and ELL code with fuselage results at CRM flight conditions at $X/C_{ref}=2.5$	108
Fig. 7.20 Dynamic pressure of the CRM geometry scaled at wind tunnel sizes. Comparison of the CFD and ELL code with fuselage results at CRM flight conditions at $X/C_{ref}=5$	109
Fig. 7.21 Vortex core radius of the CRM geometry scaled at wind tunnel sizes. Comparison of the CFD and ELL code with fuselage results at CRM flight conditions at various X/C_{ref}	110
Fig. 7.22 Core circulation of the CRM geometry scaled at wind tunnel sizes. Comparison of the CFD and ELL code with fuselage results at CRM flight conditions at various X/C_{ref}	110
Fig. 7.23 Total vortex circulation of the CRM geometry scaled at wind tunnel sizes. Comparison of the CFD and ELL code with fuselage results at CRM flight conditions at various X/C_{ref}	111
Fig. 7.24 V_z velocity of the of the CFD results of the CRM geometry scaled at wind tunnel conditions without tail and of the CRM geometry full-scale with tail at flight condition 3	112
Fig. 7.25 Vectors of the CRM geometry full-scale of the Fluent CFD at flight condition 1 at $X/C_{ref}=7.5$	113
Fig. 7.26 Downwash angle of the CRM geometry full-scale with tail. Comparison of the Fluent CFD and ELL code results with flight condition 1 at $X/C_{ref}=7.5$	114

Fig. 7.27 CFX CFD non-dimensional axial vorticity (ζ_b/V_∞) of the CRM geometry full-scale with flight condition 1 at $X/C_{ref}=7.5$115

Fig. 7.28 Downwash angle of the CRM geometry full-scale. Comparison of the CFX CFD and ELL code results with flight condition 1 at $X/C_{ref}=7.5$ 115

Fig. 7.29 Yaw angle of the CRM geometry full-scale. Comparison of the CFX CFD and ELL code results with flight condition 1 at $X/C_{ref}=7.5$ 116

Fig. 7.30 CFD non-dimensional axial vorticity (ζ_b/V_∞) of the CRM geometry full-scale with flight condition 2 at $X/C_{ref}=5$ 117

Fig. 7.31 Yaw angle of the CRM geometry full-scale. Comparison of the CFD and ELL code results with flight condition 2 at $X/C_{ref}=2.5$ 118

Fig. 7.32 Yaw angle of the CRM geometry full-scale. Comparison of the CFD and ELL code with fuselage results with flight condition 2 at $X/C_{ref}=5$ 118

Fig. 7.33 Yaw angle of the CRM geometry full-scale. Comparison of the CFD and of the standard settings ELL code with fuselage results with flight condition 2 at $X/C_{ref}=2.5$ 119

Fig. 7.34 Vectors of the CRM geometry full-scale of the standard settings ELL code with fuselage results with flight condition 2 at $X/C_{ref}=2.5$ 120

Fig. 7.35 Yaw angle of the CRM geometry full-scale. Comparison of the CFD and of the standard settings ELL code with fuselage results with flight condition 2 at $X/C_{ref}=5$ 120

Fig. 7.36 Vectors of the CRM geometry full-scale of the standard settings ELL code with fuselage results with flight condition 2 at $X/C_{ref}=5$ 121

Fig. 7.37 $V_{\theta_{peak}}$ at different X/C_r for flight condition 2.....121

Fig. 7.38 Total vortex circulation at different X/C_r for flight condition 2 122

Fig. 7.39 Downwash of the CRM geometry full-scale. Comparison of the CFD and ELL code with fuselage results with flight condition 3 at $X/C_{ref}=5$.. 123

Fig. 7.40 Horizontal traverse V_y and V_z values of the CRM geometry full-scale. Comparison of the CFD and ELL code with fuselage results with flight condition 3 123

Fig. 7.41 V_y induced velocity of the CRM geometry full-scale. Comparison of the CFD and ELL code with fuselage results with flight condition 4 at $X/C_{ref}=5$ 125

Fig. 7.42 Vectors of the CRM geometry full-scale. Comparison of the CFD and ELL code with fuselage results at flight condition 4 (the vector magnitude is on the same scale) at $X/C_{ref}=0.5$	126
Fig. 7.43 Vectors and yaw angle of the CRM geometry full-scale of the standard settings ELL code with fuselage results with flight condition 1 at $X/C_{ref}=0.5$	126
Fig. A.1 Downstream locations of the considered planes	137
Fig. A.2 Tangential velocity vectors in the $X/C_r=1$ plane (the vector magnitude is on the same scale)	138
Fig. A.3 Tangential velocity vectors in the $X/C_r=2$ plane (the vector magnitude is on the same scale)	138
Fig. A.4 Tangential velocity vectors in the $X/C_r=2.75$ plane (the vector magnitude is on the same scale)	139
Fig. A.5 V_y velocity component in the $X/C_r=1$ plane	140
Fig. A.6 V_y velocity component in the $X/C_r=2$ plane	140
Fig. A.7 V_y velocity component in the $X/C_r=2.75$ plane	141
Fig. A.8 V_z velocity component in the $X/C_r=1$ plane	141
Fig. A.9 V_z velocity component in the $X/C_r=2$ plane	142
Fig. A.10 V_y velocity component in the $X/C_r=2.75$ plane	142
Fig. A.11 V_x velocity component in the $X/C_r=1$ plane	143
Fig. A.12 V_x velocity component in the $X/C_r=2$ plane	143
Fig. A.13 V_x velocity component in the $X/C_r=2.75$ plane	144

List of Tables

Table 3.1 Comparison between the available geometries and the A330	31
Table 3.2 Main characteristics of the available geometries.....	32
Table 3.3 Main DLR-F6 geometry CFD simulations	33
Table 3.4 Wing-body CRM geometry at wind tunnel scale CFD simulations....	40
Table 3.5 CRM geometry at wind tunnel scale boundary conditions.....	40
Table 3.6 Full-scale wing-body-tail CRM geometry CFD simulations.....	41
Table 3.7 Air-refuelling flight conditions agreed.....	41
Table 3.8 Grids of the CRM geometry	43
Table 3.9 CFD simulations of the “Gerontakos swept wing”	45
Table 3.10 Boundary conditions of the “Gerontakos swept wing”	45
Table 4.1 DLR-F6 geometry characteristics.....	59
Table 4.2 CFD simulations boundary conditions	59
Table 5.1 CRM geometry scaled at wind tunnel conditions characteristics	69
Table 5.2 C_L and C_d values.....	70
Table 6.1 Boundary conditions of the “Gerontakos swept wing” simulation.....	79
Table 7.1 Geometric characteristics of the considered wing	94
Table 7.2 Flight conditions applied in the ELL code	94
Table 7.3 Cases and running times	97
Table 7.4 Geometric characteristics of the considered fuselage.....	98
Table 7.5 Flight conditions applied in the ELL code	98
Table 7.6 CRM geometry wing-body-tail full-scale CFD simulations.....	111
Table A.1 Geometric characteristics of the considered wing.....	136
Table A.2 Flight conditions applied in the ELL code	137

Nomenclature

AR	Aspect ratio (b^2/S_{ref})
b	Wing span
b_0	Lateral distance between two trailing vortices
C	Chord
C_r	Root chord
C_{ref}	Mean reference chord
C_d	Drag coefficient
C_L	Lift coefficient
L	Lift
M_∞	Free-stream Mach number
Re	Reynolds number
r_c	Viscous core radius
r_v	Vorticity radius
S_{ref}	Wing reference area
V_∞	Free-stream velocity
V_x	Axial (streamwise) velocity
V_y	Lateral (spanwise) velocity
V_z	Vertical velocity
\bar{V}_x	Axial (streamwise) mean velocity
\bar{V}_y	Lateral (spanwise) mean velocity
\bar{V}_z	Vertical mean velocity
x, y, z	Cartesian coordinates

Greek Symbols

α	Angle of attack
Γ	Circulation
Γ_0	Root circulation
δ	Pressure ratio

θ	Temperature ratio
$\Lambda_{C/4}$	Sweep of C\4 line
λ	Taper ratio
ξ	Non-dimensional mean axial vorticity
ω	Vorticity
ω_x	Mean axial vorticity

Abbreviations

2D	Two-dimensional
3D	Three-dimensional
A330	Airbus A330
AIAA	American Institute of Aeronautics and Astronautics
AOA	Angle of attack
CFD	Computational Fluid Dynamics
CPU	Central Processing Unit
CRM	Common Research Model
DES	Detached Eddy Simulation
DLR	German Aerospace Centre
ELL	Extended Lifting Line
FAS	Full Approximation Storage Method
FC	Flight Condition
ILU	Incomplete Lower Upper
LES	Large Eddy Simulation
MIL	Million
MRTT	Multi Role Tanker Transport
NACA	National Advisory Committee for Aeronautics
NASA	National Aeronautics and Space Administration
NED	North-east-down reference frame
NSEG	Number of panels
NTF	National Transonic Facility
RANS	Reynolds-averaged Navier–Stokes
RHS	Right Hand Side

RMS	Root Mean Square
SA	Spalart-Allmaras
SST	Shear-Stress Transport
TCL	Two-component Limit
TWT	Transonic Wind Tunnel
WB	Wing-body configuration
WBPN	Wing-body-pylon-nacelle configuration
WBT	Wing-body-tail configuration

Chapter 1

Introduction

1.1 Introduction to work

The understanding of the wake and of the pair of counter-rotating vortices generated by an aircraft's wing tips is an important area of study in the aviation industry and academic research fields. Much of this work is related to their hazardous effects on flight safety [1]. Even though in the literature there are several experimental and Computational Fluid Dynamics (CFD) studies concerning the prediction of aircraft wakes and trailing vortices, most of them are focused on safety aspects for civil wake encounter avoidance and most of the analyses are about the far-field characteristics, the time evolution and the wake behaviour for landing and take-off aircraft [2]-[9]. From the air-to-air refuelling point of view, the typical flight environments are the in-cruise conditions and the wake flow fields of interest are the near or mid-field. There are very few publications regarding CFD work in the specific area of air-to-air refuelling [10]. Past studies concerning the analysis and understanding of these specific conditions and zones are relatively few. The aim of this MSc-by-research thesis is to increase the knowledge in this area.

1.2 Project rationale

The present research was carried out in the framework of the ASTRAEA II project, in collaboration with Cobham Mission Equipment. One part of the overall ASTRAEA II project purpose is to design an autonomous air-refuelling system based on a wake model computed in real-time, which allows the flow field to be visualised in a Synthetic Environment. Many organisations are

involved in the project, covering a large spectrum of knowledge and aspects in the aerospace field.

In a previous part of the ASTRAEA II project a MATLAB® code was developed based on the extended lifting line method which provides a refuelling tanker wake model, referred to as the “ELL code” [11][12]. The code presents many advantages, particularly the ability to be incorporated into a real-time system, but it has a disadvantage in the fidelity of the predicted tanker wake. Indeed one of the principal deliverables of this MSc thesis is to provide an evaluation of the capability of the ELL code to predict the vortical flow field through the use of higher fidelity CFD methods.

1.3 Scope of the project

This project covers the study of the near and mid-field of the wake and the vortices generated by a modern transport aircraft in cruise and refuelling conditions. The investigation was carried out through CFD simulations. The scope is to perform an investigation in the air-refuelling configurations and to achieve a better understanding of the wake generated by a refuelling tanker aircraft. Since the study is about the near and mid-field region, the receiver aircraft is not included in the CFD model. The reference tanker for this project is the Airbus A330, however the aircraft geometry that was used for the numerical simulations is a simpler, open-source version of a real tanker and therefore the jet engines, flaps and winglets are not present in the geometry. The final scope of the project is the validation of the low fidelity ELL code in which the aircraft is modelled as a pair of wings and a flat plate fuselage. For this reason, the computational results do not involve a complex aircraft geometry and the general flow field and the wing tip vortex characteristics are the main results which are assessed.

1.4 Aim and objectives

The aim of this thesis is to understand the tanker wake and to provide more detailed flow field predictions through the use of CFD methods. In particular the study’s goal is to predict the flow field of the wing wake in the near-field

region and to compare the results with the ELL code flow field in order to evaluate this low fidelity method.

The specific objectives of the research are:

- to define a geometry as much as possible similar to the A330;
- to find a validation test case for the wake velocity field and the tip vortex;
- to understand and quantify the tip vortices generated by an aircraft;
- to simulate, through CFD methods, a full-scale aircraft geometry with air-to-air refuelling conditions;
- to compare the CFD results and the ELL code and to provide an evaluation of the low fidelity model's behaviour.

1.5 Project roadmap

To achieve the aim of the project and validate the ELL code several steps were necessary. Fig. 1.1 summarises the steps of the project. The first critical part involved the individuation and selection of the test cases used in the project. The CFD validation section was carried out through two main parts: the first concerned the force and moment data and the latter regarded the wake downstream velocity flow field. The obtained results were compared with the ELL code in order to achieve a first evaluation of the code. A study about the CFD codes, grids and turbulence models was carried out as well. As a final step, simulations with the air-refuelling flight conditions were performed and the results were compared with the ELL code to achieve a final evaluation of it.

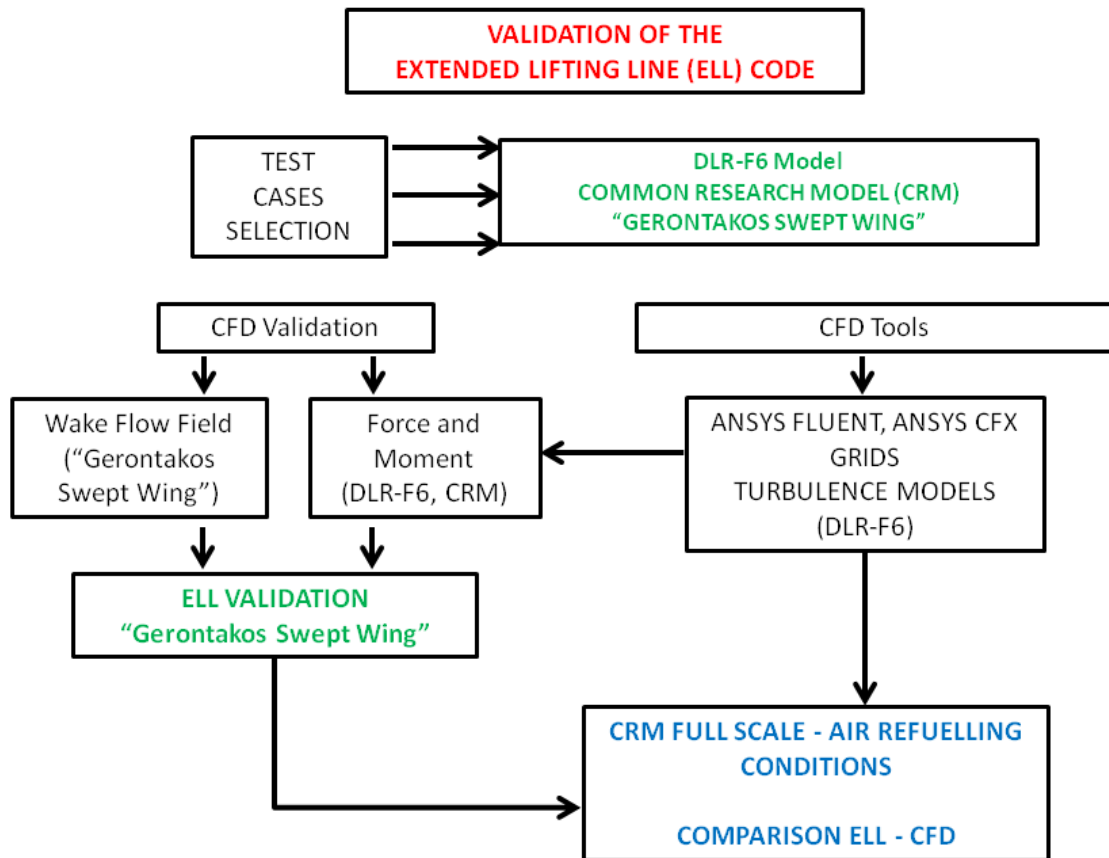


Fig. 1.1 Project roadmap

1.6 Thesis outline

This thesis is composed of eight chapters and its structure is described below:

- *Chapter 1 – Introduction:* in this chapter the background information of this thesis is introduced. The aims and objectives are stated together with the project rationale and scope.
- *Chapter 2 – Literature review:* in this chapter the theories of wake flow field and vortices are described. A literature review of past studies is presented and a description of two important experimental and CFD studies about commercial modern aircraft is included as well. Furthermore, a review of the lifting line theory is provided, since it is the basis of the ELL code.
- *Chapter 3 – Project overview and methodology:* this chapter describes the test cases that were used in the study, the grids that were generated and the CFD codes that were adopted. Moreover, the utilised post-processing techniques are described.

- *Chapter 4 and 5 – CFD results:* these two chapters describe the validation results of the two aircraft geometries test cases in terms of forces and pressure distributions. Furthermore, a study about the turbulence models, the boundary conditions and the codes themselves was carried out.
- *Chapter 6 – Validation test case results:* this chapter presents the CFD results of the validation test case for the downstream velocities compared with the experimental data.
- *Chapter 7 – Results from the ELL method:* this chapter describes the evaluation of the ELL code, through comparisons between the CFD and the ELL code results while applying various models and boundary conditions. The final evaluation of the ELL code is performed with the air-refuelling flight conditions.
- *Chapter 8 – Conclusions:* this chapter is dedicated to a conclusion of the research and includes a summary of the performances of the ELL code.

Chapter 2

Literature review

2.1 Air-refuelling

The trailing vortex field generated by an aircraft in flight affects the dynamics of the follower aircraft flying closely behind it. This aerodynamic effect was perceived as a mixed blessing in the aerospace community. For example, while in a formation flight, the effect of the leader's vortices on the follower can be beneficial in reducing drag and fuel consumption [13], the influence of the tanker's vortices on the receiver aircraft during air-refuelling is harmful to the stability of the receiver aircraft. Likewise, the effect of the wake vortex from the preceding aircraft is a cause for major concern during aircraft takeoff and landing operations [13].

In today's refuelling fleet the two most common refuelling methods are the "flying boom" and the "hose-and-drogue" (Fig. 2.1). The former consists of a rigid, telescoping tube (the boom) that an operator on the tanker aircraft extends and inserts into a receptacle on the aircraft being refuelled. The latter utilises a flexible hose that trails from the tanker aircraft; a drogue at the end of the hose stabilises it in flight and supplies a funnel for the refuelled aircraft, which inserts a probe into the hose [16]. The "flying boom" method is used by the US Air Force fixed-wing aircraft. US Air Force helicopters, Navy and Marine Corps as well as NATO countries and some of their allies use the "hose-and-drogue" method. Also the converted Airbus A330 Multi Role Tanker Transport (MRTT) of Cobham Mission Equipment employs the "hose-and-drogue" refuelling system [16].



Fig. 2.1 Air-refuelling “flying boom” [14] and “hose-and-drogue” [15] methods.

In literature there are many studies about the aerodynamic influence of a tanker on the receiver [13]-[25], but only very few of them are CFD studies. All the studies and simulations are based on different approximated models, such as the vortex lattice method. Hoganson [20] used a vortex lattice code to evaluate the effects of KC-135 and KC-10 tankers on a B-52 receiver. It was discovered that the upwash from the B-52 wing increased the KC-10 lift by about 3%. Most of this increase was at the tail, which would result in a nose down moment. Even though no comparisons were made with test data, the results were in qualitative agreement with the effects noted by pilots during actual refuelling. Bloy and Trochaldis [21] found that a hybrid horseshoe vortex-vortex lattice technique well compared with flight test results of tanker-receiver combinations of comparable size. In another paper [22] the results were compared with more detailed wind tunnel experiments that were performed. Furthermore, Blake et al. [23] captured the tanker wake effect on the receiver with a vortex lattice method.

The success of the development of fully autonomous refuelling systems depends upon the accurate prediction of the movement of the paradrogue assembly and the position of the receiver airplane. This kind of prediction is an ambitious task. It is important to take into account all the major factors that influence the dynamics of the follower aircraft. The most significant one is the aerodynamic coupling of the receiver with the tanker aircraft through the trailing wake-vortex system, because this system generates a non-uniform flow field over the follower aircraft, which induces additional forces and moments [25].

2.2 Wake flow field and tip vortices

A vortex flow is an aerodynamic flow that involves free shear layers and vortex cores, and these features are very important in aircraft aerodynamics [26]. As discussed in the previous paragraph, understanding the wake flow field behind an aircraft in air refuelling is critical. The follower aircraft that encounters a trailing wake vortex can be affected by different phenomena depending on its position relative to the vortex: upwind or downwind field, induced rolling moment and velocity fluctuations (Fig. 2.2).

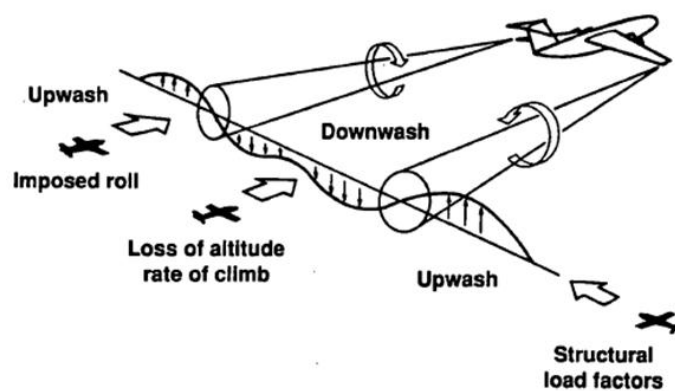


Fig. 2.2 Aircraft trailing vortices [26]

In the literature there are numerous review papers that summarise the state of the art regarding the wake vortex research activity during the years. One of these is the paper written by Breitsamter [27] where experimental and CFD results are presented along with various definitions. The wake vortex mechanism of formation is described as a consequence of the lift produced by an aircraft. For a wing generating lift, the pressure on the lower surface is higher than the pressure on the upper surface. The flowing of the air around the wing tip from the lower surface to the upper surface produces a strong vortex, called “wing tip vortex”(Fig. 2.3). Furthermore, there is the formation of a free shear layer (vortex sheet), due to the fact that the fluid coming from the upper and lower surfaces has a different sense of direction at the wing trailing edge. This vortex sheet rolls up with the tip vortex into a “single rolled up vortex for the left and right wings, respectively” [27].

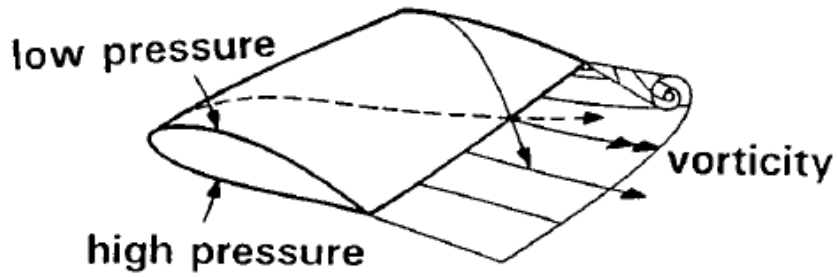


Fig. 2.3 Tip vortex formation at the trailing edge [26]

Breitsamter [27] presents also an exact definition of the difference between the near, middle and far field of the aircraft wake. “Considering the downstream development, a vortex wake can be divided in four regions:

- The near field, $x/b \leq 0.5$, which is characterized by the formation of highly concentrated vortices shed at all surfaces discontinuities.
- The extended near field, $0.5 < x/b \leq 10$, where the wake roll up process takes place and the merging of dominant vortices occurs, which leads gradually to two counter-rotating vortices.
- The mid and far field, $10 < x/b \leq 100$, where the wake is descending in the atmosphere and linear instabilities emerge.
- The dispersion region, $x/b > \sim 100$, where fully developed instabilities cause a strong interaction between the two vortices until they collapse.”

Breitsamter defines and illustrates the basic quantities that define the wake vortex flow-field. The velocity field is described from the three time dependant components of the velocity, V_x , V_y and V_z . V_x is the axial component directed as the flow, V_y is the lateral component and V_z is the vertical component. These are usually expressed by a mean (time averaged) value (\bar{V}_x) and a fluctuation part (V'_x). For example for the axial component it is:

$$V_x(x, y, z, t) = \bar{V}_x(x, y, z) + V'_x(x, y, z, t) \quad (1)$$

The mean axial vorticity is the axial component of the vorticity vector. The strength of the wake is quantified by this quantity. The vorticity vector is:

$$\omega = \left(\frac{\partial V_z}{\partial y} - \frac{\partial V_y}{\partial z} \right) i + \left(\frac{\partial V_x}{\partial z} - \frac{\partial V_z}{\partial x} \right) j + \left(\frac{\partial V_y}{\partial x} - \frac{\partial V_x}{\partial y} \right) k \quad (2)$$

Then the mean axial vorticity is expressed by:

$$\omega_x = \left(\frac{\partial \bar{v}_z}{\partial y} - \frac{\partial \bar{v}_y}{\partial z} \right) \quad (3)$$

A dimensionless representation of free-stream velocity, V_∞ , and the wing half span, $b/2$, or the reference chord, C_{ref} , is commonly used, resulting in:

$$\xi = \frac{\omega_x b}{2V_\infty} \quad (4)$$

$$\xi = \frac{\omega_x C_{ref}}{V_\infty} \quad (5)$$

The circulation is a quantity related to the aerodynamic lift and is defined as “the negative of the line integral of velocity around a closed curve in the flow” [28]:

$$\Gamma = - \oint_C V \cdot ds \quad (6)$$

The minus in the equation is placed in order to obtain a clockwise positive circulation. As described by Breitsamter [27] the circulation can be also obtained applying the Kutta-Joukowski theorem to the lift expression:

$$dL = \rho_\infty V_\infty \Gamma(y) dy \quad (7)$$

with $L = \rho_\infty V_\infty \Gamma_0 b_0$. The dimension b_0 corresponds to the lateral distance of the rolled-up vortices. It reflects the left and right centres of the free circulation. Moreover, circulation is related to vorticity from the following equation:

$$\Gamma \equiv - \oint_C V \cdot ds = - \iint_S (\nabla \times V) \cdot ds \quad (8)$$

Then, the circulation about a curve C is defined as equal to the vorticity integrated over any open surface bounded by C. It has to be noticed that $\Gamma=0$ if the flow is irrotational everywhere within the contour of the integration. Breitsamter gives also a definition of the viscous core radius, r_c , and of the vorticity radius, r_v . The viscous core radius is defined as “half the distance between the maxima of the vortex induced circumferential velocities”. Fig. 2.4 illustrates a schematic representation of a simplified model configuration of a pair of counter-rotating axisymmetric vortices of equal strength.

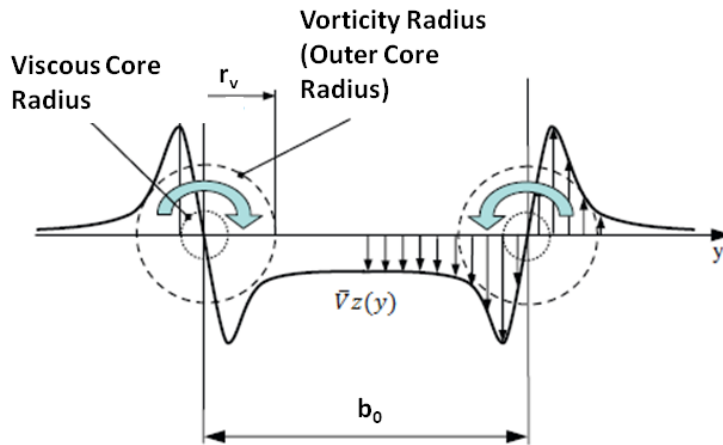


Fig. 2.4 Schematic representation of a simplified model configuration [27]

Within this model Breitsamter [27] divides the vortex induced velocity field into “three areas starting at the vortex centre and progressing outward:

- an inner vortex core, strongly dominated by viscosity and defined by the viscous core radius, r_c ;
- the rotational core, where there is a gradual change in the dominance of viscous and convective forces, quantified by the vorticity radius, r_v ;
- an outer region where the induced velocities can be approximately represented by inviscid flow modelling due to a potential vortex.”

Another important quantity that defines the vortex is the tangential velocity, V_θ , defined as:

$$V_\theta = \frac{\Gamma}{2\pi r} \quad (9)$$

outside the core of an axisymmetric vortex [1]. The tangential velocity can be also defined as the azimuthal component of the velocity in angular coordinates, and therefore in a vortex based reference system.

2.3 Experimental studies

In literature there are many experimental aerodynamic investigations about generic transport aircraft, performed in order to analyse the aerodynamic characteristics and performances of the considered model. One of these is the experimental analysis conducted by Rudnik et al. [17] on the DLR-F6 geometry,

performed in the ONERA S2MA wind tunnel facility. A free-stream Mach number of 0.75 was considered along with a range of angle of attacks from -4° to $+2^\circ$. Measurements of forces and moments, surface pressure and model deformations were obtained for a wing-body configuration of the geometry with a Reynolds number of 3×10^6 . Surface visualisations of the flow over the wings were also provided. Another study is the one of Rivers and Dittberner [18] in which an experimental investigation was performed of the NASA Common Research Model (CRM) in the NASA Langley National Transonic Facility and the NASA Ames 11-ft wind tunnel [18]. The results are presented as force and moment values for various configurations (wing-body, wing-body-tail and wing-body-pylon-nacelle) with a Reynolds number of 5×10^6 . The free-stream Mach number is 0.85 and the considered range of angle of attacks is from -3° to $+12^\circ$. Since these studies do not consider or measure the wake velocity flow field, they were used in the present research only as validation cases for the forces and moments (see section 3.5).

A validation test case of the CFD modelling of the wake and the tip vortex was required for this project. In literature there are many experimental studies about tip vortices, but most of them are about rectangular unswept wings, which are different from the wings that are used on modern transport aircraft. Furthermore, most of the studies are about the mid- and far-field of the wake, because these are the areas of interest in take-off and landing aircraft separation distances. For this reason, finding a suitable experimental study to be used as a wake and tip vortex validation test case was challenging. An experimental study about the near-field tip vortex behind a swept wing model performed by Gerontakos and Lee [31] was chosen. The downstream velocity field and the wake vortices characteristics were investigated and measured.

2.3.1 “Gerontakos swept wing”

Gerontakos and Lee studied the near-field flow structure of a tip vortex behind an untwisted sweptback and tapered NACA 0015 wing (Fig. 2.5) with a squared tip. The mean-tip vortex velocities at six distances downstream of the trailing edge of the wing were measured for $\alpha=8^\circ$. The variation of this quantities with α at $x/c_r=2.75$ for $\alpha=4-14^\circ$ were also evaluated.

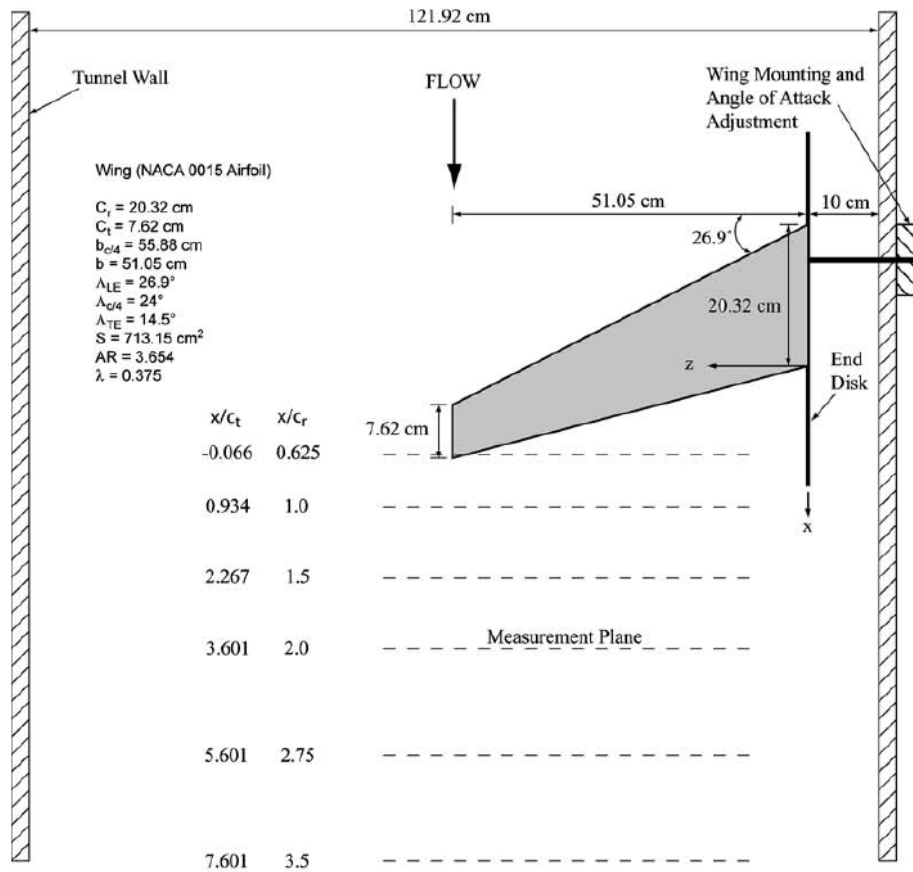


Fig. 2.5 Geometric characteristics of the Gerontakos and Lee model [31]

The free-stream velocity was fixed at 13.84 m/s and the root-chord Reynolds number has resulted to be 1.81×10^5 . Boundary-layer transition strips were not placed on the model and wind tunnel wall corrections were not applied to the measurements. Furthermore, the lift and drag forces were measured and calculated. It was found that the peak tangential velocity and the vorticity increased with the downstream distance and decreased with the angle of attack. The core radius was about $0.03C_r$ and it was noticed that it does not vary with the increase of the angle of attack and the downstream distance. Furthermore, the core and overall circulation of the tip vortex kept almost constant up to $X/C_r=3.5$. The Reynolds number of this experimental study is very low in comparison with the considered CFD cases of the research and this was taken into account. Furthermore, since the flow of the Gerontakos study has a free Mach number of 0.041 it is incompressible and there are no shocks in comparison with the transonic conditions of the CFD cases. Unfortunately, it was not possible to find an experimental test case of a swept wing with an

higher Reynolds and Mach numbers available during the period of this research. Despite this aspects, the use of the Gerontakos as a validation test case for the tip vortex is still valid, because the CFD simulations of this case were performed with the same boundaries and conditions of the experimental study.

2.4 Numerical studies

The numerical prediction of the downstream trailing vortices created by an aircraft is particularly challenging in terms of CFD. It is not only important to predict the vortex convection itself, but it is also fundamental to compute accurately the flow over the wing to resolve the boundary-layer roll up and shedding which provide the initial conditions for the free vortex [2]. In fact there are several challenges to successfully model the trailing-vortex flow development with CFD. The flow over the outboard part of the wing develops into a highly skewed, three-dimensional boundary layer that, as it detaches, rolls up to form the strong, nearly-axisymmetric trailing vortex [2]. Hence, the whole wing boundary layer (on both the pressure and suction surfaces) has to be computed to provide the initial conditions for the vortex computation itself. One important element to be considered is the computational turbulence model since it has to be capable to capture the complex wing boundary layer as well as the swirling free shear flow downstream. Subsequently, as a result of the complexity of the process, it is not surprising that there are relatively few CFD studies about the near and mid-field region of the wake behind a modern commercial aircraft, in particular in the air-refuelling field [2].

One of the first computational 3D studies of the near-field of a wingtip vortex flow generated from a NACA0012 half-wing configuration was carried out in 1995 by Dacles-Mariani et al. [3]. The basic model of turbulence used was the Baldwin-Barth [4] one-equation eddy-viscosity model, however a number of ad hoc variants were applied in order to have a better agreement with the measurements. The inaccuracies due to the finite differences technique, grid resolution and turbulence modelling were explored. Grid independence was achieved for a grid spacing of 5×10^{-3} chords. Furthermore, it was found that fifth-order accurate upwind-biased differencing of the convective terms is one

method to reduce numerical dissipation and to achieve reasonable agreement with measured vortex velocity profiles.

Since the investigations of Dacles-Mariani et al. [3] the performance of computers has substantially developed and the CFD methodologies have improved, which enables the evaluation of more complex configurations and with more accurate results. Benkenida et al. [5] performed numerical simulations of the wake vortices induced by the high lift system of an aircraft model up to the extended near field with high-quality meshes and high-order schemes using an Euler code. It was stated that one of the main issues in the study of vortical flow is to obtain high quality grids to control the numerical dissipation. One of the methods that can be applied to try to limit this dissipation is to use adaptive mesh techniques that allow a finer mesh in the vortex zones. It was also found that the circulation of the tip vortex increases with the angle of attack. It was demonstrated that CFD could provide results good enough to analyse the characteristics of the wake vortices.

While the previous cited studies treated the vortices as laminar or as inviscid, Shur et al. [6] solved the Reynolds-averaged Navier–Stokes (RANS) equations with a turbulence model. The CFD results were compared to the experimental data up to thirteen spans downstream. A few different turbulence models were considered, and it was found that the SA model [7] with rotation and curvature corrections provided the best overall agreement with the experiments. Although vortex merger was seen to occur too late, trajectories of the tip and flap vortices were found to agree generally well with the experimental data. The differences between the numerical predictions and experimental data that were observed were probably due to the limitations in the empirical initialisation of the eddy viscosity and the domain size.

Craft et al. [2] performed a numerical study to explore the ability to calculate the roll-up of the tip vortex of a NACA0012 wing and its near-field development. It was reported that with a linear $k-\epsilon$ model the roll-up process at the wing-tip was well calculated, but it was much more difficult to predict the correct acceleration characteristics and to maintain the high velocity in the vortex core. To calculate the correct acceleration and decay of the vortex core velocity a second-moment closure approach was required with the two-component limit

(TCL) model of Craft et al. [8]. It was also confirmed that the accelerated vortex core is caused primarily by the pressure gradient generated along the vortex axis and, although vorticity and low-momentum fluid from the boundary is “wrapped-up” in the vortex, it does not penetrate into the vortex core.

Czech et al. [9] performed an experimental and numerical investigation of the mid-field (up to about 20 spans) development of trailing vortices generated from a generic aircraft model, with unswept wings and a tail. The quasi-3D Reynolds-averaged Navier–Stokes (RANS) equations were solved with a Spalart-Allmaras (SA) one-equation turbulence model, with rotation and curvature correction. Experimental results were used to initialise the CFD calculations, and to validate the CFD in the prediction of the near-field development. Various configurations of the flaps of the aircraft were considered, all on landing approach. The wing span was 0.91 m and the chord Reynolds number was of 3.6×10^6 . Good agreement was obtained with the experimental data up to ten spans and it was stated that CFD properly predicts the number, strength and position of the vortices in the mid-field. Moreover, it was found that the addition of the turbulence effects was essential to capture the near-field development. This work also confirmed that the inclusion of fuselage-wake turbulent-mixing effects is essential to capture the correct near-field development and this implies the importance of the presence of a fuselage if an airplane-like vortex sheet is to be considered.

The numerical studies show that nowadays it is possible to perform a Reynolds-averaged Navier–Stokes CFD simulation, with a one or two-equation turbulence model, of the vortices generated from a detailed aircraft model and to obtain acceptable results. To succeed in this kind of analysis one fundamental aspect is the use of high quality grids, with an elevated number of cells in the wake of the wing and in particular in the area of the vortex core. Regarding this aspect the use of adaptive mesh techniques is a task that permits to achieve better grids, with a saving in the total number of elements. All these considerations were taken in account to perform the numerical studies of this project in the most appropriate way and to achieve the scope of the present research.

2.5 Low fidelity model (ELL code)

The ELL code is based on the work of Saban [11][12]. Saban, during her PhD at Cranfield University, developed a computational method and a simulation model for the development of multiple Unmanned Aerial Vehicles. In this work, a MATLAB-Simulink® method is used to implement a generic wake vortex model based on Weissenger’s extended lifting-line theory. The code was successively modified to the version that is used in the ASTRAEA II project to predict the vortices behind the tanker aircraft in real time. The code computes the steady-state velocity induced by the wake of a pair of wings and a fuselage modelled as a flat plate. The simplified geometric characteristics that describe the wing are span, aspect ratio, taper ratio, sweep, twist and dihedral angle. This version of the code does not consider the thickness of the wing, the camber, the friction drag, compressibility effects and the roll-up of the vortex.

2.5.1 Prandtl’s classical lifting line theory

The ELL code is a low fidelity model based on Weissenger’s extended lifting-line theory, which derives from Prandtl’s classical lifting line theory. These two theories are reviewed to understand the concepts on which the code is based. Prandtl’s classical lifting line theory consists in replacing the wing with a finite or infinite number of horseshoe vortices of different widths, all centred around the wing centre-line, and bound to the quarter-chord line of the wing, also referred to as the “lifting line” (Fig. 2.6). The circulation may vary from one horseshoe vortex to another but it remains constant along the different branches of a given horseshoe vortex. The vortex sheet, made of the trailing branches of the horseshoe vortices, extends downstream to infinity in parallel with the incident velocity V_∞ .

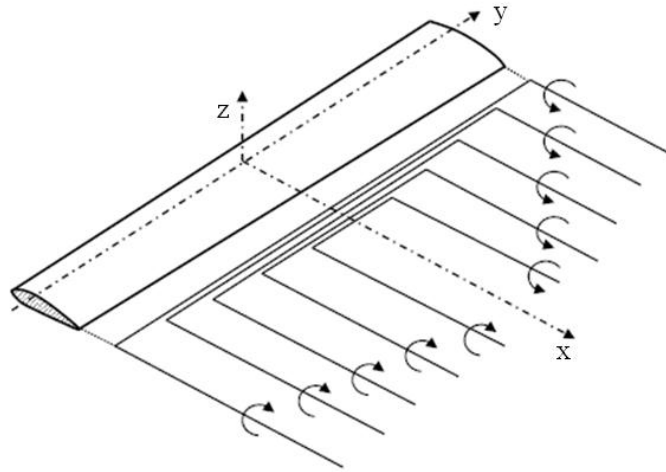


Fig. 2.6 Superposition of horseshoe vortices along the lifting line in Prandtl's classical lifting line theory [12]

The total lift and induced drag can be derived from the Kutta-Joukowski lift theorem, once the total vortex circulation is obtained. The total lift is given from:

$$L = \rho_{\infty} V_{\infty} \int_{-b/2}^{b/2} \Gamma(y) dy \quad (10)$$

where ρ_{∞} is the free-stream density, V_{∞} is the free-stream velocity, $\Gamma(y)$ is the spanwise vorticity and b is the wing span. The induced drag is:

$$D_i = -\rho_{\infty} \int_{-b/2}^{b/2} \Gamma(y) V_i(y) dy \quad (11)$$

where ρ_{∞} is the free-stream density, $\Gamma(y)$ is the spanwise vorticity and b is the wing span. The wing rolling and yawing moments can be directly computed from the spanwise lift distribution.

The lifting line theory has some limitations. In fact it is valid for inviscid, incompressible and steady flows, but is limited to wings with straight quarter-chord lines (unswept wings). Furthermore, accurate results are only obtained for wings with high aspect ratios [12]. Finally, the pitching moment cannot be computed from the spanwise lift distribution as the latter is collapsed to a single line along its 1/4-chord line.

2.5.2 Weissinger's extended lifting line theory

The extended lifting line theory was first introduced by Weissinger for the case of swept-back wings [32]. Compared to Prandtl's classical lifting line theory it has the advantages that can be applied to wings of any planform and aspect ratio. Furthermore, it allows an approximate value for the pitching moment to be estimated from the spanwise lift distribution.

The main difference between the two lifting line theories consists in the distribution of horseshoe vortices along the lifting line. In Prandtl's classical lifting line theory, horseshoe vortices are all centred around the wing centre-line, therefore positioned one into the other (Fig. 2.6), while in the extended lifting line theory, horseshoe vortices (although also bound to the quarter-chord lifting line) are positioned one next to the other (Fig. 2.7). This characteristic allows swept wings to be modelled. Furthermore, a different boundary condition is used to determine the value of the circulation along each horseshoe vortex. This condition – also called the kinematic flow condition, or the “Weissinger condition” in reference to the main developer of this method – stipulates that the airflow is tangential to the surface of the wing at its three-quarter chord line. For each horseshoe vortex, one “control point” (filled circles in Fig. 2.7) is defined at the intersection of the horseshoe vortex centre-line and the wing three-quarter chord line. The control points are represented by filled circles. The Weissinger condition, applied at each collocation point, can be formulated as:

$$(V_i + V_\infty) \cdot n = 0 \quad (12)$$

where V_i is the velocity induced by all the horseshoe vortices at the collocation point, V_∞ is velocity vector of the upstream airflow and n is the unit vector normal to the wing surface at the collocation point.

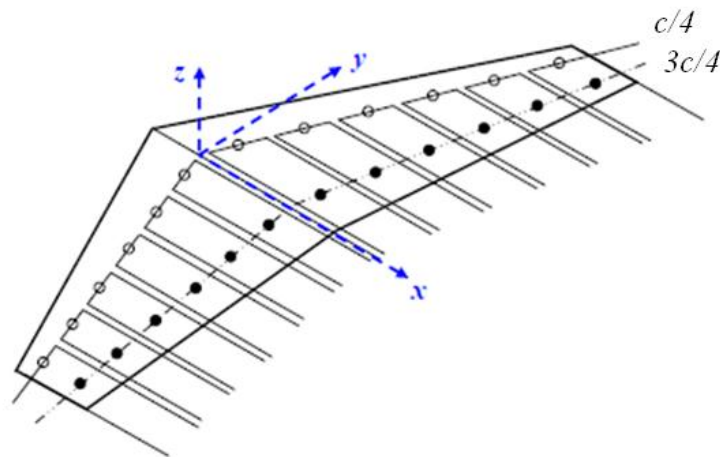


Fig. 2.7 Superposition of horseshoe vortices along the lifting line in Weissinger's extended lifting line theory [12]

2.5.3 ELL code summary

Despite the characteristics of the Weissinger theory, the ELL code is a low fidelity code based on an approximated model. The code presents many limitations since it does not consider the thickness of the wing, the camber, the friction drag, compressibility effects and the roll-up of the vortex. Since the tip vortices are modelled as inviscid and the flow is analysed as a mathematical formulation, the flow physics of the vortex structure, which has viscous effects, is not taken in account. Moreover, the fuselage is modelled as a flat plate and this introduces more important approximation in the solution of the modelled flow field that can lead to have results with a very low fidelity compared with the real flow. For these reasons a CFD study was needed to understand how far from the real flow field generated from a tanker aircraft is the field generated in the ELL code.

Chapter 3

Project overview and methodology

3.1 Introduction

In the previous chapter the literature review showed that research regarding vortices and wakes in the far-field and concerning general theories is extensive and detailed. Nevertheless, there are very few CFD or experimental studies of the near and mid-field region of the wake behind a modern commercial aircraft, in particular in the air-refuelling field.

The purpose of this project is to investigate the near and mid-field wake behind a modern commercial aircraft, such as the Airbus A330, and the nature and characteristics of the tip vortices generated by the wings, through the test cases described in the next paragraphs.

3.2 Numerical codes

The numerical codes used in this project are the commercial codes ANSYS Fluent [38] version 12.1 and ANSYS CFX [41] version 13. The simulations are all steady and 3D. The *Shear-Stress Transport* (SST) $k-\omega$ [43][44] and the *Spalart-Allmaras* (SA) [7] turbulence models were used in this study. The Fluent numerical results are second order accurate in space and time, moreover, a second order least-squares reconstruction was considered for the gradient evaluation. All the CFX simulations were performed with a high resolution advection scheme and turbulence numerics.

3.2.1 ANSYS Fluent code

Fluent is a commercial 2D-3D unstructured mesh solver, which adopts multi grid solution algorithms [38]. Fluent has two different numerical methods that

can be chosen:

- *Pressure-based* solver;
- *Density-based* solver.

The former method was developed for low-speed incompressible flows and the latter for high-speed compressible flows. In both solvers methods the velocity field is derived from the momentum equations. The density field is obtained from the equation of state in the pressure-based solver and from the continuity equation in the density-based method. Furthermore, in the pressure-based solver, the pressure field is calculated by a pressure or pressure correction equation, obtained from the continuity and momentum equations. In both the methods the code solves the governing integral equations for the conservation of mass and momentum and, when requested, also the energy and other scalars, as turbulence models, are solved. All flow data are stored in the cell-centres due to the type of grid used in the code. The code converts a general scalar transport equation into an algebraic equation that is solved numerically. This is based on a control-volume technique that integrates the transport equation for each control volume and produces a discrete equation that expresses the conservation law on a control-volume basis.

The pressure-based solver uses an algorithm categorised in the class of projection methods [39]. Due to the structure of this method and since the governing equations are nonlinear and coupled, the iterative process involves the entire set of governing equations, that are solved repeatedly until the convergence of the solution. There are two different pressure-based algorithm available. A segregated algorithm, where the governing equations are solved sequentially, and a coupled algorithm, where a coupled system of equations, that includes the momentum and the continuity equation, is solved. The density-based method solves the governing equations at the same time. Since the governing equations are non-linear and coupled, numerous iterations of the solution loop need to be performed until the convergence is achieved.

With regard to the spatial discretisation, Fluent uses an upwind scheme, which means that the face value is obtained from the cell upstream quantities, or “upwind”, relative to the direction of the normal velocity [38]. Fluent has various upwind schemes that can be chosen:

- *First-order upwind* scheme;
- *Second-order upwind* scheme;
- *Power-law* scheme;
- *QUICK* scheme.

The first-order scheme can be used when a first-order accuracy is sought. In this case the face quantities are the same as the cell-centre quantities. The second-order scheme has to be used when a second-order accuracy is needed. The quantities at cell faces are calculated by a “multidimensional linear reconstruction approach” [40].

In order to discretise the convection and diffusion terms in the flow conservation equations, the gradient, ∇ , of a given variable is used [38]. The gradients are calculated with the methods below:

- *Green-Gauss Cell-Based*;
- *Green-Gauss Node-Based*;
- *Least Squares Cell-Based*.

As stated in the previous chapters of this thesis turbulence modelling is another important component of a simulation. Fluctuating velocity fields characterise the turbulent flows. Quantities like momentum and energy are mixed and carried by the fluctuation. These causes the fluctuation of the quantities themselves. The computational simulation of the fluctuations is not practical as these can be of small scale and high frequency, consequently a high amount of computational resources is required. In order to solve the problem with a less expensive computational constraint, the governing equations are manipulated to remove the small scales. This results in a modified set of equations that contain additional unknown variables. Turbulence models are introduced to obtain the solution of these unknown variables. Fluent offers various turbulence models: Spalart-Allmaras model (SA) , k- ϵ models, k- ω model, v2-f model, Reynolds stress model, detached eddy simulation (DES) model and large eddy simulation (LES) model.

The principal turbulent model that was used for the Fluent simulations of this research is the Shear-Stress Transport (SST) k- ω . This model was developed by Menter [43][44] to combine the precise formulation of the k- ω

model in the near-wall region with the free-stream independence of the $k-\epsilon$ model in the far-field. This was achieved by the conversion of the $k-\epsilon$ model into a $k-\omega$ formulation. Although its similarity to the standard $k-\omega$ model, the SST $k-\omega$ model contains some improvements:

- both models, the standard $k-\omega$ and the SST $k-\omega$, are multiplied by a blending function and added together. This blending function is designed to be one in the near-wall region and zero away from the surface. In the former case the transformed $k-\epsilon$ model is activated, in the latter the standard $k-\omega$ model is activated;
- in the SST $k-\omega$ model is incorporated a damped cross-diffusion derivative term in the ω equation;
- in order to consider the transport of the turbulent shear stress, the definition of the turbulent viscosity is modified;
- the modelling constants are different.

The above described features make the SST $k-\omega$ model more accurate and reliable for a broader class of flows (e.g. adverse pressure gradient flows, airfoils, transonic shock waves) than the standard $k-\omega$ model. Other modifications involve the addition of a cross diffusion term in the ω equation and a blending function to guarantee that the model equations perform suitably in both the near-wall and far-field zones [38].

3.2.2 ANSYS CFX code

The ANSYS CFX code solves the discretised Navier-Stokes equations using a node centred, finite volume scheme, formed around each mesh node and bounded by edges. The control volume's edges are formed by joining the mid-points of each element edge with the neighbouring element centres. In these finite control volumes the mass, momentum and energy are conserved. All of the solution flow field properties are stored at the nodes.

The discretisation process of the Favre-averaged Navier-Stokes equations within CFX is unknown. Therefore, each equation is presented as Reynolds-averaged as this method is used for the explanation in the CFX-Solver theory guide [41]. In order to be solved by the finite volume method the RANS

equations are expressed in integral forms. Consequently, the continuity equation, the momentum equation and the arbitrary transported scalar equations, as the turbulence properties, are written as volume and surface integrals. Using the divergence theorem the volume integrals are transformed to surface integrals. The equations are then discretised to become a set of linear algebraic approximations. Due to the finite terms of the expansion series used to represent the continuous calculus formulations the equations contain a discretisation error. The implicitly discretised linear mass and momentum equations are coupled and solved on a non-staggered mesh to obtain the solutions of the pressure and velocity fields. The energy and turbulence equations are segregated and solved separately. For steady state simulations a physical timescale is used to advance the simulation in false time and to obtain a converged solution. The physical timescale acts as a relaxation factor for the equations and is applied to the right hand side (RHS) of each equation:

$$RHS + \frac{\Phi^{t+1} - \Phi^t}{t} \quad (14)$$

where Φ is an arbitrary dependent variable. A relatively large physical timescale is used for implicit methods to accelerate the convergence to a steady state solution. The timescale depends on the type of the considered flow field. The CFX high resolution scheme calculates all the advection terms at the integration points from the upwind nodes. In order to reach second-order accuracy the slope limiter is adjusted in the code to be as close to unity as possible without any dissipative oscillations. The diffusion terms are calculated by the derivatives of finite element shape functions, formulated for each element type, at the integration points.

In the CFX-Solver theory guide [41] it is explained that CFX solves the matrices of the linear system of equations. This can require large amounts of memory storage for the coupled mass and momentum equations coefficients, with an Incomplete Lower Upper (ILU) factorisation method. The equations are solved iteratively from an preliminary guessed solution. Successively, an algebraic multigrid technique is introduced to improve the performance and precision of the solution method. A multigrid technique solves the equations by interpolating the solutions on coarser meshes to accelerate the solution towards

convergence. Errors associated with the larger wavelengths, which can span across multiple elements in the original meshes and are more difficult to remove on the finer meshes, are eliminated. When this procedure is completed the solution is interpolated back to the original mesh. As the coarsening and refining processes are wholly numerical, the reconstruction of an actual geometry or mesh is not involved.

3.3 Identification of the test cases

The reference aircraft tanker for this research is the Airbus A330 (Fig. 3.1). Since the A330 geometry was not available, the first target in the development of this study was to find an open source geometry as much as possible similar to the Airbus A330.

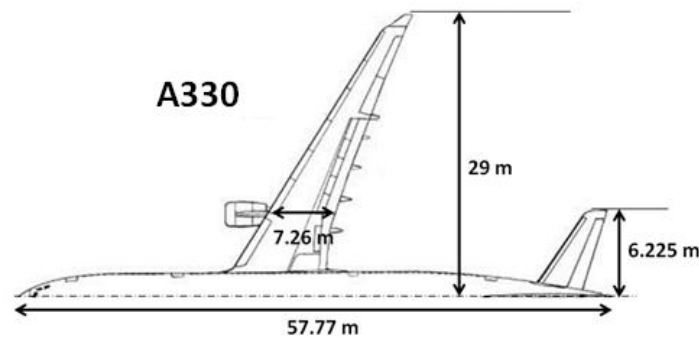


Fig. 3.1 Airbus A330 main dimensions [33]

In literature, there are two open-source geometries that have a good agreement with the A330: the DLR-F6 [34] and the Common Research Model (CRM) [35]. These geometries were developed and used in the 2nd and 4th AIAA Drag Prediction Workshops [36][37]. The workshops focused on aerodynamic investigations of the considered geometries through various CFD simulations performed by many organisations. Most of the CFD data of the workshops are openly available [36][37]. Experimental results of C_L , C_d , C_m and C_p distributions are available too.

The DLR-F6 configuration is a modern, twin-engine, transport aircraft, with a designed cruise speed of $M_\infty=0.75$, which corresponds to a lift coefficient (C_L) of 0.5 [34]. Fig. 3.2 shows the dimensions of the wind tunnel model of the DLR-F6. The CRM geometry was specifically created to be a public aircraft model that can be used for academic and research purposes [35]. The geometry is a

wing-body-nacelle-pylon-horizontal tail aircraft with a typical contemporary transonic supercritical wing design. There are many versions of the geometry (e.g. with or without the nacelle-pylon group or with or without tail). The designed cruise Mach number is $M_\infty=0.85$, which corresponds to a lift coefficient of 0.5. Fig. 3.3 shows the main dimensions of the full-scale CRM geometry. The scaled geometry used in the wind tunnel has a scale of 1:37.

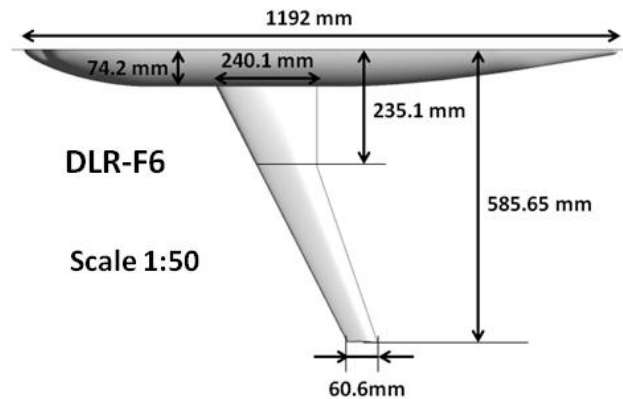


Fig. 3.2 DLR-F6 main dimensions at model scale [36]

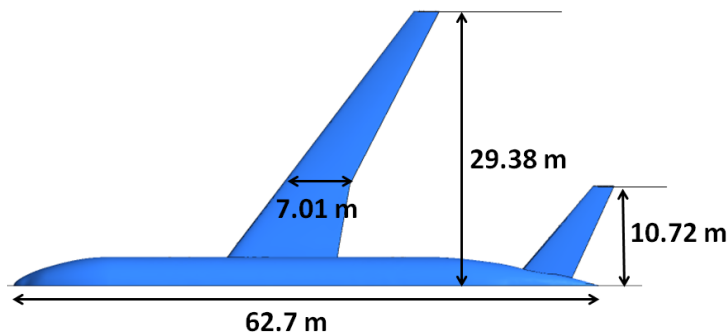


Fig. 3.3 Main dimensions of the full-scale CRM geometry [37]

To understand which geometry was more appropriate for this study a comparison between the available geometries and the A330 (Table 3.1) was performed. The main considered wing characteristics (Fig. 3.4) for the comparison are:

- the wings span, b ;
- the reference chord, C_{ref} ;
- the taper ratio, λ , defined as the ratio between the tip chord and the root chord, C_{tip}/C_{root} ;

- the sweep of C/4 line, $\Lambda_{C/4}$, defined as the angle between the wing quarter chord line and the y-axis of the aircraft (y is the spanwise direction coordinate);
- the reference wing area, S_{ref} , defined as the surface wing area.

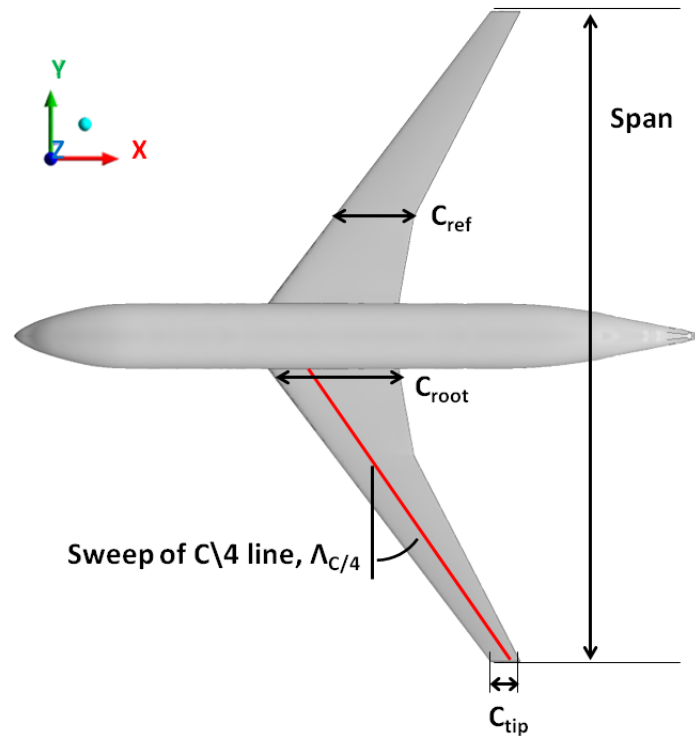


Fig. 3.4 Aircraft geometric characteristics

Both geometries have analogies with the A330. The DLR-F6 is more analogous for some geometric wing characteristics, as for example the wing reference area, which is $S_{ref}=363.25 \text{ m}^2$ for the DLR-F6 and $S_{ref}=363.1 \text{ m}^2$ for the A330, while for the CRM is $S_{ref}=383.69 \text{ m}^2$. Another similarity is in the taper ratio, which is $\lambda=0.25$ for the DLR-F6 and $\lambda=0.251$ for the A330, while for the CRM is $\lambda=0.275$. Despite that, the CRM has a cruise Mach number of 0.85, very close to the A330's one, which is $M=0.82$, while the DLR-F6 cruise Mach number is 0.75. The DLR-F6 is available with and without the pylon-nacelle group. The CRM geometry exists in literature with and without the pylon-nacelle group, but the only geometry available in the public domain is the one without the engine group.

	A330	CRM	CRM geometry scale (1:37)	DLR-F6 geometry scale (1:50)
Cruise Mach number, M [-]	0.82	0.85	0.85	0.75
Nominal lift condition, CL [-]	0.5	0.5	0.5	0.5
Reynolds Number, Re [-]	$4.002 \times 10^{^7}$	$4 \times 10^{^7}$	5, 19.8, 30 x $10^{^6}$	$3, 5 \times 10^{^6}$
Sref [m²]	363.1	383.69	0.2796	0.1453 (363.25)
Trap-Wing Area [m²]	-	371.612	0.2714	-
Cref [m]	7.26	7.00532	0.18923	0.1412 (7.06)
Span [m]	58	58.763	1.5867	1.1714 (58.57)
Taper-ratio, λ [-]	0.251	0.275	0.275	0.25
Sweep of C\4 line, $\Lambda_{C/4}$ [°]	30	35	35	25
Wing aspect ratio, AR [-]	9.26	9	9	9.5
Thickness-to- chord ratio [%]	12.8	10.8	10.8	-
Nacelle	Yes	No	No	Yes
Total Number of Nacelles	2	/	/	2
Tail	Yes	Yes	Yes	No
Winglet	Yes	No	No	No
Winglet tall [m]	2.74	/	/	/

Table 3.1 Comparison between the available geometries and the A330

The last considered test case is the one based on the Gerontakos and Lee [31] swept wing (“Gerontakos swept wing” model), which was used as a validation test case for the downstream velocity and the near-field wake vortices (see

section 3.6). Table 3.2 reassumes the principal characteristics of the available geometries that will be deeply analysed in the following paragraphs.

	Geometry	M > 0.8	High Re	Exper. Cd, Cl	Downstream measurement	Other CFD Data	Description
a.	 DLR-F6	x	✓	✓	x	x	- Geometry and meshes available. - Cd, Cl, Cp, Cm experimental data available. - Geometry similar to the A330.
b.	 CRM NO_TAIL WIND TUNNEL SCALE	✓	✓	✓	x	x	- Geometry available. - Only Cd and Cl experimental data available. - Geometry similar to the A330.
c.	 CRM TAIL WIND TUNNEL SCALE	✓	✓	✓	x	x	- Geometry available. - Only Cd and Cl experimental data available. - Geometry similar to the A330.
d.	 CRM TAIL FULL-SCALE	✓	✓	✓	x	✓	- No Experimental Data available. - CFD data available. - Geometry similar to the A330.
e.	 Gerontakos Swept Wing	x	x	✓	✓	x	- Geometry and experimental data available. - Downstream measurements available.

Table 3.2 Main characteristics of the available geometries

3.4 DLR-F6 geometry

3.4.1 Introduction

The primary issues that needed to be addressed in the research were:

- to understand which was the more appropriate CFD code to use out of the two available (ANSYS Fluent and ANSYS CFX) and validate it;
- to find the right boundary conditions;
- to understand the most appropriate turbulence model.

The first step was to perform various simulations to achieve a comparison of the turbulence models, the boundary conditions and the codes themselves. Due to the larger amount of available experimental data it was decided to perform this analysis with the DLR-F6 geometry (Fig. 3.5). The available experimental data includes C_L , C_d , C_m and C_p distributions. Table 3.3 shows the matrix of the simulations carried out to enable these comparisons.



Fig. 3.5 DLR-F6 wind tunnel model [17]

	Code	Solver	Mesh size	Mach	Re	Turb. Model
DLR-F6	FLUENT	Density B.	5MIL	0.75	3×10^6	SST
	FLUENT	Density B.	5MIL	0.75	3×10^6	SA
	FLUENT	Density B.	9MIL	0.75	3×10^6	SST
	CFX	NA	5MIL	0.75	3×10^6	SST
	CFX	NA	5MIL	0.75	3×10^6	SA
	CFX	NA	9MIL	0.75	3×10^6	SST

Table 3.3 Main DLR-F6 geometry CFD simulations

3.4.2 Experimental data available

The experimental analysis of the DLR-F6 model was performed in the ONERA S2MA wind tunnel facility by Rudnik et al. [17]. Forces and moments, surface pressure and model deformations for a wing-body configuration of the model with a Reynolds number of 3×10^6 were measured. Surface visualisations are available as well.

The DLR-F6 configuration was designed by DLR German Aerospace Centre as a generic twin engine medium range single aisle commercial aircraft. It is composed of a glass fibre reinforced polymer fuselage and a pair of steel wings, which are mounted to an internal steel balance block. The basic DLR-F6 wing-body configuration can optionally be equipped with several different flow-through nacelles. Pressure distributions were measured on the right wing by 288 pressure orifices located in 8 span-wise wing sections, 47 locations in 3

radial sections of the left nacelle and 9 locations on the left pylon. During the tests, the model was mounted on a fin sting. This set-up is well adapted for precise balance force measurements for performance tests. Similar sting blades as well as the internal balances and the balance adaptors were available for testing in the ONERA S2MA and the NASA National Transonic Facility (NTF).

The main purpose of the test was to address specific issues and findings from the previous NASA NTF test, as well as to provide more detailed and additional flow field information of the wing/body juncture flow for two configurations with different measurement techniques. Force and moment data, static pressure distributions on the wing and on the fuselage of the wing/body configuration were measured.

3.4.3 CFD simulations domain and boundary conditions

The far-field domain used in the CFD simulations of the DLR-F6 geometry is the same used in the 2nd AIAA Drag Prediction Workshop. The far-field domain is Cartesian (Fig. 3.6). The far-field length is 100 reference chords (C_{ref}) away from the aircraft model. As stated in the 2nd Drag Prediction Workshop results, this length was found to minimise the effect of the outer boundary condition treatment on the computed lift and drag values.

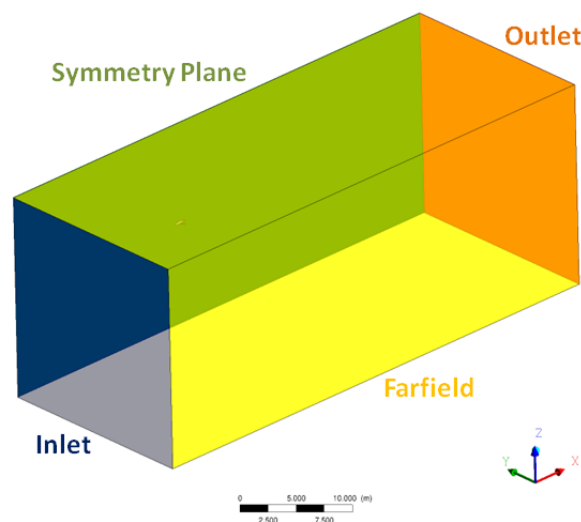


Fig. 3.6 Cartesian far-field domain of the DLR-F6 geometry

In the simulation performed with Fluent the boundaries are *pressure-far-field* for the inlet, outlet and far-field and *symmetry* for the symmetry plane

[38]. In the simulation performed with CFX the boundaries are *subsonic inlet* for the inlet, *opening* for the outlet and the far-field and *symmetry* for the symmetry plane [41]. The cruise lift coefficient for this geometry is 0.5. The available experimental data are C_L , C_d and C_p . Full experimental C_d and C_L polar are available, but the experimental pressure coefficient distributions are available only for a C_L of 0.5. Various simulations were carried out to find the angle of attack that corresponds to a $C_L=0.5$ for every mesh. Since the creation of every grid requires a significant time, a fixed geometry with a zero angle of attack was used and the angle of the inlet flow was changed to simulate the different flight conditions.

3.4.4 Grids

All the computational grids used in this study were generated using the ANSYS commercial tool ICEM CFD 12.1 [42]. Three grids, available from the 2nd AIAA Drag Prediction Workshop [36], were considered:

- a coarse grid of 3 million cells;
- a medium grid of 5 million cells (Fig. 3.7);
- a fine grid of 10 million cells.

The 5 million cells grid was refined to obtain a better resolution of the wake field, since the principal purpose of the grids used in the workshop was only to understand the wing aerodynamics characteristics and not the downstream flow field. A new 9 million cells grid was generated by adding some finer densities zones in the near-field behind the aircraft until a distance corresponding to 50 metres in a full-scale model (Fig. 3.8). The choice of 50 metres corresponds to the near and mid-field distance ($x/b \approx 0.9$), which is of interest in air-refuelling purposes. Both grids have 35 prism layers, with a first prism layer height from the surface of 0.001 mm and a maximum y^+ of 0.4.

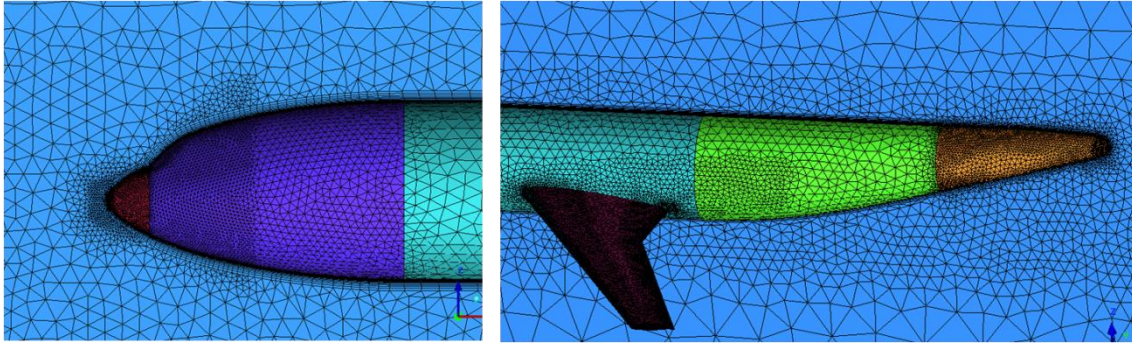


Fig. 3.7 Surface mesh of the medium grid (5 million cells)

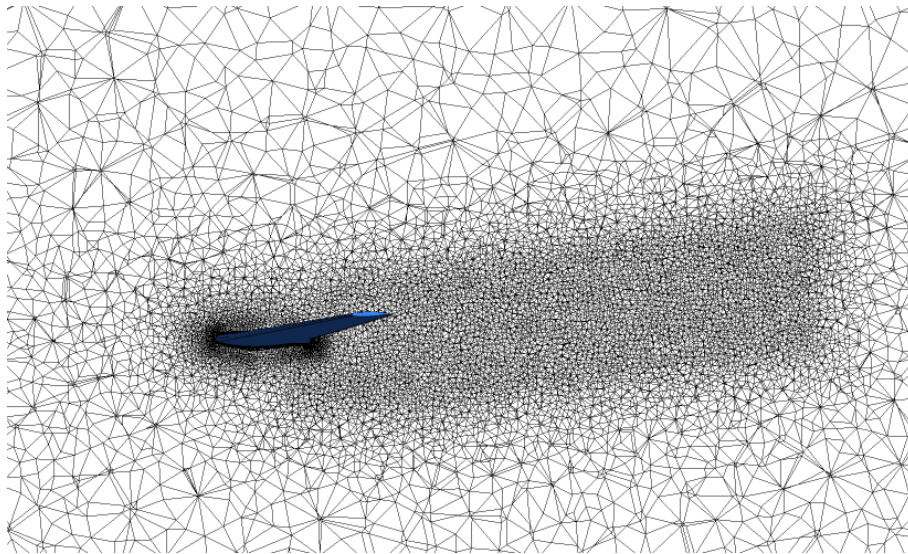


Fig. 3.8 Density of the volume mesh in the wing wake of the 9 million cells grid

3.5 Common Research Model (CRM)

3.5.1 Introduction

The final scope of the research was to perform CFD simulations of a full-scale aircraft geometry as much as possible similar to the Airbus A330 with air-refuelling flight conditions. The geometry that was chosen to perform these simulations is the CRM, because of the more appropriate cruise Mach number and Reynolds number of this geometry and due to the presence of the tail. This is an element that needs to be analysed for the understanding of the near-field wake behaviour.

A study about the turbulence models, the boundary conditions and the CFD codes was performed with the DLR-F6 scaled to the wind tunnel model size. Validation results were obtained as well. Despite the DLR-F6 analysis, further

simulations of the CRM scaled to the wind tunnel model size were needed to validate the results also with this geometry and at a higher Mach number. Furthermore, these simulations were utilised to compare the obtained CFD results with the results of the first version of the ELL code, available at that point of the research. Since the ELL code does not include a tail, the CRM geometry wing-body configuration (without tail) was chosen to perform these wind tunnel conditions simulations. Finally the simulations of the CRM geometry full-scale with tail were carried out with typical air-refuelling flight conditions agreed with Cobham Mission Equipment.

3.5.2 Experimental data available for the CRM

Rivers and Dittberner performed the experimental investigation of the CRM in the NASA Langley National Transonic Facility and the NASA Ames 11-ft wind tunnel [18]. The results are presented as force and moment values for various configurations (wing-body, wing-body-tail and wing-body-pylon-nacelle) with a Reynolds number of 5×10^6 .

NASA National Transonic Facility (NTF) is a wind tunnel facility where aircraft are tested at various conditions that range from subsonic to low supersonic speed at Reynolds number up to full-scale flight values. The NTF is a conventional, closed circuit, continuous-flow, fan-driven pressurised wind tunnel. At the NTF is possible to operate both with dry air at warm temperatures and with nitrogen, through temperatures ranging from warm to cryogenic. Tests at the highest Reynolds numbers are carried out thanks to the combination of elevated pressures with cryogenic temperatures. The test section size is 2.5 x 2.5 x 7.6 m and has a slotted floor and ceiling. The Unitary Plan Wind Tunnel consists of three tunnel legs: the 3.4 x 3.4 m transonic wind tunnel (TWT) , known as “Ames 11-ft TWT”, the 2.7 x 2.1 m supersonic wind tunnel, and the 2.5 x 2.1 m supersonic wind tunnel. A three-stage axial-flow compressor drives the Ames 11-ft TWT. It is a closed-circuit, variable-pressure, continuous operation wind tunnel. There are a subsonic Mach number control and a supersonic Mach number control. The former involves setting the compressor drive speed to one of ten set points and using variable-camber inlet guide vanes for fine Mach number control. The latter involves setting the flexible wall nozzle

to achieve the proper area ratio in addition to setting the compressor drive speed and the inlet guide vanes.

The aspect ratio of the NASA Common Research Model is 9.0, the leading edge sweep angle is 35 deg, the wing reference area is 0.28 m², the wing span is 1.59 m, and the mean aerodynamic chord is 0.19 m (Fig. 3.11).



Fig. 3.9 NASA CRM wind tunnel model [18]

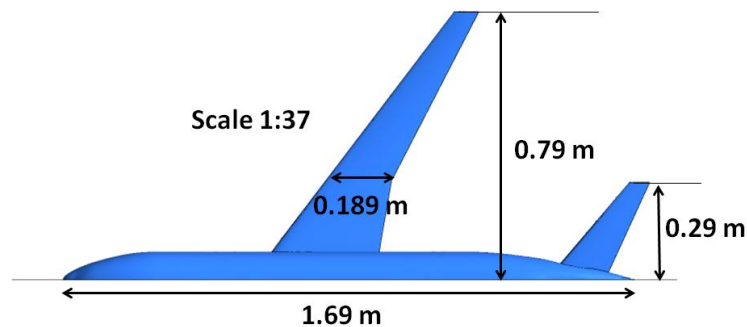


Fig. 3.10 NASA Common Research Model at wind tunnel scale main dimensions [18]

The model moment reference centre is located 0.91 m back from the fuselage nose and 0.05 m below the fuselage centreline. The nacelles used for this test were simple, flow through nacelles. The model is mounted in the wind tunnel using a blade sting arrangement in both tunnels with the only differences occurring downstream of the model support system. No corrections were made in either data set for this mounting arrangement. Five different configurations were tested: the wing-body (WB) alone, wing-body-pylon-nacelle (WBPN), wing-body-tail=0° (WBT0), wing-body-tail=+2° (WBT+2) and wing-body-tail=-2° (WBT-2).

An objective of the experimental study was to determine the tail effects for the CRM geometry. For the $C_L=0.5$ and $M=0.85$ condition, there was a decrease in drag, an increase in lift and an increase in nose down pitching moment when going from a -2° to a $+2^\circ$ tail setting for both wind tunnels, with negligible difference between the wind tunnel lift and pitching moment actual values. The drag values give a difference of approximately five drag counts ($DCd=-0.0005$) for the WBT-2 setting and a difference of approximately seven drag counts ($DCd=-0.0007$) for the WBT0 and WBT+2 settings. Another effect that was investigated was the addition of a nacelle-pylon group and it resulted to give an increase in drag, decrease in lift and a less nose down pitching moment around the design lift condition of 0.5.

3.5.3 CFD simulations domain and boundary conditions

3.5.3.1 CRM geometry scaled at wind tunnel conditions

Various simulations were carried out, both in ANSYS Fluent and ANSYS CFX, with the same 7 million cells mesh (Table 3.4) and boundaries using the model scale CRM geometry and under wind tunnel conditions. The objective was to have a final indication on which was the more appropriate solver to perform this research. The results obtained with the DLR-F6 geometry indicated that the Fluent solver was more appropriate than CFX with an unstructured hybrid grid, but since the CFX solver is much faster than Fluent a further check was carried out with the CRM geometry, which has a $M_\infty=0.85$. The results of these simulations confirmed the trend of the DLR-F6 results, which showed that the Fluent code better resolved the kind of problem analysed in this thesis project (see section 4.1). Consequently, the Fluent solver was selected for all the other simulations of the research. The cruise lift coefficient for this geometry is 0.5 and the experimental results are available for this condition. Various simulations were carried out to find the angle of attack that corresponds to a $C_L=0.5$ for every mesh. As the creation of each grid requires a significant time, a fixed geometry with a zero angle of attack was used and the angle of the inlet flow was changed to simulate the different flight conditions. Furthermore, the 15 million cells mesh test case was simulated at various angles of attack (in a range from -2° to 5°) to build the C_L and C_d curves and to compare them with

the experimental data. Table 3.5 shows the boundary conditions of the considered cases. The simulations that were completely post-processed (pressure coefficient distributions, wake velocity flow field and tip vortex characteristics) and compared with the experimental data are the two with a C_L of ≈ 0.5 , which correspond to the 7 million cells mesh with an angle of attack of 2.6° and to the 15 million cells mesh with an angle of 2.26° .

Geometry	Code	Solver	Mesh size	Mach Number [-]	Reynolds Number [-]	Turbulence model
CRM_NOTAIL	FLUENT	Density B.	7MIL	0.85	5×10^6	SST
WIND_TUNNEL_SCALE	FLUENT	Density B.	15MIL	0.85	5×10^6	SST

Table 3.4 Wing-body CRM geometry at wind tunnel scale CFD simulations

Geometry	Code	Mesh size	Turb. Model	T. I. [%]	Length Scale [m]	AOA [°]	Ts [K]	Ps [Pa]
CRM_NOTAIL WIND_TUNNEL_SCALE	FLUENT	7MIL	SST	1	0.0132	2.6	311	148942
	FLUENT	15MIL	SST	1	0.0132	-2	311	148942
	FLUENT	15MIL	SST	1	0.0132	-1	311	148942
	FLUENT	15MIL	SST	1	0.0132	0	311	148942
	FLUENT	15MIL	SST	1	0.0132	1	311	148942
	FLUENT	15MIL	SST	1	0.0132	2.26	311	148942
	FLUENT	15MIL	SST	1	0.0132	2.78	311	148942
	FLUENT	15MIL	SST	1	0.0132	4	311	148942
	FLUENT	15MIL	SST	1	0.0132	5	311	148942

Table 3.5 CRM geometry at wind tunnel scale boundary conditions

The far-field domain used in the CFD simulations of the CRM geometry is Cartesian (Fig. 3.11). The boundary conditions that were applied are *pressure-far-field* for the inlet, outlet and far-field and *symmetry* for the symmetry plane [38]. The far-field length is 100 reference chords (C_{ref}) away from the aircraft model. As stated in the 4th Drag Prediction Workshop results [37], this length was found to minimise the effect of the outer boundary condition treatment on the computed lift and drag values.

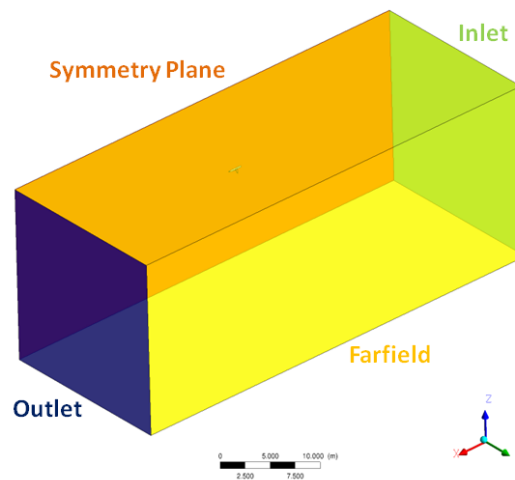


Fig. 3.11 Cartesian far-field domain of the CRM geometry

3.5.3.2 Full-scale CRM geometry

The simulations with the air-refuelling flight conditions, carried out with the CRM full-scale wing-body-tail geometry, are listed in Table 3.6. The domain characteristics and the CFD boundaries applied are the same of the CFD geometry scaled at wind tunnel conditions illustrated in the previous paragraph.

	Flight Condition	Code	Mesh size	Mach [-]	Re [-]	AOA [°]	C_L [-]
CRM_TAIL_FULLSCALE	FC1	FLUENT - CFX	18MIL	0.398	36×10^6	8.5	0.95
	FC2	FLUENT	18MIL	0.441	40×10^6	6.2	0.77
	FC3	FLUENT	18MIL	0.548	50×10^6	3.5	0.5
	FC4	FLUENT	18MIL	0.704	64×10^6	1.07	0.3

Table 3.6 Full-scale wing-body-tail CRM geometry CFD simulations

The four flight conditions chosen to perform this full-scale analysis were calculated from the air-refuelling altitude and velocity conditions agreed with Cobham Mission Equipment (Table 3.7).

Flight Condition	Indicated airspeed	Altitude
FC1	180KCAS	20,000ft
FC2	200KCAS	20,000ft
FC3	250KCAS	20,000ft
FC4	325KCAS	20,000ft

Table 3.7 Air-refuelling flight conditions agreed with Cobham Mission Equipment

As the given velocities were in indicated airspeed, they were converted in true airspeed with the following equation [29]:

$$\frac{V}{V_{cal}} = \left\{ \theta \left[\frac{[f(V_{cal})/\delta + 1]^{(\gamma-1)/\gamma-1}}{[f(V_{cal})+1]^{(\gamma-1)/\gamma-1}} \right] \right\}^{1/2} \quad (15)$$

where:

$$V_{cal} = \left[\frac{2a_{SL}^2}{(\gamma-1)} \left[\left(\frac{p_o-p}{p_{SL}} + 1 \right)^{(\gamma-1)/\gamma} - 1 \right] \right]^{1/2} \quad (16)$$

and $f(V_{cal})=(p_o-p)/P_{SL}$.

Since the detailed flight operating conditions for the A330 were not available, the lift coefficients correspondent to the four flight conditions were calculated with the following process:

- the A330 empty mass was found on Jane's Aerospace [30];
- a maximum payload (including fuel) of 45,000 kg was considered;
- the total mass (mid-payload mass and gross aircraft mass) of 190,000 kg was assumed;
- it was assumed that in air-to-air refuelling the aircraft is in straight and level flight;
- the required lift force to balance the mass was determined;
- from the lift forces of each flight condition the required four lift coefficients were determined
- an estimated angle of attack was determined from the CRM geometry at wind tunnel scale experimental data.
- various CFD simulations were performed to find the angle of attack that corresponds to the lift coefficient of each flight conditions.

3.5.4 Grids

Several grids of the CRM geometry were generated. Table 3.8 summarises the grids that were realised for this geometry with various configurations. All the grids have finer densities zones in the near-field behind the aircraft until a distance that corresponds to 50 metres in a full-scale model, since this correspond to the near-field zone of interest for air-refuelling purposes ($x/b \approx 0.9$).

The two grids of the wing-body (no tail) wind tunnel scale geometry have 30 prism layers, with a first prism layer height from surface of 0.012 mm ($6.34 \times 10^{-5} z/c_{\text{ref}}$) and a maximum y^+ of 5. The 19 million cells grid of the wing-body-tail full-scale geometry has 29 prism layers, with a first prism layer height from surface of 0.3 mm ($4.28 \times 10^{-5} z/c_{\text{ref}}$) and a maximum y^+ that depends on the considered flight condition. For the flight condition with the highest Reynolds number the maximum y^+ is of 10. Fig. 3.12 to Fig. 3.14 illustrate the surface mesh, the far-field and the density behind the wing of the no-tail CRM geometry scaled to the wind tunnel size 7 million cells grid.




		CRM Model	Grid 1	Grid 2	Grid 3
a.		NO-TAIL WIND TUNNEL SCALE	7 MIL	15 MIL	NA
b.		TAIL WIND TUNNEL SCALE	5 MIL	8 MIL	10MIL
c.		TAIL FULL-SCALE	5 MIL	10 MIL	19MIL

Table 3.8 Grids of the CRM geometry

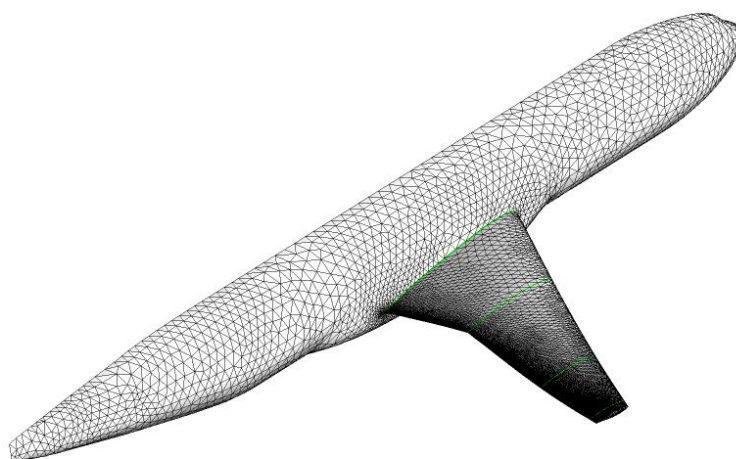


Fig. 3.12 Surface mesh on the CRM geometry of the no-tail scaled at wind tunnel conditions 7 million cells grid

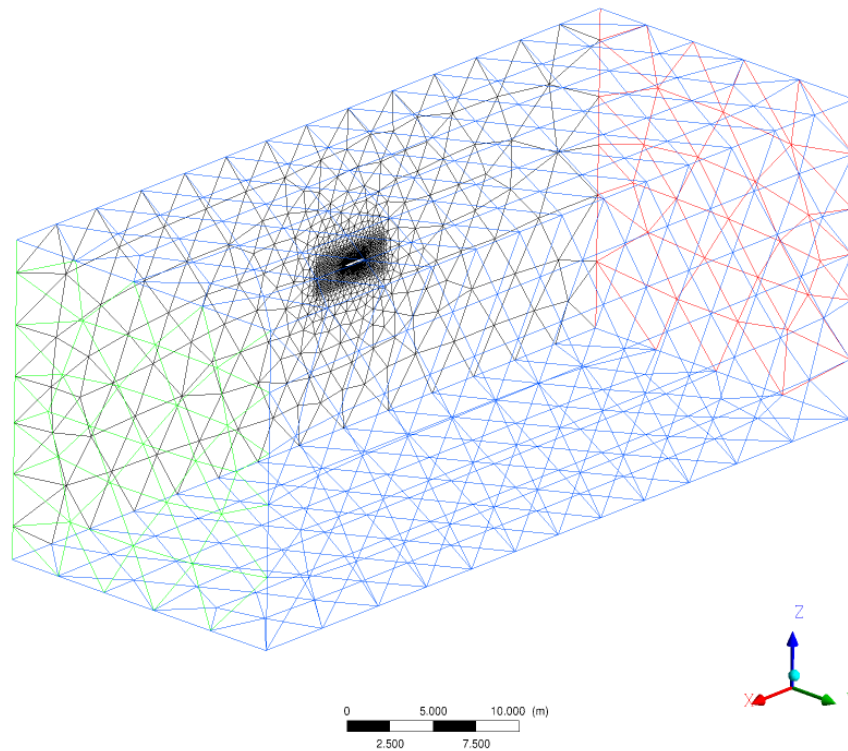


Fig. 3.13 Far-field of the no-tail scaled at wind tunnel conditions 7 million cells grid

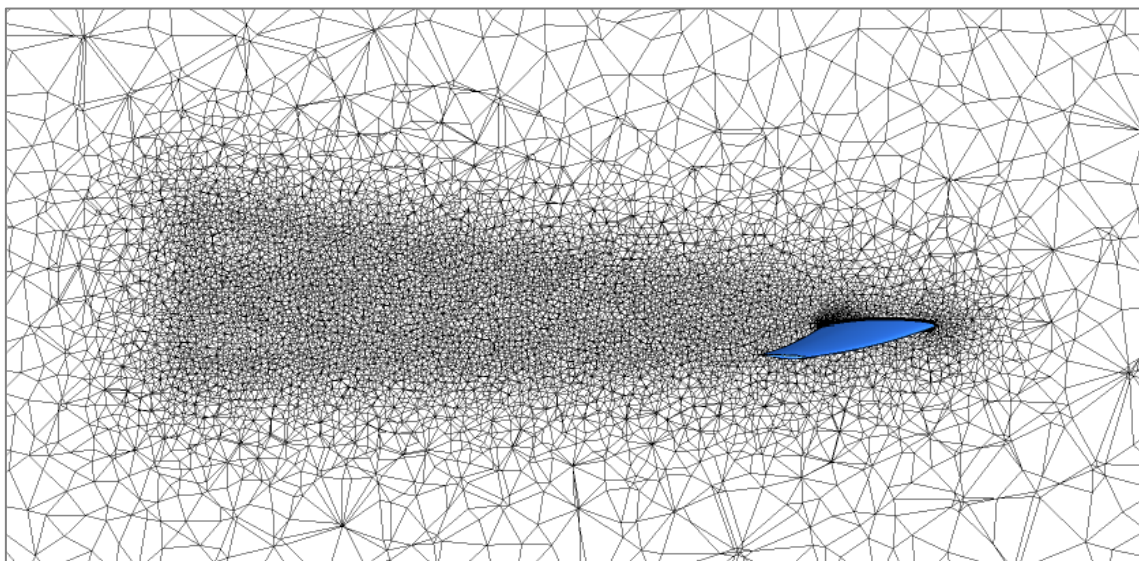


Fig. 3.14 Density of the volume mesh in the wing wake of the 7 million cells grid

3.6 CFD models of the Gerontakos swept wing test case

3.6.1 Introduction

As stated in the background section (chapter 2), in literature there are very few experimental studies which provide both the geometry and wake flow field

velocity measurements of modern commercial aircraft geometries. For this reason it was decided to choose a different validation test case for the wake and the tip vortex quantities. The Gerontakos and Lee swept wing case was chosen [31]. CFD simulations of the wing tested in the study were carried out as a validation test case for the downstream velocities calculation (Table 3.9).

	Code	Solver	Mesh size	Mach [-]	Re [-]	Turb. Model
Gerontakos Wing	FLUENT	Pressure B.	5MIL	0.041	1.81×10^5	SST
	FLUENT	Pressure B.	7MIL	0.041	1.81×10^5	SST
	FLUENT	Pressure B.	5MIL	0.041	1.81×10^5	SST
	FLUENT	Pressure B.	12MIL	0.041	1.81×10^5	SST
	FLUENT	Pressure B.	12MIL	0.041	1.81×10^5	SA

Table 3.9 CFD simulations of the “Gerontakos swept wing”

3.6.2 Experimental data available

The reported experimental results are tangential velocity, V_θ , axial vorticity, ζ , and V_x velocity component distributions, in vortex coordinates [31]. Furthermore, the total and core vortex circulation in the six considered planes were plotted. Some vector plots and contours of axial vorticity and velocity are reported as well. All the data are reported in chapter 6 with the wind tunnel settings as well.

3.6.3 CFD simulations domain and boundary conditions

Since Gerontakos and Lee do not report the temperature and pressure conditions of the wind tunnel, a total temperature of 288K and a static pressure of 95105 Pa were assumed. From the assumed total temperature value, using the Reynolds and Bernoulli equations, the reference density and static pressure were calculated. To achieve the same C_L as the experimental case, simulations at different angles of attack were carried out (Table 3.10).

Geometry	Code	Mesh size	Turb. Model	T. I. [%]	Length Scale [m]	AOA [°]	Ttot [K]	Ts [K]	Ps [Pa]
Gerontakos Wing	FLUENT	5MIL	SST	0.03	0.014224	6.5	288	287.9	95105
	FLUENT	7MIL	SST	0.03	0.014224	8	288	287.9	95105
	FLUENT	5MIL	SST	0.03	0.014224	9.5	288	287.9	95105
	FLUENT	12MIL	SA	0.03	0.014224	9.5	288	287.9	95105
	FLUENT	12MIL	SST	0.03	0.014224	9.5	288	287.9	95105

Table 3.10 Boundary conditions of the “Gerontakos swept wing”

The domain used in the CFD simulations of the “Gerontakos swept wing” represents the wind tunnel configuration that Gerontakos and Lee [31] used to

perform the measurements of the downstream velocities (Fig. 3.15). It consists of the wing model mounted horizontally at the centre of the wind tunnel test section. A circular endplate with a diameter of $D/C_{ref}=2.46$ with a sharp leading edge was fitted to the one end of the wing model, located at $Z/C_{ref}=0.49$ from the sidewall of the test section, to isolate the free-end effects. The origin of the coordinate system was situated at the trailing edge of the root of the wing with the x , y , and z axes in the streamwise, transverse, and spanwise directions, respectively.

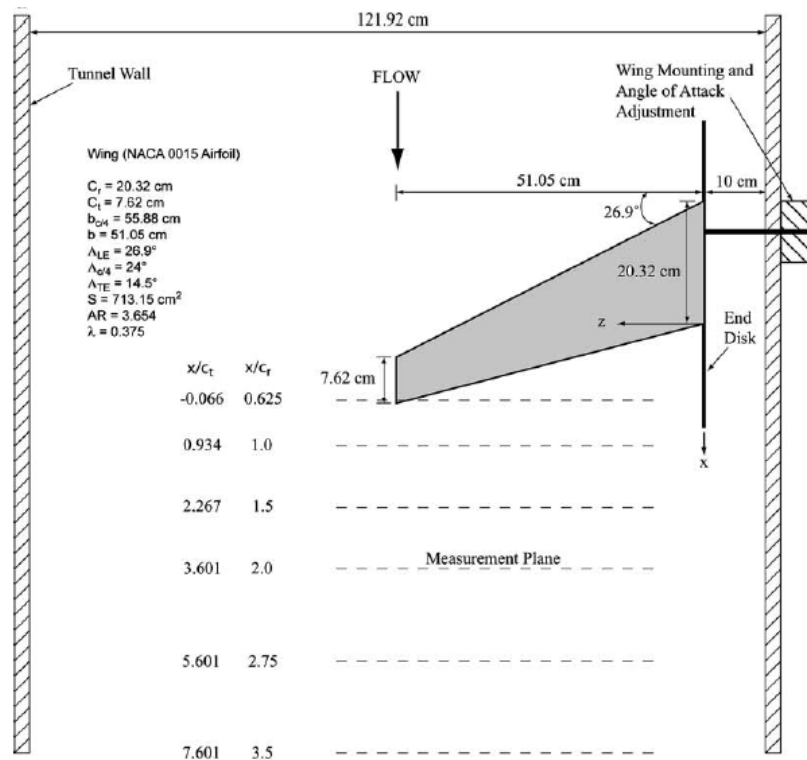


Fig. 3.15 “Gerontakos swept wing” downstream velocity measurements configuration [31]

The boundary conditions are *velocity-inlet* for the inlet, *pressure-outlet* for the outlet, *slip wall* for the wind tunnel walls and *no-slip wall* for the wing lateral wall (Fig. 3.16 – left image) [38]. Fig. 3.16 (right image) reports the main dimensions of the domain used in the simulations.

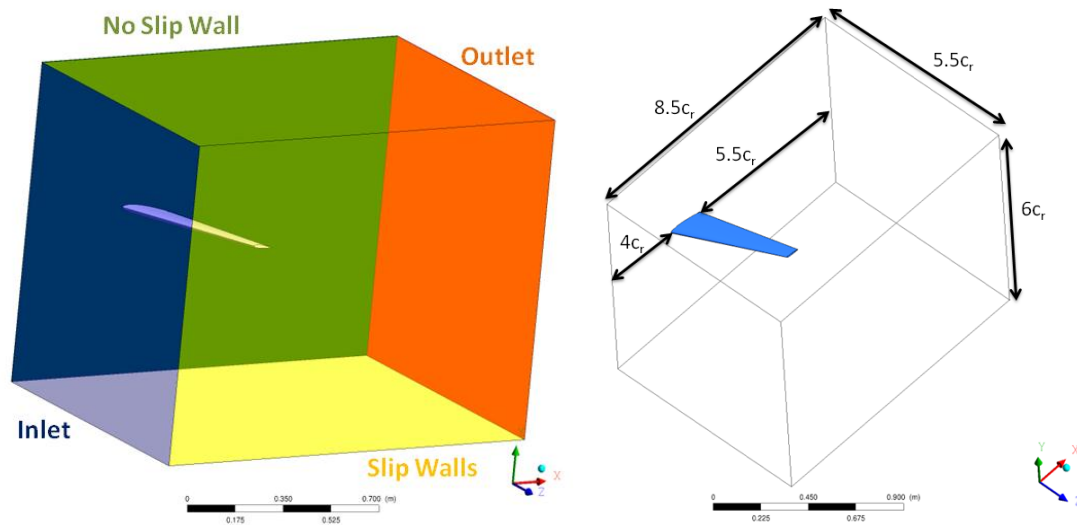


Fig. 3.16 Domain (left image) and boundaries main dimensions (right image) of the “Gerontakos swept wing” model

3.6.4 Grids

Various grids at different angles of attack were generated to reproduce the wing and the wind tunnel described by Gerontakos and Lee [31]. Since no wind tunnel corrections were applied to the experimental measurements, the wind tunnel walls were reproduced in the CFD model as well. This means that for each incidence setting, a new grid was required to ensure that the tunnel effects were not neglected.

The first one has 7.8 million cells and is a hybrid unstructured mesh with prism layer structured cells on the wing surface and on the wind tunnel walls (Fig. 3.17 - Fig. 3.18). The first layer is 0.018 mm high ($8.8 \times 10^{-5} y/c_r$) and the total number of prism layers is 16, for a total height of 1.574 mm ($0.0077 y/c_r$). Since the lift coefficient (C_L) of the results obtained with this mesh did not match the one of Gerontakos and Lee, other meshes were generated with different angles of attack to find the right C_L and build a C_L curve. Then other two grids of 5 millions cells were created respectively with an angle of attack of 6.5° and of 9.5° . The C_L obtained with the grid where the angle of attack equalled 9.5° was almost identical to the one of the experimental study. For this reason the grid was modified and three different densities were inserted in the wake in order to obtain a finer grid in the tip vortex zone (Fig. 3.19 and Fig.

3.20) and to have at least 6 nodes in the vortex core (Fig. 3.21). The new grid has 12 million cells.

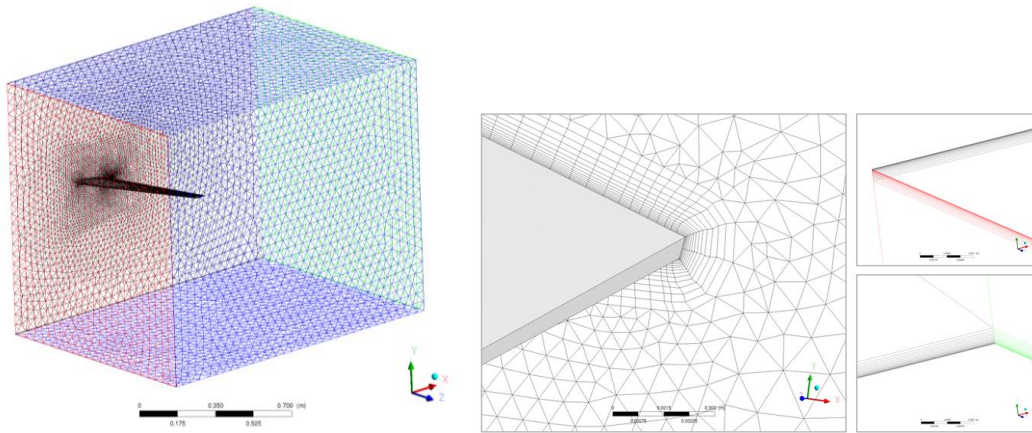


Fig. 3.17 Far-field (left image) and prism layers (right image) of the “Gerontakos swept wing” 7 million cells grid

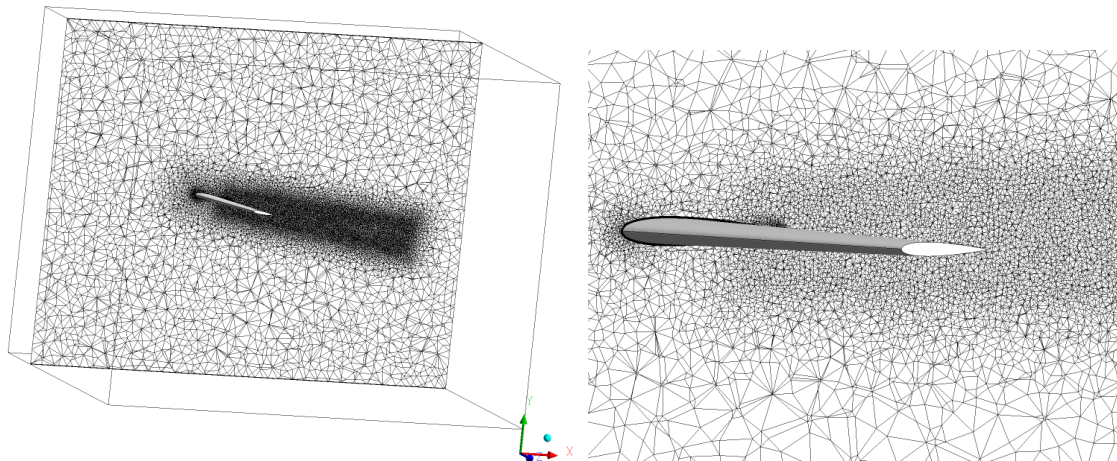


Fig. 3.18 Densities of the volume mesh in the wing wake of the “Gerontakos swept wing” 7 million cells grid

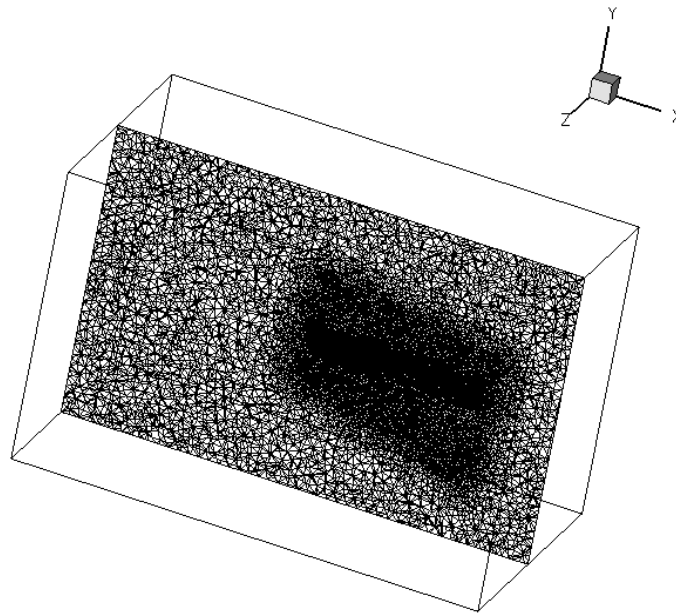


Fig. 3.19 Densities of the volume mesh in the wing wake of the “Gerontakos swept wing” 12 million cells grid

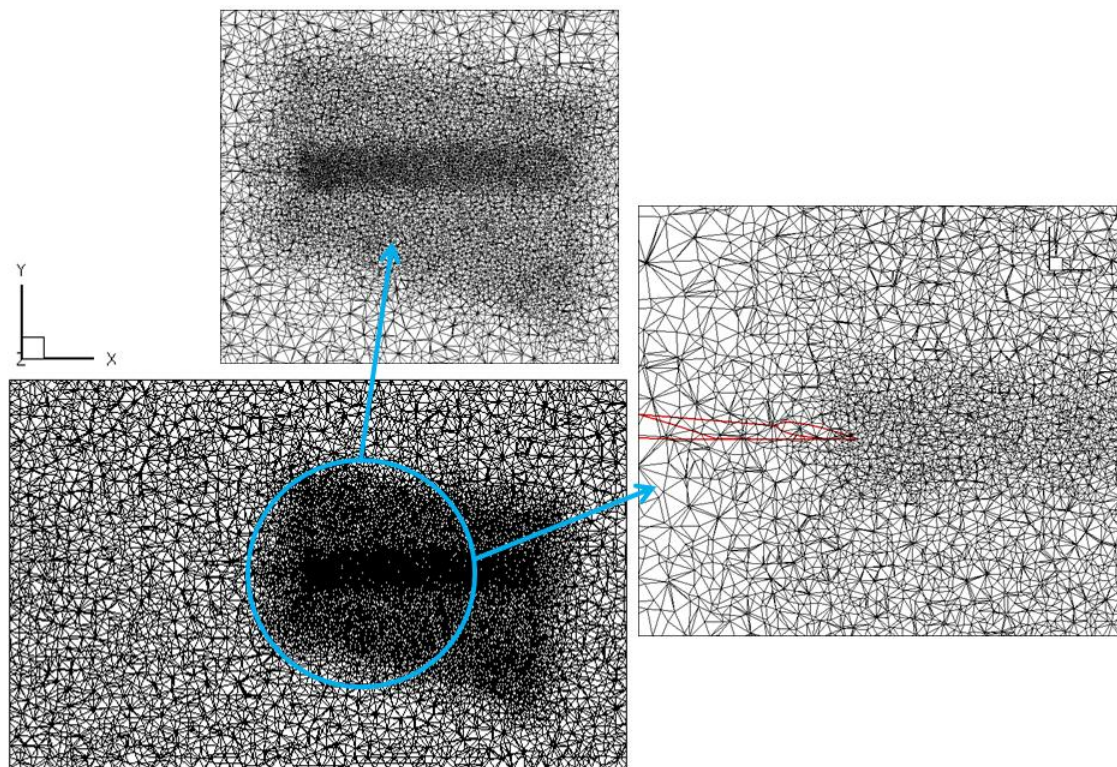


Fig. 3.20 Detail of the densities of the volume mesh in the wing wake of the “Gerontakos swept wing” 12 million cells grid in a XY plane

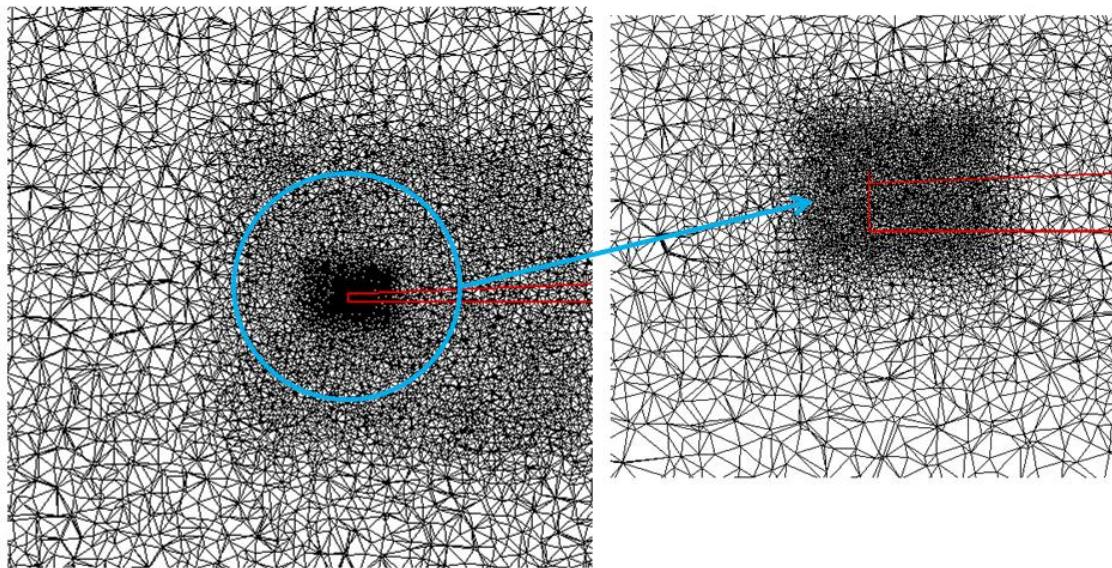


Fig. 3.21 Detail of the densities of the volume mesh in the wing wake of the “Gerontakos swept wing” 12 million cells grid in a YZ plane

3.7 Convergence criteria

The convergence of the simulations was based on the residual equations. The C_L and C_d values were monitored. The convergence criteria and monitoring were different in the two used solvers, ANSYS Fluent and ANSYS CFX.

3.7.1 ANSYS Fluent criteria

Since ANSYS Fluent was run on batch mode the graphical visualisation of the residual was not possible. The residuals were monitored and at the end of the calculations all the residuals were equal or below 10^{-2} . Fig. 3.22 shows a typical residual plot of a CRM geometry simulation, which needed around 7000 iterations to converge. The residuals up to 3000 iterations represent the first order solution and the others are the second order. Fig. 3.23 illustrates the monitored C_L and C_d coefficients, used as indicators for the convergence of the solution. Fig. 3.24 shows a typical residuals plot of a Gerontakos swept wing case simulation, that needed around 2000 iterations to converge. The residuals up to 1500 represent the first order solution and the others are the second order. As can be seen, the residual are not all lower of 10^{-5} . This is due to the big considered far-field domain where the mesh is coarser and to the physic of the considered problem. Despite this, the results are still acceptable since the residual in the zones of interest (wing and wake flow field) are lower than 10^{-4} .

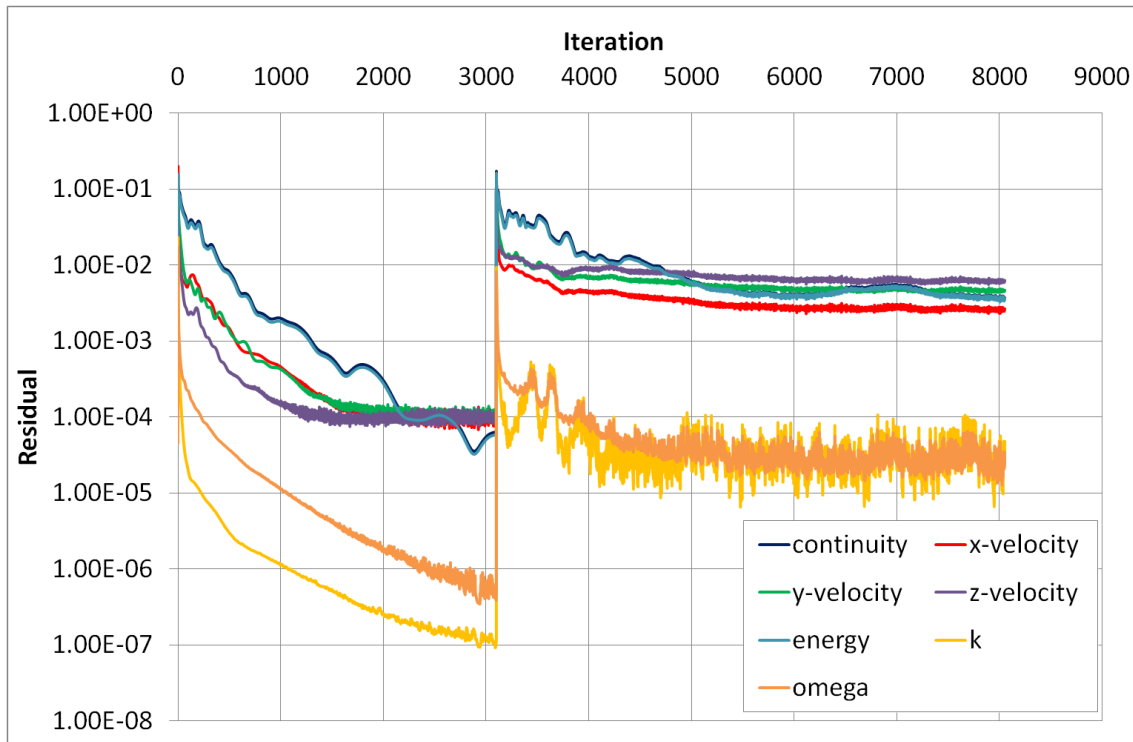


Fig. 3.22 Typical residual plot of a CRM geometry simulation

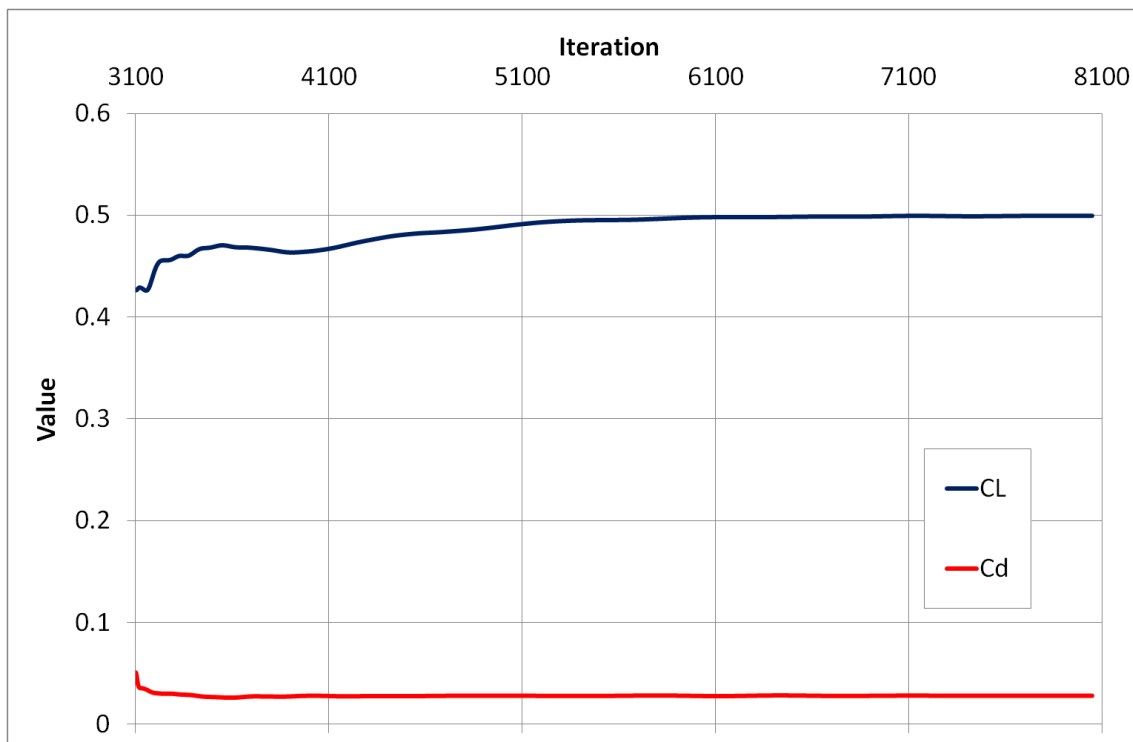


Fig. 3.23 Lift and drag coefficients monitor plot of a CRM geometry simulation

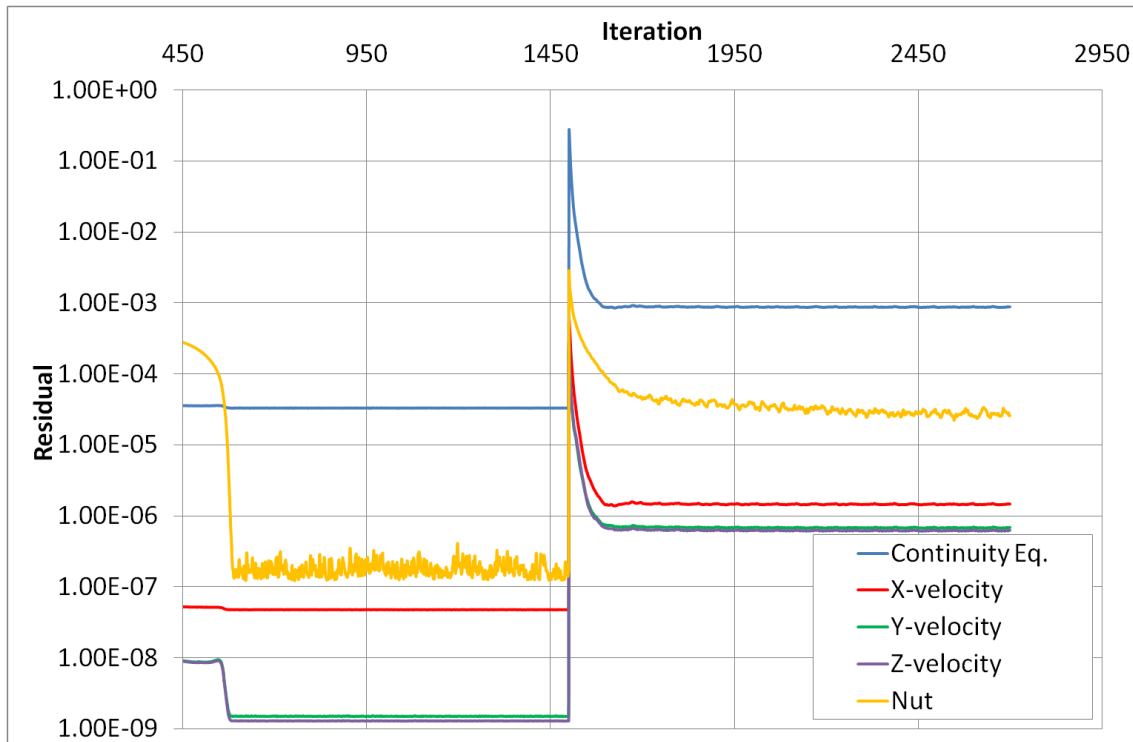


Fig. 3.24 Typical residual plot of a Gerontakos swept wing case simulation

3.7.2 ANSYS CFX criteria

In the CFX-Solver Modelling Guide [41] is provided a guidance regarding the convergence and the target root mean square (RMS) residual levels that are expected to be reached for CFX simulations:

- values larger than $1e-4$ may be adequate to achieve a qualitative understanding of the flow field;
- $1e-4$ is fairly loose convergence, but may be satisfactory for many engineering applications;
- $1e-5$ is good convergence, it is usually adequate for most engineering applications;
- $1e-6$ or lower is very tight convergence. It is sporadically necessary for geometrically sensitive problems. It is often not possible to accomplish this level of convergence, in particularly when using a single precision solver.

The comparison of the convergence and residual criteria of individual CFD solvers is not always applicable as the methodology and implementation of the physical models and numerical techniques are generally different. Fig. 3.25 shows a typical residual plot of a CRM geometry simulation, which needed

around 200 iterations to converge. Fig. 3.26 illustrates the monitored C_L and C_d coefficients, used as indicators for the convergence of the solution. As can be seen, the residuals are not all lower of 10^{-5} . This is due to the big considered far-field domain where the mesh is coarser and to the physic of the considered problem. Despite that the results are still acceptable since the residual in the zones of interest (wing and wake flow field) are lower than 10^{-4} .

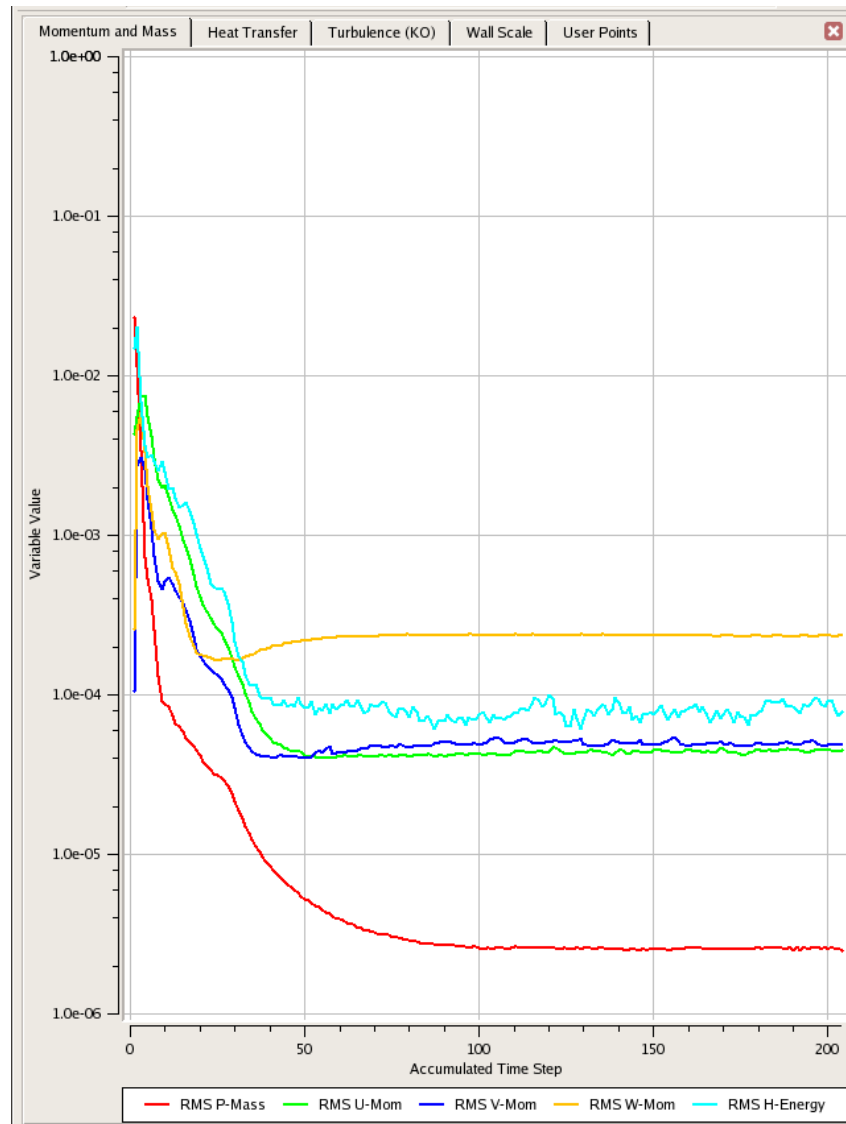


Fig. 3.25 Typical residual plot of a CRM geometry simulation

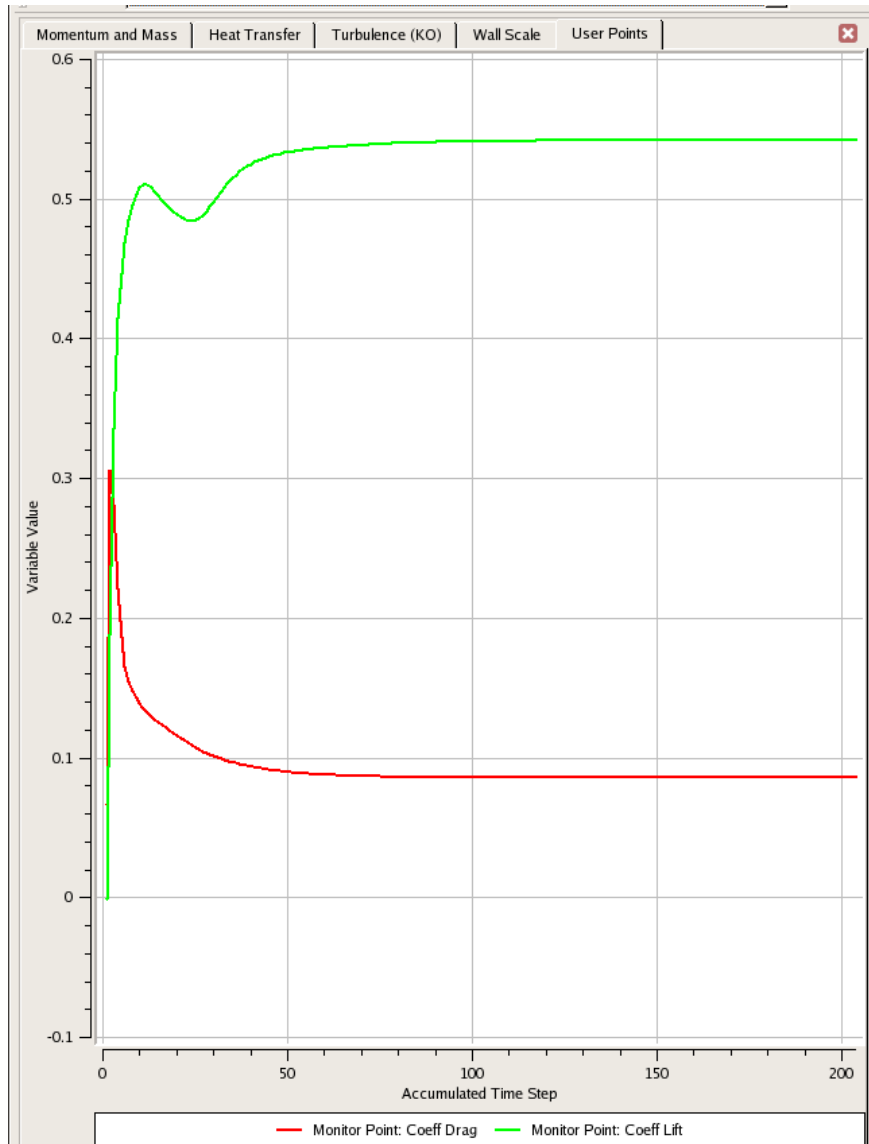


Fig. 3.26 Lift and drag coefficients monitor plot of a CRM geometry simulation

3.8 Post-processing

3.8.1 Tecplot

For the post-processing of the CFD results the software Tecplot 360[®] was used, that is a software package used in the post-processing of numerical simulations. This is a powerful tool for visualising a wide range of technical data. Common tasks associated with post-processing analysis of flow solver data (like Fluent data) include:

- the calculation of grid quantities such as aspect ratios, skewness, orthogonality and stretch factors;

- the normalisation of data and derivation of flow field functions like the pressure coefficient or the vorticity magnitude;
- the verification of the solution convergence;
- the estimation of the order of accuracy of solutions;
- the interactive exploration of data through cut planes (a slice through a region), isosurfaces (3D maps of concentrations) and particle paths (dropping an object in the "fluid" and observing its movement patterns).

The software provides the possibility to play or record macros and these functions were used to post-process the tip vortex quantities. Macros are very useful to perform repetitive operations such as setting up frames, reading in data and layout files, manipulating data and creating plots.

3.8.2 Vortex core and circulation

A specific post-processor was developed in MATLAB to evaluate the vortex V_θ distributions and the circulation (Γ). The post-processor is based on a circular zone disk method and it calculates the circulation from the axial vorticity distribution and the core size of the vortex from the V_θ distribution. The vortex characteristics are calculated by a two-dimensional analysis of the vortex in a y - z plane, normal to the streamwise direction. The input of the MATLAB script is an ASCII data file specifically created in Tecplot. To generate this data file three Tecplot macros were used.

The first macro creates n slices at different streamwise locations in an y - z plane perpendicular to the axial direction of the flow. The choice of the slices locations is based on the streamwise locations of the vortex that are selected for the analysis. The second macro creates a circular zone for each slice with the centre located in the centre of the vortex, that corresponds to the point of maximum axial vorticity (Fig. 3.27 and Fig. 3.28). Furthermore, this circular zone has circular coordinates and the radius of the zone is an input in the macro and is chosen based on the wing reference chord. The third macro exports the created circular zones as an ASCII data file ready to be read by the MATLAB script.

The MATLAB script reads only one circular ASCII data file at time, therefore it has to be run as many times as the number of slices. The inputs of the script are the x , y , z coordinates, the V_x , V_y , V_z velocity components and the axial vorticity. Tecplot expresses the coordinates in terms of x , y , z also for the circular zone disc, but the points of the disc are already plotted and exported in circular coordinates (Fig. 3.29).

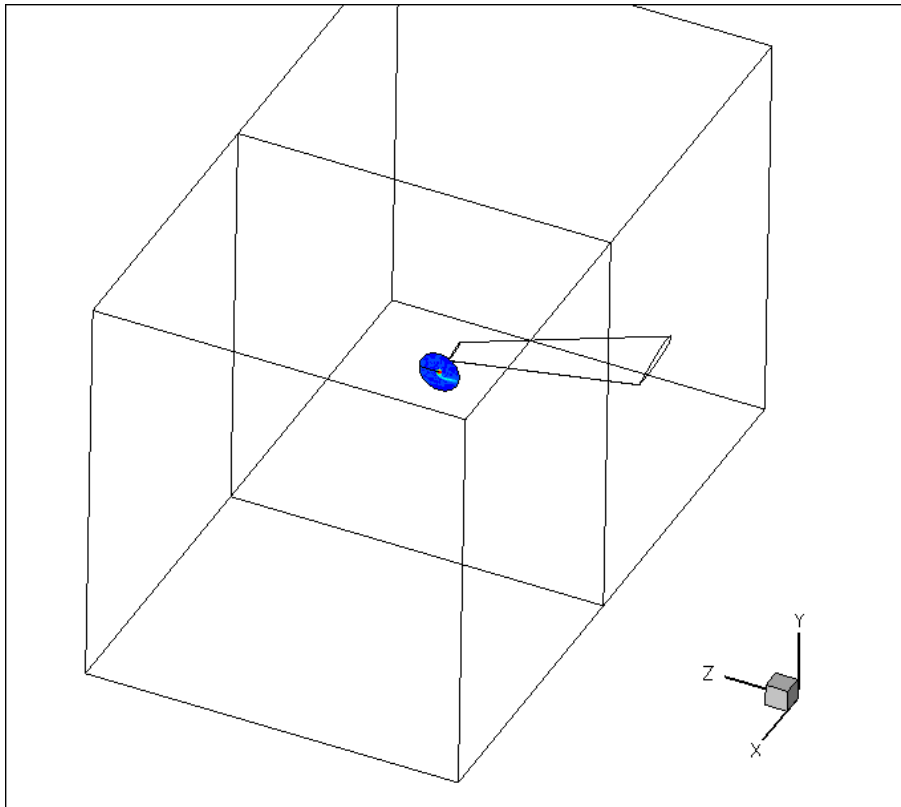


Fig. 3.27 Example of circular zone for one of the slices with the centre located in the centre of the vortex

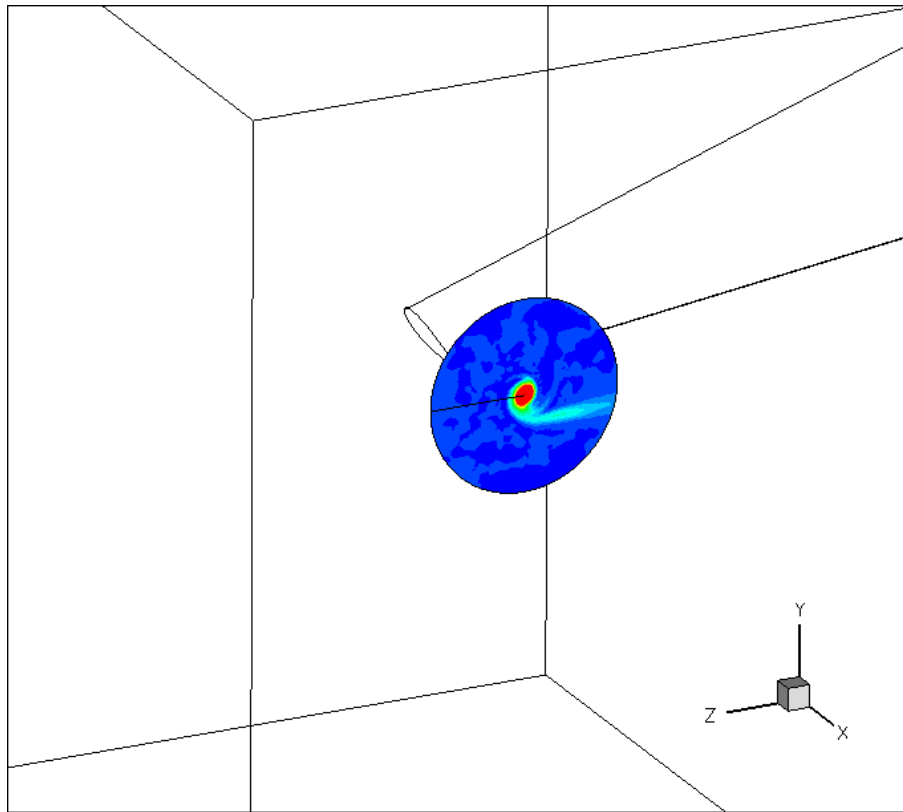


Fig. 3.28 Example of circular zone for one of the slices with the centre located in the centre of the vortex

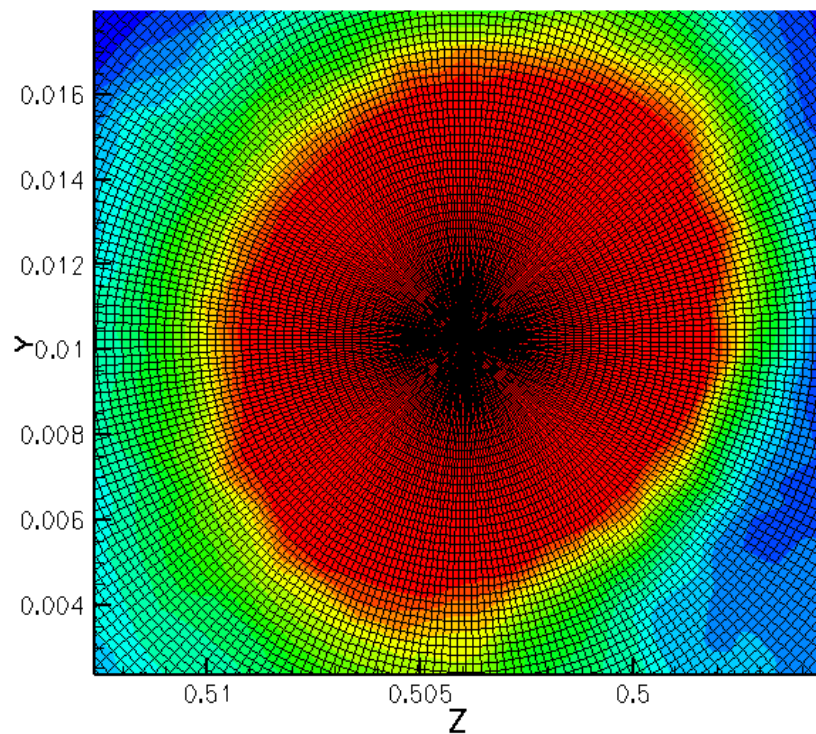


Fig. 3.29 Circular zone disc mesh

The script finds the vortex centre and calculates the radial distance from the centre and the θ angle for each point of the circular zone. The θ angle is

calculated as the $\text{atan2}((z_i-z_c),(y_i-y_c))$. Once the circular coordinates are expressed in r and θ , the script calculates the tangential velocity V_θ with the following expression:

$$V_\theta = -v_y \sin \theta + v_z \cos \theta \quad (16)$$

The script exports the values of V_θ as a function of r . The radius corresponding to the maximum value of the tangential velocity is the vortex core radius, according to its definition [27]. The script calculates also the circulation by the area integral over vorticity (Eq. 8). The output is the circulation as a function of the radius. The core circulation is the circulation at the vortex core radius.

Chapter 4

DLR-F6 results and analysis

4.1 Introduction

The first step in the research was to perform simulations to achieve a comparison of the turbulence models, the boundary conditions and the codes themselves. Due to the larger amount of available experimental data it was decided to perform this analysis with the DLR-F6 geometry. The available experimental data includes C_L , C_d , C_m and C_p distributions.

4.2 DLR-F6 Results

A comparison between the turbulence models, the boundary conditions and the CFD codes was carried out with the DLR-F6 geometry scaled to wind tunnel conditions (Table 4.1 and Table 4.2).


	Model	M > 0.8	High Re	Exper. Cd, Cl	Downstream measurement	Other CFD Data	Description
a. 	DLR-F6	x	✓	✓	x	x	- Geometry and meshes available. - Cd, Cl, Cp, Cm experimental data available. - Geometry similar to the A330.

Table 4.1 DLR-F6 geometry characteristics

Geometry	Code	Mesh size	Turb. Model	T. I. [%]	Visc. Ratio [-]	AOA [°]	C_l [-]	Ts [K]	Ps [Pa]
DLR-F6	FLUENT	5MIL	SST	2	3	0.2007	0.499	305	128921
	FLUENT	5MIL	SA	2	3	0.2007	0.531	305	128921
	FLUENT	9MIL	SST	2	3	0.2007	0.505	305	128921
	CFX	5MIL	SST	2	3	0.2007	0.472	305	128921
	CFX	5MIL	SA	2	3	0.2007	0.505	305	128921
	CFX	9MIL	SST	2	3	0.2007	0.489	305	128921

Table 4.2 CFD simulations boundary conditions

As stated in Chapter 3, the experimental data are available as C_L and C_d curves and pressure coefficient distributions, C_p . Since the cruise Mach number of the

DLR-F6 geometry is 0.75 for a corresponding $C_L=0.5$, and the C_p results are available for this condition, a C_L of around 0.5 was obtained for each of the considered cases (Table 4.2). While a C_L of 0.498 in the experiments is achieved with an angle of attack of 0.49° , in the CFD it was obtained approximately with an angle of attack of 0.201° in both the considered solvers. This outcome is probably due to the deformation effects of the model that are present in the wind tunnel and not in the CFD.

A comparison of the sensitivity of the calculated C_L and C_d values to the mesh resolution (5 and 9 million cells) was carried out (Fig. 4.1 and Fig. 4.2). With the Fluent code the differences between the results of the two considered grids are very low. The difference in the C_L values between the 5 and 9 million cells grids is only of 1% and in the C_d values the difference is of 3.5%. This means that the mesh sensitivity of Fluent on the results is very low. With the CFX code the differences between the results of the two considered grids are higher. The difference in the C_L values between the 5 and 9 million cells grids is only of 3.5% and on the C_d values is of 15.5%. This means that in the CFX code the results are influenced by the mesh resolution. The mesh sensitivity is higher than in Fluent for the two considered meshes and the mesh independency is not achieved.

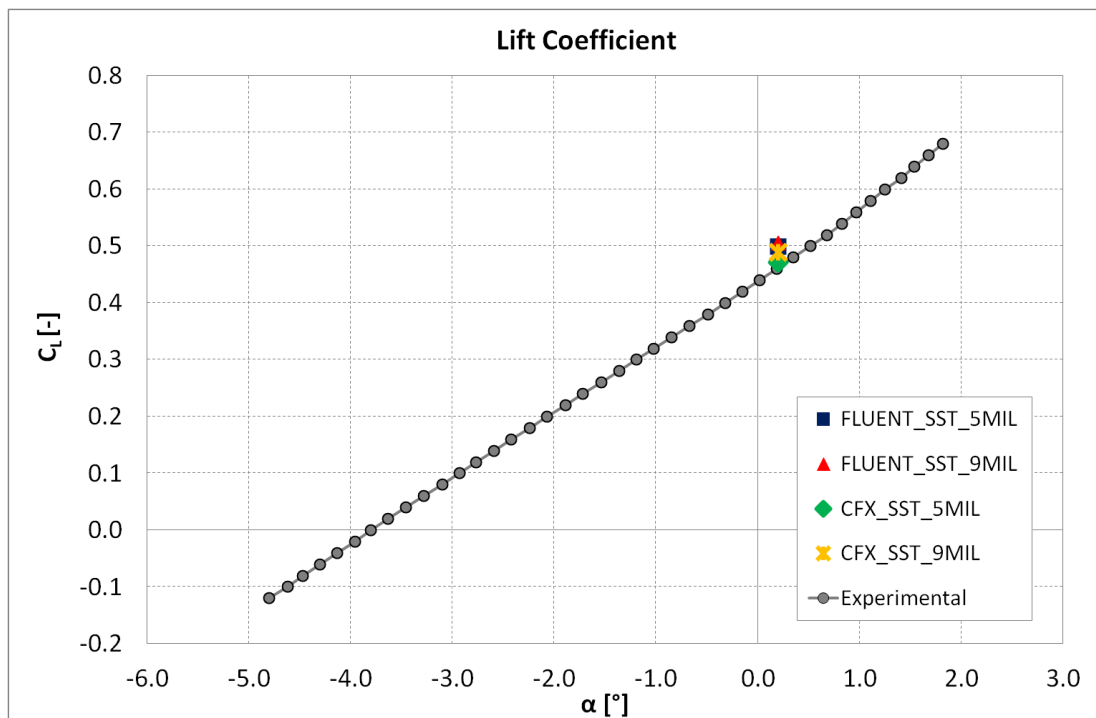


Fig. 4.1 Comparison of the lift coefficient values with different solvers and grids

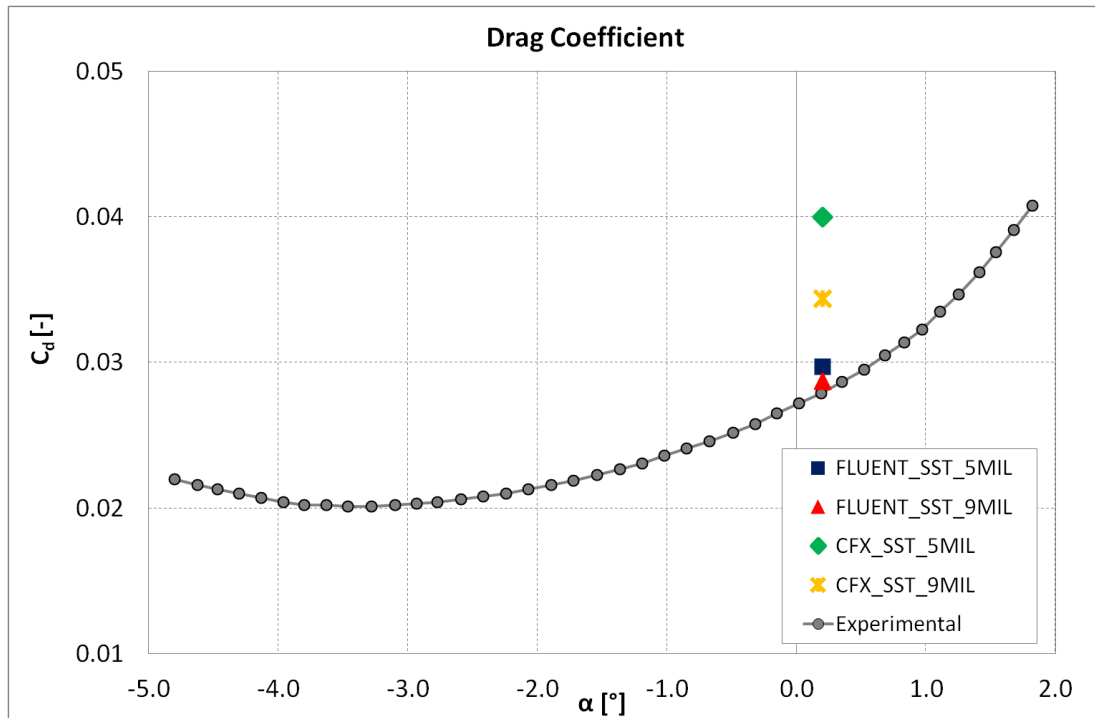


Fig. 4.2 Drag coefficient values with different solvers and grids

Furthermore, a comparison between the two considered codes was carried out with the same two considered grids of 5 and 9 million cells, the same angle of attack of 0.201° for a corresponding C_L of around 0.5. The Fluent solver has a better agreement with the experimental results than the CFX solver. Fluent predicts the values of the C_d considerably better than CFX. While the C_d results of Fluent have a maximum error of 1% compared with the experimental data, the C_d results of CFX have an error of 41% with the 5 million cells mesh and 18% with the 9 million cells mesh compared with the experimental data (Fig. 4.2). Moreover, a study on the turbulence model was performed. Simulations of the 5 million cells grid were carried out with the SST and the SA turbulence models in both the CFD codes (Fig. 4.3 and Fig. 4.4). With the Fluent code the results obtained with the SST turbulence model are in better agreement with the experimental data than the results obtained with the SA turbulence model. The error in the C_d value compared with the experimental data for the SST results is less than 1%, while with the SA results is of 4%. With the CFX code the results obtained with the two turbulence models have both high errors compared with the experimental data. The error in the C_d value compared with the

experimental data for the SST results is around 41%, while with the SA results is of 35%.

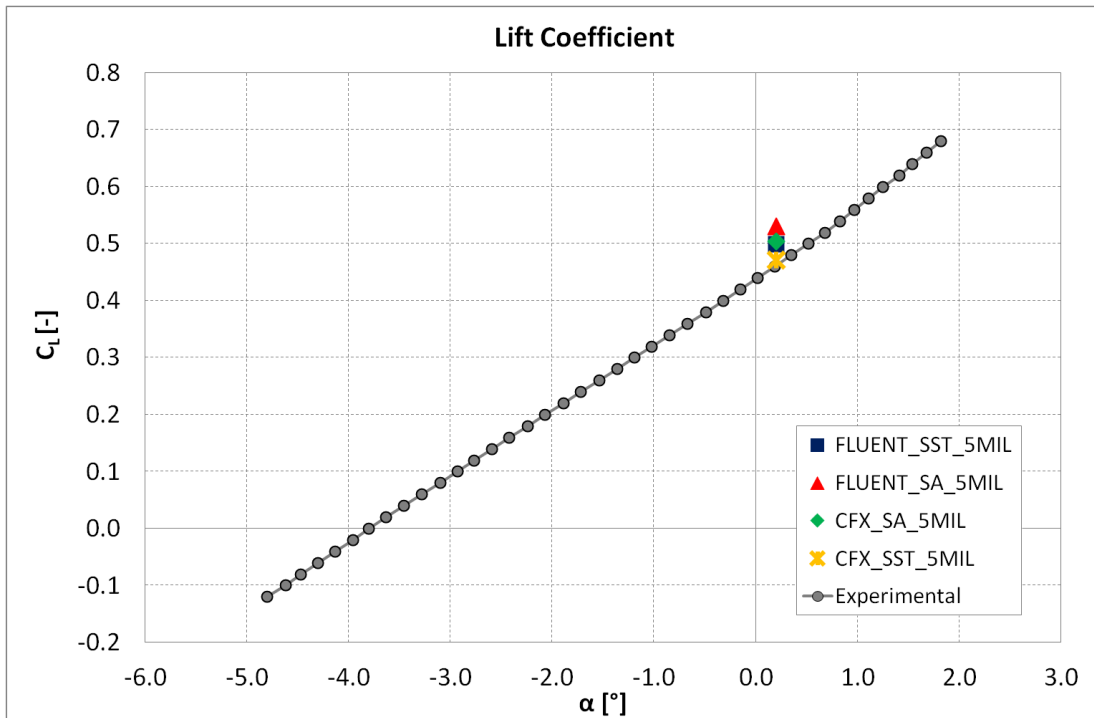


Fig. 4.3 Comparison of the lift coefficient values of the 5 million cells grid with different solvers and turbulence models

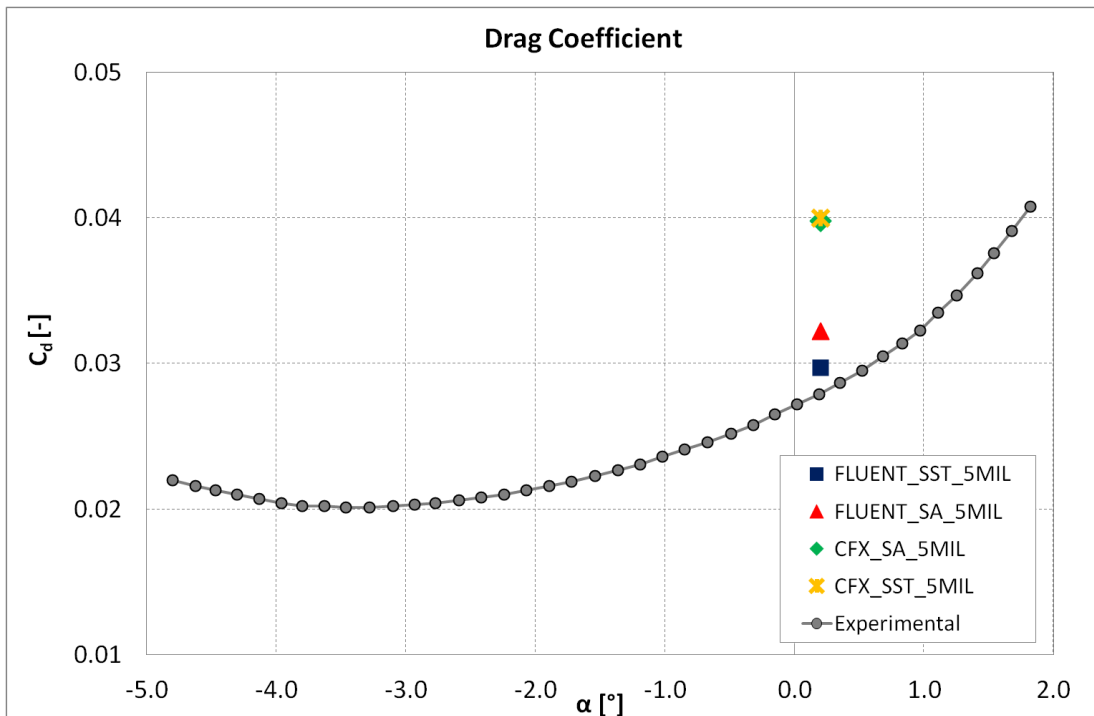


Fig. 4.4 Drag coefficient values of the 5 million cells grid with different solvers and turbulence models

The pressure distribution on the wing is one of the factors that determine the formation of the tip vortex, consequently the pressure coefficients, C_p , at various locations on the wing span were post-processed and compared with the experimental data. For compressible aerodynamics flows the common expression is:

$$C_p = \frac{2}{\gamma M_\infty^2} \left(\frac{p}{p_\infty} - 1 \right) \quad (17)$$

Fig. 4.5 represents the non-dimensional wing span locations, $\eta=y/(b/2)$, that were analysed.

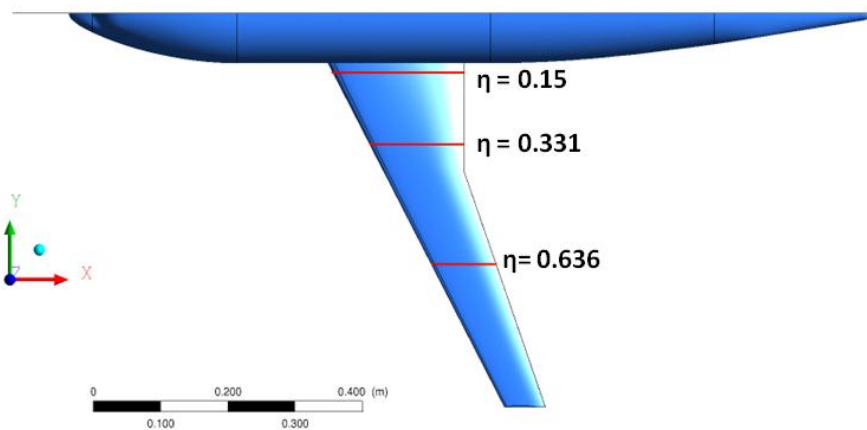


Fig. 4.5 Location of different η on the DLR-F6 geometry

A comparison between the pressure coefficient distributions of the experimental data and the ones calculated with Fluent and CFX at various η for the 5 million cells grid was performed (Fig. 4.6 - Fig. 4.8). The Fluent results are in better agreement with the experimental data than the CFX results. In Fluent the location of the shock is reasonably predicted in comparison with the experimental data (Fig. 4.7). In the plots are also reported the results obtained with the two considered turbulence models. As can be seen the C_p plots confirm that both in Fluent and CFX codes the differences between the two turbulence models are low. Furthermore, a comparison between the experimental data and the pressure coefficient distributions calculated with the two different grids (5 million and 9 million cells) with the SST turbulence model at various η was carried out (Fig. 4.9 - Fig. 4.11). Using the 9 million cells grid it can be observed an improvement in the CFX results, but the Fluent results are still in better

agreement with the experimental data.

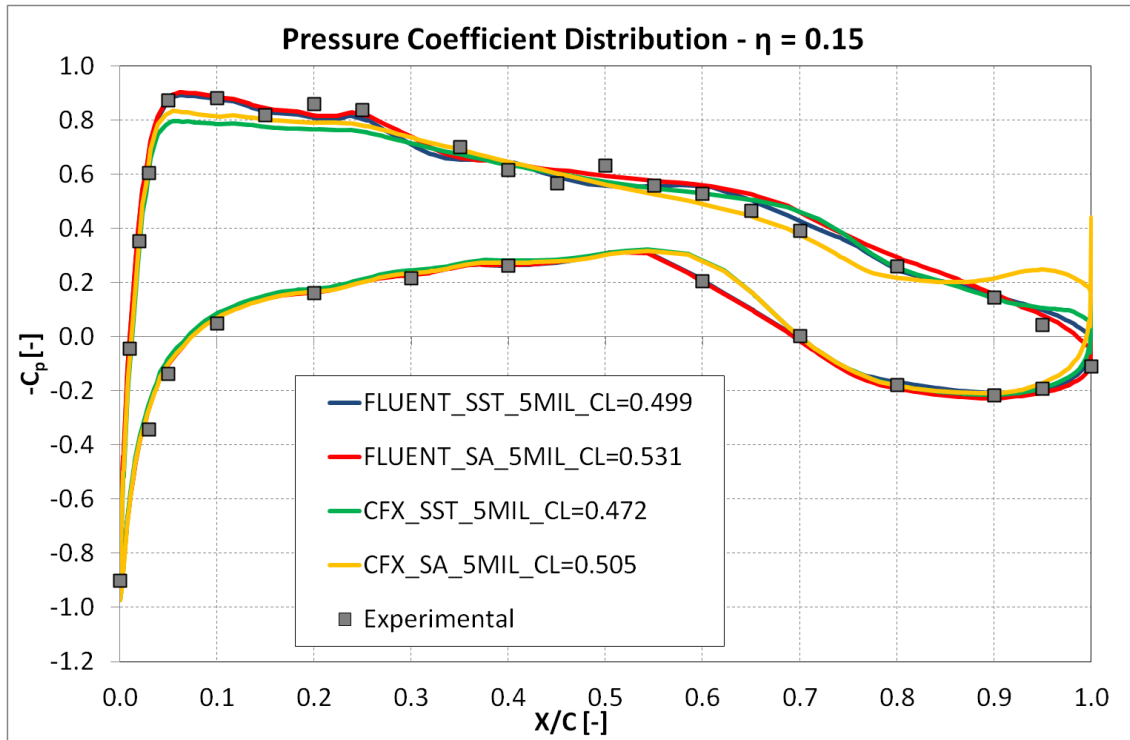


Fig. 4.6 Pressure coefficient distributions at $\eta=0.15$ of the 5 million cells grid with different solvers and turbulence models – $Re=3 \times 10^6$, CFD $\alpha=0.2007^\circ$, EXP $\alpha=0.490^\circ$ $C_L=0.4984$

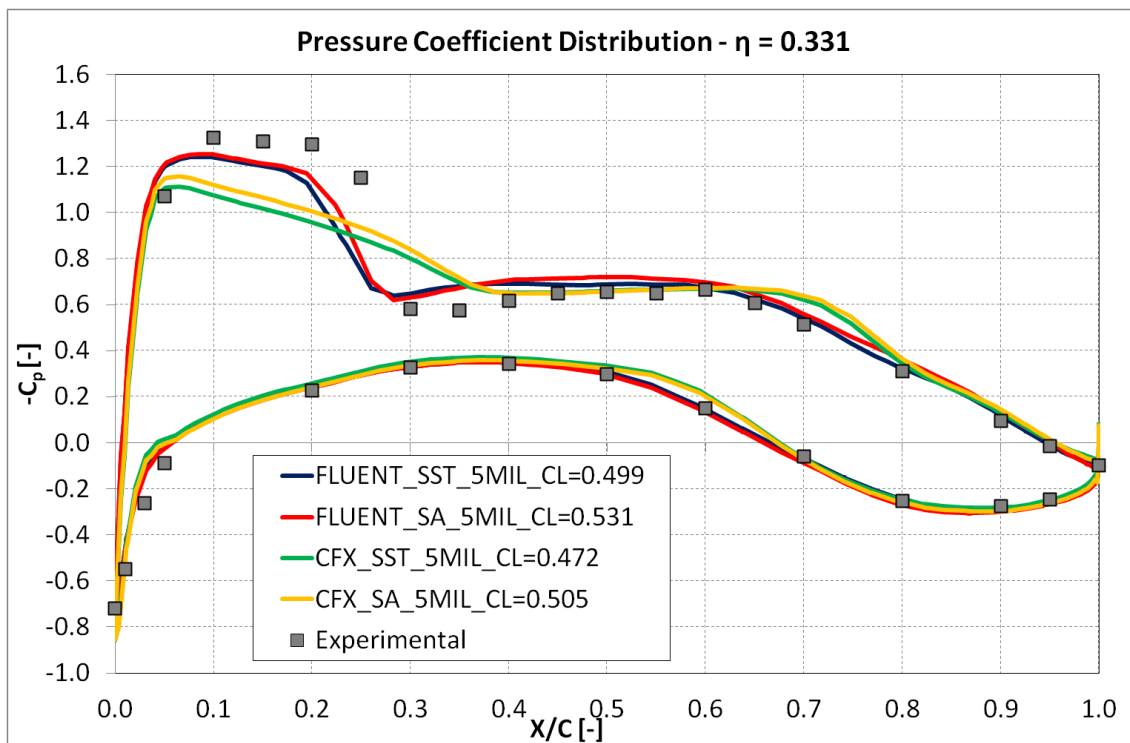


Fig. 4.7 Pressure coefficient distributions at $\eta=0.331$ of the 5 million cells grid with different solvers and turbulence models – $Re=3 \times 10^6$, CFD $\alpha=0.2007^\circ$, EXP $\alpha=0.490^\circ$ $C_L=0.4984$

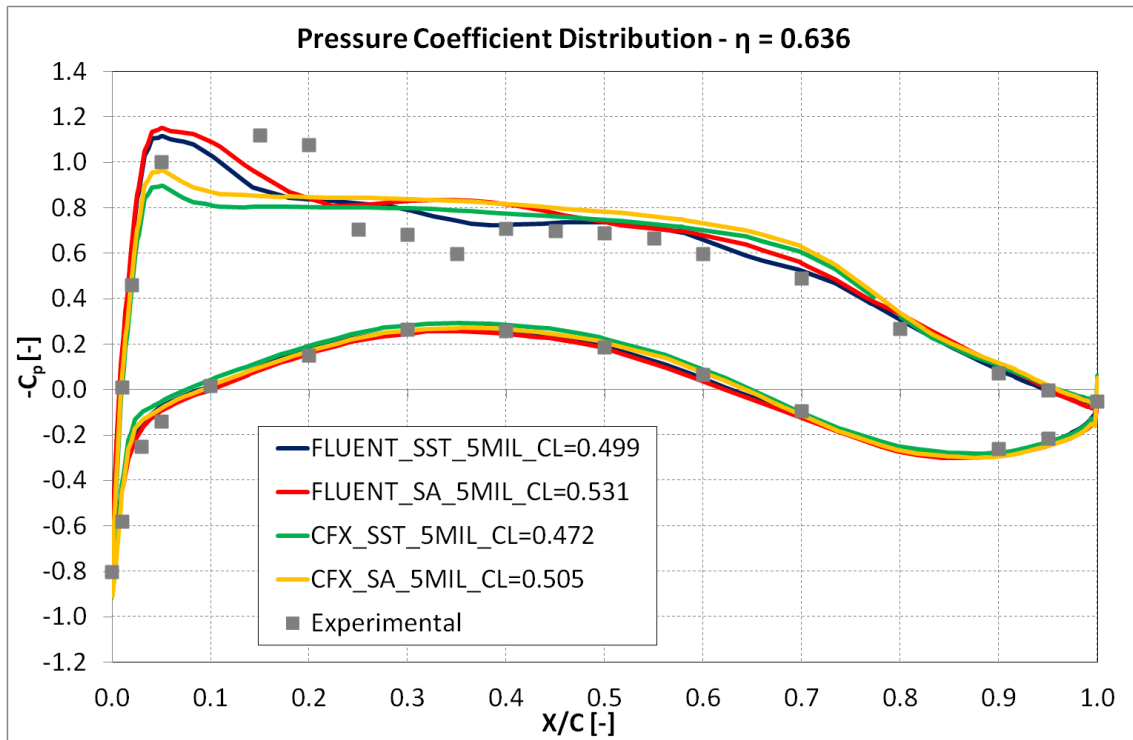


Fig. 4.8 Pressure coefficient distributions at $\eta=0.636$ of the 5 million cells grid with different solvers and turbulence models – $Re=3 \times 10^6$, $\underline{CFD} \alpha=0.2007^\circ$, $\underline{EXP} \alpha=0.490^\circ C_L=0.4984$

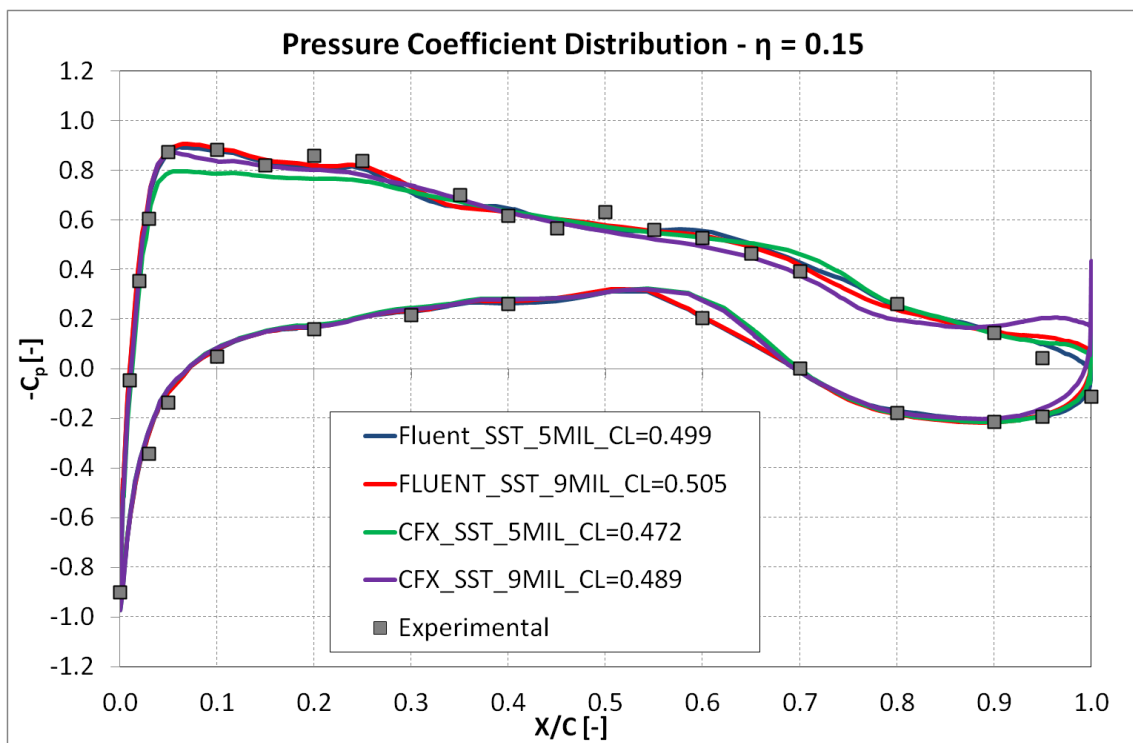


Fig. 4.9 Pressure coefficient distributions at $\eta=0.15$ with different solvers and grids – $Re=3 \times 10^6$, $\underline{CFD} \alpha=0.2007^\circ$, $\underline{EXP} \alpha=0.490^\circ C_L=0.4984$

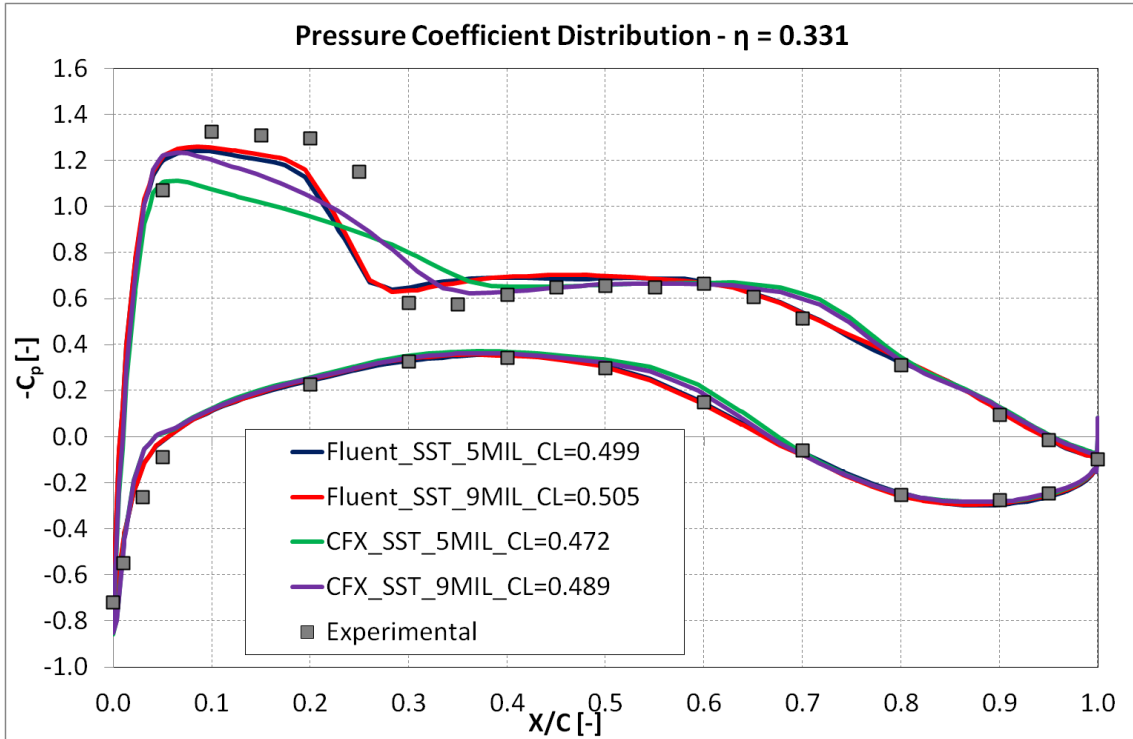


Fig. 4.10 Pressure coefficient distributions at $\eta=0.331$ with different solvers and grids – $Re=3 \times 10^6$, CFD $\alpha=0.200^\circ$, EXP $\alpha=0.490^\circ$ $C_L=0.4984$

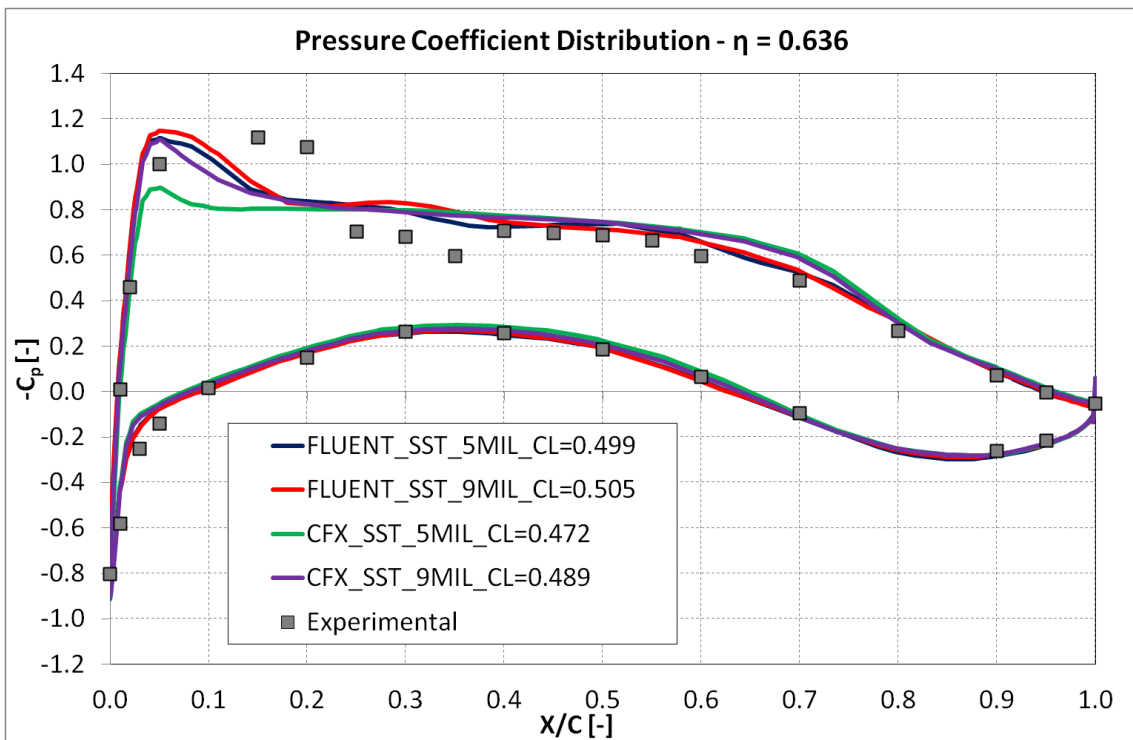


Fig. 4.11 Pressure coefficient distributions at $\eta=0.636$ with different solvers and grids – $Re=3 \times 10^6$, CFD $\alpha=0.200^\circ$, EXP $\alpha=0.490^\circ$ $C_L=0.4984$

Since for the Fluent code the mesh sensitivity was very low and the results were in better agreement with the experimental data compared with the CFX ones it can be concluded that the ANSYS Fluent solver seems to better resolve the kind of problem analysed in this project, with an unstructured hybrid grid and a Cartesian far-field. Furthermore, since the error in the C_d value compared with the experimental data for the SST results is less than 1%, while with the SA results is of 4%, the SST turbulence model was chosen to perform all the other simulations related to the project.

Chapter 5

CRM at wind tunnel scale

5.1 Introduction

A study about the turbulence models, the boundary conditions and the CFD codes was performed with the DLR-F6 scaled to the wind tunnel model size. Validation results were obtained as well. The Fluent code results were in better agreement with the experimental data compared with the CFX ones. Furthermore, the SST turbulence model was chosen to perform all the other simulations related to the project, since with this turbulence model the drag coefficient values are in very good agreement with the experimental data. Despite that, further simulations of the CRM scaled to the wind tunnel model size were needed to validate the results also with this geometry and at a higher Mach number. Furthermore, these simulations were utilised to compare the obtained CFD results with the results of the first version of the ELL code, available at that point of the research. Since the ELL code does not include a tail, the CRM geometry wing-body configuration (without tail) was chosen to perform these wind tunnel conditions simulations (Table 5.1).


	Geometry	M > 0.8	High Re	Exper. Cd, Cl	Downstream measurement	Other CFD Data	Description
b.	 CRM NO_TAIL WIND TUNNEL SCALE	✓	✓	✓	x	x	- Geometry available. - Only Cd and Cl experimental data available. - Geometry similar to the A330.

Table 5.1 CRM geometry scaled at wind tunnel conditions characteristics

5.2 Wing-body CRM geometry at wind tunnel scale results

The cruise lift coefficient for this geometry is 0.5. The available experimental results available are C_L and C_d polars. Furthermore, the CFD studies of the CRM geometry performed on the 4th Drag Prediction Workshop [37] are available for

a C_L of 0.5. Various simulations were carried out to find the angle of attack that corresponds to a $C_L=0.5$ for every mesh (Table 5.2). Furthermore, the 15 million cells mesh test case was simulated at various angles of attack (in a range from -2° to 5°) to build the C_L and C_d curves and to compare them with the experimental data. The simulations that were completely post-processed (pressure coefficient distributions, wake velocity flow field and tip vortex characteristics) and compared with the experimental data are the two with a C_L of ≈ 0.5 , which correspond to the 7 million cells mesh with an angle of attack of 2.6° and to the 15 million cells mesh with an angle of attack of 2.26° .

CRM NO_TAIL	AOA	C_L	C_d
EXPERIMENTAL	2.791	0.5	0.02489
FLUENT_SST_7MIL	2.6	0.504	0.03434
FLUENT_SST_15MIL	2.26	0.497	0.02824

Table 5.2 C_L and C_d values

C_L and C_d curves were achieved and compared with the experimental data (Fig. 5.1 and Fig. 5.2). The CFD results are in reasonable agreement with the experimental data, but as can be seen the C_L and the C_L - C_d curves are translated compared to the experimental curves. The C_L with the same angle of attack as in the experimental data is in the CFD results around 15-20% higher than the experimental one at low angles of attack. The differences in the C_L - C_d curves are around 10 drag counts.

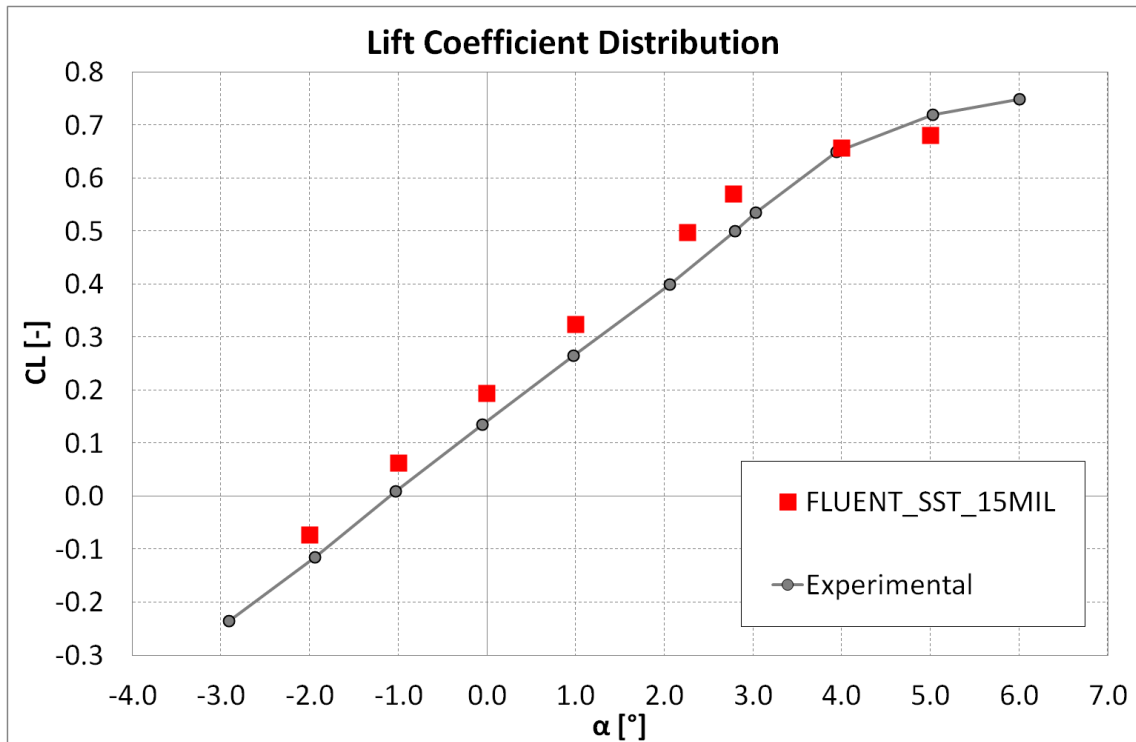


Fig. 5.1 Lift coefficient distributions of the CRM geometry at wind tunnel scale

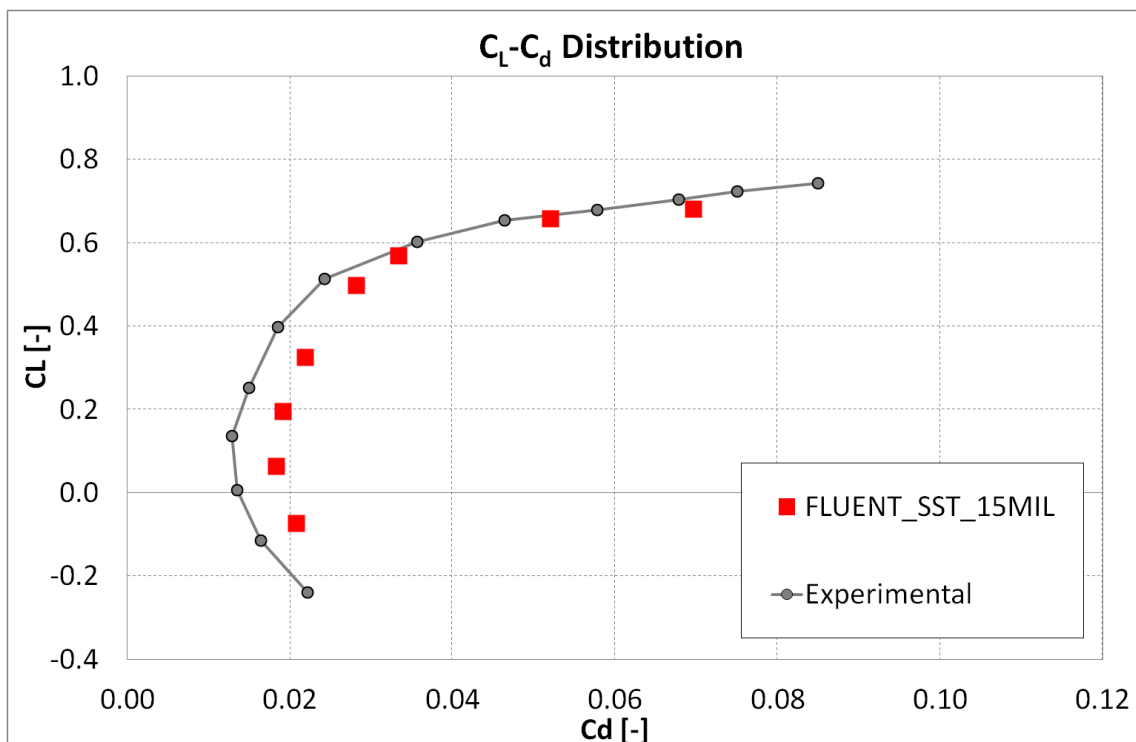


Fig. 5.2 C_L - C_d distributions of the CRM geometry at wind tunnel scale

The pressure distribution on the wing is one of the factors that determines the formation of the tip vortex, consequently the pressure coefficients, C_p , at various locations on the wing span were post-processed. Since the C_p

experimental data are not available for this geometry, the results were compared with the NASA FUN3D CFD data [37] from the 4th Drag Prediction Workshop. Fig. 5.3 represents the non-dimensional wing span locations, $\eta=y/(b/2)$, that were analysed.

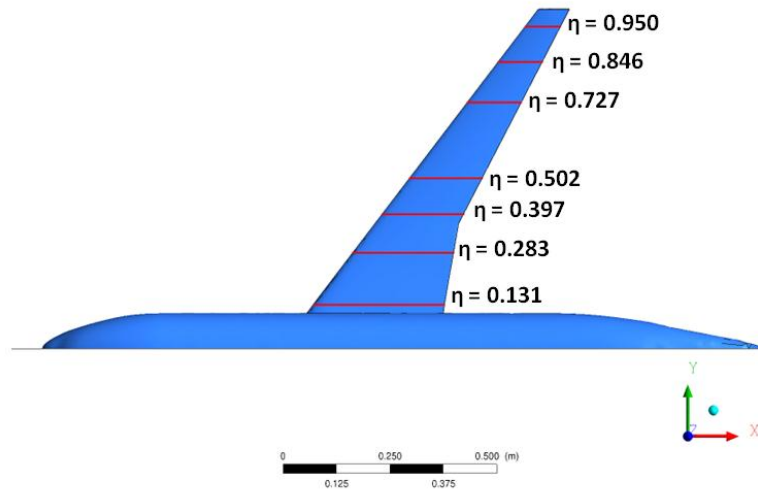


Fig. 5.3 Location of different η on the CRM geometry at wind tunnel scale

The pressure coefficient distributions calculated with Fluent for the two different grids (7 million and 15 million cells) with the SST turbulence model at various η were plotted and analysed (Fig. 5.4 - Fig. 5.10). A consideration about the size of the grids is necessary. The 7 million and 15 million cells grids generated for the present study have a very high density of elements in the wake of the wing, while the NASA 10 million cells mesh was generated with a higher density only around the aircraft. In the comparison of the C_p between the Fluent results and the NASA FUN3D results this is a detail that has to be accounted. If the grids of this project would not have the higher density in the wake, they would be respectively 4 million and 8 million cells grids, consequently less fine than the NASA 10 million cells grid.

The Fluent 15 million cells grid results are in very good agreement with the NASA FUN3D data up to $\eta=0.502$. After $\eta=0.727$ there are some differences in the prediction of the shock. Even if the comparison is between two CFD solver and not with experimental data, these plots confirm that to capture the shock system located around $\eta=0.846$, a finer mesh over the wing is needed. This is confirmed also by the results with the 15 million cells mesh which are improved

compared to the results with the 7 million cells mesh. The computational times and the scope of these simulations did not permit further investigation of the shock issue, therefore the results obtained with the 15 million cells mesh were considered accurate enough for the purposes of the research.

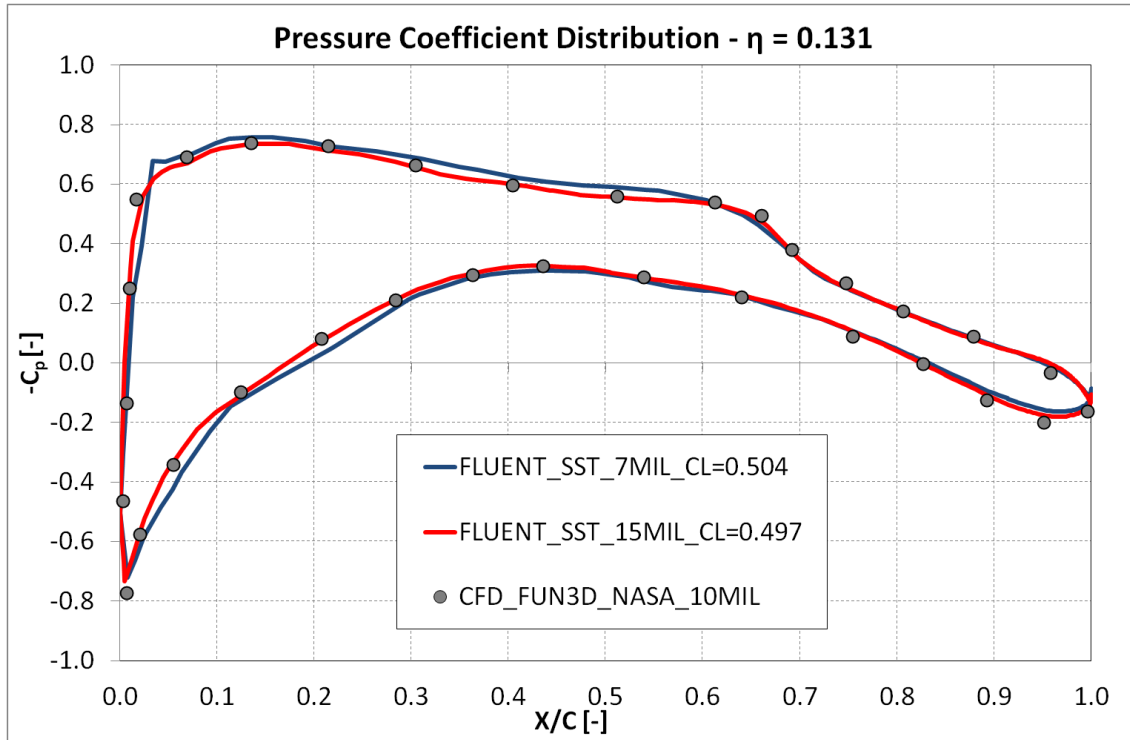


Fig. 5.4 Pressure coefficient distribution at $\eta=0.131$ of the 5 million cells and 9 million cells grids with SST turbulence model – $Re=5 \times 10^6$, 7 million cells $\alpha=2.6^\circ$, 15 million cells $\alpha=2.26^\circ$, NASA FUN3D $C_L=0.5$

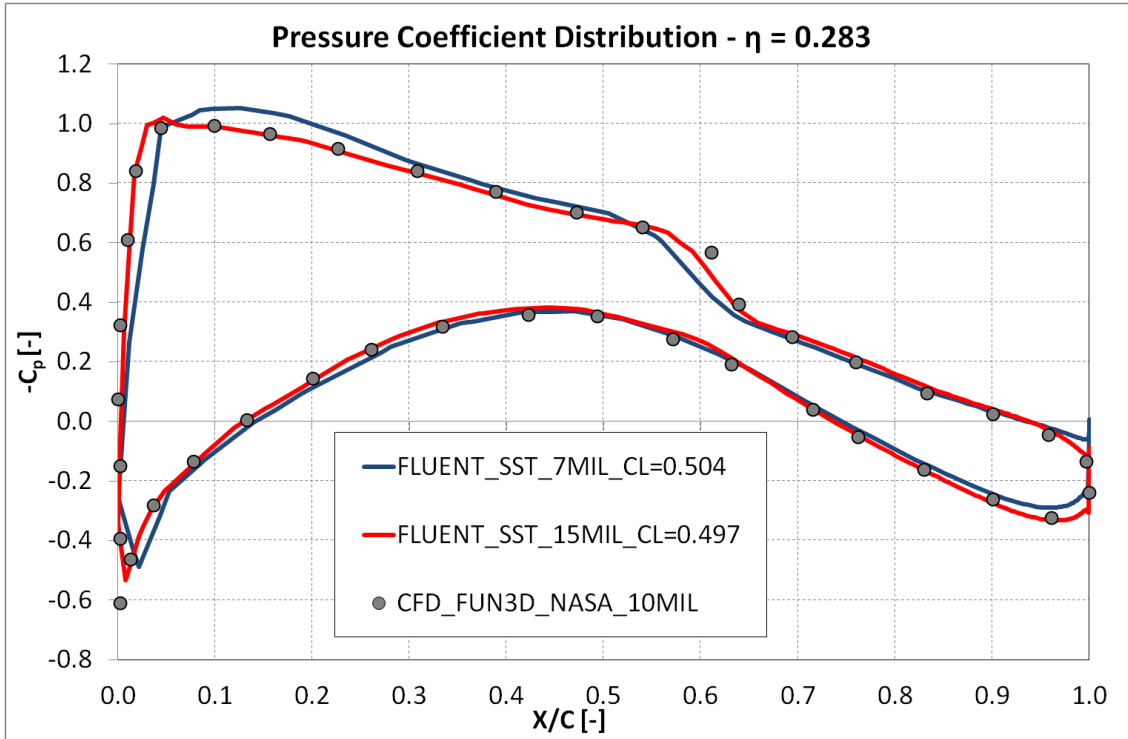


Fig. 5.5 Pressure coefficient distribution at $\eta=0.283$ of the 5 million cells and 9 million cells grids with SST turbulence model – $Re=5 \times 10^6$, 7 million cells $\alpha=2.6^\circ$, 15 million cells $\alpha=2.26^\circ$, NASA FUN3D $C_L=0.5$

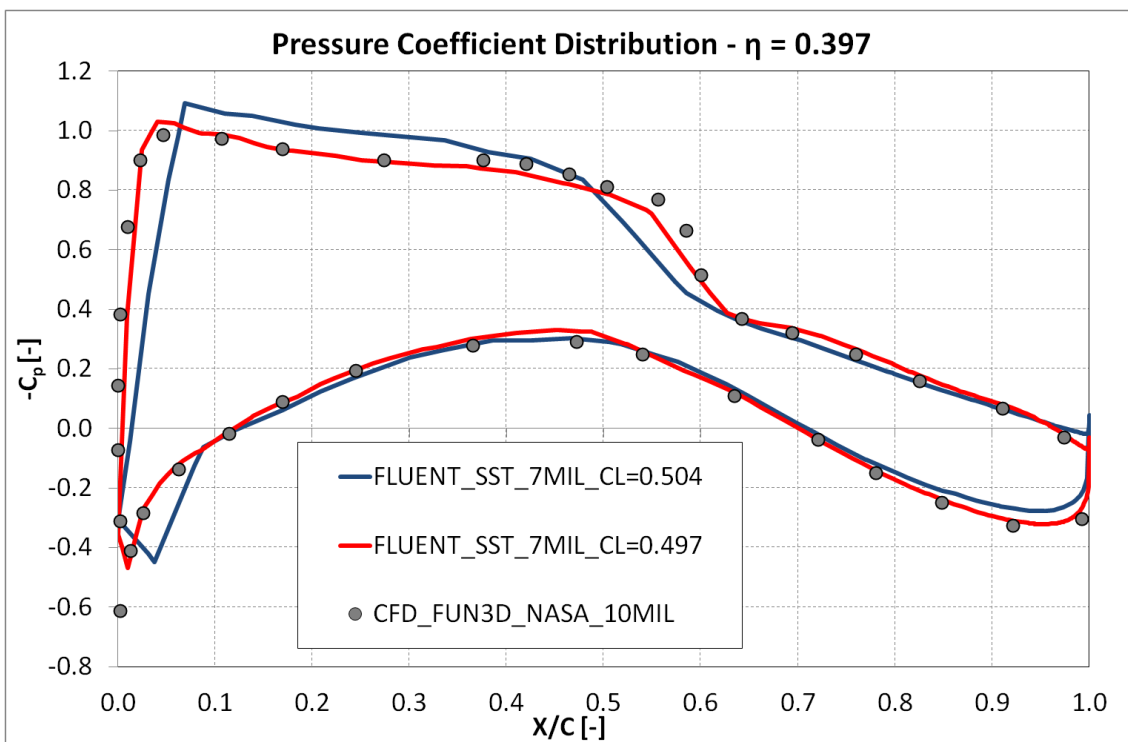


Fig. 5.6 Pressure coefficient distribution at $\eta=0.397$ of the 5 million and 9 million cells grids with SST turbulence model – $Re=5 \times 10^6$, 7 million cells $\alpha=2.6^\circ$, 15 million cells $\alpha=2.26^\circ$, NASA FUN3D $C_L=0.5$

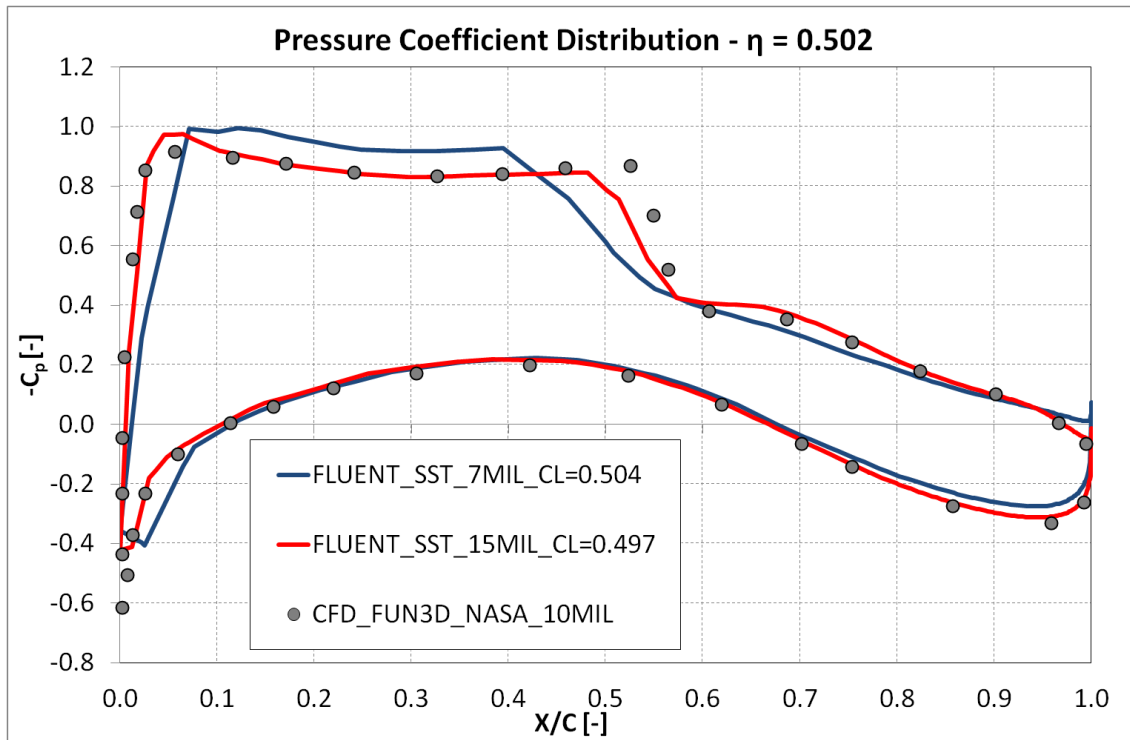


Fig. 5.7 Pressure coefficient distribution at $\eta=0.502$ of the 5 million and 9 million cells grids with SST turbulence model – $Re=5 \times 10^6$, 7 million cells $\alpha=2.6^\circ$, 15 million cells $\alpha=2.26^\circ$, NASA FUN3D $C_L=0.5$

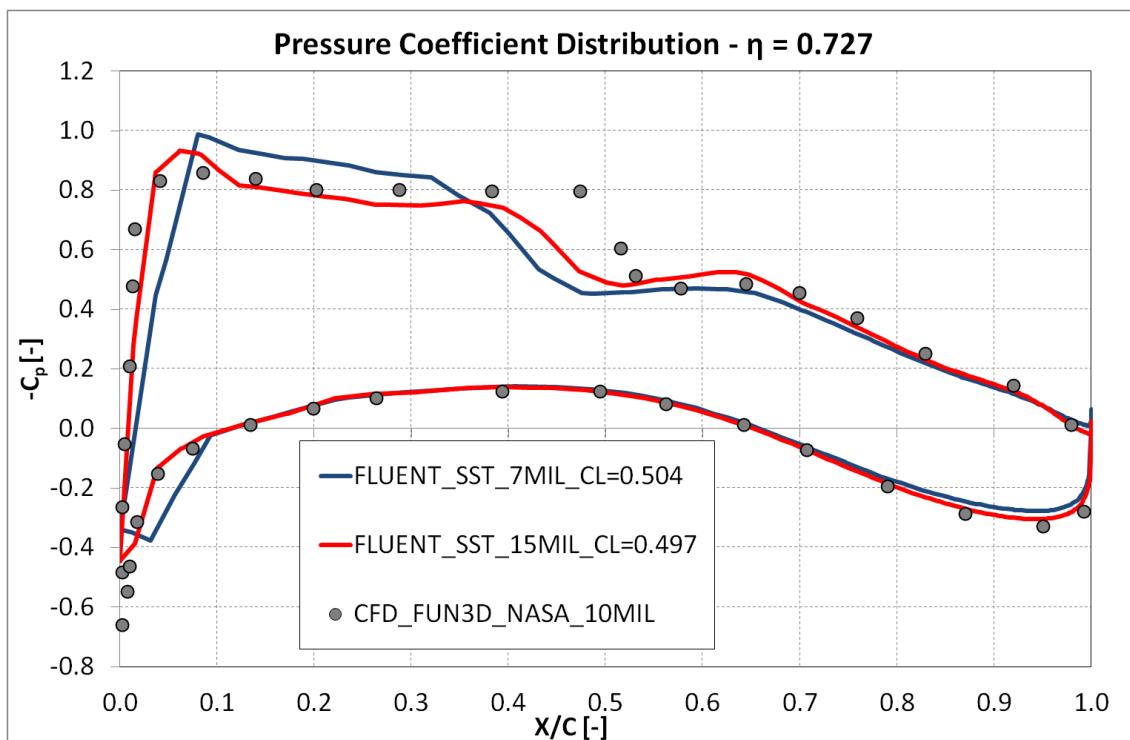


Fig. 5.8 Pressure coefficient distribution at $\eta=0.727$ of the 5 million cells and 9 million cells grids with SST turbulence model – $Re=5 \times 10^6$, 7 million cells $\alpha=2.6^\circ$, 15 million cells $\alpha=2.26^\circ$, NASA FUN3D $C_L=0.5$

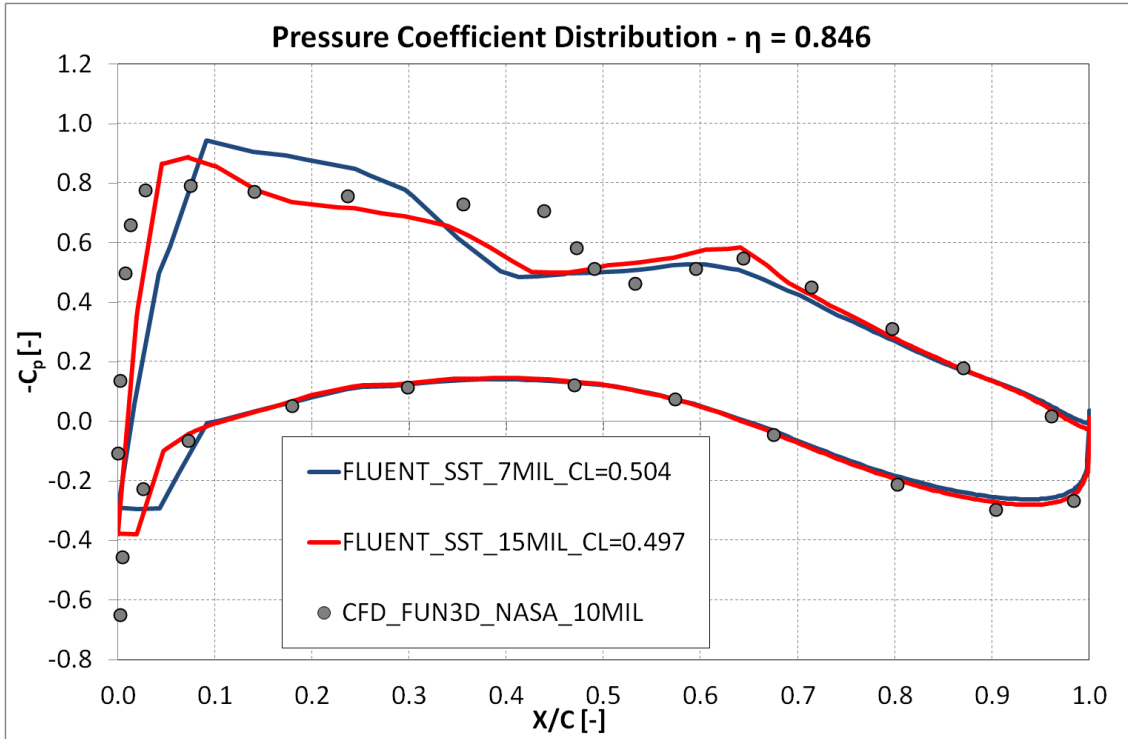


Fig. 5.9 Pressure coefficient distribution at $\eta=0.846$ of the 5 million cells and 9 million cells grids with SST turbulence model – $Re=5 \times 10^6$, 7 million cells $\alpha=2.6^\circ$, 15 million cells $\alpha=2.26^\circ$, NASA FUN3D $C_L=0.5$

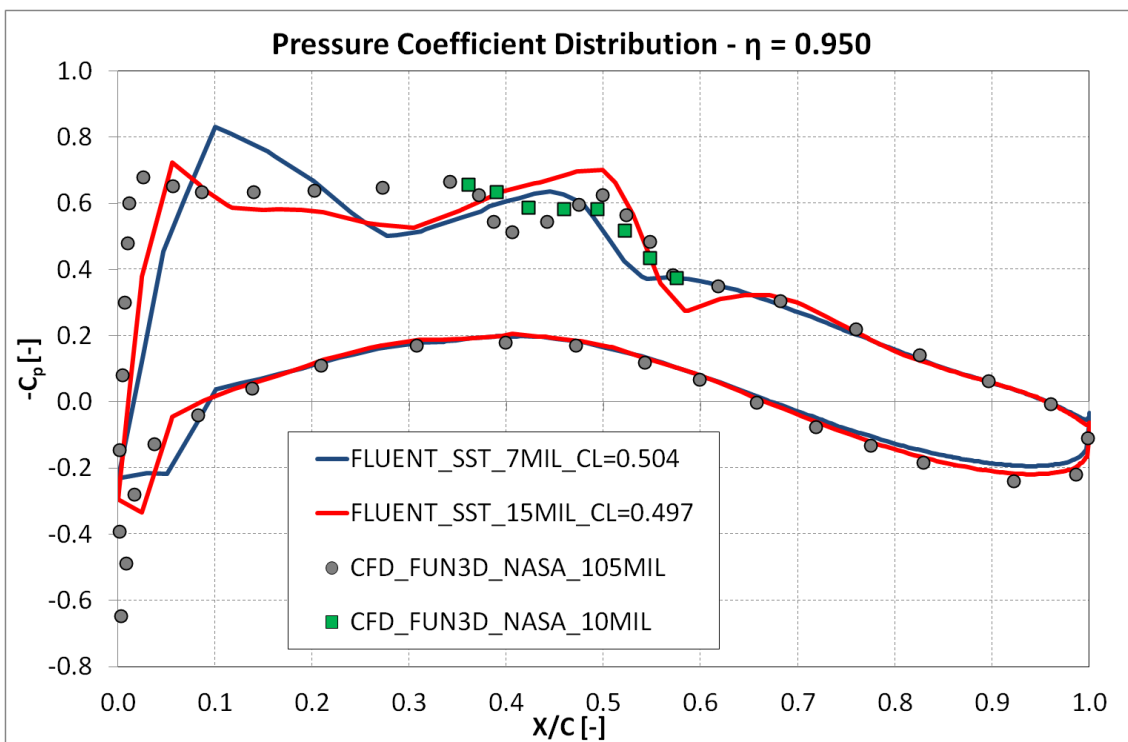


Fig. 5.10 Pressure coefficient distribution at $\eta=0.950$ of the 5 million cells and 9 million cells grids with SST turbulence model – $Re=5 \times 10^6$, 7 million cells $\alpha=2.6^\circ$, 15 million cells $\alpha=2.26^\circ$, NASA FUN3D $C_L=0.5$

The results of the CRM geometry at wind tunnel scale show that also with a higher Mach number the Fluent results are in reasonable agreement with the experimental data for a C_L of 0.5. The differences with the experimental data are around 15-20%. The pressure distribution over the wing is reasonably modelled compared to the NASA FUN3D CFD data. These results helped to guide the decision to use Fluent as the solver to perform all subsequent simulations of this research.

Chapter 6

Validation test case results

6.1 Introduction

CFD simulations of the wing tested by Gerontakos and Lee [31] were carried out as a validation test case for the calculation of the downstream velocities. Gerontakos and Lee do not report the temperature and pressure conditions of the wind tunnel, then a total temperature of 288K was assumed. From this value the reference density and static pressure were calculated by the Reynolds and Bernoulli equations (Table 6.1). The experimental C_L of 0.68 in the CFD was obtained with an angle of attack of 9.5° instead of the experimental of 8° . This is due to the configuration used in the CFD model, which is different from the experimental configuration used in the force measurements.

Geometry	Code	Mesh size	Turb. Model	T. I. [%]	Length Scale [m]	AOA [°]	Ttot [K]	Ts [K]	Ps [Pa]
Gerontakos Wing	FLUENT	5MIL	SST	0.03	0.014224	6.5	288	287.9	95105
	FLUENT	7MIL	SST	0.03	0.014224	8	288	287.9	95105
	FLUENT	5MIL	SST	0.03	0.014224	9.5	288	287.9	95105
	FLUENT	12MIL	SA	0.03	0.014224	9.5	288	287.9	95105
	FLUENT	12MIL	SST	0.03	0.014224	9.5	288	287.9	95105

Table 6.1 Boundary conditions of the “Gerontakos swept wing” simulation

6.2 “Gerontakos swept wing” simulations

Gerontakos and Lee performed experimental measurements with two different test case configurations:

- downstream velocity measurements configuration (Fig. 6.1) ;
- force measurements configuration (Fig. 6.2).

The first configuration, downstream velocity measurements, is the one that was reproduced in the CFD model. The wing model was mounted horizontally at the

centre of the wind tunnel test section. A circular endplate of 0.5 m diameter ($2.5 d/c_r$) with a sharp leading edge was fitted to the one end of the wing model, located 0.1 m ($0.5 d/c_r$) from the sidewall of the test section, to isolate the free-end effects. The origin of the coordinate system was positioned at the trailing edge of the root of the wing with the x , y , and z axes in the streamwise, transverse, and spanwise directions, respectively.

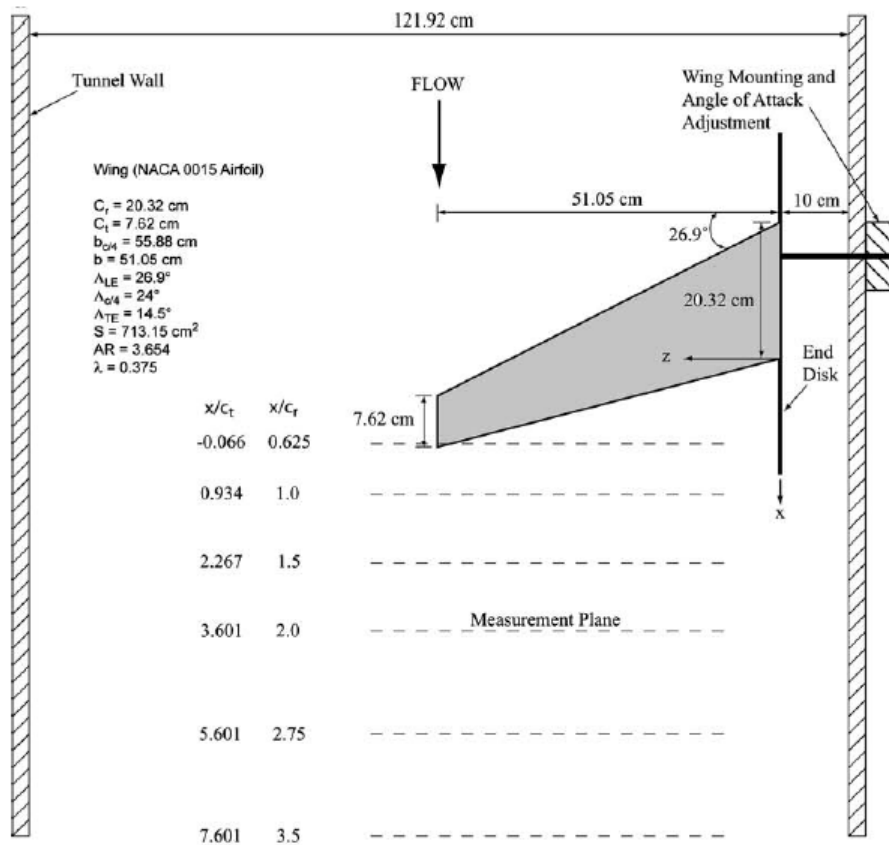


Fig. 6.1 “Gerontakos swept wing” downstream velocity measurements configuration [31]

In the second configuration, lift and drag measurements, the wing model was mounted vertically on an external two-component force balance located below the wind tunnel. The wing model was mounted vertically between two aluminium endplates with sharp leading edges. The bottom plate was fixed to the bottom wall of the test section and an aerodynamic fairing was placed around the shaft to isolate it from the tunnel flow. The top endplate was mounted on the top wall of the test section. The gaps between the airfoil and the endplates were kept at less than 1 mm to minimise leakage of flow through the

gaps. In this way the lift and drag coefficients of the wing models were calculated without the tip effects. Furthermore, were calculated also the total lift and drag coefficients by removing the top endplate. It was estimated that the maximum experimental uncertainties in the C_L and C_D results were ± 0.01 and ± 0.007 respectively.

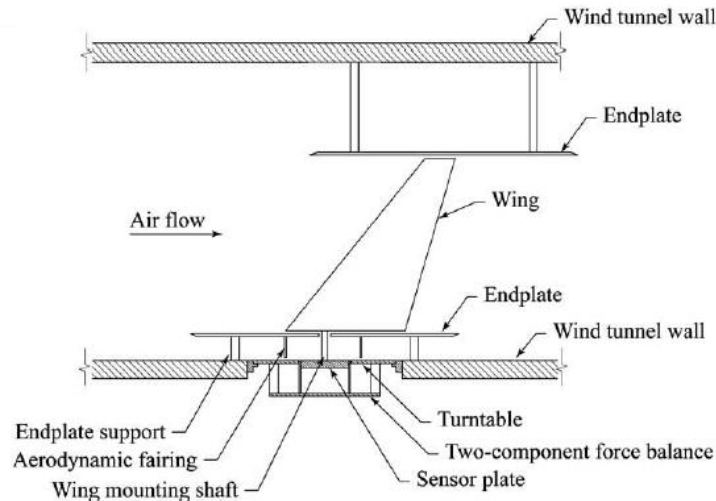


Fig. 6.2 “Gerontakos swept wing” force and moment measurements configuration [31]

The measured C_L and C_D were reported, as well as values based on the vorticity distributions inferred from the measured crossflow fields and on the inviscid lifting-line theory. Three different C_L curves are reported in the paper:

- one based on the measured forces;
- one based on the measured bound root circulation (equation 18);
- one based on the inviscid lifting-line theory (equation 19).

The second method is based on the indirect determination of the lift from the bound root circulation with the following equation:

$$C_L = 2\Gamma_{b,m}/K_1 V_\infty c_r - K_1/K_2 \quad (18)$$

where $\Gamma_{b,m}$ is the measured bound root circulation, K_1 and K_2 are two constants determined following the method of Glauert [45], c_r is the reference chord and V_∞ is the free-stream velocity. The third method uses the following equation and it is calculated in the same configuration as the CFD model:

$$L = \rho_{\infty} u_{\infty} \int_{-b/2}^{b/2} \Gamma(z) dz \quad (20)$$

where ρ_{∞} is the free-stream density, V_{∞} is the free-stream velocity and $\Gamma(z)$ is the spanwise circulation.

Fig. 6.3 shows the experimental C_L distributions compared with the CFD results. The C_L of the CFD simulation with an angle of attack of 8° does not match the experimental one calculated from the measured forces. This is due to the configuration used in the CFD model, which is different from the experimental configuration used in the force measurements, as stated above.

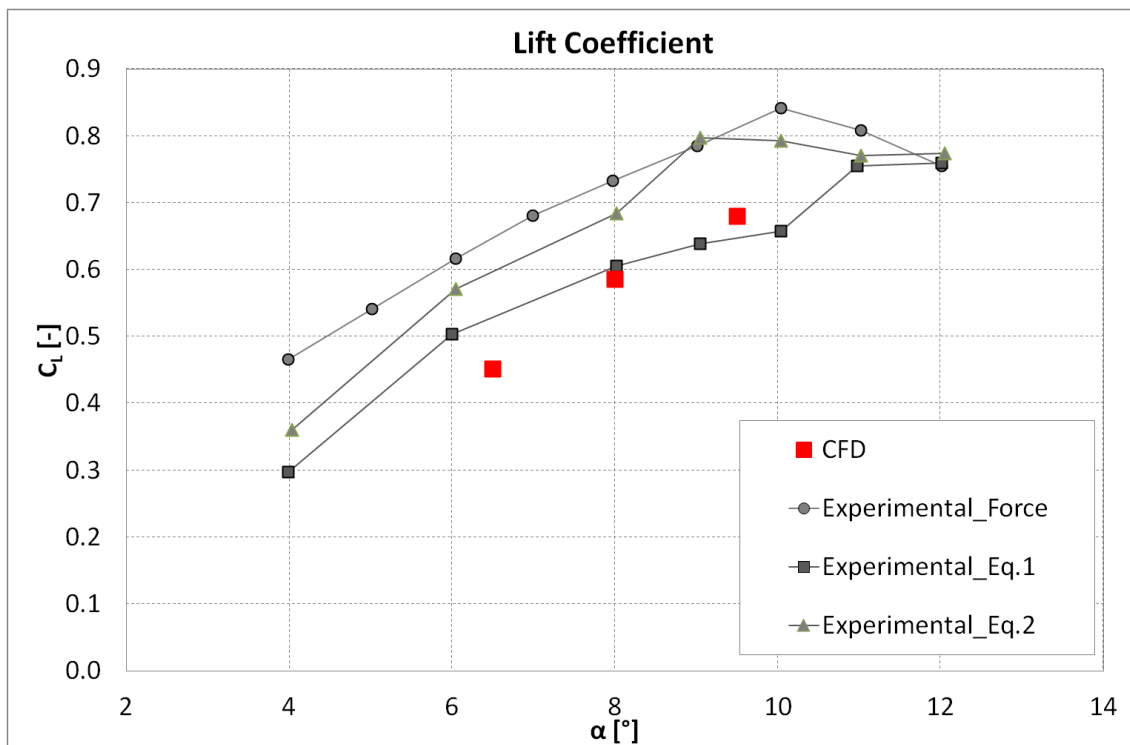


Fig. 6.3 “Gerontakos swept wing” model lift coefficient distributions

As the plots show, the C_L of 0.68 in the CFD is obtained with an angle of attack of 9.5° instead of the experimental of 8° . The results that were used for the comparison with the experimental data are those from the 12 million cells mesh with an AOA= 9.5° , since they have the same lift coefficient of the experimental data.

6.3 Comparison with the experimental data

A comparison between the CFD results of the 12 million cells mesh with an $AOA=9.5^\circ$ and the experimental data available was carried out in order to validate the CFD modelling of the wake flow field and tip vortices. The CFD data were post-processed and analysed at the same six distances downstream the wing equivalent to those of the paper (Fig. 6.4).

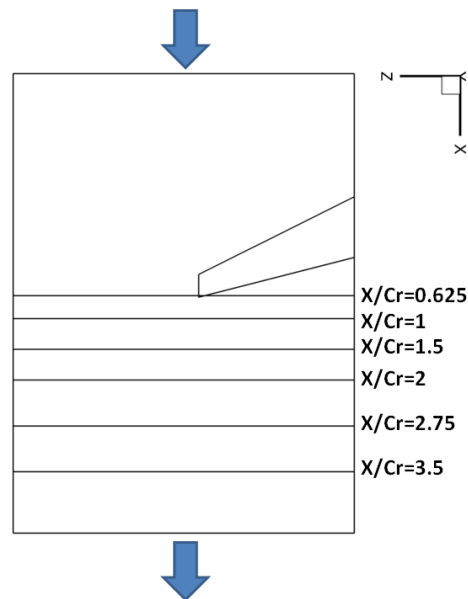


Fig. 6.4 Downstream locations of the considered planes

The measurements carried out by Gerontakos and Lee were reported in terms of local tangential velocity, V_θ , axial vorticity, ζ , and V_x velocity component distributions, in vortex coordinates. Furthermore, the total vortex and core circulation were plotted in the six considered planes.

The CFD results are in agreement with the experimental data in the $X/Cr=1$ plane with a low error (Fig. 6.5 - Fig. 6.7). As expected the CFD vortex decays more quickly compared to the experimental one. In the plane $X/Cr=2$ the difference in terms of axial vorticity is around 35% (Fig. 6.8 - Fig. 6.10). This is due to the fact that the computational schemes are dissipative and they diffuse and destroy vorticity, even without the addition of artificial viscosity. Numerical dissipation gradually weakens the strength of the vortex, but not necessarily in a manner representative of a viscous flow-field. Also, the circulation values of the CFD results are in good agreement with the experimental data in the $X/Cr=1$

plane (Fig. 6.11), while there are some differences in the $X/Cr=2$ (Fig. 6.12). The circulations values are an indicator of how the CFD models the vortex.

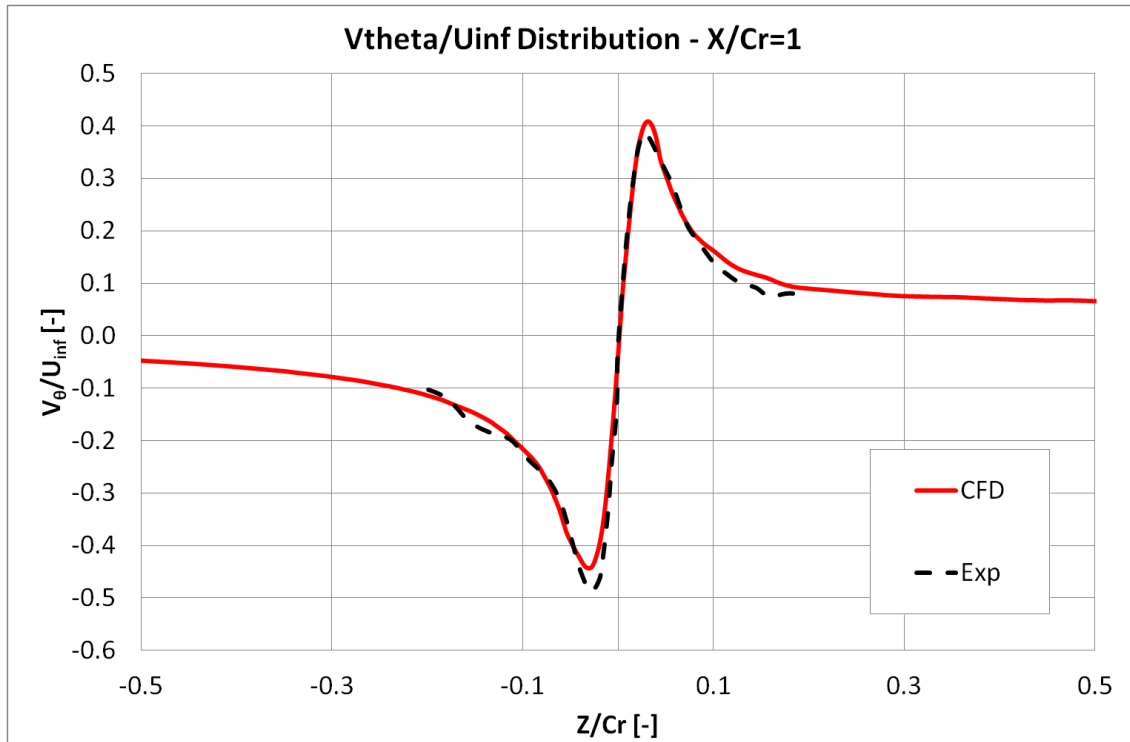


Fig. 6.5 V_θ distributions at $X/Cr=1$; $Z/Cr=0$ corresponds to the centre of the vortex

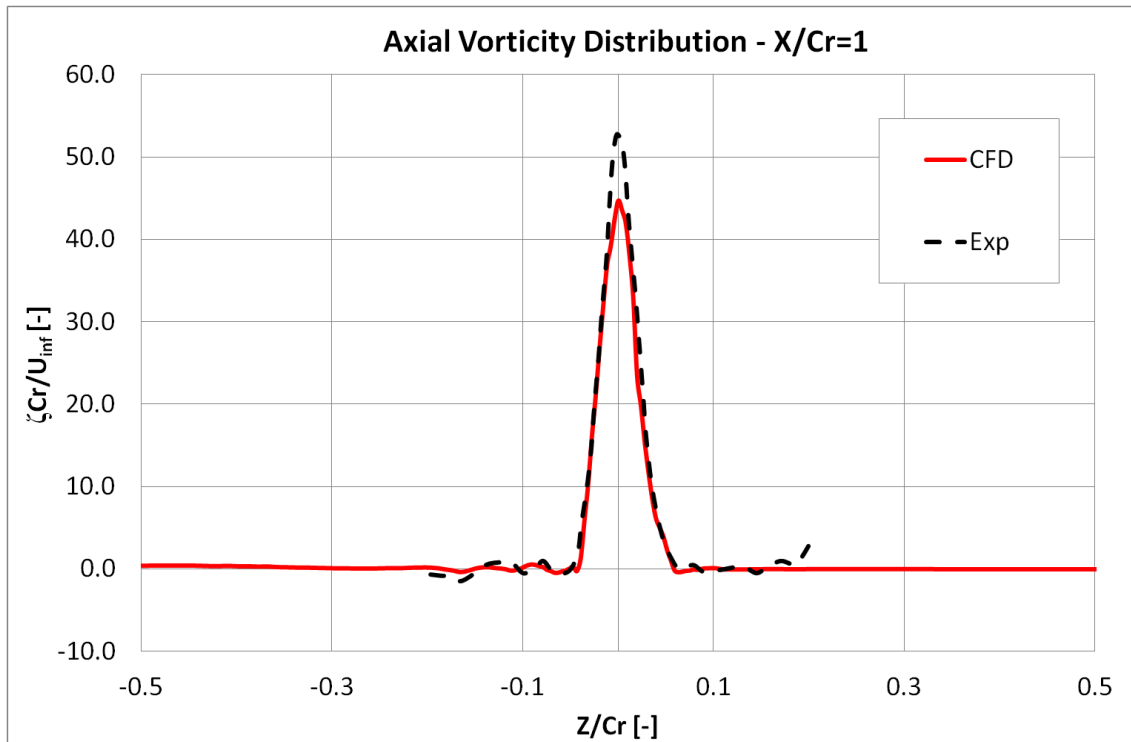


Fig. 6.6 Axial vorticity distributions at $X/Cr=1$; $Z/Cr=0$ corresponds to the centre of the vortex

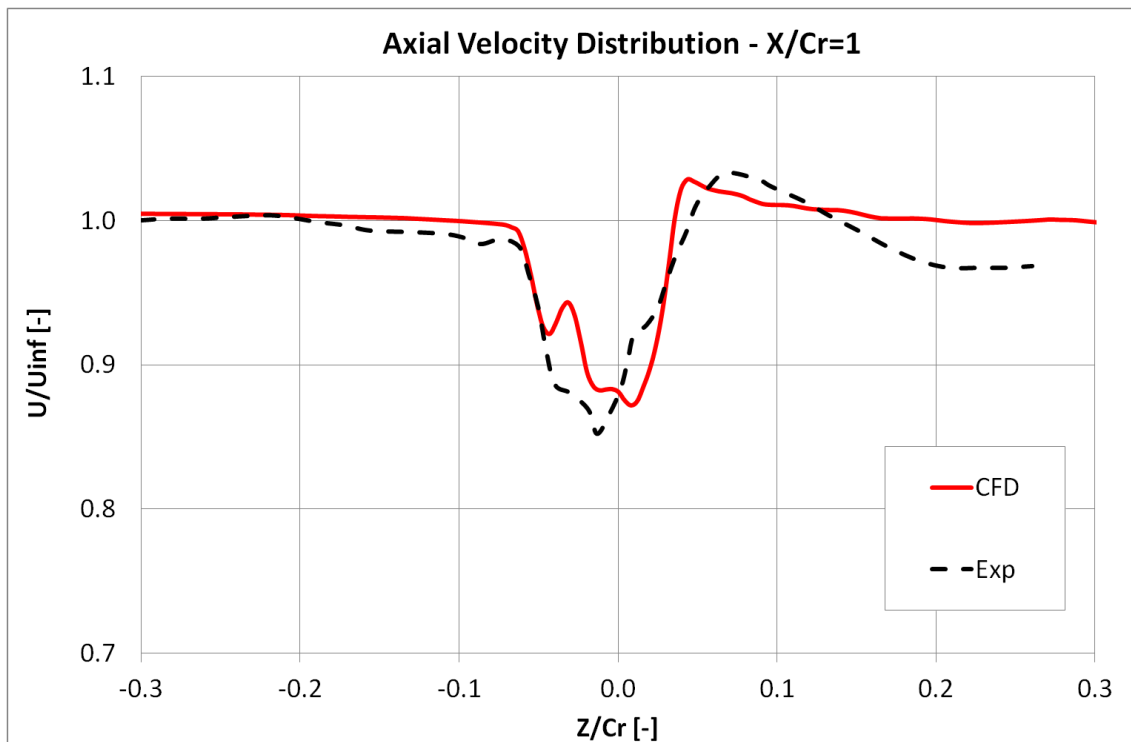


Fig. 6.7 Axial velocity distributions at $X/Cr=1$; $Z/Cr=0$ corresponds to the centre of the vortex

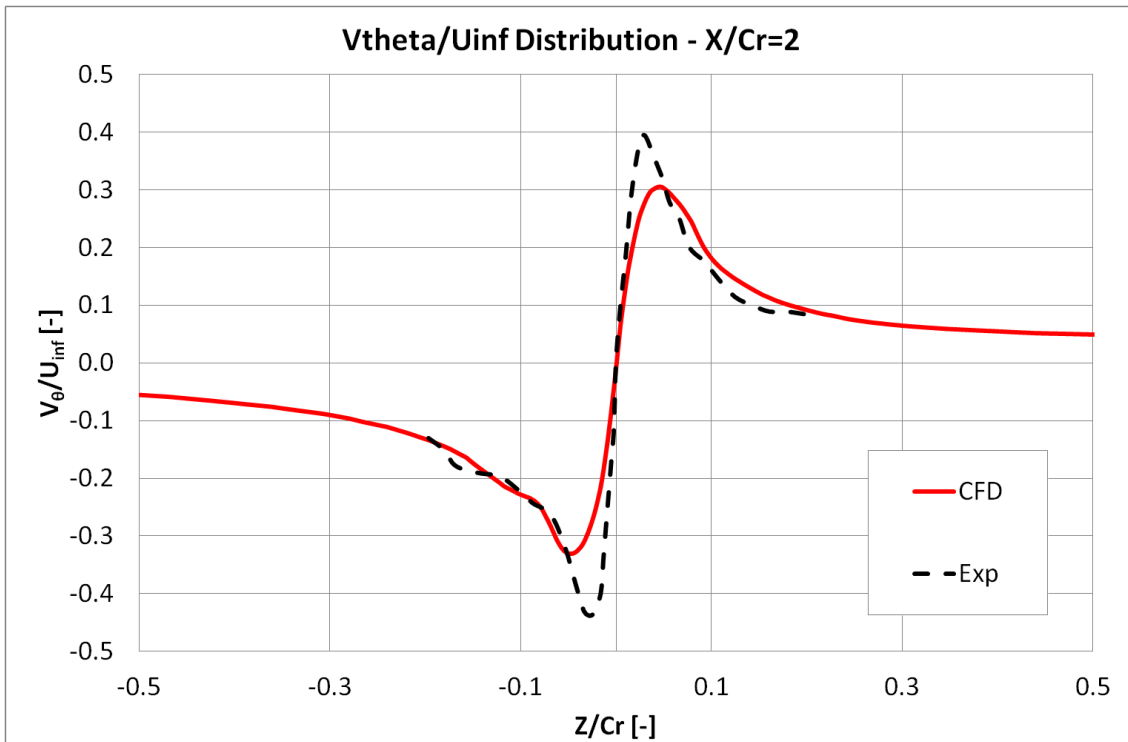


Fig. 6.8 V_θ distributions at $X/Cr=2$; $Z/Cr=0$ corresponds to the centre of the vortex

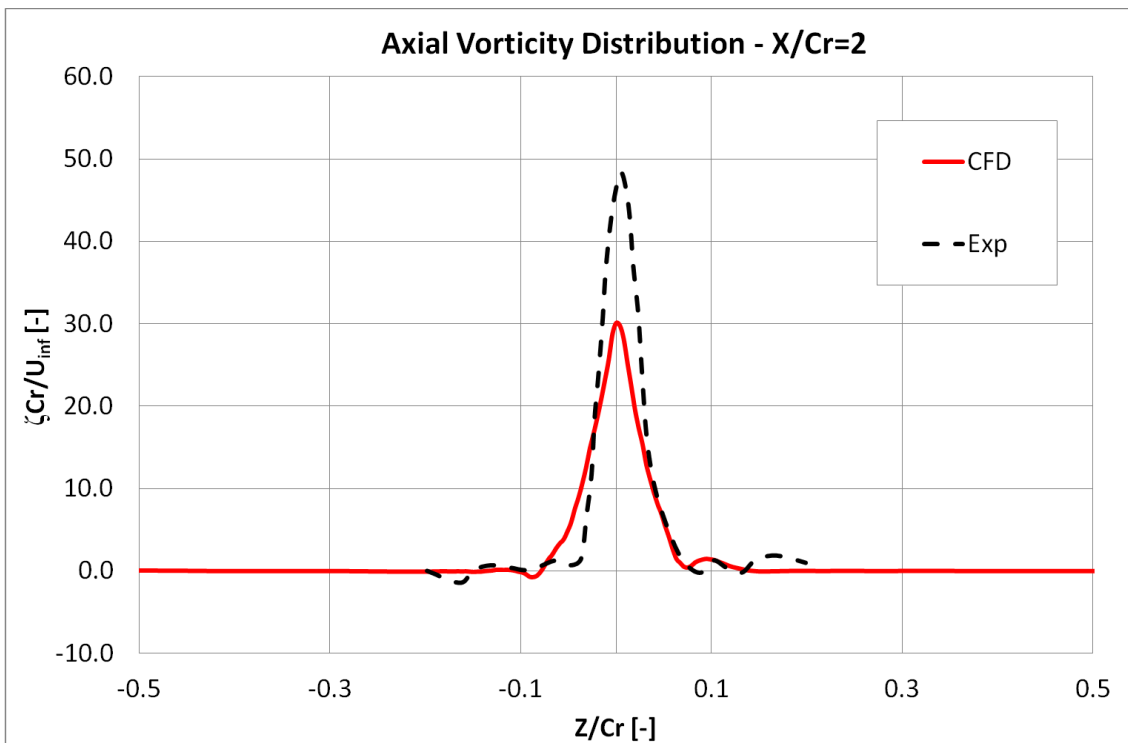


Fig. 6.9 Axial vorticity distributions at $X/Cr=2$; $Z/Cr=0$ corresponds to the centre of the vortex

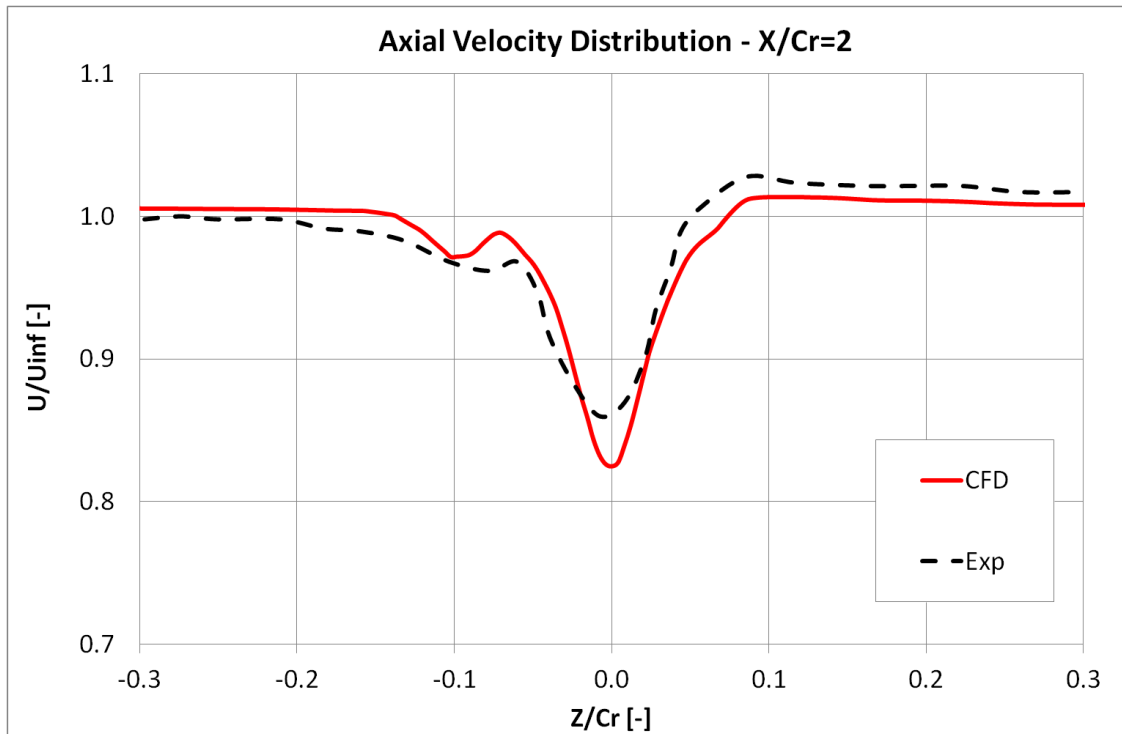


Fig. 6.10 Axial velocity distributions at $X/Cr=2$; $Z/Cr=0$ corresponds to the centre of the vortex

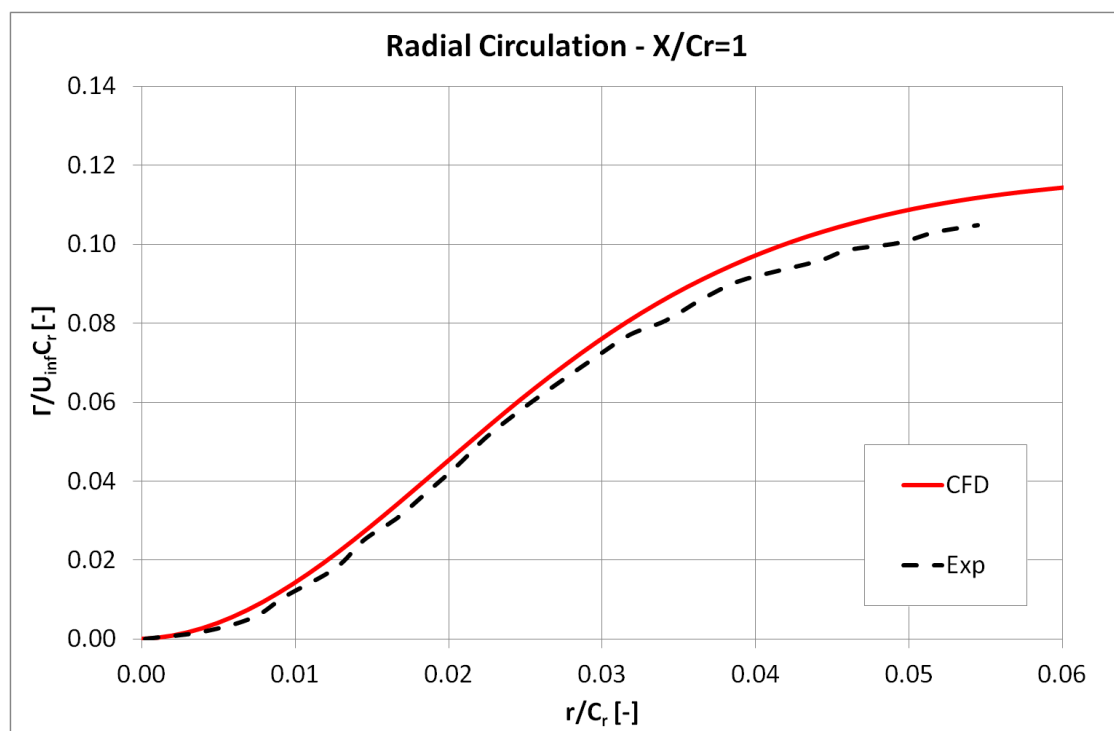


Fig. 6.11 Radial circulation distributions at $X/Cr=1$

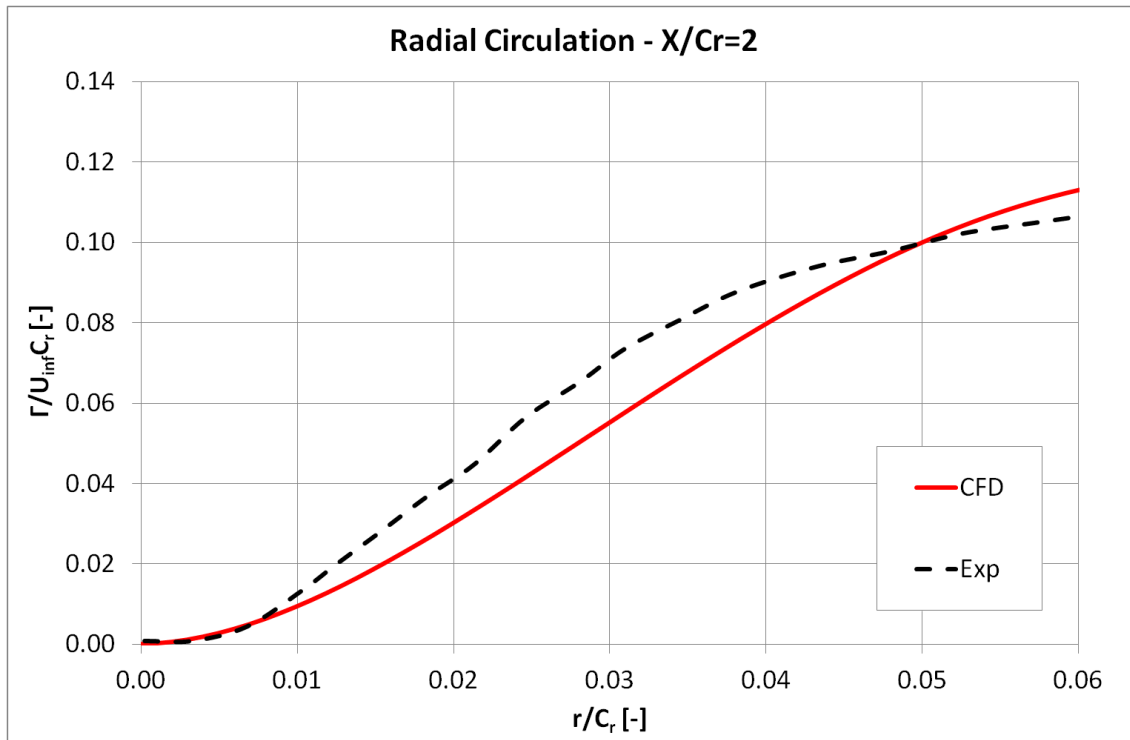


Fig. 6.12 Radial circulation distributions at $X/C_r=2$

The vortex core radius is predicted with a low error in the $X/C_r=1$ plane (Fig. 6.13) while going downstream the differences increase. The discrepancies in the vortex core prediction are strictly dependent on the grid size. In order to have a mesh independency for the vortex core radius, a very high number of nodes are required in the vortex core. In this simulation's mesh there are at least six nodes in the vortex core, but even if this is a high number, it is not enough to obtain the same vortex core of the experimental data.

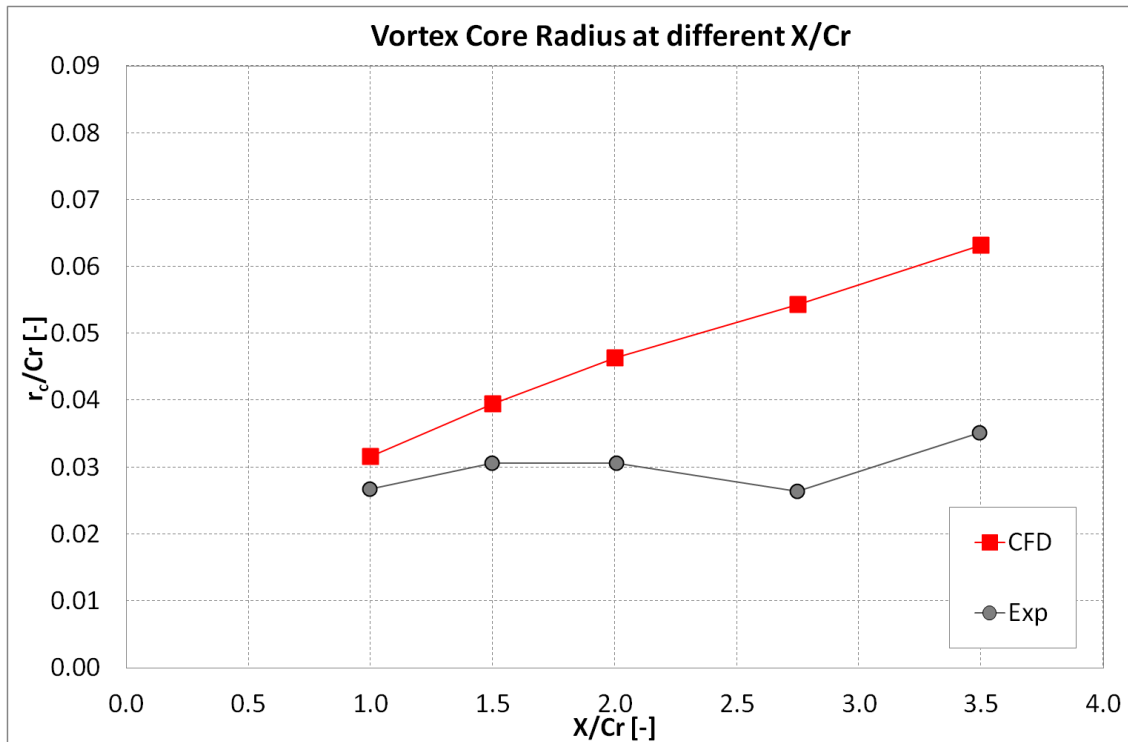


Fig. 6.13 Vortex core radius at different X/Cr planes

The $V_{\theta\text{peak}}$ value of the CFD results is lower than in the experimental data by about 20% in the $X/Cr=1$ plane and around 35% in the $X/Cr=3.5$ plane (Fig. 6.14). The velocity distribution is another value that is not easy to characterise through CFD simulations without high discrepancies. The core circulation, Γ_c , is higher in the CFD results compared to the experimental data. The difference in the $X/Cr=1$ plane is only about 10%, but it increases going downstream and it reaches a difference of about 35% (Fig. 6.15). This is also due to the fact that the vortex core radius is not predicted with a high error for the planes $X/Cr=2.75$ and $X/Cr=3.5$. The total vortex circulation is better predicted and it is almost constant in the CFD results as well (Fig. 6.16). The difference is less than 10% in all the considered planes. The fact that the total vortex circulation is almost constant in all the considered planes is an indicator that the vortex is captured by the CFD and that the roll-up of the vortex is almost completed at $X/Cr=1$.

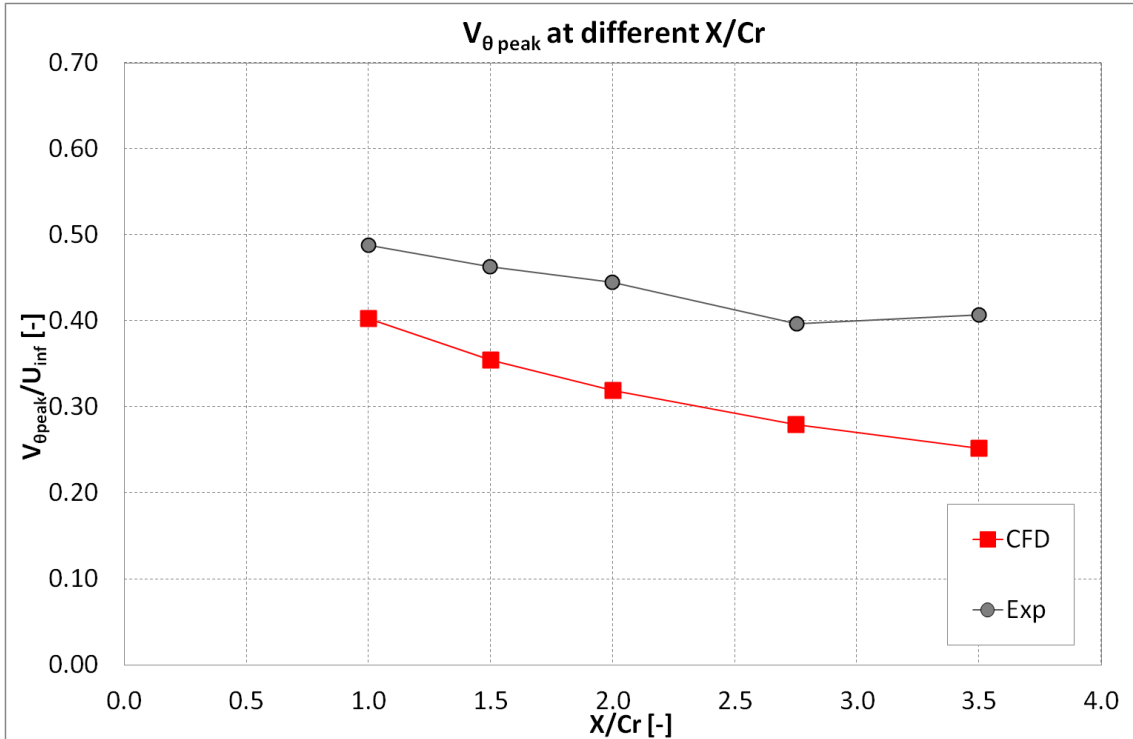


Fig. 6.14 $V_{\theta peak}$ values at different X/Cr planes

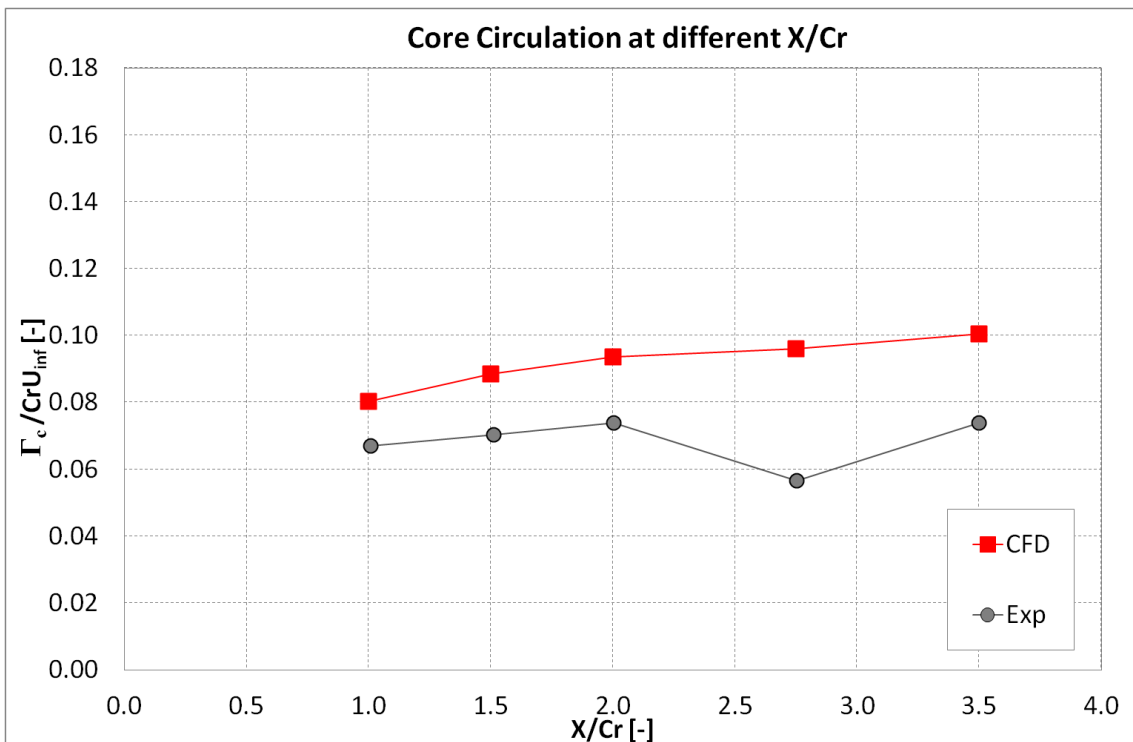


Fig. 6.15 Core circulation at different X/Cr planes

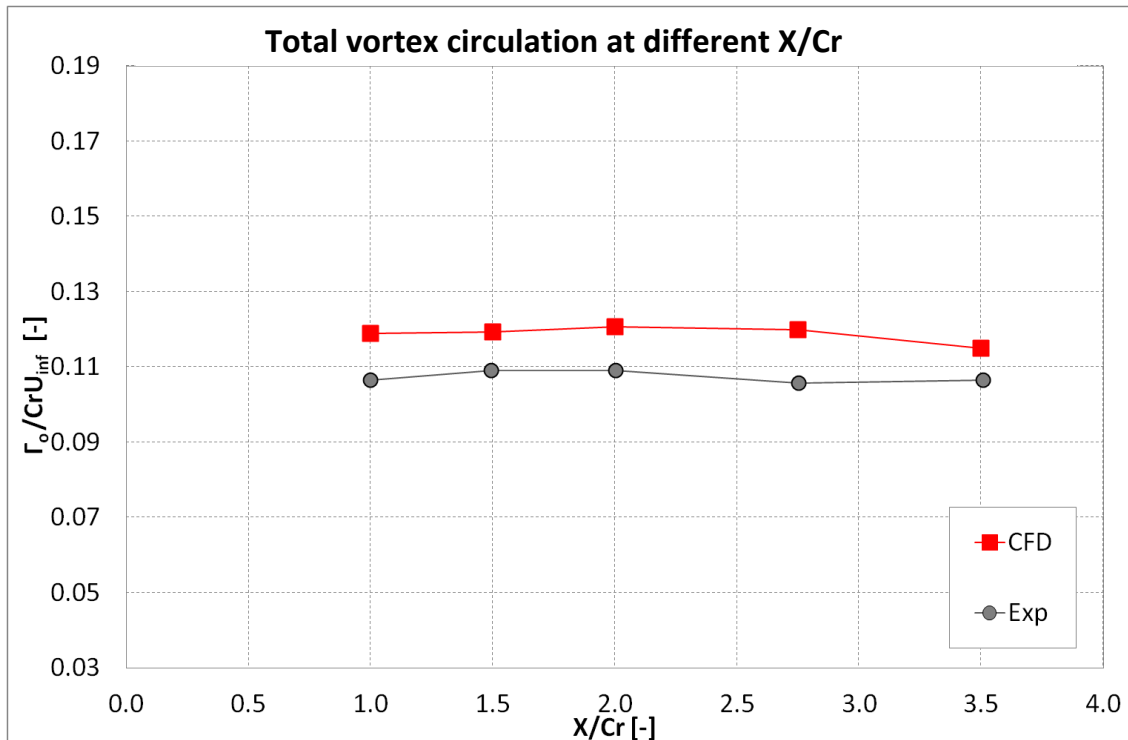


Fig. 6.16 Total vortex circulation at different X/Cr planes

The CFD results are in reasonable agreement with the experimental results up to $X/Cr=2$, but as expected, the CFD vortex decays more quickly compared to the experimental one. The total vortex circulation is predicted for all the considered planes with an error of 15% and it is almost constant going downstream. The results of the CFD simulation of the validation case reveal that the CFD is capable of modelling and solving the main characteristic of a tip vortex generated from an aircraft wing. Furthermore, it has been considered that the Reynolds number of this experimental study is very low in comparison with the considered CFD cases of the research and this was taken into account. Moreover, since the flow of the Gerontakos study has a free Mach number of 0.041 it is incompressible and there are no shocks in comparison with the transonic conditions of the CFD cases. Despite these aspects the use of the Gerontakos as a validation test case for the tip vortex is still valid, because the CFD simulations of this case were performed with the same boundaries and conditions of the experimental study. Another aspect to be taken into account is the purpose of the research and the performed CFD simulations. The simulations were carried out to be compared with a reduced fidelity code and the interest was not only in the tip vortex, but also in the general characteristics

of the near-field of the wing wake. This is an important aspect of the research, as going downstream in the wake the CFD results are less in accordance with the experimental data.

Chapter 7

Results from the ELL method

7.1 Introduction

The results and comparisons illustrated in this chapter are related to the many stages of the ELL code during this research. The ELL code was developed at Cranfield University by a dedicated research team [11][12] and when this thesis project started the code was not in its final form. Indeed, the ELL code was improved by others while the research was carried out. Since the research was completed in a one year period, it was not feasible to wait for the final version of the code to perform comparisons and evaluations of the MATLAB code. Despite that, the key comparisons, as the air-refuelling results, were performed with the latest version of the code and all the conclusions are based on the latest version of the code. Furthermore, the temporary evaluations of the code during its developments were useful also for the developers of the code itself. This chapter is composed of:

- a study to comprehend and evaluate the first version of the ELL code;
- the ELL code results of the Gerontakos swept wing;
- the ELL code results of the CRM geometry at wind tunnel conditions, performed with the second version of the code, that includes a fuselage modelled as a flat plate;
- the ELL code results of the CRM full-scale geometry with air-refuelling flight conditions.

In the ELL code there are some key settings that can be modified by the user. The developers chose a group of settings that was appropriate for the use of the code in the ASTRAEA project. In this thesis these settings are referred as the “standard settings” of the ELL code.

7.2 ELL code study

A study on the ELL code was performed to comprehend and evaluate the available first version of the code. The reference CFD geometry used for this study was the CRM at wind tunnel scale. The available version of the ELL code at the moment of this study did not consider the fuselage of the aircraft, for this reason a single wing as much as possible similar to the wing of the CRM geometry was simulated in the code. Table 7.1 shows the geometric characteristics of the considered ELL wing. Table 7.2 reports the flight conditions applied in the ELL code, which correspond to the CFD case of the CRM geometry at wind tunnel conditions.

AR [-]	9
Taper ratio [-]	0.275
Wingspan [m]	1.5868
Wing sweep [deg]	35
Dihedral angle [deg]	7.21
Wing angle of incidence [deg]	0
Wing twist [deg]	0
Number of vortex panels for each wing [-] (Fig. 7.1)	120
Smallest distance allowed between a control point and a vortex filament [m]	0.05

Table 7.1 Geometric characteristics of the considered wing

Angle of attack [deg]	2.6
Angle of sideslip [deg]	0
INDICATED airspeed [m/s]	350.69
Bank angle [deg]	0
Pitch angle [deg]	2.6
Azimuth angle [deg]	0
GEOMETRIC altitude [m]	-3340

Table 7.2 Flight conditions applied in the ELL code

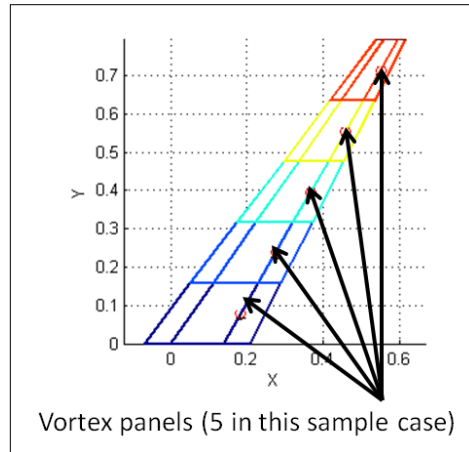


Fig. 7.1 Vortex panels sample of the ELL code wing

The ELL code reference frame has the following characteristics:

- the induced velocities of the ELL code are expressed in a North-East-Down (NED) reference frame;
- flat Earth assumption is made and the Earth's rotational effects are ignored hence the NED frame serves as an inertial reference frame;
- the origin of the NED frame is fixed to the Earth. The x-axis points to the north, the y-axis to the east and the z-axis down;
- the NED frame is a stationary frame.

Fig. 7.2 shows the wing modelled in the ELL code from four different views. The code divides the wing in a given number of panels (Nseg), illustrated in Fig. 7.1 and Fig. 7.2 by five different colours since for the sample case of the figures the number of panels is 5.

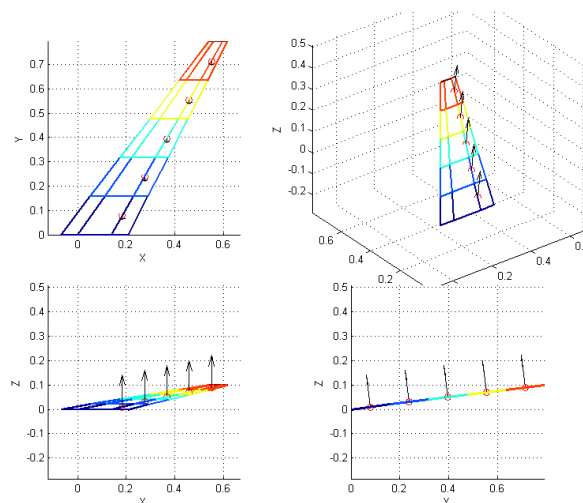


Fig. 7.2 Wing model in the ELL code

The purpose of this analysis was to evaluate the effects of:

- the grid density, with standard settings for the domain dimension;
- the number of vortex panels for each wing (Nseg);
- the smallest distance that is allowed between a control point and a vortex filament (EPS);
- the size of the domain.

The analysis was useful to understand the best settings to run the initially available version of the code with the considered geometry and to carry out a comparison between the available CFD results of the CRM geometry at wind tunnel scale and the ELL code. The CFD results were modified in order to be in the same reference frame of the ELL code. The zero of the Z axis in the CFD results was modified to be the same of the ELL code and the CFD velocities were modified to be in the NED reference frame.

7.3 ELL code with fuselage of the CRM at wind tunnel scale

The CFD simulations were performed using a geometry definition compatible with the model scale aircraft definitions used in the wind tunnel experiments. These geometries are slightly idealised relative to a full scale aircraft in that they do not include aspects such as flap track fairings, control tabs and any gaps around control surfaces. The different aircraft lift configurations are modelled by just considering the overall angle of attack. High-lift devices are not considered. The focus of this work is to perform a fair comparison between the CFD and ELL predictions. Within this context, the ELL modelling aspects were also evaluated considering the geometry definition as outlined above.

Table 7.3 shows the considered ELL code configurations. “Case A” corresponds to the standard settings of the code and its basic reference case grid consists in $x=43$, $y=26$, $z=37$ elements. This configuration is too coarse to use its results in a comparison with the CFD. Therefore, a finer grid with $x=51$, $y=106$, $z=91$ elements was used (“Case C” and “Case D”). The standard number of vortex panels of the ELL code is 12, but when the density of the grid increases it is necessary to increase the number of panels as well. Based on the geometry definition which was used for the CFD simulations, the obtained flow field

results with 12 panels are not realistic and suitable for the kind of comparisons carried out in this research (Fig. 7.3). For this reason all the ELL results analysed and presented in this thesis were run with a number of panels of 40, instead of the standard number of 12. This is a very critical point of the code, because the performances and the entire evaluation of it depend on this parameter. The changes in the number of panels lead to a higher time needed to run the code. To run the ELL code with a number of panels of 40 and a finer grid, as in the “Case D” in Table 7.3, it needs 14.3 times more than to run it with the standard setup of the code, as in “Case A”.

	Mesh	Density	Panels	Time [-]
Case_A	43x26x37 [y,x,z]	x=[-2:0.1:0.5]; y=[-2.1:0.1:2.1]; z=[-1.8:0.1:1.8];	12	1
Case_B	43x26x37 [y,x,z]	x=[-2:0.1:0.5]; y=[-2.1:0.1:2.1]; z=[-1.8:0.1:1.8];	40	1.25
Case_C	106x51x91 [y,x,z]	x=[-2:0.05:0.5]; y=[-2.1:0.04:2.1]; z=[-1.8:0.04:1.8];	12	10.9
Case_D	106x51x91 [y,x,z]	x=[-2:0.05:0.5]; y=[-2.1:0.04:2.1]; z=[-1.8:0.04:1.8];	40	14.3

Table 7.3 Cases and running times

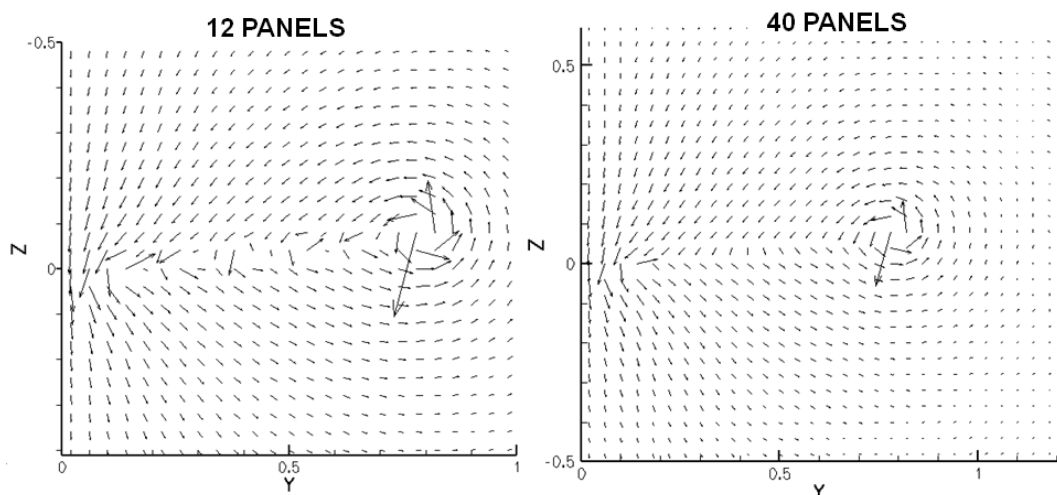


Fig. 7.3 ELL vectors with 12 (Case C) and 40 (Case D) number of panels

The latest version of the ELL code includes a fuselage, modelled as a flat plate. A fuselage as much as possible representing the CRM geometry fuselage was

inserted in the code. The geometric characteristics of the considered wing are summarised in Table 7.4 and illustrated in Fig. 7.4.

Fuselage length [m]	62.71
Fuselage diameter [m]	4.92

Table 7.4 Geometric characteristics of the considered fuselage

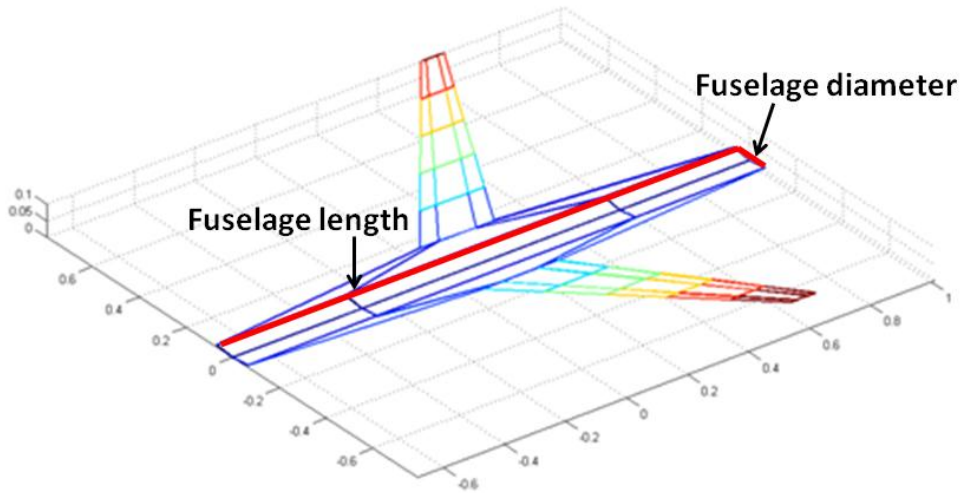


Fig. 7.4 Wing-fuselage model dimensions of the ELL code

The CFD results used for this comparison are the 15 million cells grid of the CRM geometry at wind tunnel scale without tail (see section 3.5). Table 7.5 reports the flight conditions applied in the ELL code (corresponding to the CFD flight conditions). The ELL wing characteristics are those reported in Table 7.1. Fig. 7.5 shows the wing and fuselage modelled in the ELL code.

Angle of attack [deg]	2.26
Angle of sideslip [deg]	0
INDICATED airspeed [m/s]	350.69
Bank angle [deg]	0
Pitch angle [deg]	2.26
Azimuth angle [deg]	0
GEOMETRIC altitude [m]	-3340

Table 7.5 Flight conditions applied in the ELL code

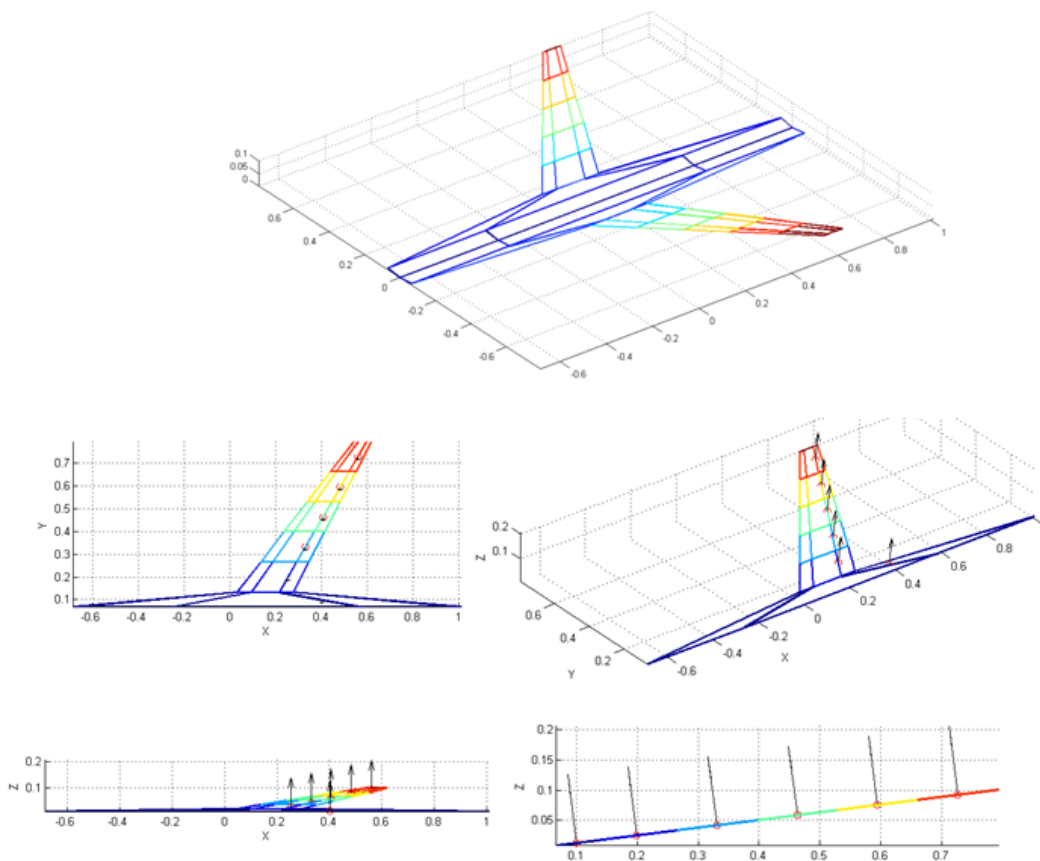


Fig. 7.5 Wing-fuselage model of the ELL code

Both in the CFD and ELL code the results were post-processed and analysed at eight planes in the aircraft wake in the near-field wake up to 1.35 metres ($X/C_{ref}=7.5$), which corresponds to 50 metres in the full-scale model (Fig. 7.6-Fig. 7.7). The ELL results were modified in order to be in the same reference frame of the CFD results. All the results are reported in the wind tunnel reference frame, where the x is the streamwise direction, y is the spanwise and z is the transverse component (Fig. 7.7). Except for the vectors that are reported in ELL code induced velocity components. The induced velocity components V_x , V_y and V_z are calculated in the CFD results as:

$$\begin{aligned}
 V_x &= X \text{ Velocity} - V_{infx} \\
 V_y &= Y \text{ Velocity} - V_{infy} \\
 V_z &= Z \text{ Velocity} - V_{infz}
 \end{aligned} \tag{20}$$

where X Velocity, Y Velocity and Z Velocity are the velocity components in the wind tunnel CFD reference frame and V_{infx} , V_{infy} and V_{infz} are calculated by the following expressions:

$$\begin{aligned}
 V_{infx} &= V_{inf} * \cos(\beta) * \cos(\alpha) \\
 V_{infy} &= V_{inf} * \sin(\beta) * \cos(\alpha) \\
 V_{infz} &= V_{inf} * \cos(\beta) * \sin(\alpha)
 \end{aligned}
 \tag{21}$$

where α and β are the Euler angles of the wing, due to the way the NED reference frame is defined in the ELL code.

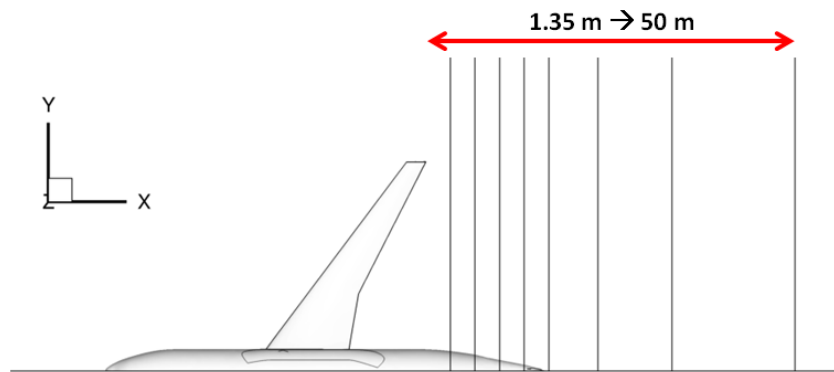


Fig. 7.6 Near-field of the CRM geometry at wind tunnel scale

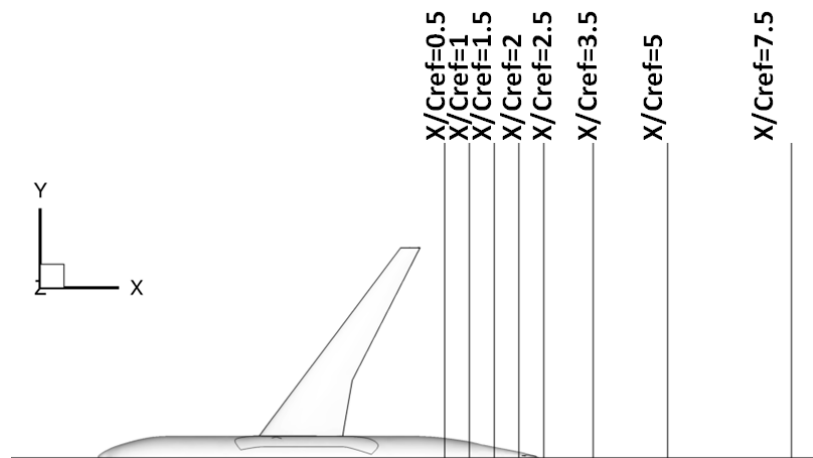


Fig. 7.7 Location of the CRM geometry wake considered planes

A comparison between the ELL results with and without the fuselage with the setup of “Case D” (Table 7.3) was carried out. From this comparison it was realised that the presence of a fuselage is important to improve the characterisation of the wake flow field generated by the aircraft (Fig. 7.8).

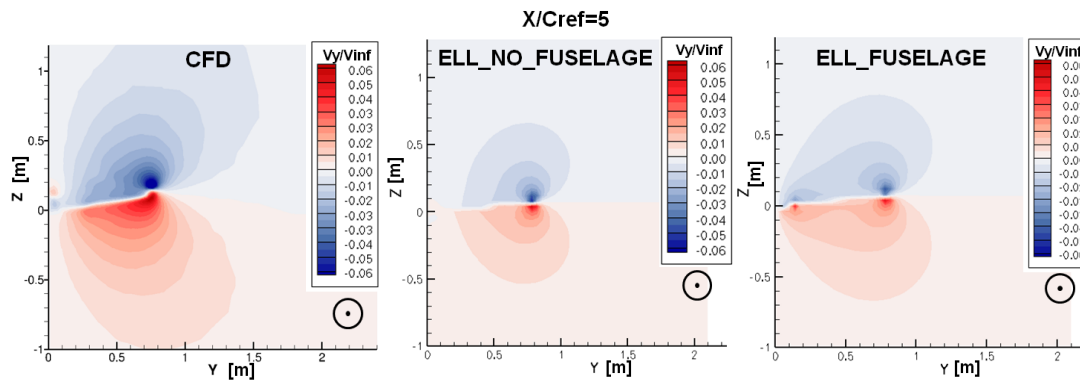


Fig. 7.8 V_y induced velocity of the ELL code with and without fuselage at $X/C_{ref}=5$ compared with the CFD results at the same wind tunnel flight conditions and downstream plane

The comparison was carried out in terms of vectors visualisations, V_x , V_y , and V_z induced velocity components, downwash (ϵ), yaw angle and dynamic pressure plots (q). With the modified settings (40 panels) the code predicts the qualitative characteristics of the wake flow field and the tip vortex, but not the quantitative variables. Due to the way the ELL code models the tip vortices it is not capable to describe the viscous characteristics of the vortex. The analysis of vortical flows through a mathematical formulation, which considers potential flows with singularities at the centre points, leads to non-physical solutions in the inner region around the centre [46]. In the vector plots from Fig. 7.9 to Fig. 7.11 it can be seen that the ELL code gives a reasonable simulation of the qualitative flow field in comparison with the CFD results. The location of the vortex centre in the ELL code is located 20% lower on the z axis in comparison with the CFD data at $X/C_{ref}=0.5$ (Fig. 7.9). The differences increase going downstream, since in the CFD results the location of the vortex moves up on the z axis and in the ELL code it remains almost constant. At $X/C_{ref}=5$ (Fig. 7.11) the location of the vortex centre in the ELL code is located 35% lower on the z axis in comparison with the CFD data. From these data (Fig. 7.9 to Fig. 7.11) it is clear that the evolution of the vortex is not modelled in the ELL code and that the vortex position is constant at all planes in the wake. The vector plots were made to have the vectors magnitude on the same scale for the CFD and the ELL code. As can be seen the induced velocities magnitudes in the ELL code are much lower compared to the CFD (Fig. 7.12 to Fig. 7.15). Since the ELL code models the vortex with a constant location and size, while the CFD models the

roll-up and decay of the vortex, and since the ELL code calculates a vortex with a lower strength compared with the CFD one, the differences between the CFD and ELL results decrease going downstream (Fig. 7.13 and Fig. 7.15). In the $X/C_{ref}=0.5$ plane the differences are higher than 50% (Fig. 7.12 and Fig. 7.14), while in the $X/C_{ref}=5$ plane they are around 30% (Fig. 7.13 and Fig. 7.15). As expected, since the fuselage is modelled as a flat plate, the ELL results are different from the CFD solutions in that region.

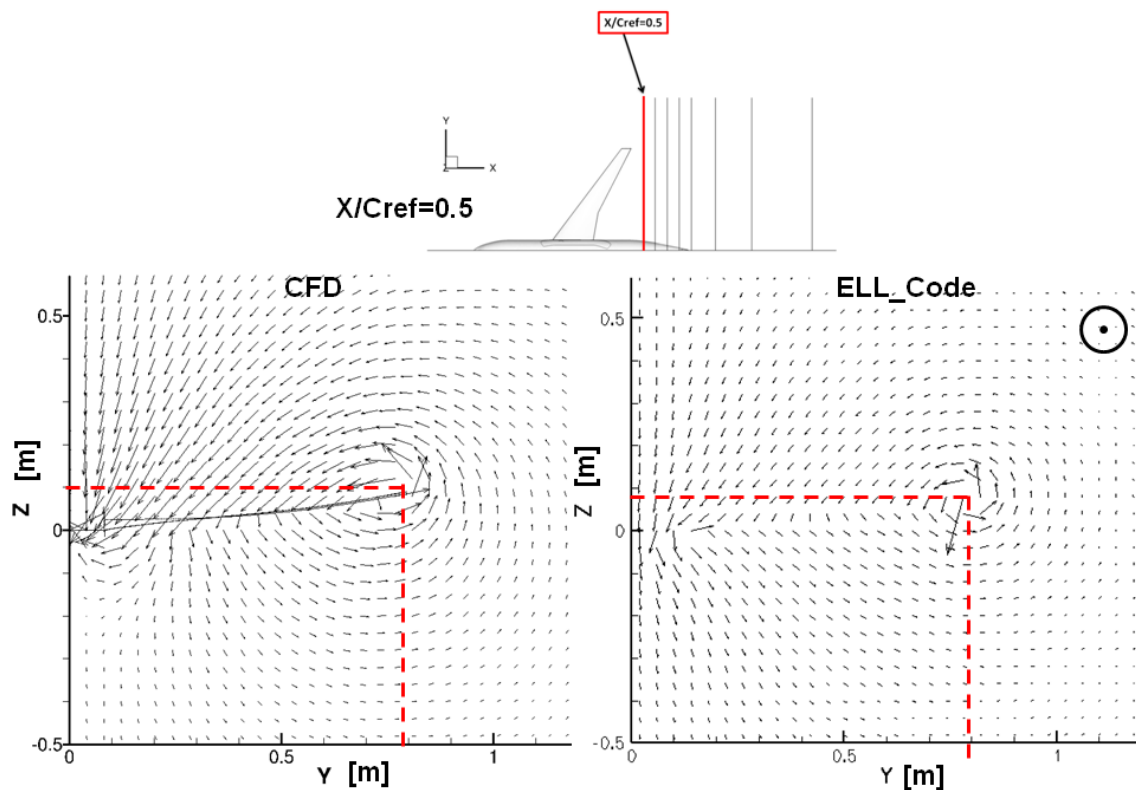


Fig. 7.9 Vectors of the CRM geometry scaled at wind tunnel sizes. Comparison of the CFD and ELL code with fuselage results at CRM flight conditions (the vector magnitude is on the same scale) at $X/C_{ref}=0.5$

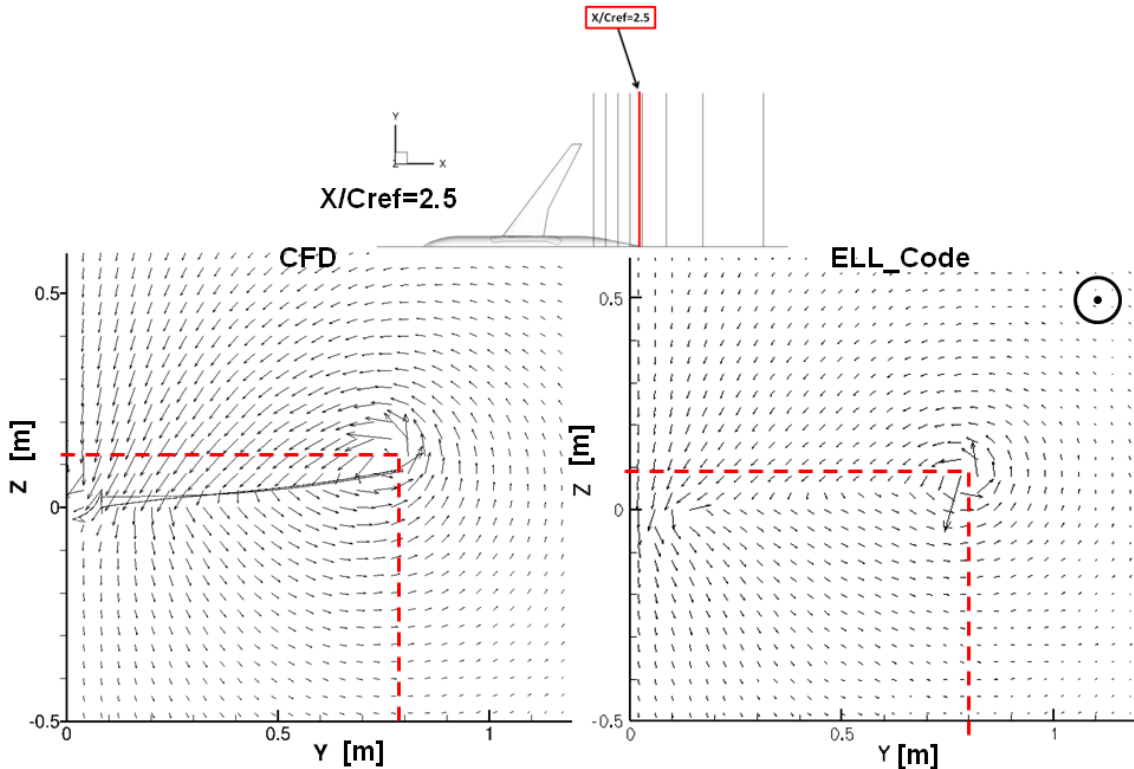


Fig. 7.10 Vectors of the CRM geometry scaled at wind tunnel sizes. Comparison of the CFD and ELL code with fuselage results at CRM flight conditions (the vector magnitude is on the same scale) at $X/C_{ref}=2.5$

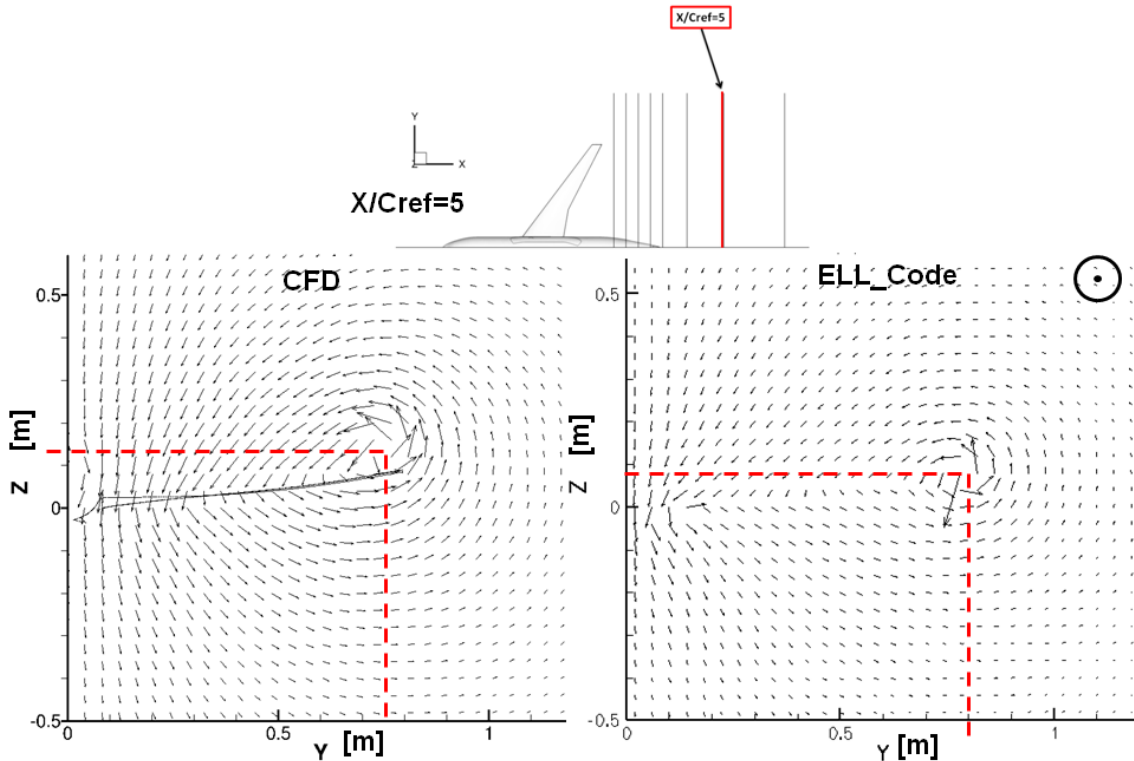


Fig. 7.11 Vectors of the CRM geometry scaled at wind tunnel sizes. Comparison of the CFD and ELL code with fuselage results at CRM flight conditions (the vector magnitude is on the same scale) at $X/C_{ref}=5$

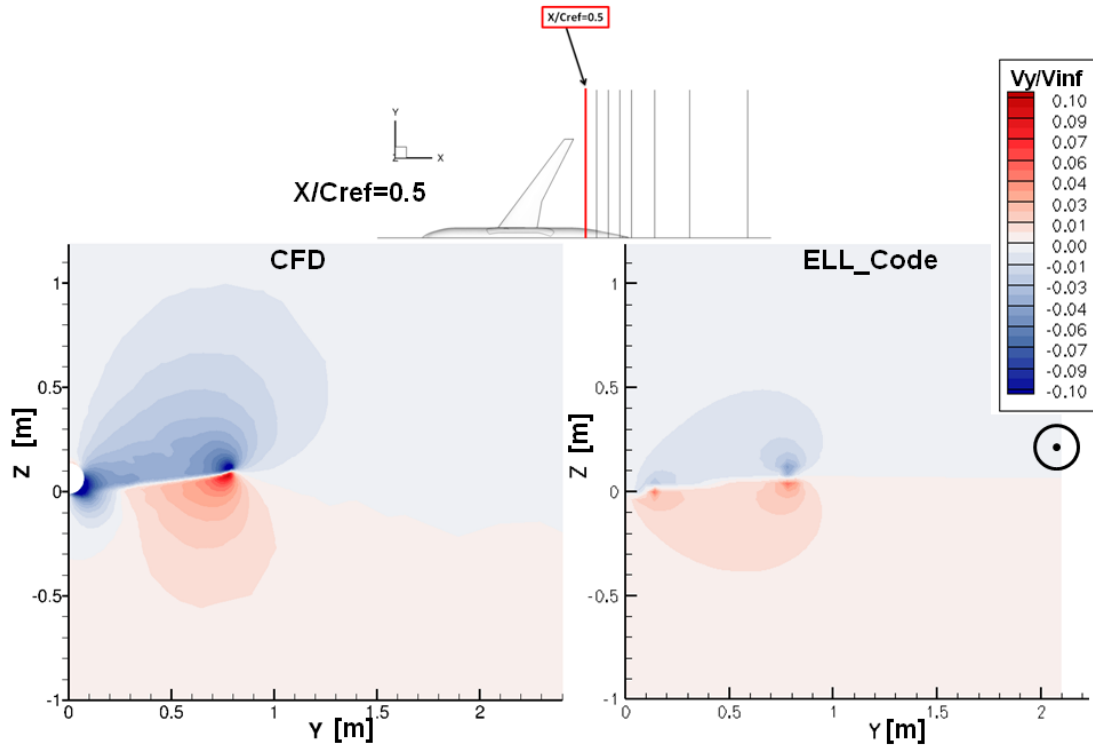


Fig. 7.12 Induced spanwise velocity field (V_y) for the CRM geometry scaled at wind tunnel sizes. Comparison of the CFD and ELL code with fuselage results at CRM flight conditions at $X/C_{ref}=0.5$

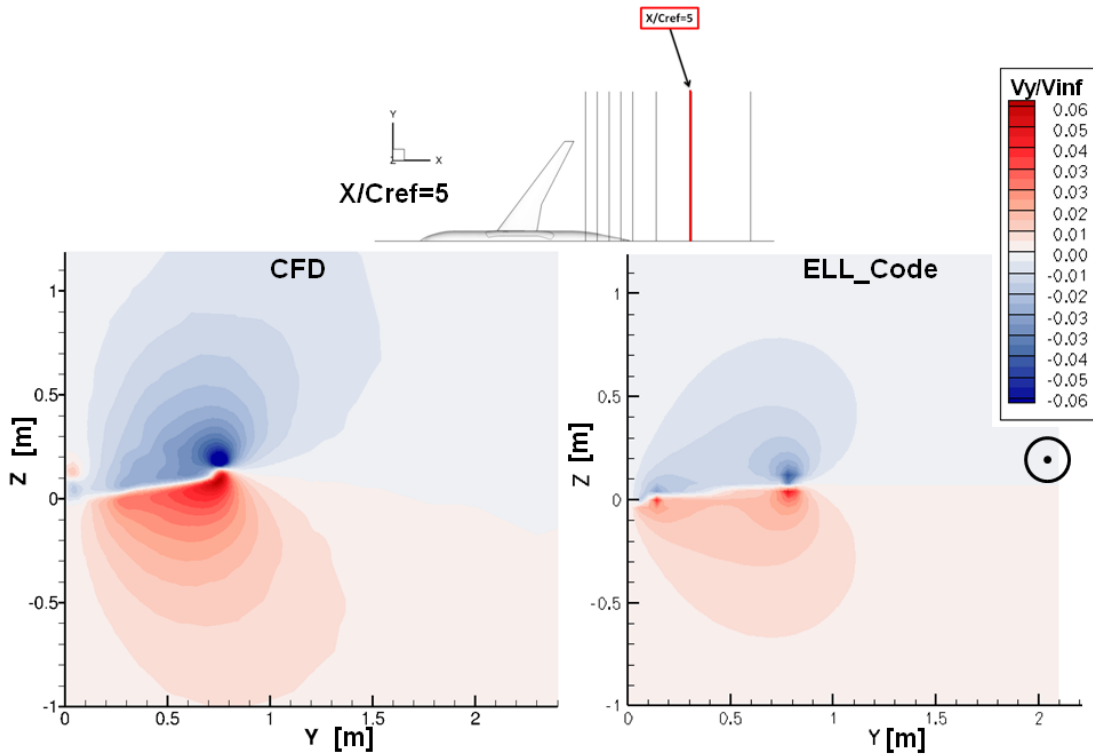


Fig. 7.13 Induced spanwise velocity field (V_y) for the CRM geometry scaled at wind tunnel sizes. Comparison of the CFD and ELL code with fuselage results at CRM flight conditions at $X/C_{ref}=5$

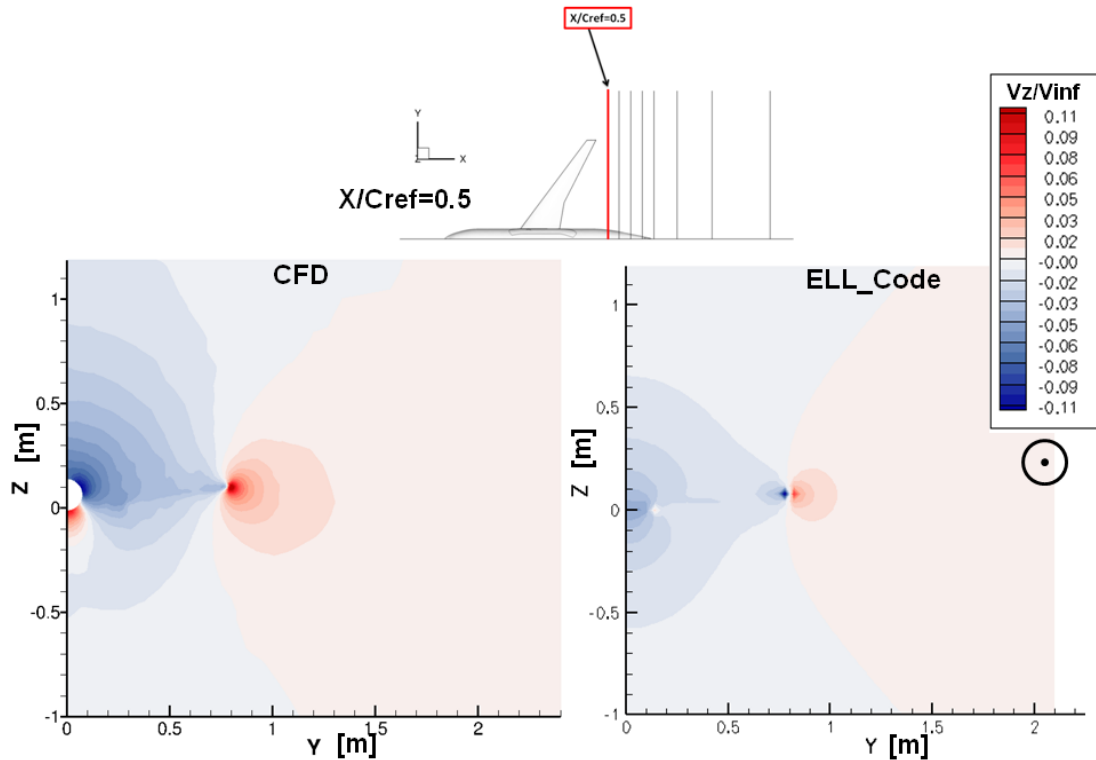


Fig. 7.14 Induced spanwise velocity field (V_z) for the CRM geometry scaled at wind tunnel sizes. Comparison of the CFD and ELL code with fuselage results at CRM flight conditions at $X/C_{ref}=0.5$

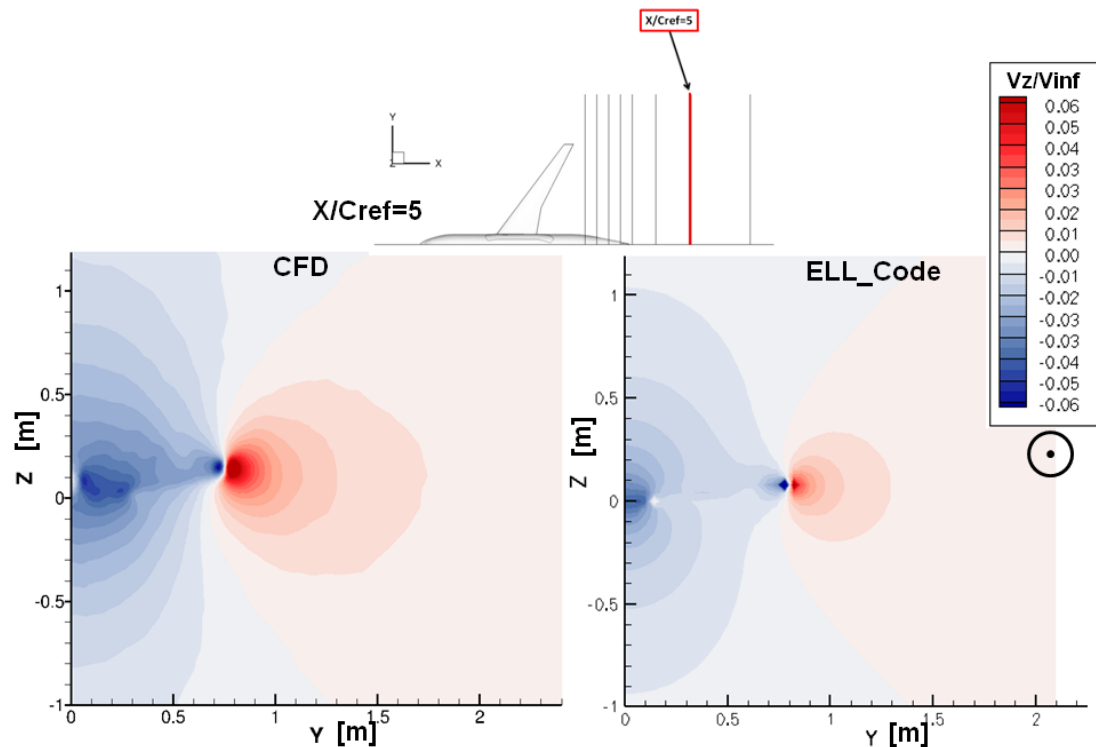


Fig. 7.15 Induced spanwise velocity field (V_z) for the CRM geometry scaled at wind tunnel sizes. Comparison of the CFD and ELL code with fuselage results at CRM flight conditions at $X/C_{ref}=5$

The values of the induced velocities V_x , V_y , V_z , the downwash and yaw angle along two traverses located on the $X/C_{ref}=0.5$ and $X/C_{ref}=5$ planes were extracted as well (Fig. 7.16 and Fig. 7.17). The traverses pass through the centre of the vortices both in the CFD and the ELL code, as a consequence they have slightly different locations. The traverse plots show more clearly the differences in the velocity magnitudes, at $X/C_{ref}=5$ they are around 30%, while in the $X/C_{ref}=0.5$ they are at more than 50%. A further characteristic of the ELL code is that the induced V_x velocity component variations are not modelled by the ELL method, as illustrated in Fig. 7.18.

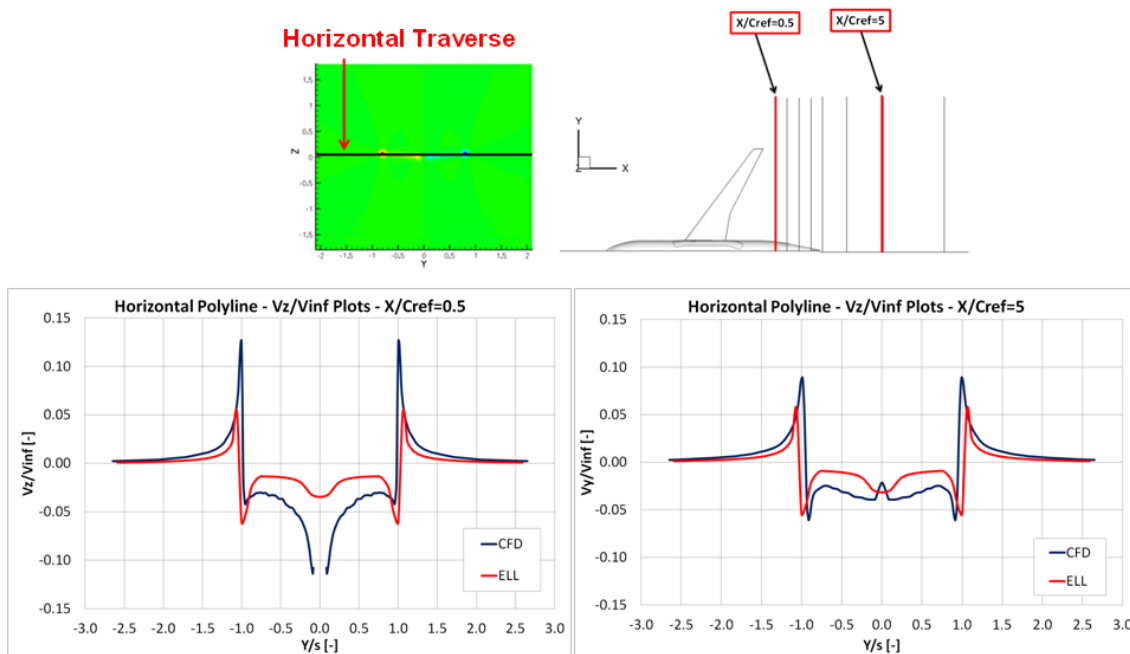


Fig. 7.16 Horizontal traverse V_z values of the CRM geometry scaled at wind tunnel sizes. Comparison of the CFD and ELL code with fuselage results at CRM flight conditions at $X/C_{ref}=0.5$ and $X/C_{ref}=5$

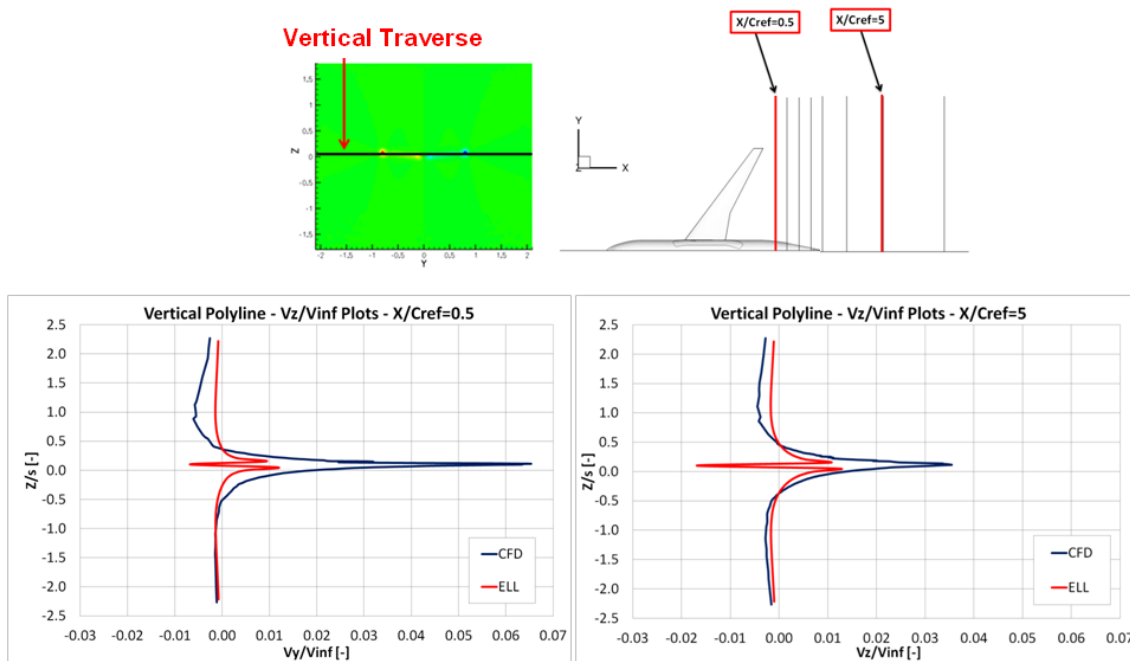


Fig. 7.17 Vertical traverse Vz values of the CRM geometry scaled at wind tunnel sizes. Comparison of the CFD and ELL code with fuselage results at CRM flight conditions at $X/C_{ref}=0.5$ and $X/C_{ref}=5$

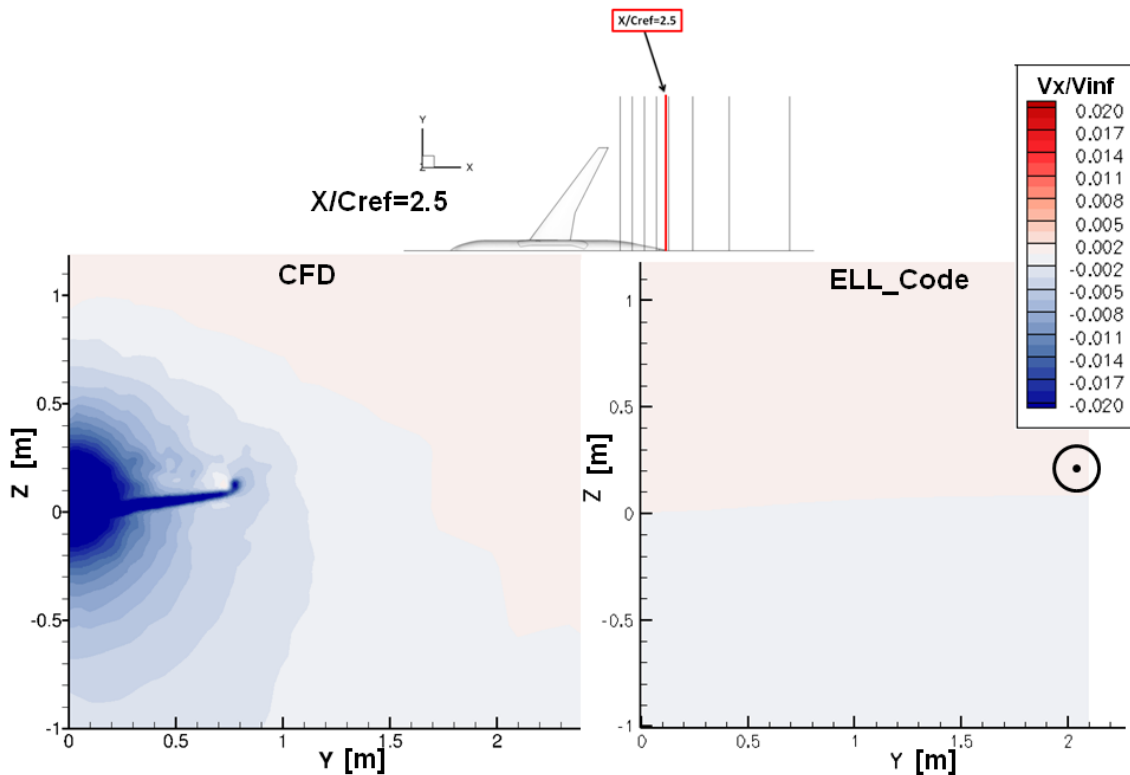


Fig. 7.18 Induced spanwise velocity field (V_x) for the CRM geometry scaled at wind tunnel sizes. Comparison of the CFD and ELL code with fuselage results at CRM flight conditions at $X/C_{ref}=2.5$

Moreover, a comparison of the dynamic pressure between the CFD and the ELL code was carried out, since this is a parameter that determines the lift and drag coefficients and then the development of tip vortex. The dynamic pressure was calculated for the CFD results with:

$$q_{CFD} = \frac{1}{2} \gamma P_s M^2 \quad (22)$$

While for the ELL code results with:

$$q_{ELL} = \frac{1}{2} \rho V^2 \quad (23)$$

Where γ is the ratio of specific heats, P_s is the static pressure, M is the Mach number, ρ is the density and V is the velocity. Since the ELL code is incompressible and the fuselage is modelled as a flat plate, the non-dimensional dynamic pressure flow-field of the ELL code is completely different in the fuselage zone (Fig. 7.19). In the $X/C_{ref}=5$ plane, which is located downstream of the fuselage (Fig. 7.7), the non-dimensional dynamic pressure values of the ELL code are overall similar to the CFD (Fig. 7.20).

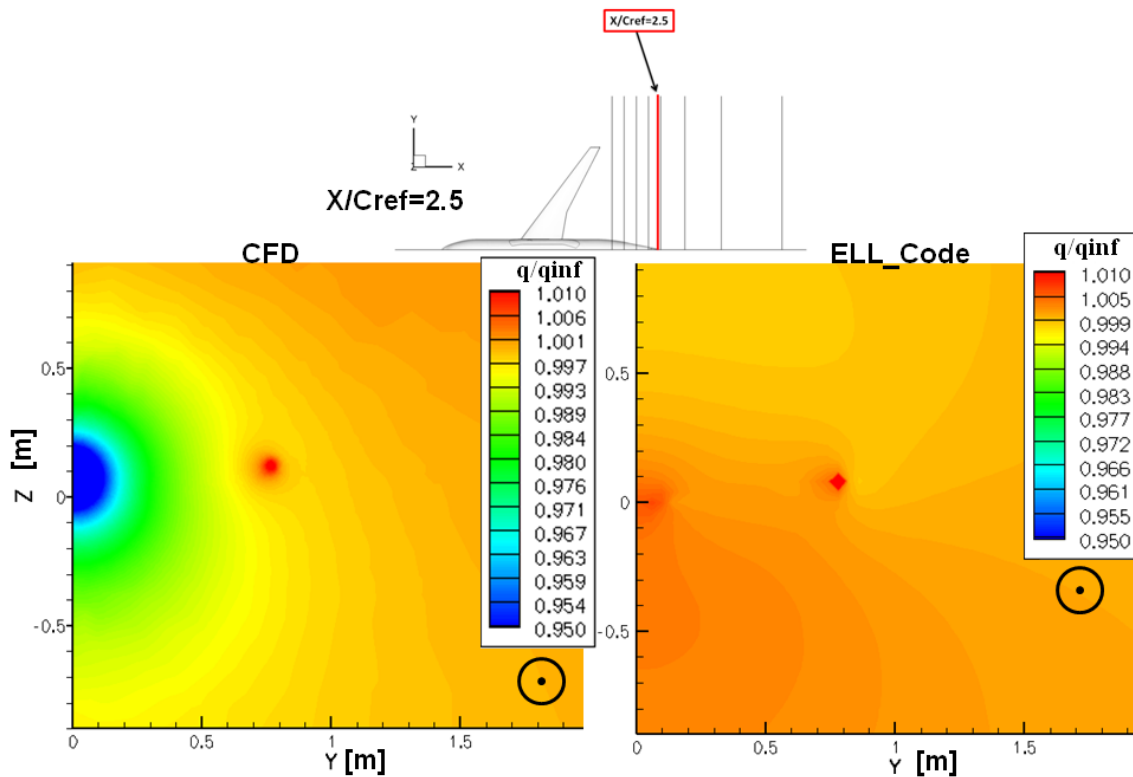


Fig. 7.19 Dynamic pressure of the CRM geometry scaled at wind tunnel sizes. Comparison of the CFD and ELL code with fuselage results at CRM flight conditions at $X/C_{ref}=2.5$

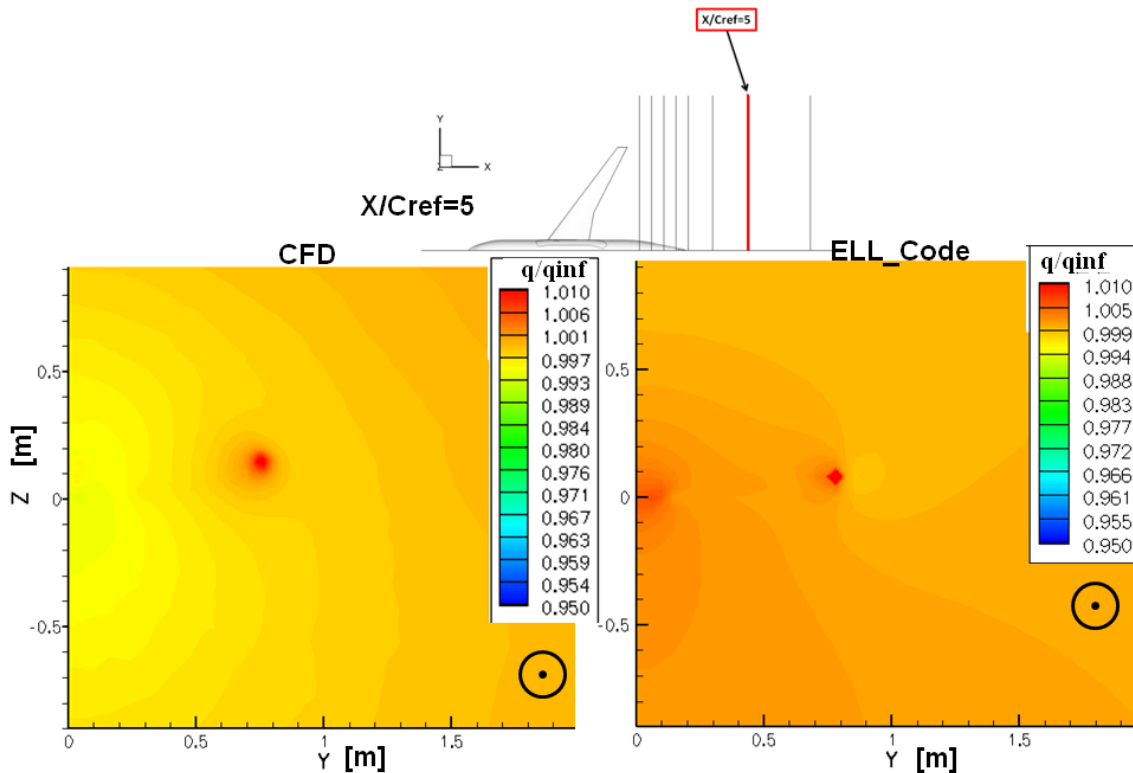


Fig. 7.20 Dynamic pressure of the CRM geometry scaled at wind tunnel sizes. Comparison of the CFD and ELL code with fuselage results at CRM flight conditions at $X/C_{ref}=5$

As expected, there are notable differences in the calculated vortex core radius calculated from the ELL code and the CFD results. The vortex core radius is not explicitly modelled in the ELL code and the values illustrated in Fig. 7.21 are only due to the mesh resolution of the code. The vortex core circulation in the ELL code is lower than the CFD in a range of 50% to almost 80% (Fig. 7.22). The total vortex circulation of the CFD results is almost constant going downstream. The ELL values are around 55% lower than the CFD (Fig. 7.23).

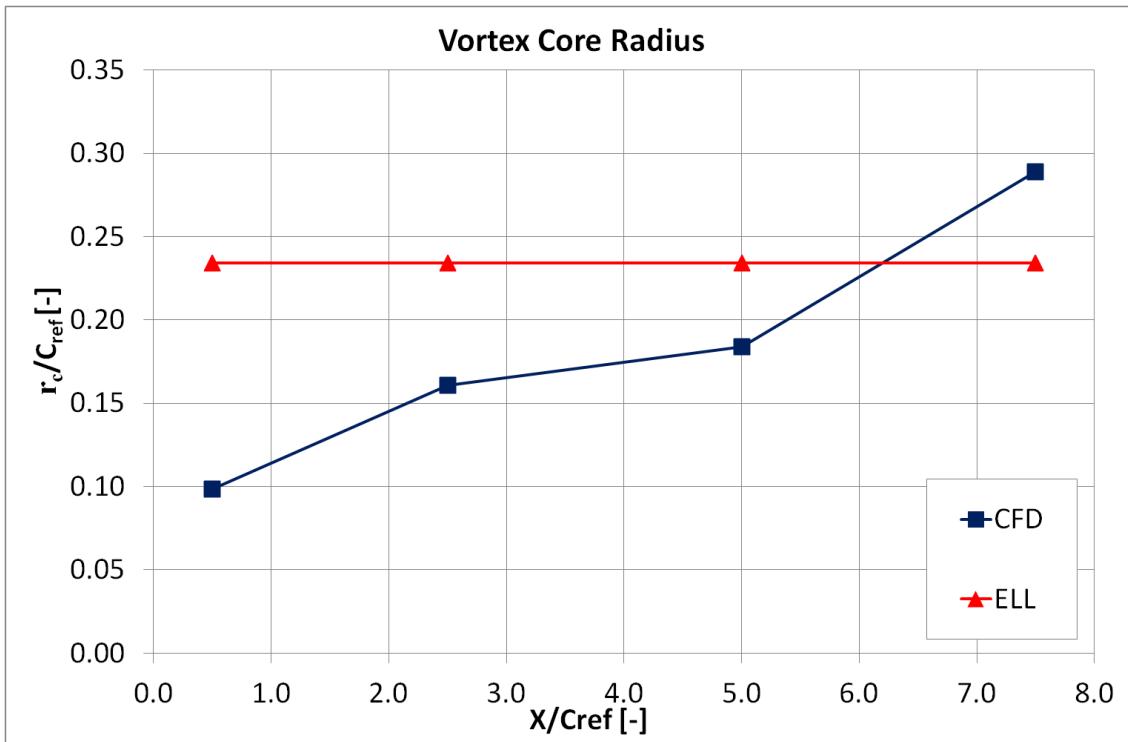


Fig. 7.21 Vortex core radius of the CRM geometry scaled at wind tunnel sizes. Comparison of the CFD and ELL code with fuselage results at CRM flight conditions at various X/C_{ref}

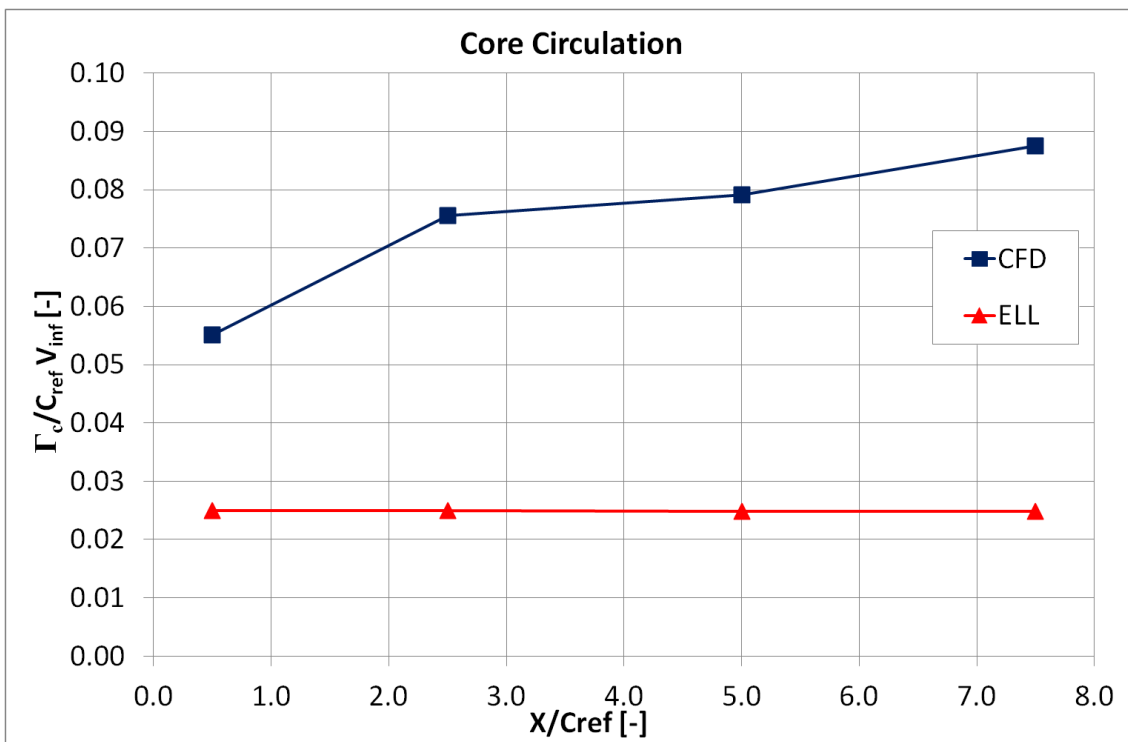


Fig. 7.22 Core circulation of the CRM geometry scaled at wind tunnel sizes. Comparison of the CFD and ELL code with fuselage results at CRM flight conditions at various X/C_{ref}

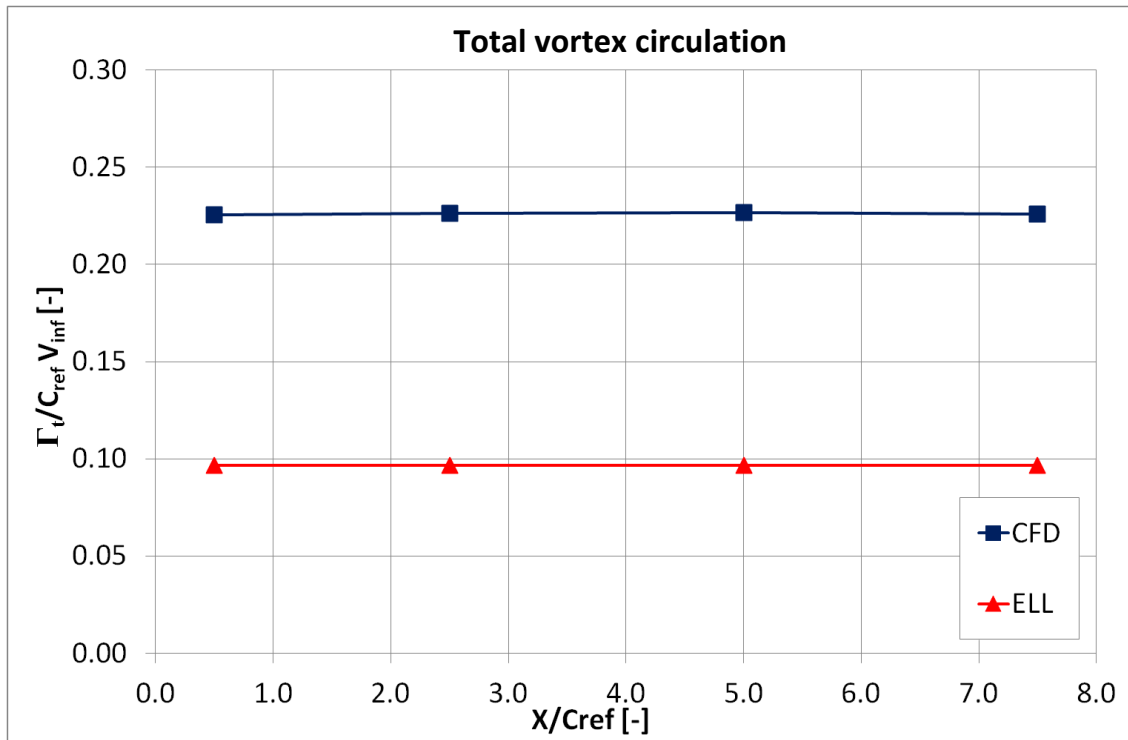


Fig. 7.23 Total vortex circulation of the CRM geometry scaled at wind tunnel sizes. Comparison of the CFD and ELL code with fuselage results at CRM flight conditions at various X/C_{ref}

7.4 ELL code of the CRM full-scale geometry under air-refuelling conditions

The CFD simulations with flight conditions 1, 2, 3 and 4 (Table 7.6) were compared with the results from the ELL code. The simulation of flight condition 1 with ANSYS Fluent has given numerous CFD problems. For this reason it was decided to run the flight condition 1 simulation also with ANSYS CFX and a structured grid.

	Flight Condition	Code	Mesh size	Mach [-]	Re [-]	AOA [°]	C_L [-]	Ts [K]	Ps [Pa]
CRM_TAIL_FULLSCALE	FC1	FLUENT - CFX	18MIL	0.398	36×10^6	8.5	0.95	248	46984
	FC2	FLUENT	18MIL	0.441	40×10^6	6.2	0.77	248	46984
	FC3	FLUENT	18MIL	0.548	50×10^6	3.5	0.5	248	46984
	FC4	FLUENT	18MIL	0.704	64×10^6	1.07	0.3	248	46984

Table 7.6 CRM geometry wing-body-tail full-scale CFD simulations

First of all, the CFD results of the CRM geometry at full-scale with tail at flight condition 3, with $M=0.548$, $AOA=3.5^\circ$ and $CL=0.5$ were compared with the results of the CRM geometry scaled at wind tunnel conditions without the tail, with $M=0.85$, $AOA=2.26^\circ$ and CL of 0.5 (Fig. 7.24). Even if the two geometries have different sizes, the comparison was possible since they have the same lift

coefficient. It was found that for low angles of attack the influence of the tail on the wake flow field is not significant and also that the tip vortex generated from the horizontal tail is much less than the one produced from the wing. This is due to the lifting surface of the tail which is much smaller compared to the surface of the wing. Furthermore, it has to be noticed that the configuration that was used has a tail mounted with a zero angle of attack. As can be seen from the results of flight conditions 1 and 2 (see paragraph 7.4.1 and 7.4.2), when the angle of attack increases the influence of the tail increases as expected.

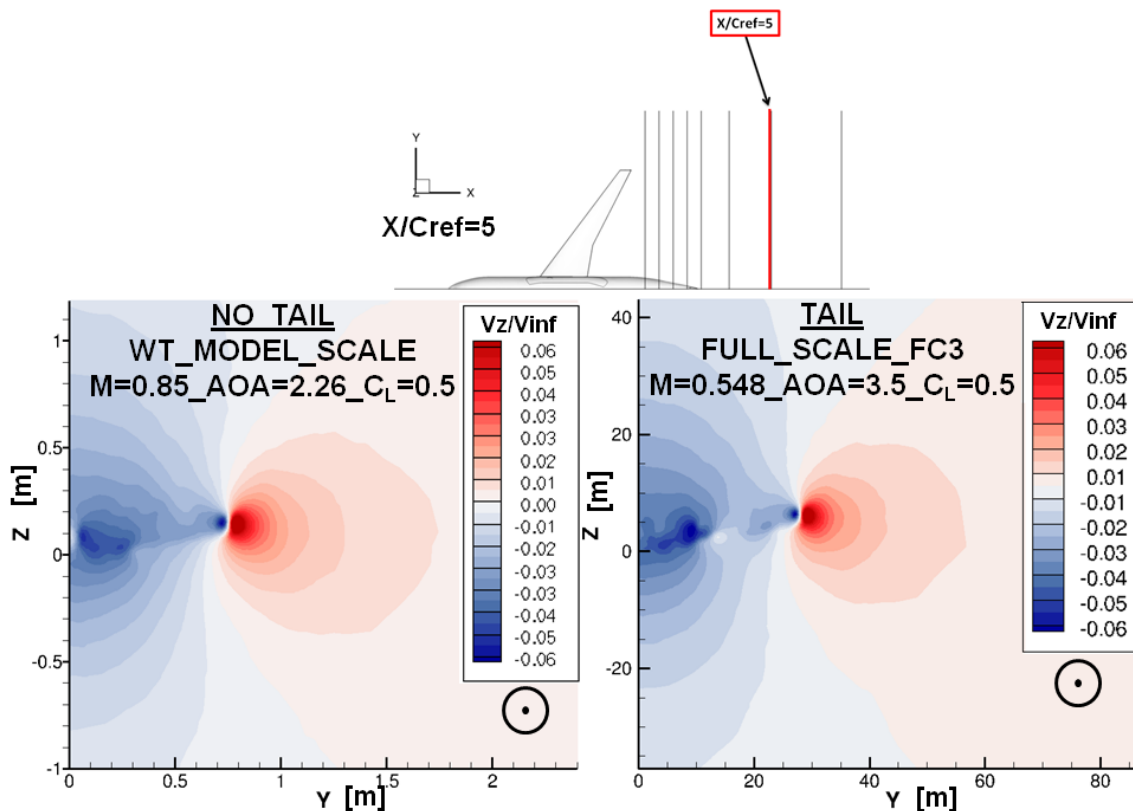


Fig. 7.24 V_z velocity of the of the CFD results of the CRM geometry scaled at wind tunnel conditions without tail and of the CRM geometry full-scale with tail at flight condition 3

7.4.1 Flight condition 1 results

Flight condition 1 has an angle of attack of 8° and a free-stream Mach number of 0.398 with a C_L of 0.95 (Table 7.6). Since this is a very high angle of attack for the considered CRM clean wing, the wing profile was partially stalled in the ANSYS Fluent simulation and the obtained C_L is lower than the calculated one of 0.95. For this reason also the results of a ANSYS CFX simulation performed with a structured grid of the 4th Drag Prediction Workshop were considered and

post-processed. In the ANSYS CFX results a C_L of 0.95 with an angle of attack equal to 8.5° was obtained. This is due to difference in how the two CFD solvers work.

7.4.1.1 ANSYS Fluent results

For this flight condition a clear second vortex appears in the wake which is the tip vortex generated by the tail (Fig. 7.25). In this configuration, and with the wing profile partially stalled, the two vortices have similar strength and the tip vortex of the tail is clearly visible also at $X/C_{ref}=7.5$ (Fig. 7.26).

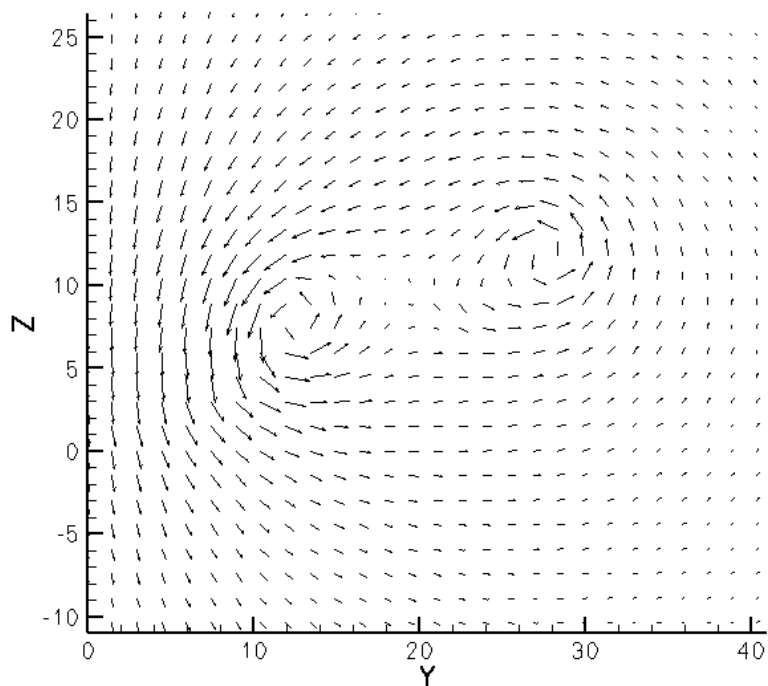


Fig. 7.25 Vectors of the CRM geometry full-scale of the Fluent CFD at flight condition 1 at $X/C_{ref}=7.5$

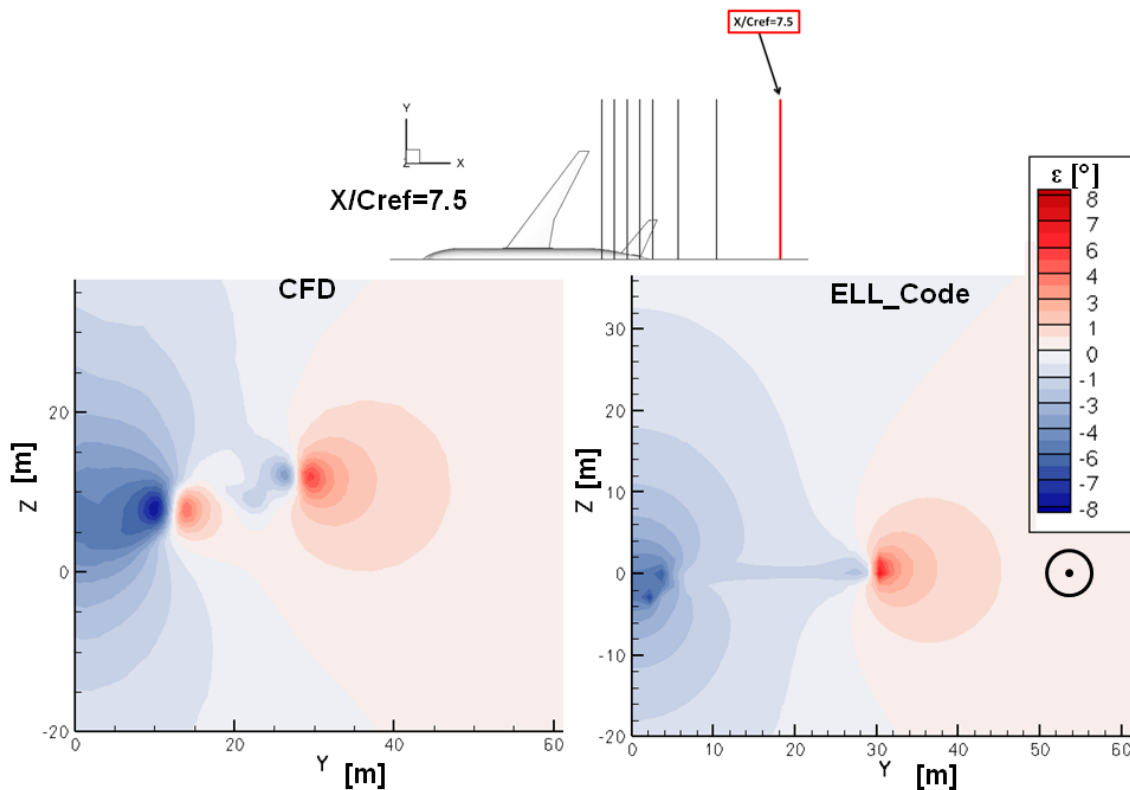


Fig. 7.26 Downwash angle of the CRM geometry full-scale with tail. Comparison of the Fluent CFD and ELL code results with flight condition 1 at $X/C_{ref}=7.5$

7.4.1.2 ANSYS CFX results

With the CFX solver, *Flight condition 1* has an angle of attack of 8.5° and a free-stream Mach number of 0.398 with a C_L of 0.95. Even if there are some differences, the results are consistent with the Fluent results and also in CFX, at this flight condition, a clear second vortex appears in the wake which is the tip vortex generated by the tail (Fig. 7.28 and Fig. 7.29). In the CFX results the tail vortex is clearly visible up to $X/C_{ref}=7.5$ (Fig. 7.27), as in the Fluent results, but in this case the strength of the tail vortex is lower compared to the wing one. This trend is confirmed also in the downwash and yaw angles plots (Fig. 7.28 and Fig. 7.29). Furthermore, the location of the vortex on the z axis of the ELL code is 90% lower than the CFD calculations (Fig. 7.28 and Fig. 7.29).

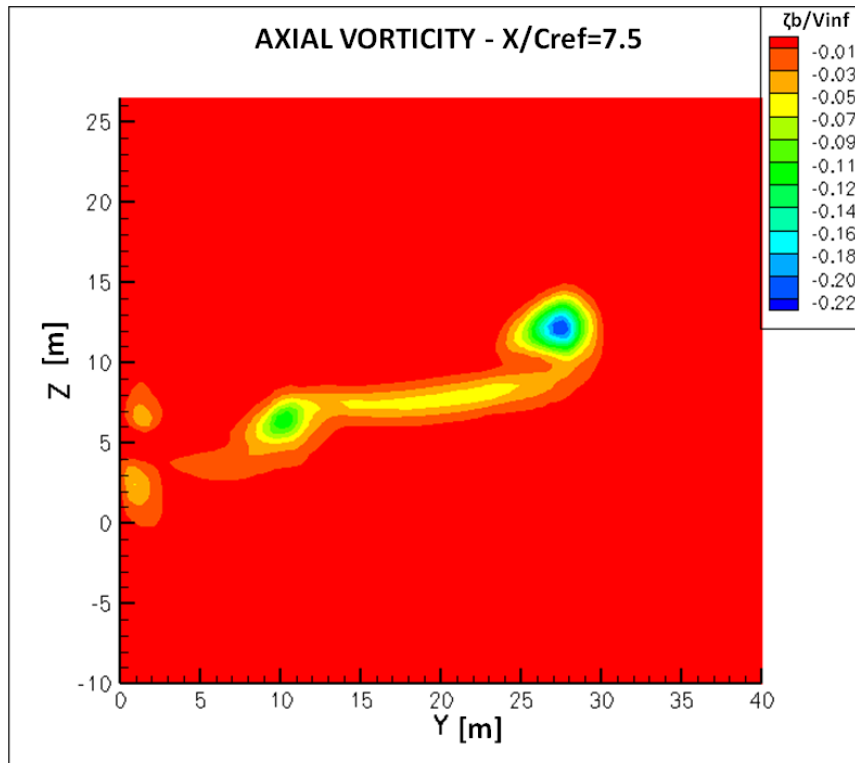


Fig. 7.27 CFX CFD non-dimensional axial vorticity (ζ_b/V_∞) of the CRM geometry full-scale with flight condition 1 at $X/C_{ref}=7.5$

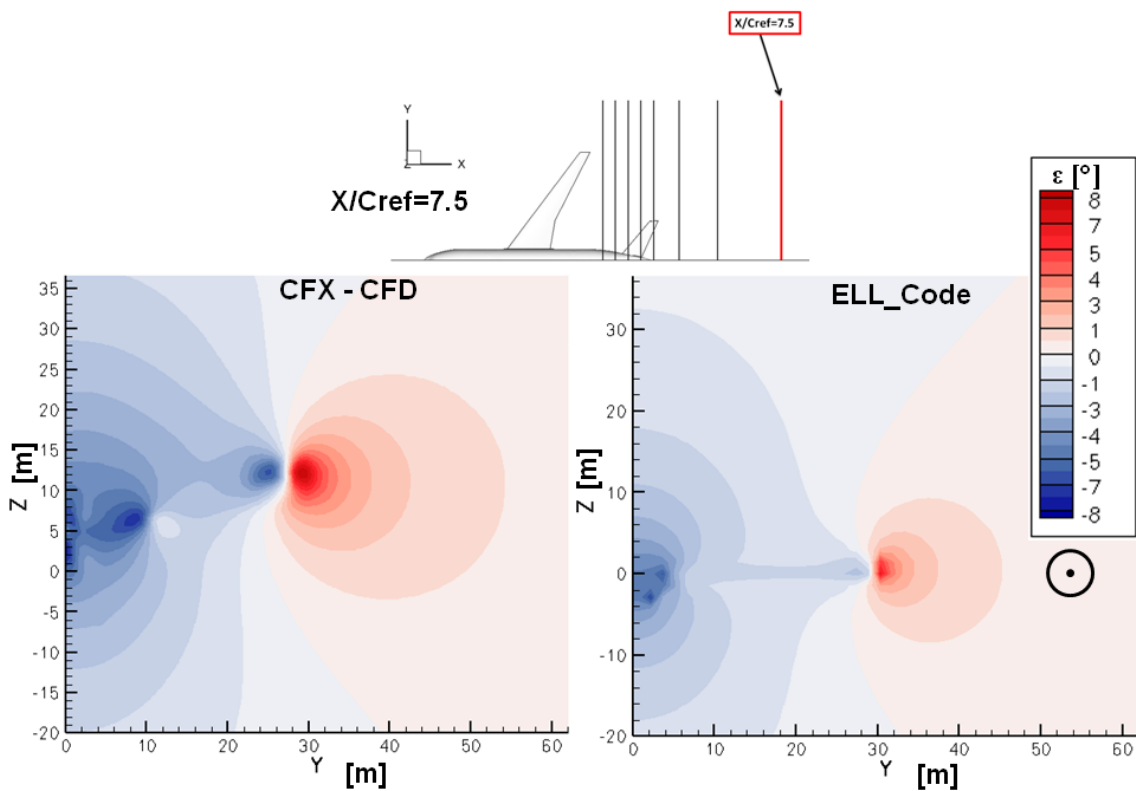


Fig. 7.28 Downwash angle of the CRM geometry full-scale. Comparison of the CFX CFD and ELL code results with flight condition 1 at $X/C_{ref}=7.5$

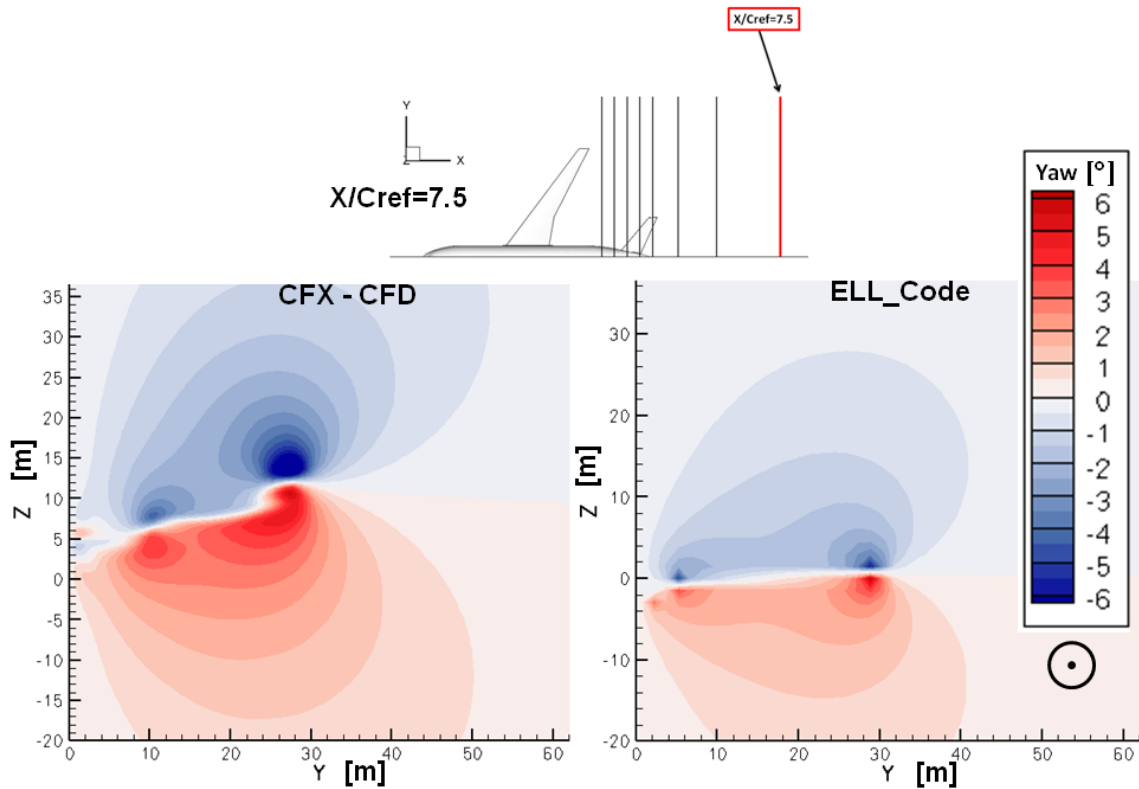


Fig. 7.29 Yaw angle of the CRM geometry full-scale. Comparison of the CFX CFD and ELL code results with flight condition 1 at $X/C_{ref}=7.5$

7.4.2 *Flight condition 2 results*

Flight condition 2 has an angle of attack of 6.2° and a free-stream Mach number of 0.441 with a CL of 0.8 (Table 7.6). As for flight condition 1, a clear second vortex appears in the wake which is the tip vortex generated by the tail (Fig. 7.30). For this flight condition, however, the tail tip vortex is much less intense compared to the wing's one.

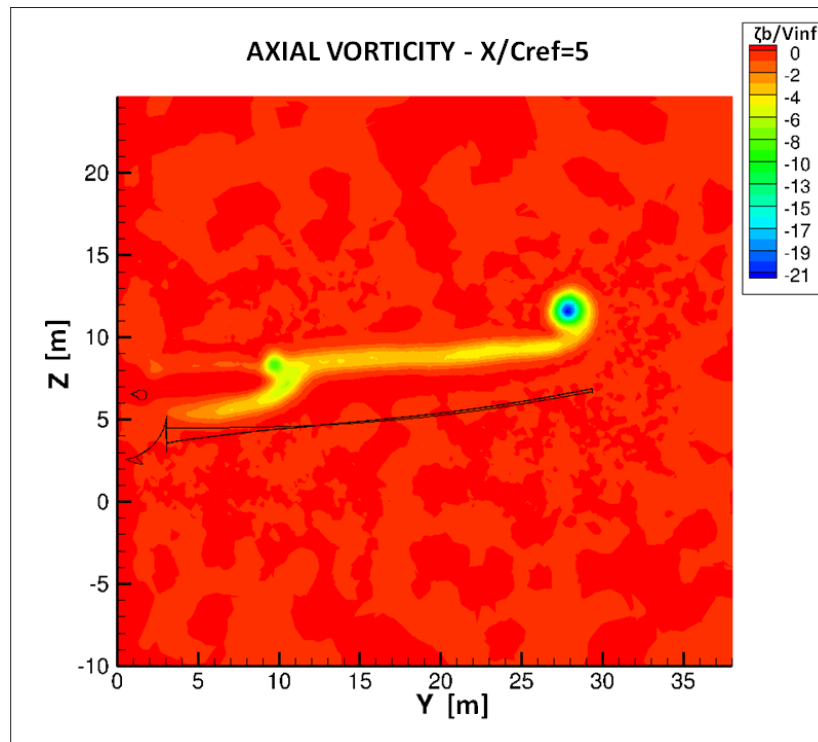


Fig. 7.30 CFD non-dimensional axial vorticity ($\zeta b/V_\infty$) of the CRM geometry full-scale with flight condition 2 at $X/C_{ref}=5$

As can be seen in Fig. 7.30, at $X/C_{ref}=5$ the axial vorticity of the tail vortex is 50% lower than the vorticity of the wing tip vortex. The fuselage is modelled in the ELL code as a flat plate, which is a considerable approximation in that part of the flow field. For this reason and based on the above result, the omission of the tail in the ELL code is not a critical approximation at an angle of attack of 6.2° , except for the downstream planes where the tail is located. The comparisons of the plots of the yaw angle show that, as expected in the $X/C_{ref}=2.5$ plane, the differences between the CFD and the ELL code results are notable, since this is one of the planes that cut the tail (Fig. 7.31). In the $X/C_{ref}=5$ plane, located further downstream, the differences between the CFD and the ELL code are smaller (Fig. 7.32). At $X/C_{ref}=5$ the yaw angle in the ELL code is 25% lower than in the CFD and the general characteristics of the wake flow field are similar, while at $X/C_{ref}=2.5$ the yaw angle of the ELL code is around 55% lower than the CFD.

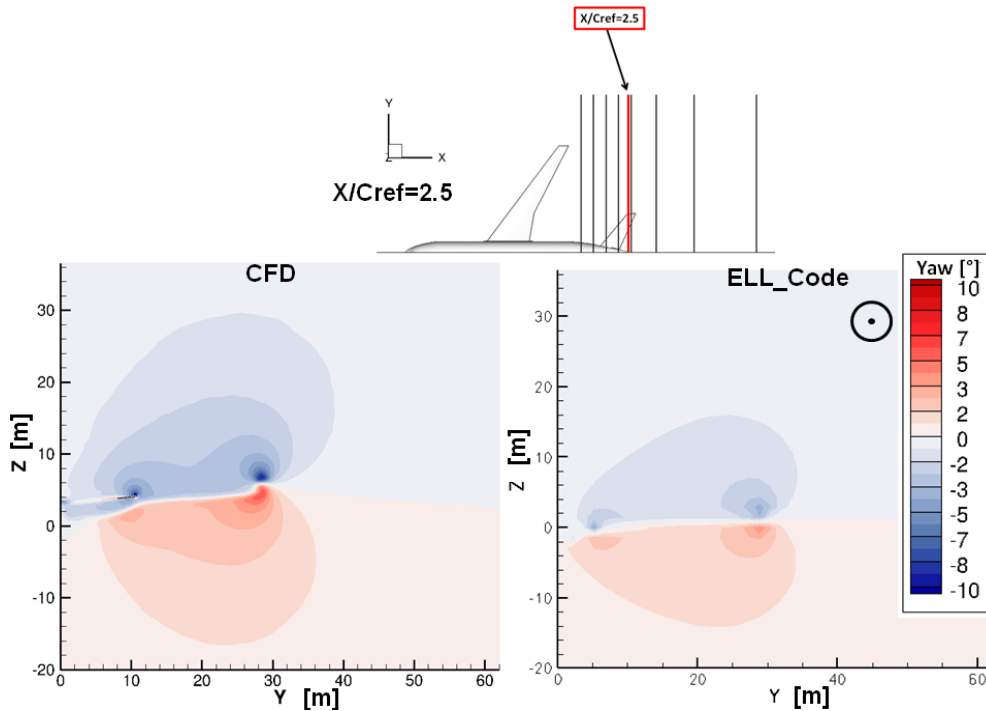


Fig. 7.31 Yaw angle of the CRM geometry full-scale. Comparison of the CFD and ELL code results with flight condition 2 at $X/C_{ref}=2.5$

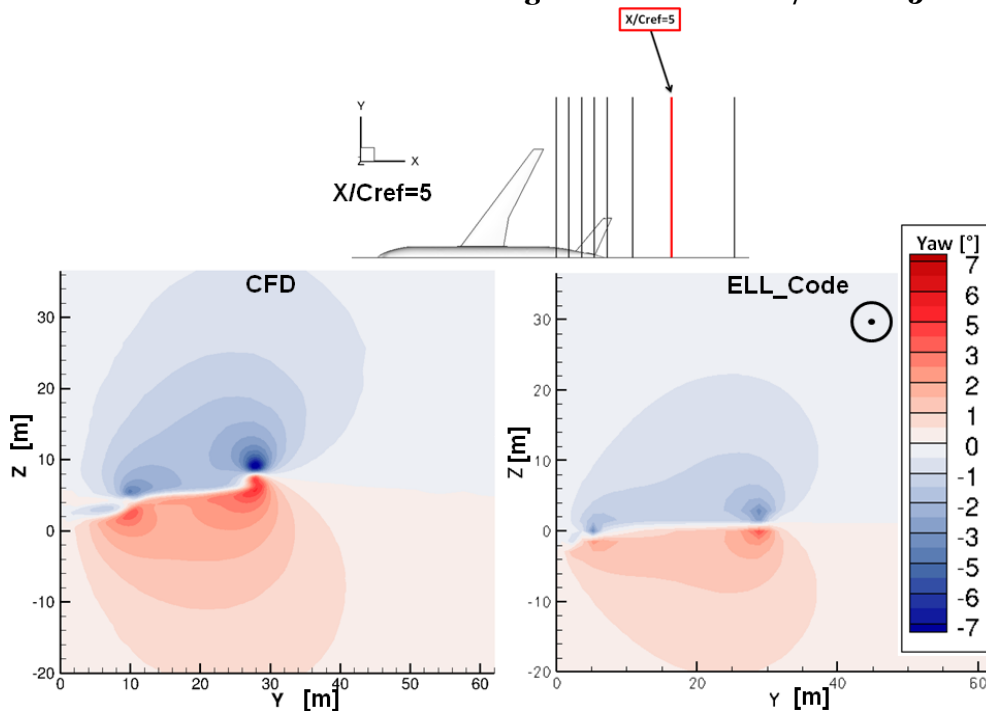


Fig. 7.32 Yaw angle of the CRM geometry full-scale. Comparison of the CFD and ELL code with fuselage results with flight condition 2 at $X/C_{ref}=5$

Fig. 7.33 to Fig. 7.36 show that, based on the geometry definition which was used for the CFD simulations, the obtained flow field results with the standard settings of the ELL show notable differences in comparison with the CFD flow

fields. Despite the presence of two vortices in the ELL code solution, the one at $y=12.5$ m (Fig. 7.33 and Fig. 7.35) is not due to the presence of a tail or the fuselage, but is an artefact of the numerical construction of the code. A comparison of the tangential velocity and the total vortex circulation between the CFD results and ELL code was carried out. The findings of the results of the CRM geometry at wind tunnel model scale were confirmed. The differences in the tangential velocity peak, $V_{\theta\text{peak}}$, are due to the fact that the ELL code does not model the viscous core of the vortex (Fig. 7.37). The total vortex circulation of the ELL code is around 55% lower compared to the CFD (Fig. 7.38).

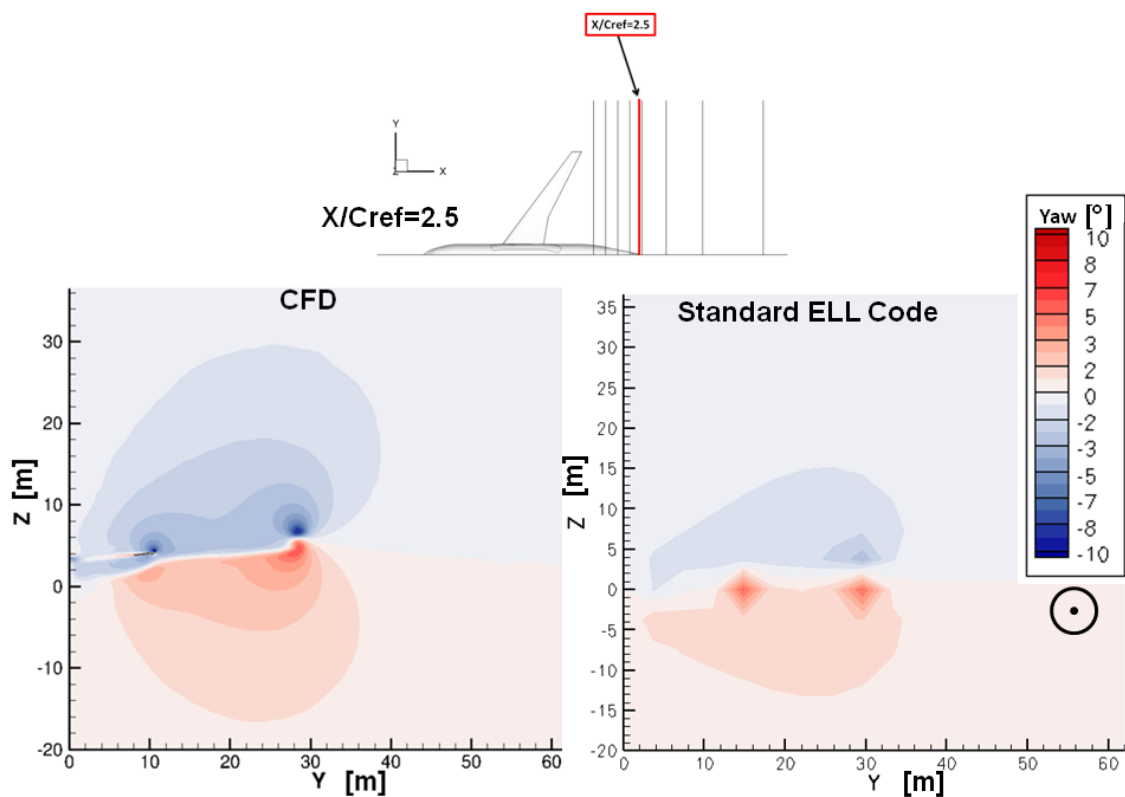


Fig. 7.33 Yaw angle of the CRM geometry full-scale. Comparison of the CFD and of the standard settings ELL code with fuselage results with flight condition 2 at $X/C_{ref}=2.5$

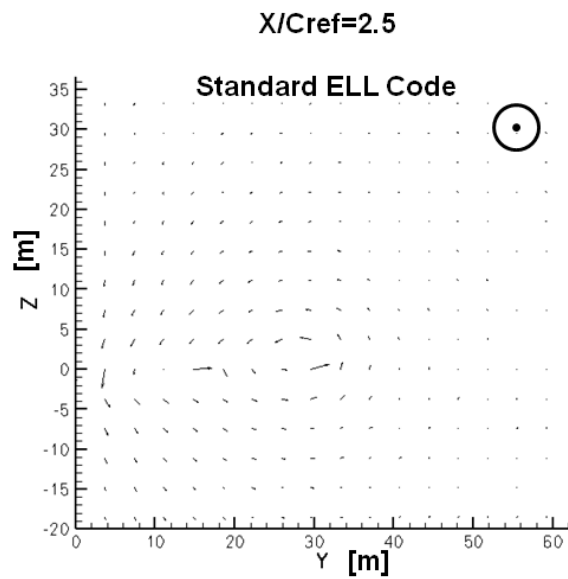


Fig. 7.34 Vectors of the CRM geometry full-scale of the standard settings ELL code with fuselage results with flight condition 2 at $X/C_{ref}=2.5$

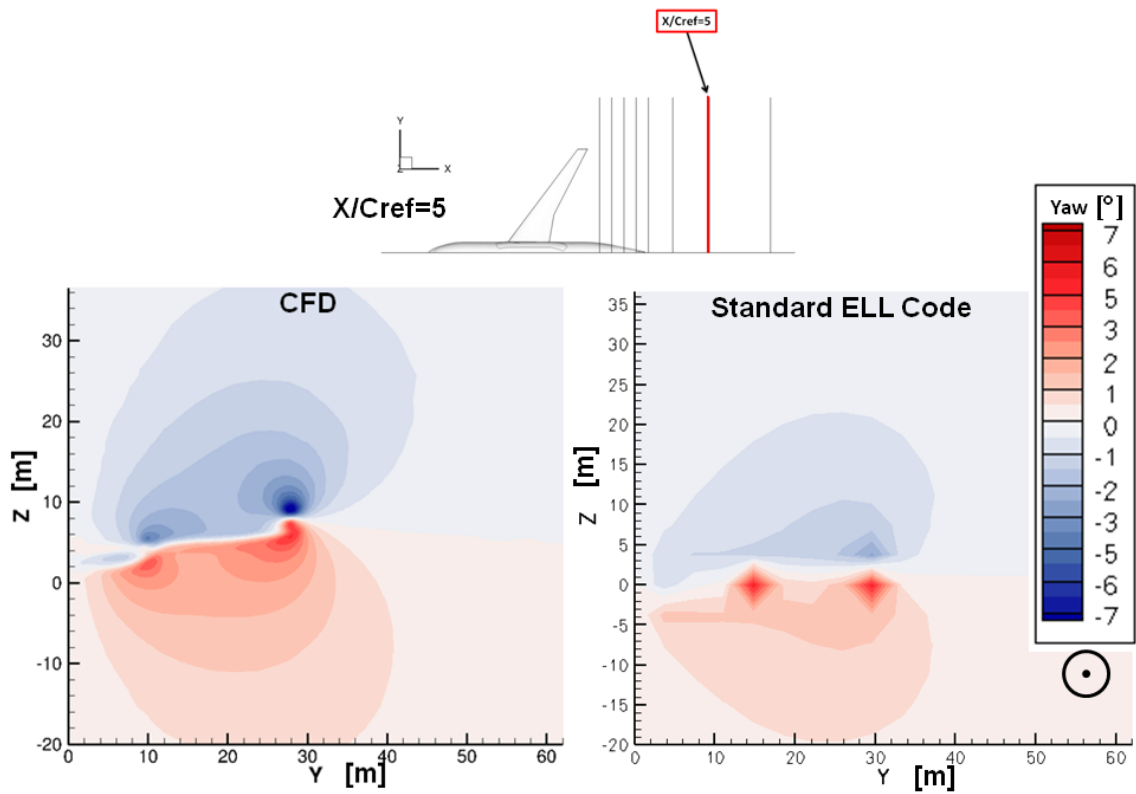


Fig. 7.35 Yaw angle of the CRM geometry full-scale. Comparison of the CFD and of the standard settings ELL code with fuselage results with flight condition 2 at $X/C_{ref}=5$

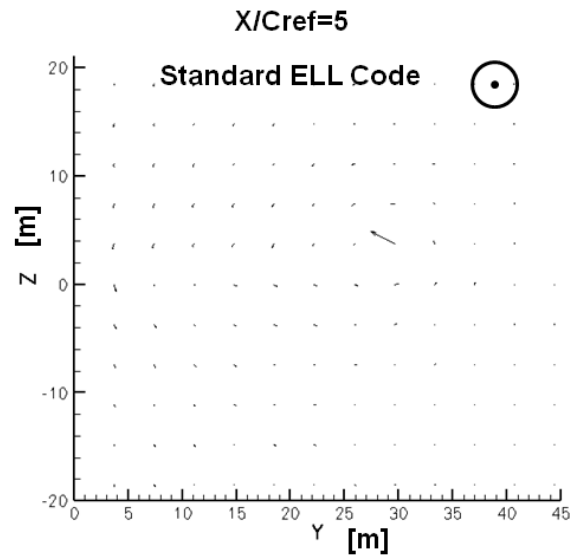


Fig. 7.36 Vectors of the CRM geometry full-scale of the standard settings ELL code with fuselage results with flight condition 2 at $X/C_{ref}=5$

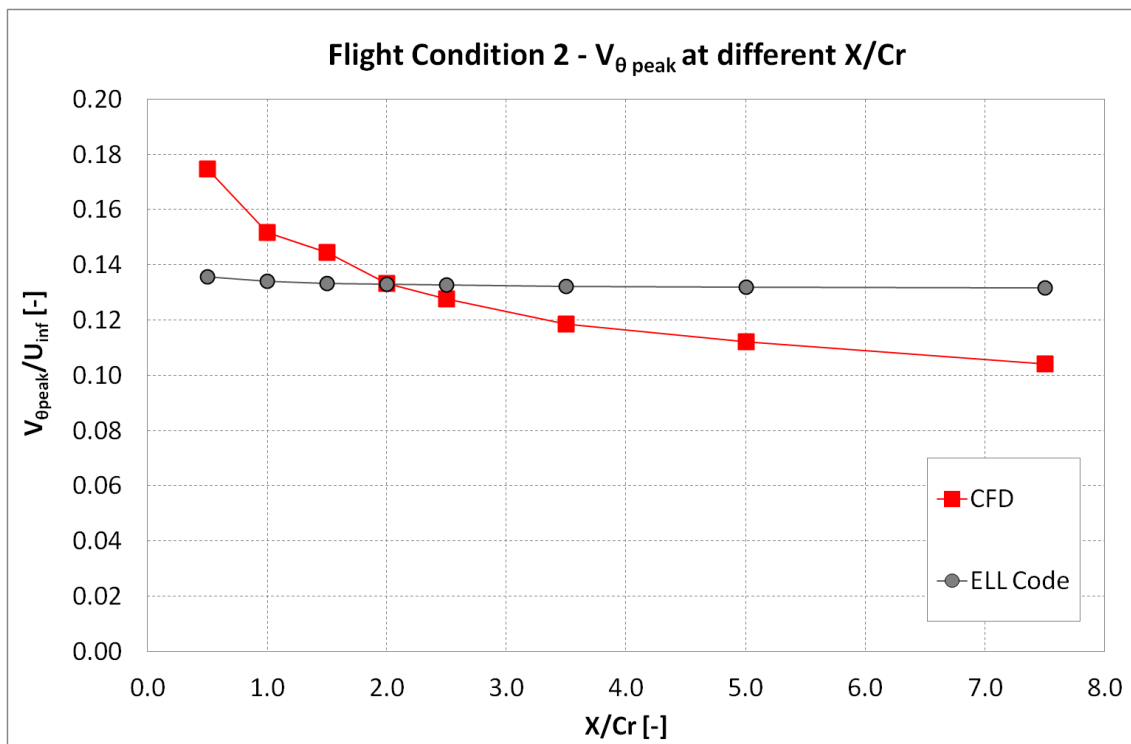


Fig. 7.37 $V_{\theta peak}$ at different X/Cr for flight condition 2

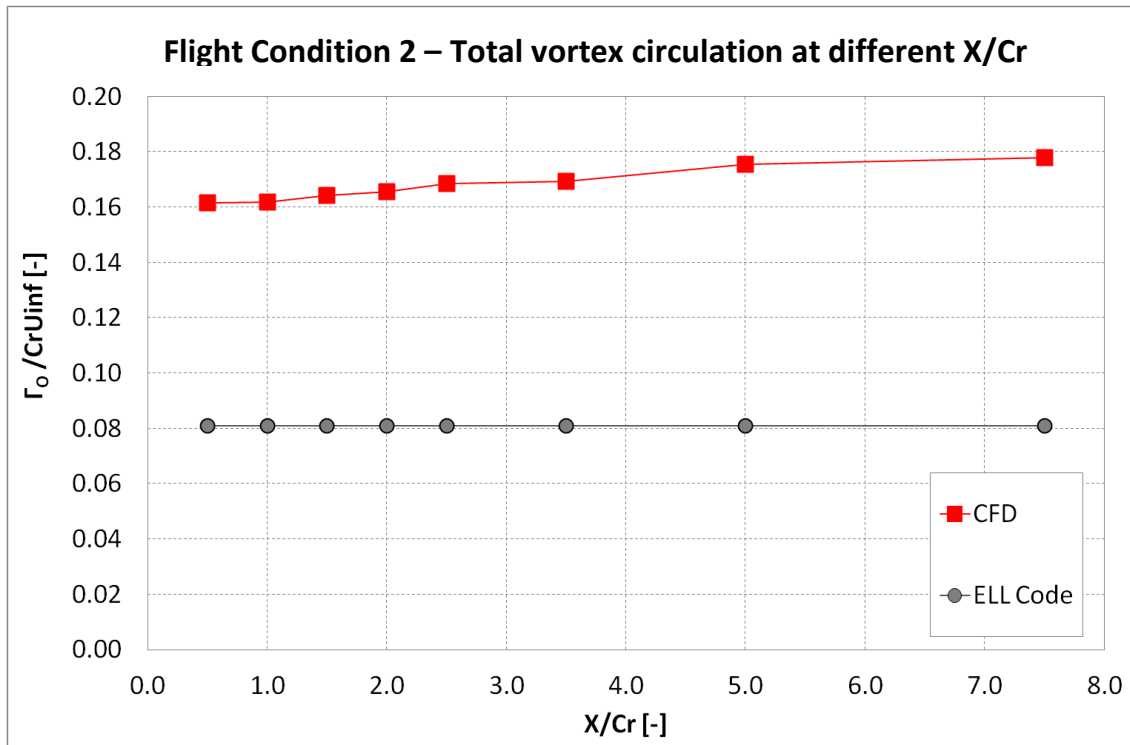


Fig. 7.38 Total vortex circulation at different X/Cr for flight condition 2

7.4.3 Flight condition 3 results

Flight condition 3 has an angle of attack of 3.5° and a free-stream Mach number of 0.548 with a CL of 0.5 (Table 7.6). The downwash plots show that at the $X/C_{ref}=0.5$ plane the downwash that a following aircraft or the hose could suffer is up to 7° , while in the $X/C_{ref}=5$ plane the maximum value of the downwash is 5° . In comparison with the CFD, the ELL code underestimates the values of the downwash, with differences up to 40%, but the general wake flow-fields are similar (Fig. 7.39). This trend is confirmed also from the extrapolated V_y and V_z values along a horizontal traverse at $X/C_{ref}=0.5$ (Fig. 7.40). This is the nearest plane behind the wing and is here that the differences between the CFD and the ELL code results are higher. At this plane the V_y and V_z induced velocities values of the ELL code are up to 70% lower than the CFD values.

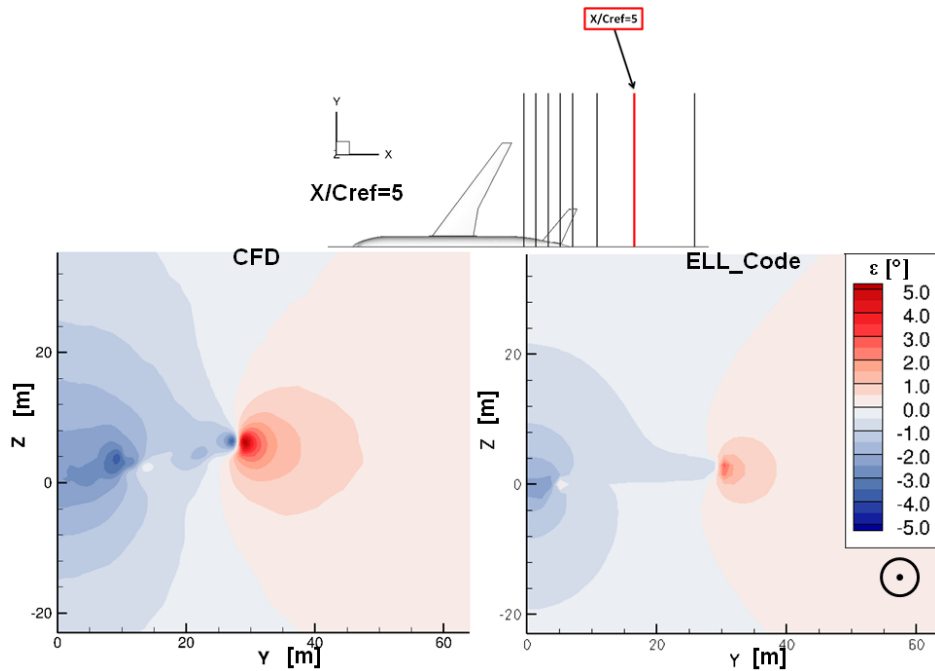


Fig. 7.39 Downwash of the CRM geometry full-scale. Comparison of the CFD and ELL code with fuselage results with flight condition 3 at $X/C_{ref}=5$

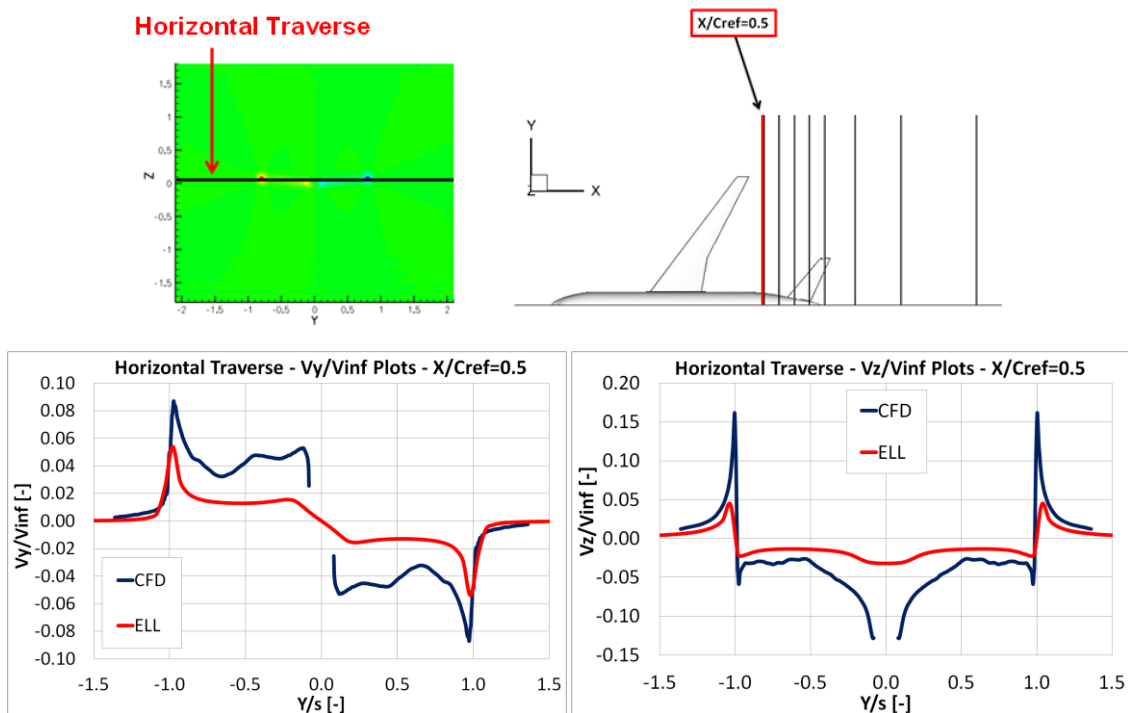


Fig. 7.40 Horizontal traverse V_y and V_z values of the CRM geometry full-scale. Comparison of the CFD and ELL code with fuselage results with flight condition 3

7.4.4 Flight condition 4 results

Flight condition 4 has an angle of attack of 1.07° and a free-stream Mach number of 0.704 with a C_L of 0.3 (Table 7.6). The comparison between the CFD and the ELL code results shows that the findings reported in paragraph 7.3 about the CRM at wind tunnel scale case are confirmed. The qualitative behaviours of the wake flow field of the ELL code and the CFD results are similar in the zones far from the tail and the fuselage and at $X/C_{ref} > 3.5$ (planes that are downstream of the tail). From a quantitative point of view, at this flight condition, the values of the analysed quantities are up to 60% lower in the ELL compared to the CFD ones (Fig. 7.41). This seems to indicate that differences between the ELL and CFD calculations of the wake flow field and tip vortices are greatest at lower angles of attack, where the vortices are less strong and the underestimation of them is proportionally higher. That can be seen also in the vector plots as the vector magnitude is on the same scale for the CFD and the ELL code and the vectors of the ELL have a much lower magnitude compared to the CFD ones, in particular in the planes in the immediate near-field behind the wing (Fig. 7.42). Consequently, although the differences in the magnitude of the perturbation field are proportionally larger, the absolute levels are generally relatively low under these conditions. Fig. 7.43 shows that also for this flight condition the results from the ELL code, using the standard setting (section 7.3), for the CRM clean wing geometry are different from the CFD results.

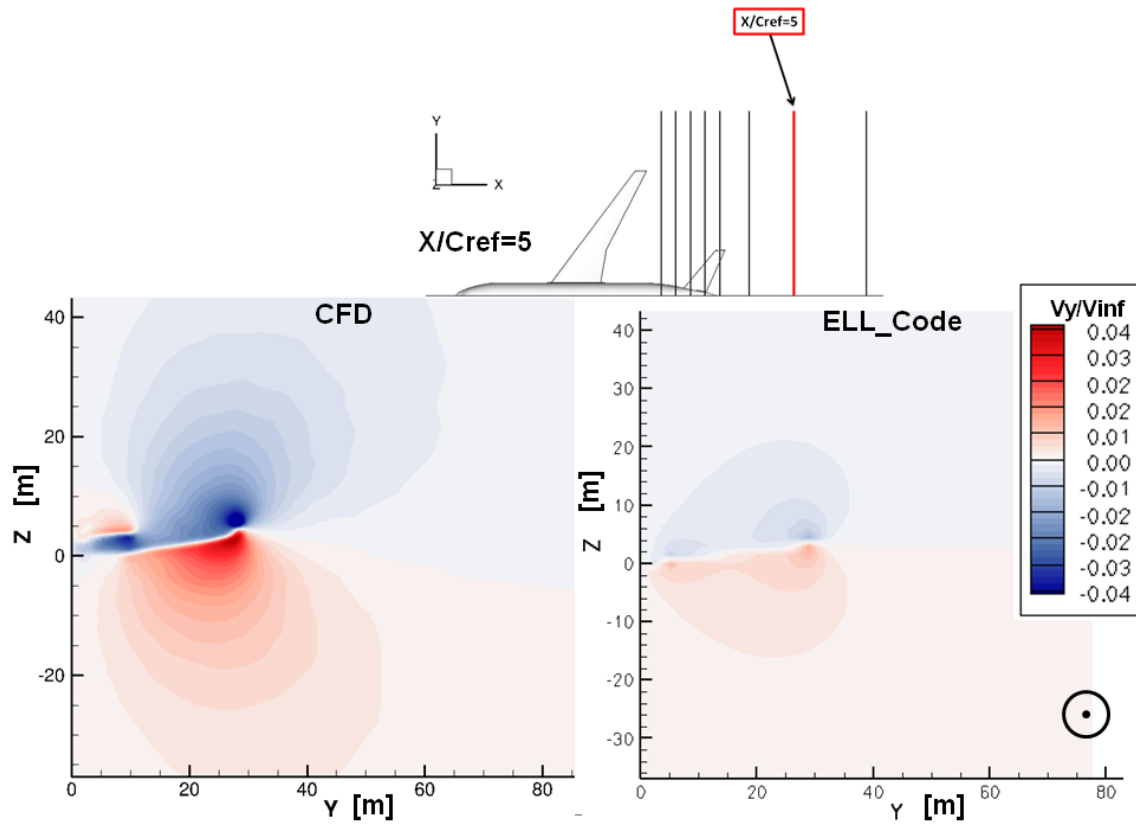


Fig. 7.41 V_y induced velocity of the CRM geometry full-scale. Comparison of the CFD and ELL code with fuselage results with flight condition 4 at $X/C_{ref}=5$

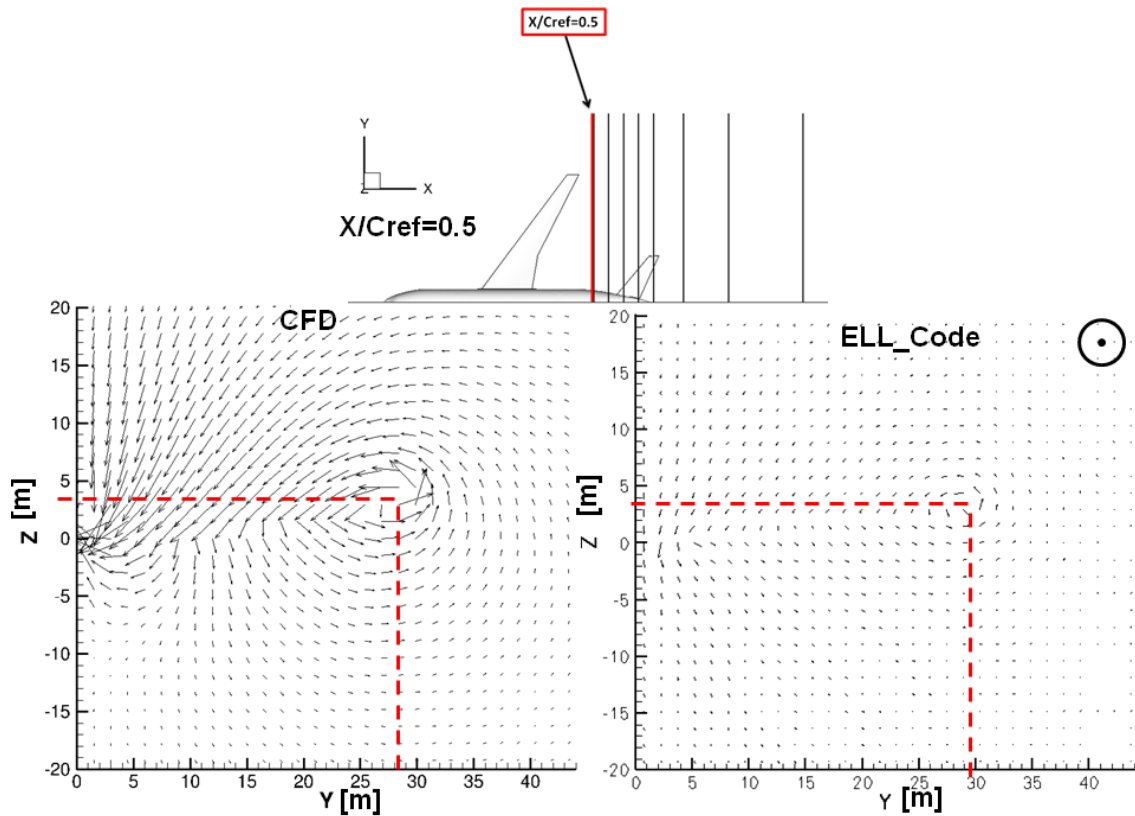


Fig. 7.42 Vectors of the CRM geometry full-scale. Comparison of the CFD and ELL code with fuselage results at flight condition 4 (the vector magnitude is on the same scale) at $X/C_{ref}=0.5$

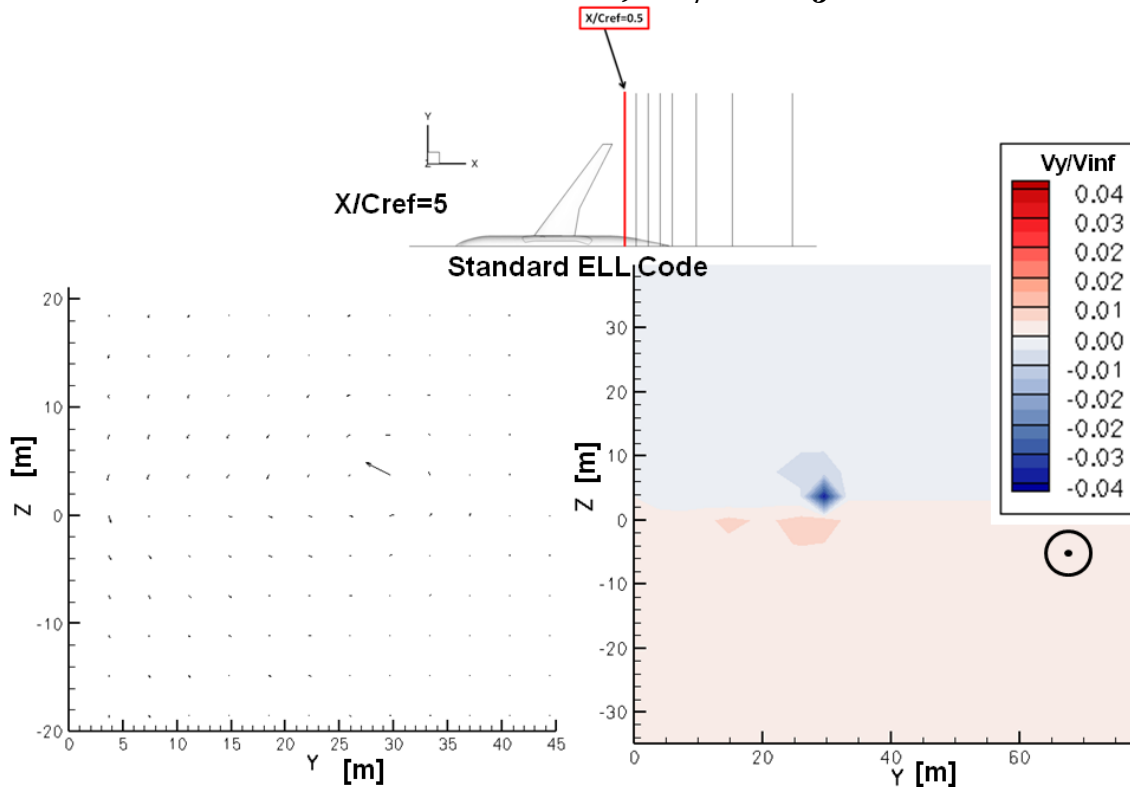


Fig. 7.43 Vectors and yaw angle of the CRM geometry full-scale of the standard settings ELL code with fuselage results with flight condition 1 at $X/C_{ref}=0.5$

7.5 Summary of findings

The evaluation of the ELL code was performed through comparisons with the CFD results of the CRM geometry scaled at wind tunnel conditions and full-scale at air-refuelling flight conditions. Before this evaluation was carried out, a study on the ELL code into the effects of the grid density, the number of vortex panels for each wing, the smallest distance that is allowed between a control point and a vortex filament and the dimension of the domain was performed. The conclusions of the study is that the ELL code, with the standard value of the numbers of panels and a coarse mesh, gives results which are different from the CFD calculations for the wake flow of an aircraft based on the clean wind tunnel model geometry. With a higher number of panels and a finer grid there is better qualitative agreement between the methods, but this leads to a notable increase in the time needed to obtain the solution. The ELL code results obtained with the higher number of panels were used in the comparisons with the CFD simulations. The comparison between the CFD and ELL code results of the CRM geometry scaled at wind tunnel conditions showed that although the ELL code simulates the qualitative characteristics of the wake flow field and the tip vortex, there are notable quantitative differences. This is primarily because the ELL code is a reduced fidelity model that models the vortex as an inviscid, incompressible flow field. The insertion of a fuselage modelled as a flat plate resulted in a notable improvement in the results. Similar observations and comparisons between the CFD and ELL results were made under both wind tunnel cruise conditions as well as under full-scale air-refuelling flight conditions. For low angles of attack, the influence of the tail on the wake flow field is not significant and the tip vortex generated from the tail is not relevant compared to the one produced from the wing. When the angle of attack is increased the influence of the tail increases and the differences between the ELL code and the CFD calculations increase as well.

In conclusion, when using an appropriate setting standard for the ELL code, there are broad similarities between the general flow field of the aircraft wake calculated by the CFD and ELL methods. However, there are quantitative differences in terms of the tip vortex position and the strength of the induced

velocities. The CFD calculates a total tip vortex strength which can be up to 60% times stronger than the ELL results. Similarly, the induced velocities associated with the tip vortex at local points in the flow can be up to 70% times greater than the ELL results.

Chapter 8

Conclusions

8.1 Introduction

The present research has been carried out in the framework of the ASTRAEA II project, in collaboration with Cobham Mission Equipment. One part of the overall ASTRAEA II project is to design an autonomous air-refuelling system based on a wake model computed in real-time, which allows the flow field to be visualised in a Synthetic Environment. In a previous part of the ASTRAEA project a MATLAB® code has been developed based on the extended lifting line method (referred to as the ELL code) which provides a refuelling tanker wake model. The aim of this project was to understand the tanker wake, to provide more detailed flow field predictions and to compare the results with the results from the ELL code to validate this reduced fidelity method. The understanding of the tanker wake and tip vortices has been carried out through the use of computational fluid dynamics (CFD) methods.

8.2 Main findings

A numerical study about the wake and vortices in the near and mid-field of a modern transport aircraft was carried out. The scope of the project was to achieve a validation of the reduced fidelity code (ELL code) through CFD simulations and to develop an improved understanding of the wake flow field of the tanker under refuelling conditions:

The main findings are summarised below:

- The CFD simulations were performed using a geometry definition compatible with the model scale aircraft definitions used in the wind tunnel experiments. These geometries are slightly idealised relative to a full scale aircraft in that

they do not include aspects such as flap track fairings, control tabs and any gaps around control surfaces. High lift devices were not included.

- Based on the geometry definition which was used for the CFD simulations, to achieve a realistic solution, it was needed to run the ELL code with an improved set-up different from the standard one;
- the insertion of a fuselage in the ELL code achieved an improvement in the agreement between the CFD results and the ELL calculations;
- the main differences between the CFD results and the ELL calculations occur in the region of the tip vortex and the near fuselage area;
- the ELL code does not model the roll-up and evolution of the vortex. This results in larger differences in the immediate near-field behind the wing;
- relative to the CFD results, the ELL calculated strength and the intensity of the vortex are underestimated, especially in the immediate near-field of the wake;
- the V_x velocity component variations are not modelled by the ELL method;
- the presence of the tail does not have a significant influence on the wake and the tip vortex for low angles of attack. At higher angle of attack this effect is mostly limited to the tail near field region.

In conclusion, for the geometry considered in this work, there are broad similarities in the wake and tip vortex flow field characteristics calculated using the ELL and the CFD methods. However, the quantitative differences in the local flow field show that the CFD predicted induced velocity perturbations can be up to 70% greater than the ELL results. For the integrated strength of the tip vortex the CFD results are also typically 60% greater than that calculated using the ELL method.

References

- [1] Spalart, P. R., 1998, "Airplane Trailing Vortices", *Annual Review Fluid Mechanics*, 30, pp. 107-124.
- [2] Craft, T.J., Gerasimov, A.V., Launder, B.E., and Robinson, C.M.E., 2006, "A Computational Study of the Near-Field Generation and Decay of Wingtip Vortices", *International Journal of Heat and Fluid Flow*, 27, pp. 684-695.
- [3] Dacles-Mariani, J., Zilliac, G.G., Chow, J.S. and Bradshaw, P., 1995, "Numerical/Experimental Study of a Wingtip Vortex in the Near Field", *AIAA Journal*, 33(9), pp. 1561-1568.
- [4] Baldwin B.S. and Barth, T.J., 1991, "A One-Equation Transport Model for High Reynolds Number Wall-Bounded Flows", AIAA paper 91-0610, January 1991.
- [5] Benkenida, A., Jonville, G. and Darracq, D., 2001, "Numerical Study of Wake Vortices of a Generic Aircraft Model", *19th AIAA Applied Aerodynamics Conference*, 11-14 June 2001, Anaheim, California.
- [6] Shur, M., Strelets, M., Travin, A., Spalart, P., 1998, "Two Numerical Studies of Trailing Vortices", AIAA Paper 98-0595, January 1998.
- [7] Spalart, P., and Allmaras, S., 1992, "A One Equation Turbulence Model for Aerodynamic-Flows", *AIAA Paper 92-0439*.
- [8] Craft, T.J., and Launder B.E., 2001, "Principles and Performance of TCL-Based Second-Moment Closures", *Flow, Turbulence and Combustion*, 66, pp. 355-372.
- [9] Czech, M., Miller, G., Crouch, J., Strelets, M., 2005, "Predicting the Near-Field Evolution of Airplane Trailing Vortices", *C.R. Physique*, 6, pp. 451-466.

-
- [10] Jackson, D. K. J., Tyler, C., and Blake, W. B., 2007, "Computational Analysis of Air-to-Air Refuelling", *25th AIAA Applied Aerodynamics Conference*, 25-28 June 2007, Miami, Florida.
- [11] Saban, D., and Whidborne, J., 2009, "Modeling of Wake Vortex Effects for Unmanned Air Vehicle Simulations", 2009, *AIAA Modeling and Simulation Technologies Conference*, Chicago, Illinois.
- [12] Saban, D., 2010, "Wake Vortex Modelling and Simulation for Air Vehicles in Close Formation Flight", *PhD in Department of Aerospace Sciences*, Cranfield University.
- [13] Venkataramanan, S., and Dogan, A., 2004, "Modeling of Aerodynamic Coupling Between Aircraft in Close Proximities", *AIAA Atmospheric Flight Mechanics Conference and Exhibit*, 16-19 August 2004, Providence, Rhode Island.
- [14] Air-refuelling "flying boom", 2012, available at: <http://www.airforce-technology.com> (accessed on 18/7/2012).
- [15] Air-refuelling "hose-and-drogue", 2012, available at: <http://air-ace.blogspot.co.uk> (accessed on 18/7/2012).
- [16] Bolkcom, C., 2006, "Air Force Aerial Refueling Methods: Flying Boom versus Hose-and-Drogue", *Congressional Research Service, The Library of Congress*.
- [17] Rudnik, R., Sitzmann, M., Godard, J. L., and Lebrun, F., 2009, "Experimental Investigation of the Wing-Body Juncture Flow on the DLR-F6 Configuration in the ONERA S2MA Facility", *27th AIAA Applied Aerodynamics Conference*, San Antonio, Texas.
- [18] Rivers, M. B., and Dittberner, A., 2011, "Experimental Investigations of the NASA Common Research Model in the NASA Langley National Transonic Facility and NASA Ames 11-Ft Transonic Wind Tunnel", *49th AIAA Aerospace Sciences Meeting including the New Horizons Forum and Aerospace Exposition*, Orlando, Florida.

-
- [19] Haag, C., Schwaab, M., and Blake, W., 2010, "Computational Analysis of the Bow Wave Effect in Air-to-Air Refueling", *AIAA Atmospheric Flight Mechanics Conference*, 2-5 August 2010, Toronto, Ontario Canada.
- [20] Hoganson, E. H., 1983, "A Study of the Aerodynamic Interference Effects During Aerial Refueling", *Air Force Institute of Technology Thesis*, GAE/AA/83D-8, December 1983.
- [21] Bloy, A.W., and Trochalidis, V., 1989, "The Performance and Longitudinal Stability and Control of Large Receiver Aircraft During Air-to-Air Refueling", *Aeronautical Journal*, 93, December 1989, pp. 367-378.
- [22] Bloy, A.W., and Trochalidis, V., 1990, "The Aerodynamic Interference Between Tanker and Receiver Aircraft During Air-to-Air Refueling", *Aeronautical Journal*, 94, May 1990, pp. 165-171.
- [23] Blake, W.B., Dickes, E.G., and Gingras, D.R., 2004, "UAV Aerial Refueling – Wind Tunnel Results and Comparison with Analytical Predictions," *AIAA paper*, 2004-4820, August 2004.
- [24] Vachon, M.J., Ray, R.J., and Calianno, C., 2004, "Calculated Drag of an Aerial Refueling Assembly Through Airplane Performance Analysis", *AIAA paper*, 2004-0381.
- [25] Dogan, A., and Lewis, T.A., 2008, "Flight Data Analysis and Simulation of Wind Effects During Aerial Refueling", *Journal of Aircraft*, 45(6), November–December 2008.
- [26] Hoeijmakers, H.W.M., 1996, "Vortex Wakes in Aerodynamics", *Proc The Characterisation & Modification of Wakes from Lifting Vehicles in Fluids*, AGARD–CP–584, pp. 1–12, Trondheim, Norway, May.
- [27] Breitsamter, C., 2011, "Wake Vortex Characteristics of Transport Aircraft", *Progress in Aerospace Sciences*, 47, pp. 89-134.
- [28] Anderson, J.D., 2007, "Fundamentals of Aerodynamics", Fourth ed., Boston: McGraw-Hill.
-

-
- [29] McCormick, B.W., 1994, "Aerodynamics, Aeronautics, and Flight Mechanics", J. Wiley & Sons.
- [30] Jane's Aerospace, 2012, available at: <http://www.janes.com/products/janes/index.aspx>.
- [31] Gerontakos, P., and Lee, T., 2006, "Near-field Tip Vortex Behind a Swept Wing Model", *Experiments in Fluids*, 40, pp. 141-155.
- [32] Weissinger, J., 1947, "The Lift Distribution of Swept-Back Wings", *Technical Memorandum 1120 NACA*.
- [33] Aerospaceweb, 2012, *Airbus A330*, available at: <http://www.aerospaceweb.org/aircraft/jetliner/a330> (accessed on 1/9/2012).
- [34] Gatlin, G. M., Rivers, M. B., Goodliff, S. L., Rudnik, R., and Sitzmann, M., 2008, "Experimental Investigation of the DLR-F6 Transport Configuration in the National Transonic Facility", *26th AIAA Applied Aerodynamics Conference*, Honolulu, Hawaii.
- [35] Vassberg, J. C., DeHaan, M. A., Rivers, S. M., and Wahls, R. A., 2008, "Development of a Common Research Model for Applied CFD Validation Studies", *26th AIAA Applied Aerodynamics Conference*, Honolulu, Hawaii.
- [36] AIAA, 2003, *2nd AIAA Drag Prediction Workshop*, available at: <http://aaac.larc.nasa.gov/tsab/cfdlarc/aiaa-dpw/Workshop2/workshop2.html> (accessed on 1/9/2012).
- [37] AIAA, 2009, *4th AIAA Drag Prediction Workshop*, available at: <http://aaac.larc.nasa.gov/tsab/cfdlarc/aiaa-dpw/Workshop4/workshop4.html> (accessed on 1/9/2012).
- [38] User Manual ANSYS FLUENT 12.1, 2009, ANSYS Inc., Canonsburg, PA.
- [39] Chorin, A. J., 1968, "Numerical Solution of Navier-Stokes Equations", *Mathematics of Computation*, 22, pp. 745-762.

- [40] Barth, T. J., and Jespersen D., 1989, “The Design and Application of Upwind Schemes on Unstructured Meshes”, *Technical Report AIAA-89-0366, AIAA 27th Aerospace Sciences Meeting*, Reno, Nevada.
- [41] User Manual ANSYS CFX , ANSYS Inc., Canonsburg, PA.
- [42] User Manual ANSYS ICEM CFD 12.1, 2009, ANSYS Inc., Canonsburg, PA.
- [43] Menter, F.R., 1993, “Zonal two-equation $k-\omega$ turbulence model for aerodynamic flows”, *AIAA Paper 2906*.
- [44] Menter, F.R., 1994, “Two-equation eddy-viscosity turbulence models for engineering applications”, *AIAA-Journal*, 32(8), pp. 269-289.
- [45] Glauert, T.H., 1926, “The Elements of Airfoil and Airscrew Theory”, *Cambridge University Press*, London.
- [46] Das, A., and Wichmann, G., 2004, “On the Physics and Kinematics of Vortex Motion in the Downstream of a High Aspect Ratio Wing with High-Lift Devices”, *Aerospace Science and Technology*, 8, pp. 489-498.

Appendices

Appendix A

ELL code of the “Gerontakos swept wing”

A comparison between the CFD results of the “Gerontakos swept wing” and the ELL code was carried out as well. Since these comparisons were not carried out with the final version of the ELL code and of the CFD results of the “Gerontakos swept wing”, the results are illustrated in the Appendix. Furthermore, the evaluation of the code based on the simulation of a single wing are not in the purpose of this research. Since the considered geometry is a single wing, no fuselage was included. Table A.1 shows the geometric characteristics of the considered wing. Table A.2 reports the flight conditions applied in the ELL code.

AR [-]	7.308
Taper ratio [-]	0.375
Wingspan [m]	1.021
Wing sweep [deg]	24
Dihedral angle [deg]	0
Wing angle of incidence [deg]	0
Wing twist [deg]	0
Number of vortex panels for each wing [-]	12
Smallest distance allowed between a control point and a vortex filament [m]	0.05

Table A.1 Geometric characteristics of the considered wing

Angle of attack [deg]	8
Angle of sideslip [deg]	0
INDICATED airspeed [m/s]	350.69
Bank angle [deg]	0
Pitch angle [deg]	8
Azimuth angle [deg]	0
GEOMETRIC altitude [m]	0

Table A.2 Flight conditions applied in the ELL code

The results were post-processed and the velocity flow field was analysed on some planes at different downstream locations equivalent to the one analysed by Gerontakos and Lee [31]. Only some of them will be reported in this thesis and they are illustrated in red in Fig. A.1. The CFD results were modified in order to be in the same reference frame of the ELL code.

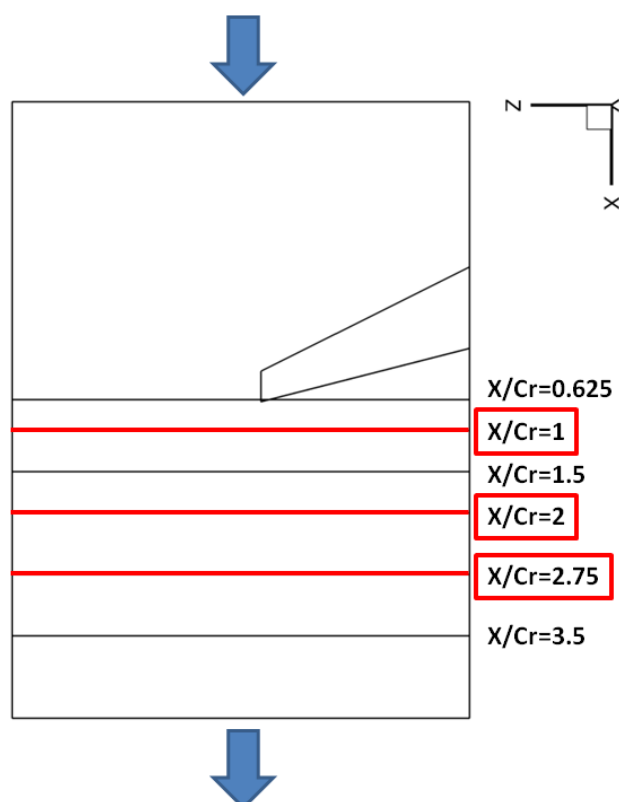


Fig. A.1 Downstream locations of the considered planes

In order to compare the vectors of the ELL code with the CFD, the CFD solution was interpolated on a rectangular grid with the same size of the grid used in the ELL code. From Fig. A.2 to Fig. A.4 the tangential velocity vectors in the three considered planes is shown. The general behaviour and the vortex size of the ELL code is similar to the CFD results, but the location of the vortex centre is slightly different in all the planes.

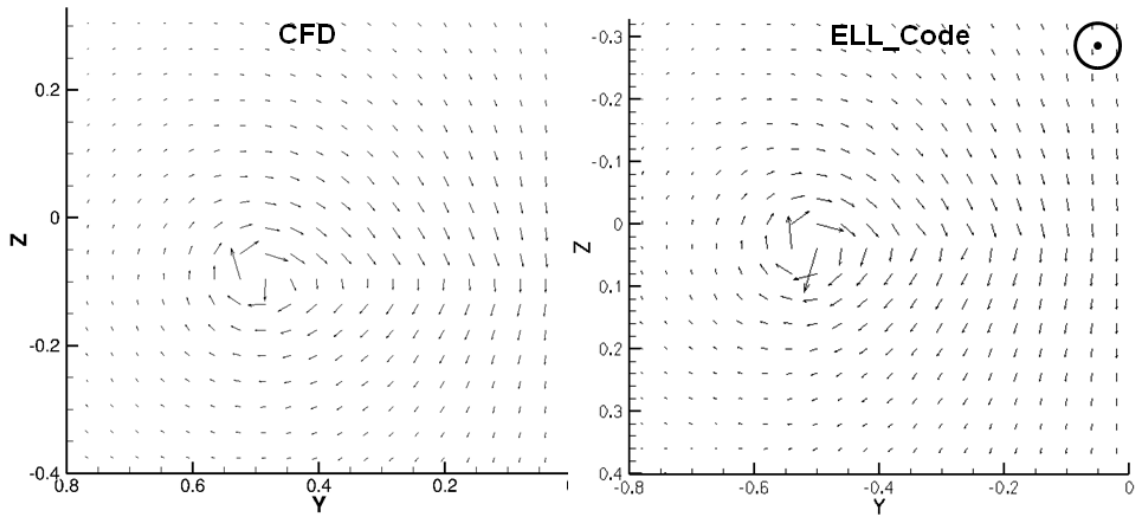


Fig. A.2 Tangential velocity vectors in the $X/Cr=1$ plane (the vector magnitude is on the same scale)

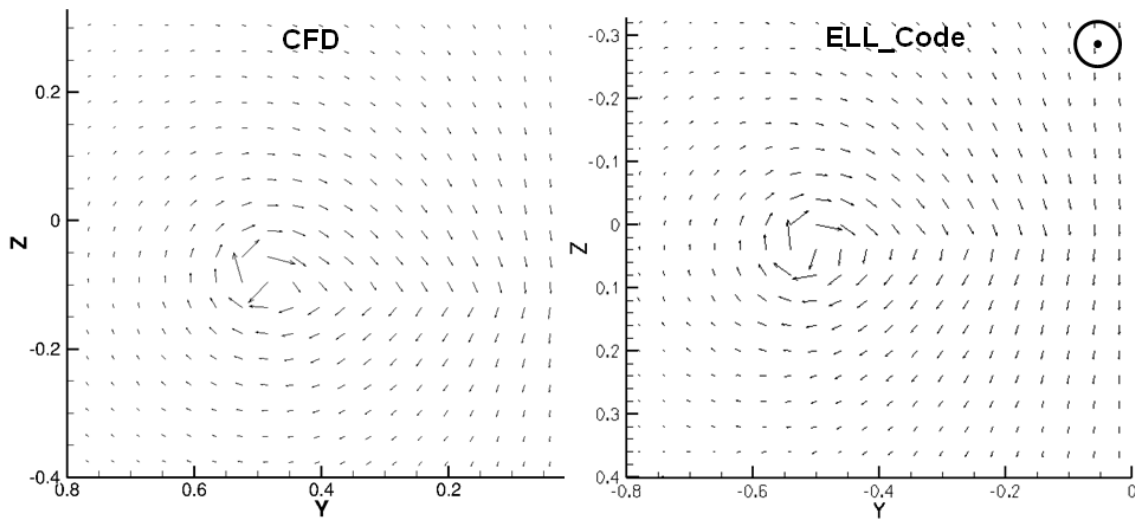


Fig. A.3 Tangential velocity vectors in the $X/Cr=2$ plane (the vector magnitude is on the same scale)

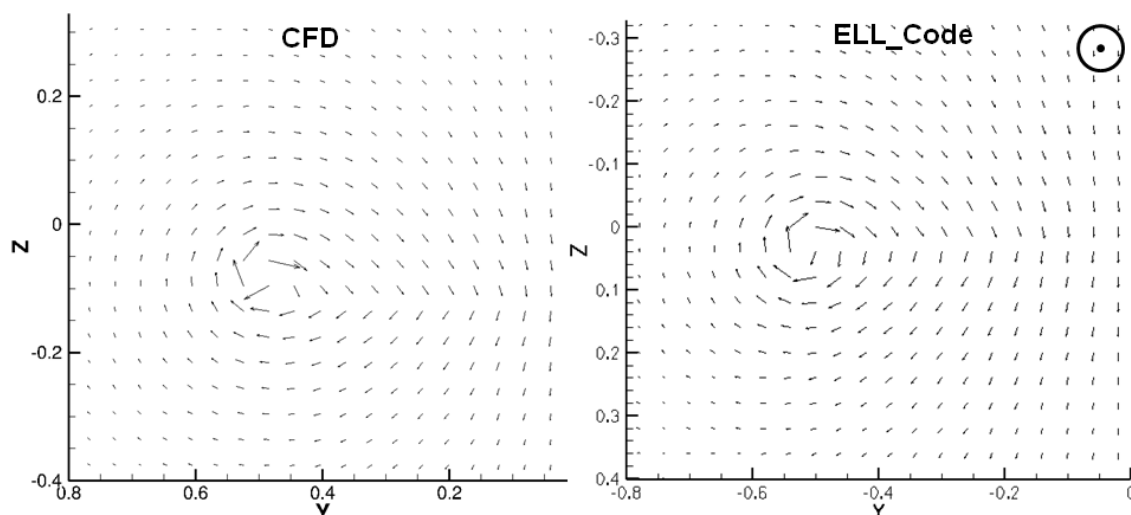


Fig. A.4 Tangential velocity vectors in the $X/Cr=2.75$ plane (the vector magnitude is on the same scale)

From Fig. A.5 to Fig. A.13 the contour plots of the induced V_x , V_y and V_z velocity components in the considered planes are reported. The general behaviour of V_y and V_z in the ELL code is similar to the CFD, but the magnitudes are different. The magnitudes in the ELL code are lower than the CFD. The main differences are in the V_x velocity plots and are due to the presence of the walls and the wing's thickness in the CFD results.

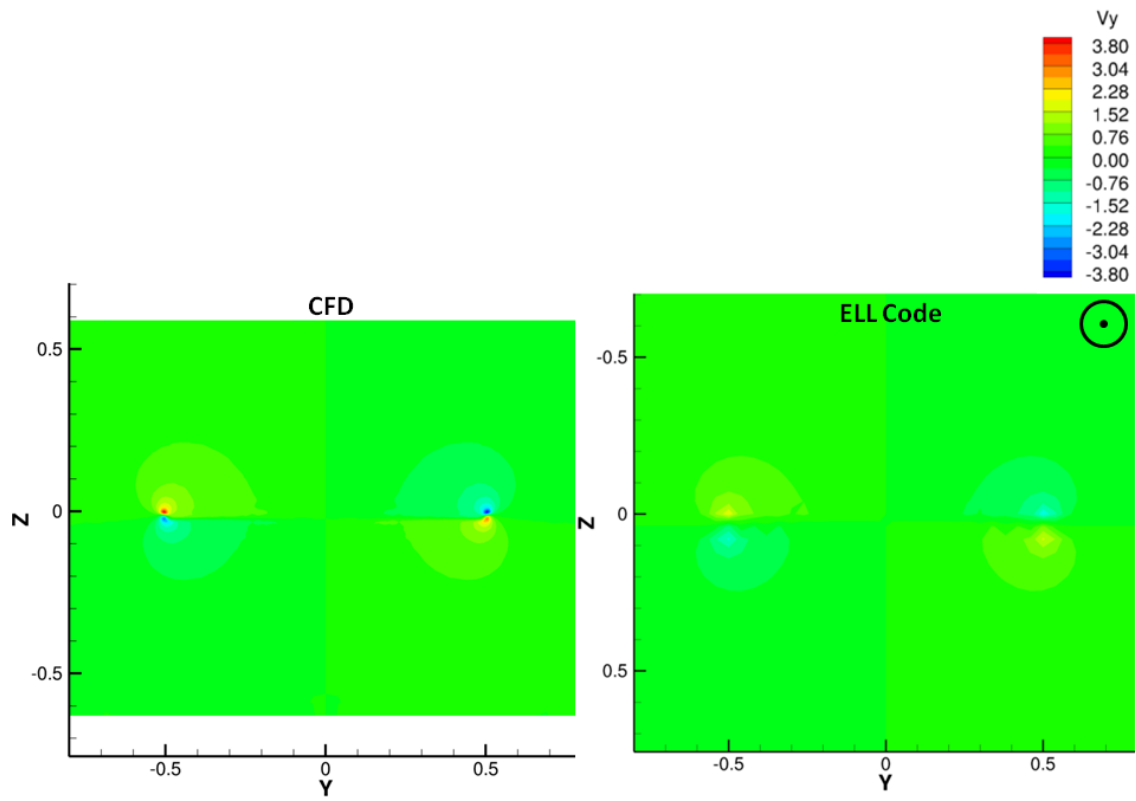


Fig. A.5 V_y velocity component in the $X/Cr=1$ plane

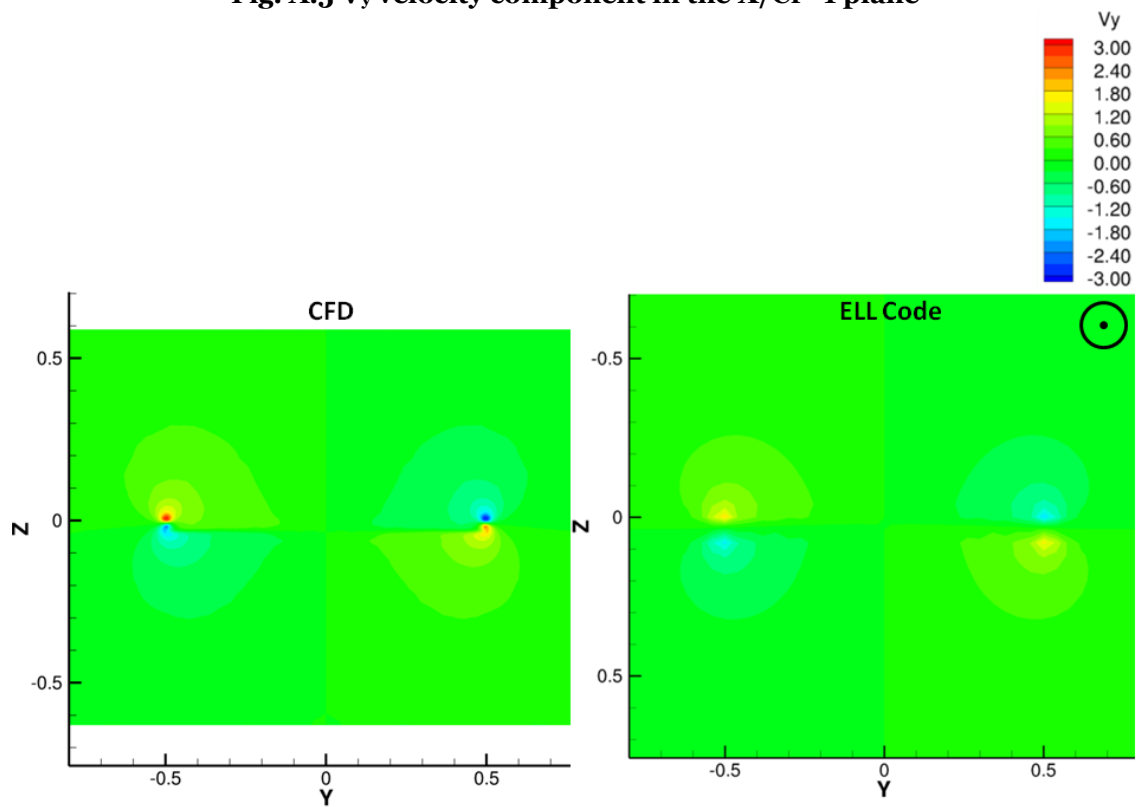


Fig. A.6 V_y velocity component in the $X/Cr=2$ plane

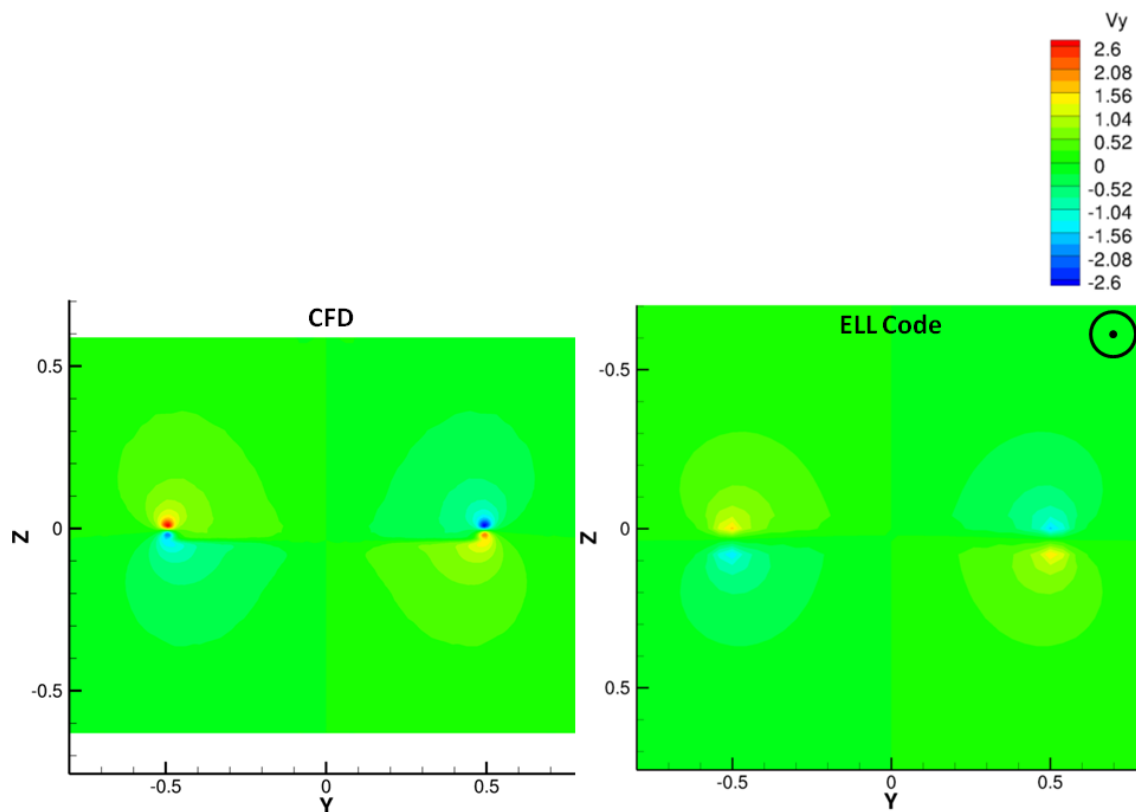


Fig. A.7 V_y velocity component in the $X/Cr=2.75$ plane

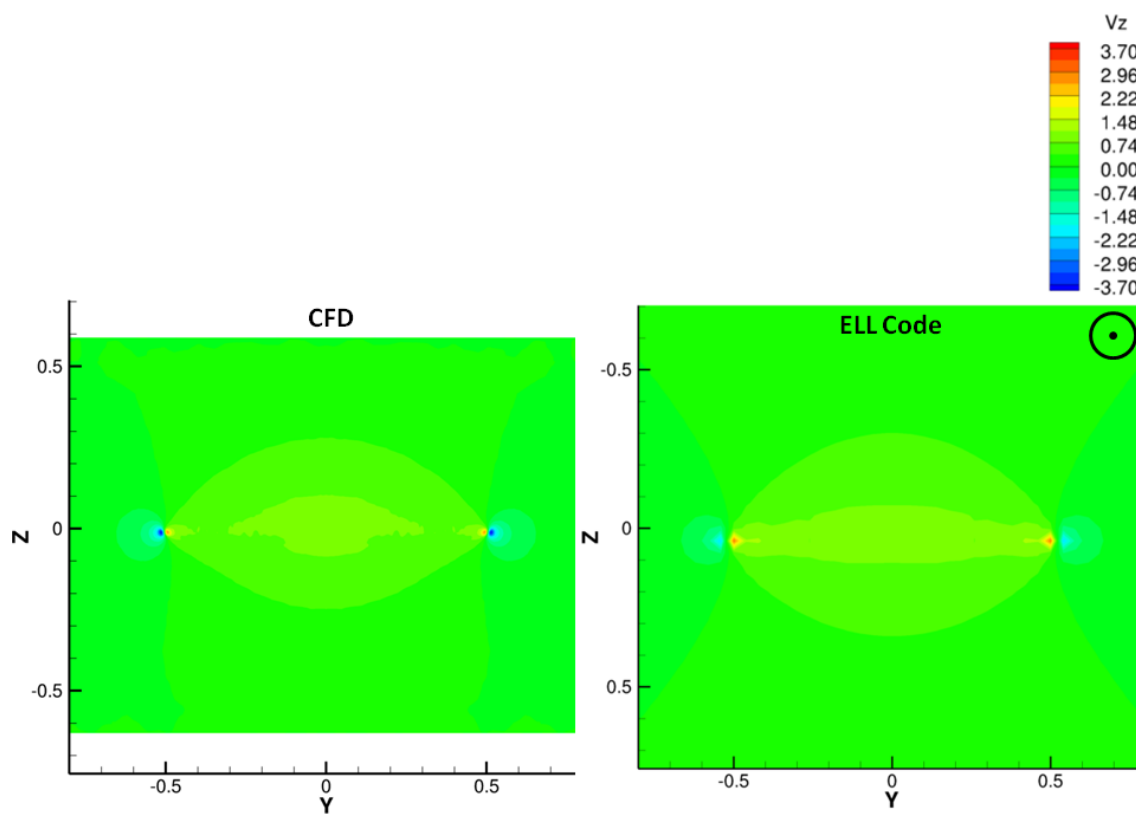


Fig. A.8 V_z velocity component in the $X/Cr=1$ plane

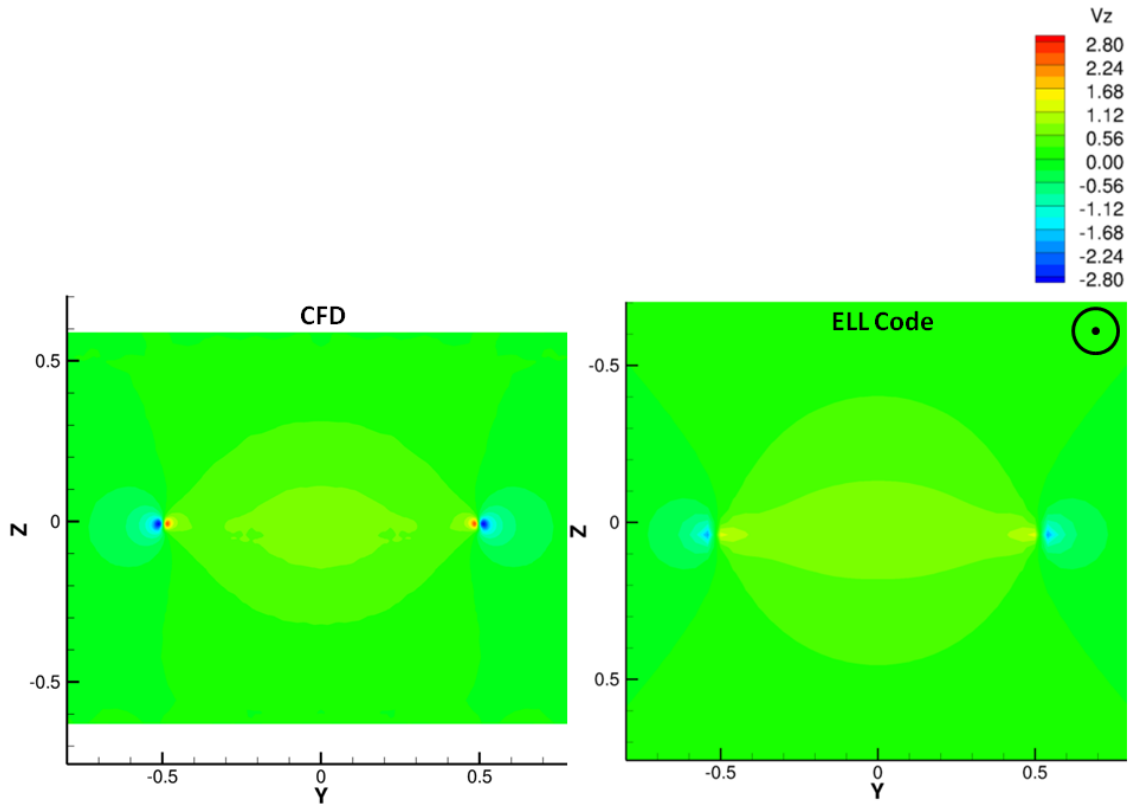


Fig. A.9 V_z velocity component in the $X/Cr=2$ plane

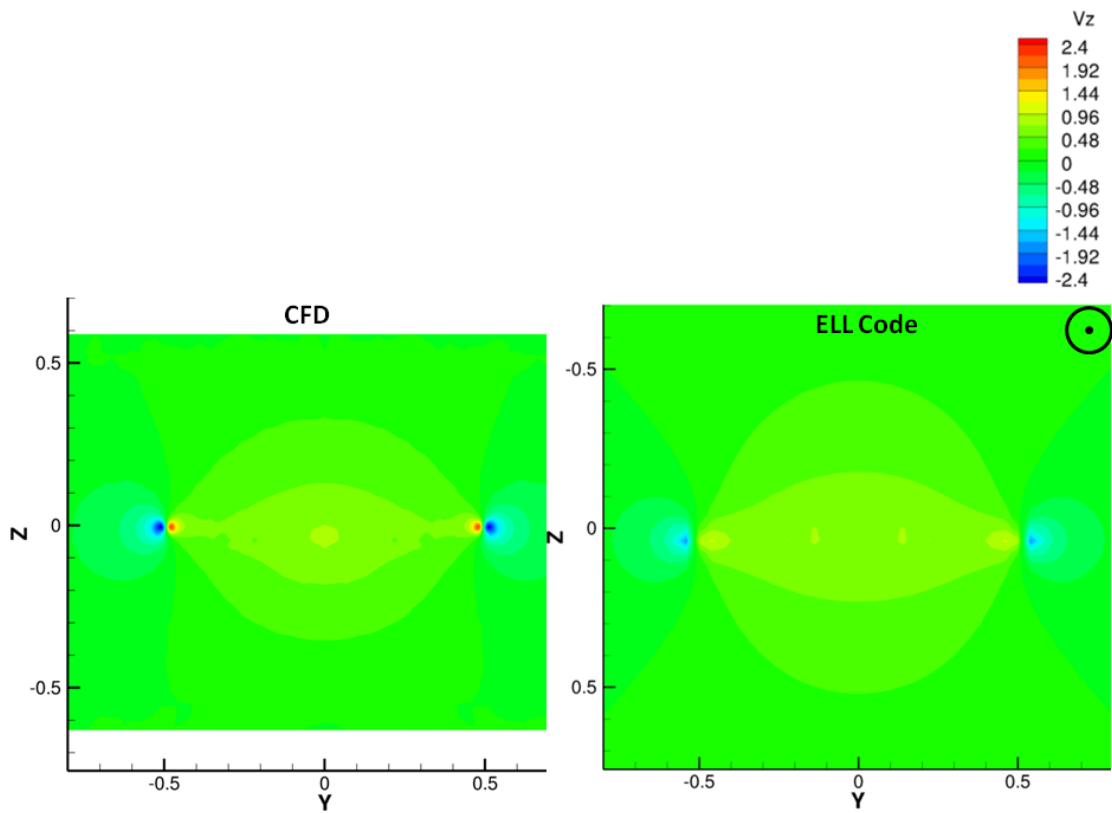


Fig. A.10 V_y velocity component in the $X/Cr=2.75$ plane

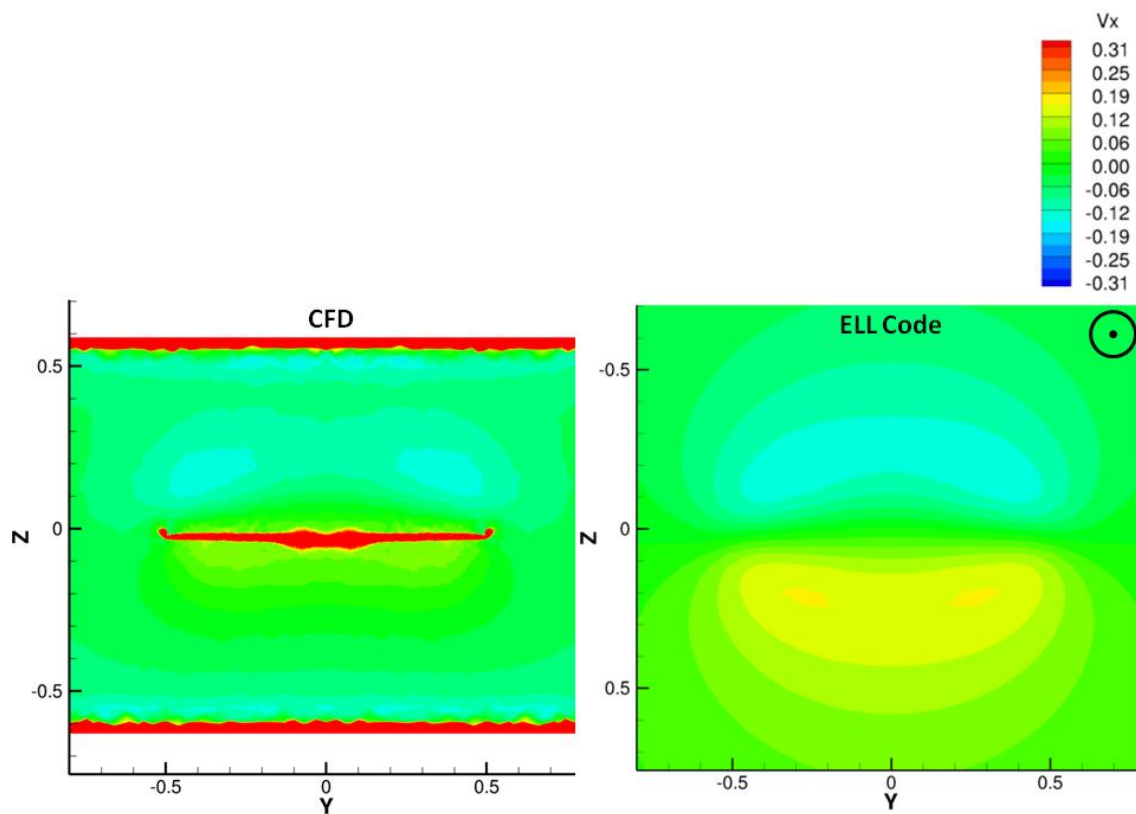


Fig. A.11 V_x velocity component in the $X/Cr=1$ plane

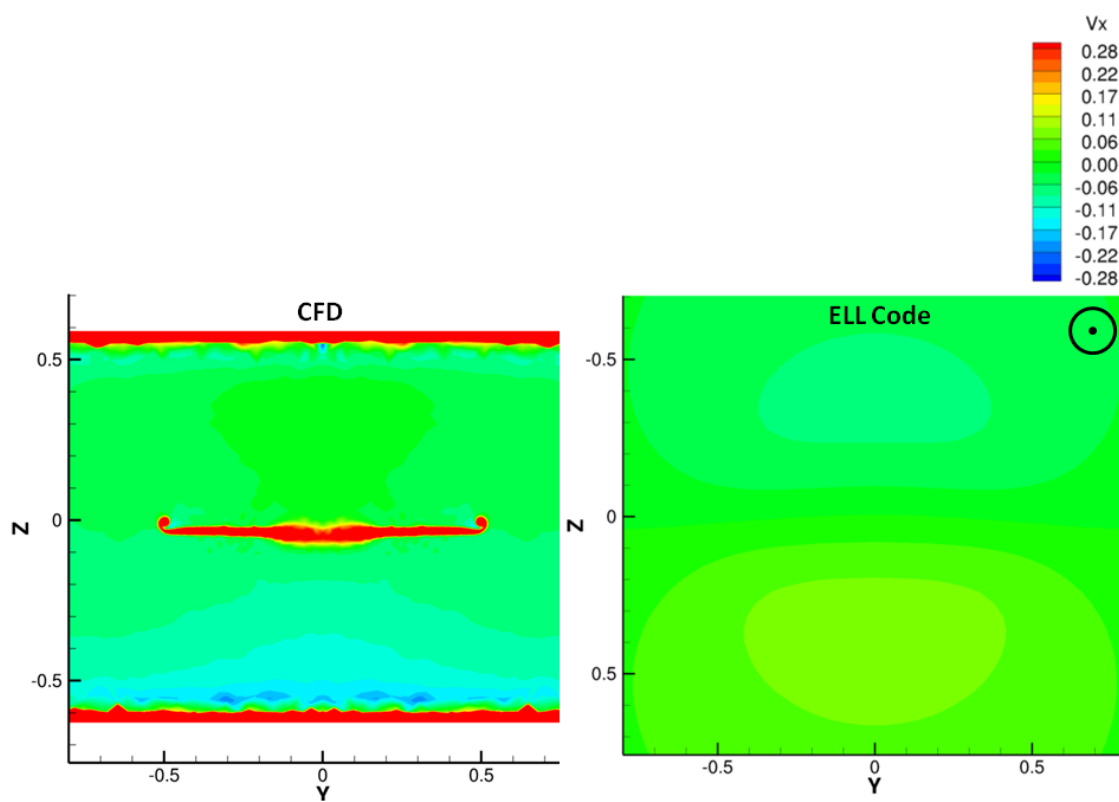


Fig. A.12 V_x velocity component in the $X/Cr=2$ plane

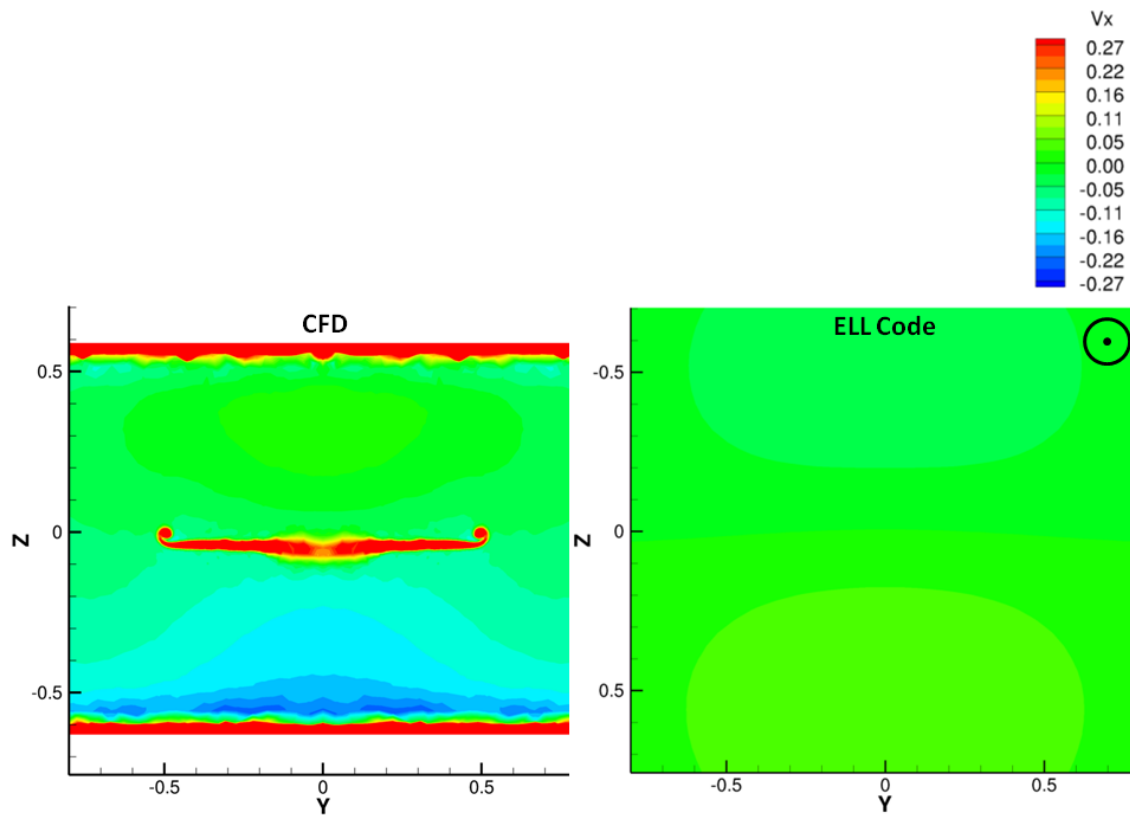


Fig. A.13 V_x velocity component in the $X/Cr=2.75$ plane